Ultrafast terahertz pulse generation from quantum cascade lasers

Feihu Wang

THESE DE DOCTORAT DE

L'UNIVERSITE PIERRE ET MARIE CURIE

Spécialité : **Physique de la Matière Condensée**

Ecole Doctorale 397

Préparée au **Laboratoire Pierre Aigrain**

DÉPARTEMENT DE PHYSIQUE DE

L'ÉCOLE NORMALE SUPÉRIEURE

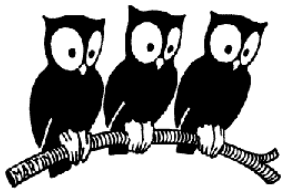

présenté par

Feihu WANG

pour obtenir le grade de

DOCTEUR DE l'UNIVERSITE DE PARIS-VI

Sujet de la thèse :

Ultrafast terahertz pulse generation from quantum cascade lasers

soutenue le 17 Octobre 2016 devant le jury composé de :

Mme. Miriam VITIELLO	Rapporteur
M. Francis HINDLE	Rapporteur
M. William SACKS	Examinateur
M. Daniel DOLFI	Examinateur
M. Arnaud GARNACHE	Examinateur
M. Sukhdeep DHILLON	Directeur de thèse (encadrant)
M. Jérôme TIGNON	Directeur de thèse

Doctor of Philosophy

in Physics

Feihu WANG

Ultrafast Terahertz Pulse Generation From Quantum Cascade Lasers

DEPARTMENT OF PHYSICS OF
L'ÉCOLE NORMALE SUPÉRIEURE

Acknowledgments

During the 3 years and 8 months at the Laboratory Pierre Aigrain, many individuals and organisations that have helped me leading up to this PhD thesis.

First of all, many thanks to all the members of the jury to have carefully reviewed my thesis and given me very useful comments: Miriam Vitiello, Francis Hindle, William Sacks, Daniel Dolfi, Arnaud Garnache, Sukhdeep Dhillon and Jérôme Tignon.

Then I would like to thank the European Union's Horizon 2020 research and innovation programme and the French National Research Agency for funding the scientific projects that I worked on during my PhD in the ultrafast THz group at the department of physics of the École Normale Supérieure in Paris. I would also like to thank the French Ministry of Research and the Doctoral School 397 for funding me through these 3 years.

Here, I would like to take this opportunity to say "merci beaucoup" to Sukhy and Jérôme. Without your help, I cannot successfully complete my thesis and cannot receive my PhD. Sukhy has helped me a lot: organize the experiments, discuss the experimental results and write the scientific articles. Especially, you spent a lot of time on correcting my thesis before the defense. Jérôme has given me a lot of excellent advices and comments on my thesis and how to improve my presentation. Especially you helped me a lot on the administrative work such as renewing my "titre de séjour", signing my doctoral contract, looking for my postdoctoral position.

I would like to thank Jean for helping me a lot with gentile support in research and life during my internship and the beginning of my thesis. We often had dinner together in the canteen of ENS or in a good French or Chinese restaurant. I arrived at LPA the same day with Sarah (you arrived a few minutes earlier than me). During the 3 years, you gave me a lot of help in many aspects, especially helped me prepare the "pot" of my defense. I would like to thank all the other members in the THz group: Juliette (currently, my best publication is with you), Josh (the first person that I worked with in this group), Armand, Matthieu, Kenneth, Anaïs, Pierrick, Valentino, Panhui and Sylvan.

I would also like to thank Simon, Camille in the theory group and Raphaël, Ombline in the optics group. Besides, I would like to thank the administrative and technical staff at laboratory Pierre Aigrain and the physics department: Olivier and Florent for cryogenic support, Anne Matignon and Fabienne Renia for administrative and financial support, Anne Denis, David Darson, Philippe Pace, Pascal Morfin for electronics support.

During these 3 years, our collaborators have provided us excellent samples and allowed us to get very good results. Many thanks to them: Edmund Linfield and Giles Davies's group at the University of Leeds, Raffaele Colombelli's group at the Université Paris-sud, Carlo Sirtori's group at the Université Paris-Diderot, Nathan Jukam's Group at the Ruhr-Universität Bochum, David Ritchie's Group at the University of Cambridge and the III-V Labs at Alcatel-Thales.

Finally, I would like to thank my parents. No one has provided me more love and support than you. Thank you very much!

Feihu WANG

Paris, October 2016

My work place: Department of Physics of the École Normale Supérieure – Paris

Contents

Introduction

The generation of ultrafast and intense light pulses via mode-locking [1] is an underpinning technology throughout the electromagnetic spectrum enabling the study of fundamental light-matter interactions [2], as well as industrial exploitation in a plethora of applications across the physical, chemical and biological sciences [3] [4] [5]. There have been impressive developments in mode-locked semiconductor-based devices for pulse generation in the optical range [6] [7] [8]. These benefit from low system costs and are an enabling technology in new application domains including high speed communications [9] and the potential to replace Ti:Sapphire [10] systems.

In the terahertz (THz) [11] frequency range (~0.5-5 THz), with its proven applications in areas such as imaging, metrology and non-destructive testing [12] [13], a semiconductor based technology platform for intense and ultrashort pulse generation has yet to be realised. This is in contrast to the optical and near-infrared domain where ultrashort pulse generation exists from devices such as external cavity VECSELS [14] [15] [16]. Ultrafast excitation of photoconductive switches [17] or nonlinear crystals [18] offer only low THz powers (~µW), low frequency modulation and broadband emission with little control of the spectral bandwidth. The latter is a particular disadvantage for metrology, fundamental material excitations or THz communications where select frequency bands are required. An alternative approach is based on free electron lasers [19] or large table-top optical ultrafast laser systems. While ultrashort and intense pulses with controlled frequencies can then be realised, the size and costs involved inhibit commercial uptakes, and often render impossible, their use for many applications.

THz quantum cascade lasers (QCLs) [20] [21] are a foundational semiconductor device for laser action in the THz range. These devices, first realised in 2002, are one of the only practical semiconductor systems that offers gain in the THz range, hence making them suitable medium for pulse generation. The ‘band structure-by-design’ nature of QCLs allows the frequency, and bandwidth to be entirely engineered. However, THz pulse generation via passive mode-locking of these devices is difficult. This is a result of the QCL’s ultrafast gain recovery time being up to an order of magnitude shorter than the photon round-trip time [22] [23], which inhibits stable pulse generation. Current solutions to generate pulses from THz QCLs, based on active mode-locking with microwave frequencies [24] [25], have been limited to large pulse widths no matter the gain bandwidth. To date, the generation of THz pulses from QCLs has been limited to ~10 - 20 ps despite several years of research effort [26] [27]. The first devices that could be mode-locked had low spectral bandwidths. Although THz QCLs with extremely large gain bandwidths have been realized for frequency comb generation, this has not translated directly into the formation of stable short pulses in the THz range [28] [29].

In this thesis, I will show how this bottleneck in QCL technology can be overcome and demonstrate a novel method to realize ultra-short pulses in the THz range from this compact

semiconductor device. This is based on a coupled cavity scheme that permits THz pulses that are considerably shorter than the state-of-the art. I will further show the potential roles of dispersion compensation and hybrid mode-locking of a mode-locked THz QCL using a Gires-Tournois interferometer (GTI) and an air-gap loss modulator, respectively. The GTI and air-gap are monolithically integrated with the QCL and permits stable pulse generation with pulse widths as short as ~ 4 ps. This flexible approach of on-chip passive modulation and dispersion compensation opens up a direct route to the generation of sub-picosecond pulses in the terahertz range from a semiconductor source. Furthermore, ultrashort THz pulses from QCLs will permit THz frequency comb spectroscopy that are engineered and controlled by microwave signal generators.

Towards this final objective and realization of my thesis, I will also show several milestones that permitted our goal of short pulses from QCLs to be achieved. Starting off from the current state-of-the-art, using narrow spectral bandwidth QCLs in single-plasmon waveguides, I will demonstrate ~20 ps long THz pulses at low temperatures (~10K). This is followed by, for the first time, mode-locking of broad spectral bandwidth QCLs in sub-wavelength metal-metal waveguides at 'high' temperatures (77K). As a result, we will show ~ 11 ps that are limited by the electrical modulation and the index dispersion and, importantly, not limited by the inherent spectral bandwidth. This will then bring us to resolve these limitations and generate ultrashort pulses (~4 ps) with the potential to go considerably further to the single-cycle regime.

This manuscript consists of 7 chapters that can be divided into 2 parts. The first part, chapters 1, 2 & 3, consists of the background knowledge and the foundations for this thesis. The THz QCL (chapter 1), the ultrafast detection scheme employed for the time resolved QCL emission (chapter 2), and the principle of mode-locking (chapter 3) will be presented, respectively. The second part, chapters 4, 5, 6 & 7, present the experimental results taken over the thesis period. The first three of these (chapters 4, 5 and 6) are the dedicated to mode-locking demonstrations and present the reduction of the THz pulse width, step by step, from ~ 20 ps down to ~ 4 ps through the advances detailed above. Finally, chapter 7 is an independent study of the far-field of metal-metal QCLs and how they can be simply engineered for high power output while conserving a broad spectra response. I will give a brief introduction to each chapter separately below.

Chapter 1 – THz QCLs: This chapter will give a brief introduction to THz QCLs. The THz range will be introduced (section 1.1) and inter-subband transitions in quantum wells will be discussed and how they can be engineered for energies in the THz range (section 1.2). In section 1.3, the working principle, the active regions, the waveguides and geometries of THz QCLs will be presented in detail. At the end of this chapter (section 1.4), the active layer growth technologies and ridge processing steps will be briefly discussed.

Chapter 2 – Ultrafast detection of THz QCL emission: To demonstrate mode-locking of THz QCLs and investigate their ultrafast properties on the femtosecond (*fs*) scale, ultrahigh-speed THz detectors are needed. However, there is currently a lack of such THz detectors. In order to solve this problem, I will describe a time-resolved *injection seeding* system, developed in

our group, that allows us to coherently detect the QCL's electric field in the time domain with a *femtosecond* resolution. I will detail this coherent detection technique, based around time domain spectroscopy (TDS) for the generation and detection of phase resolved THz pulses using femtosecond lasers. These pulses are injected into the QCL waveguide, permitting to lock the QCL emission to the femtosecond laser, and hence detect the emission in the time domain. Finally, as an example, the time-resolved emission of a QCL will be experimentally demonstrated.

Chapter 3 - Principles of mode-locking: This chapter will be used to discuss the principles of mode-locking in the time and frequency domains. The role of the ultrafast gain recovery time of QCLs will be presented and why passive mode-locking is difficult. Mode-locking will be briefly presented (section 3.1) followed by a more in-depth discussion (section 3.2) by introducing the susceptibility of an active medium and the resulting dispersion in the Fabry-Pérot cavity. Finally, in section 3.3, the application of passive and hybrid mode-locking to generate ultrafast laser pulses from violet to near-infrared ranges will be mentioned.

Chapter 4 - Active Mode-locking of Narrowband single plasmon THz QCLs: Active mode-locking of narrow spectral bandwidth QCL will be shown with the resulting demonstration of ~20 ps THz pulses at 10 K. The QCL active region, based on bound-to-continuum design that results in narrow spectrum, will be described. This is placed in a single plasmon waveguide where the overlap of THz mode with the active region is low. I will further show the possibility to continuously tune the mode spacing (longitudinal modes) of the QCL emission beyond a range of ~2 GHz by varying the active modulation frequency from 12 GHz to 14 GHz. This tuning effect will be employed in gas spectroscopy to characterize their absorption properties.

Chapter 5 - Active Mode-Locking of Broadband metal-metal THz QCLs: Active mode-locking of broadband QCLs will be shown with an aim to realize few picosecond long THz pulses at high temperatures (77 K). The QCL active region here, a LO phonon depopulation design that inherently possesses a large spectrum at a center frequency of 2.7 THz, will be described. The active region is placed in a metal-metal waveguide which strongly confines the THz modes, as well as acting as a cavity for the active (gigahertz) modulation. Prior to active mode-locking, the coherent detection of a 'free running' QCL (i.e. no active microwave modulation) will be presented to show the mode spacing and the broadband spectrum. I will also show how this permits access to the ultrafast gain recovery time. Active mode-locking of these structures will then then demonstrated with the generated THz pulses limited to ~11 ps, much wider than expected (sub 5ps). From these results I will present the mode-locking mechanism and the key limitation for generating ultrashort THz pulses from these QCLs. Finally, I will carry out the active mode-locking experiments on a different set of broadband QCLs operating at 2.45 THz with similar results to further confirm our hypothesis.

Chapter 6 – Ultrashort THz pulse generation from mode-locked THz QCLs: In the previous chapter, ultrashort THz pulses were not observed, despite very large spectral bandwidth QCLs. In order to break this strong limitation of active mode-locking, the main aim of this thesis, I will introduce a new scheme based around a coupled cavity approach that drastically shortens the THz pulses from a mode-locked THz QCLs down to below 5 ps. The key geometry of our

device will be described, which employs a metal-metal QCL monolithically divided into a large laser cavity (~3 mm long) and a short cavity (~tens of microns long) that are separated by a small air gap (~2 μm air gap). The QCL active region will be briefly discussed, and is identical to the 2.45 THz broadband design of chapter 4. Mode-locking will then be presented for a passive geometry (and compared to a standard QCL) showing sub 5ps pulses. Correspondingly the spectrum is enlarged considerably to ~350 GHz (full width). To further prove the applicability of this concept (air gap and coupled cavity), I will describe its use in a second QCL with operation at 3.25 THz that also shows ultrashort pulse generation. Finally, I will present the exact role of the short cavity and the air-gap which introduces dispersion compensation and a sharp passive modulation.

Chapter 7 - Far-field Engineering of metal-metal waveguide THz QCLs: An important advantage of metal-metal waveguide THz is that they show high temperature operation (up to ~200K). However, their far-field patterns are highly diffracted and output powers are weakly coupled out, owing to impedance mismatching between the strongly confined cavity mode and the free-space radiative mode. These shortcomings prevent many important applications of THz QCLs at temperatures above 77K, where convenient and cost effective cryocoolers can be used. The aim of this chapter is to show that the far-field emission profile of THz QCLs in metal-metal waveguides can be controlled in directionality and form through planar horn-type shape structures, whilst conserving a broad spectral response for eventual ultrafast THz pulse generation. These structures produce a gradual change in the high modal confinement of the waveguides and permit an improved far-field emission profile and resulting in a four-fold increase in the emitted output power. The two-dimensional far-field patterns are measured at 77 K and are in agreement with 3D modal simulations. The influence of parasitic high order transverse modes is shown to be controlled by engineering the horn structure (ridge and horn widths), allowing only the fundamental mode to be coupled out.

1

Terahertz Quantum Cascade Lasers

Terahertz quantum cascade lasers (THz QCLs) are relatively recent THz sources based on inter-subband transitions in semiconductor quantum wells (i.e. GaAs/AlGaAs). This compact quantum device was experimentally demonstrated in 2002 and now is one of the most promising sources for the THz range. The laser transition takes place between two artificial subband energy levels as a result of quantum confinement of the electrons in a set of quantum wells. Their emission frequencies can therefore be easily engineered by simply varying the width of the quantum wells, permitting to cover most of the THz spectrum without introducing any other new materials. This is in contrast to conventional semiconductor lasers (i.e. laser diodes) where the emission frequencies are completely determined by the band gap between the conduction and valence band of the material.

The aim of this chapter is to give a brief introduction to THz QCLs. The THz range will be firstly introduced in section 1.1 and in section 1.2 inter-sub-band transitions in quantum wells will be discussed. In section 1.3, the working principle, the range of active regions, different waveguides and geometrical shape of THz QCLs will be presented in detail. At the end of this chapter, in section 1.4, the active layer growth technologies and ridge processing steps will be briefly discussed.

Chapter 1

1.1 Introduction

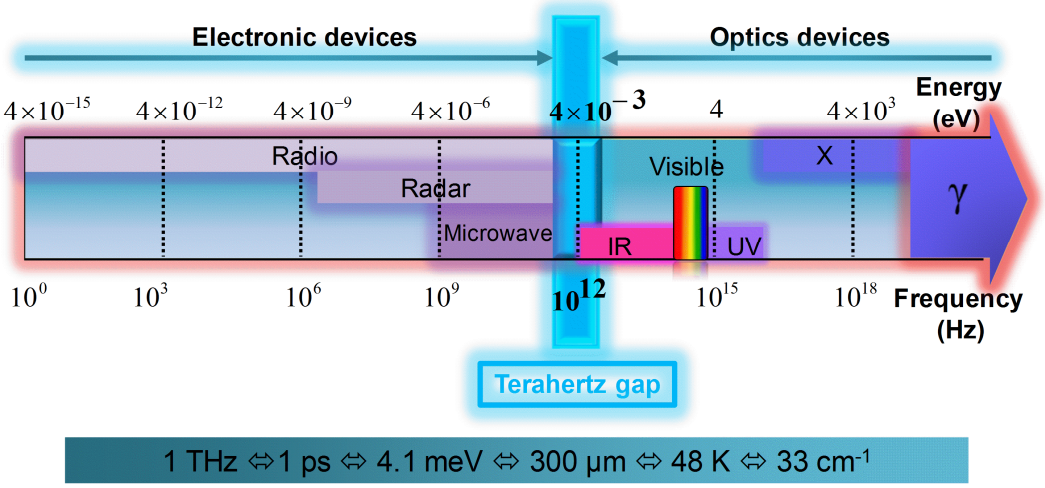

Fig 1.1 | Electromagnetic spectrum from radio-frequency to γ-rays. The terahertz range lies at the interface of microwaves and mid-infrared.

Terahertz (THz) is a unit of frequency and 1 THz = 10^{12} Hz, corresponding to a wavelength of 300 μm and a single photon energy of ~4.1 meV [11]. The THz range is located at the interface of electronic (microwaves) and optical (mid-infrared) waves as illustrated in Fig 1.1. This special location in the electromagnetic spectrum results in unique properties (i.e. strong gas absorptions, non-destructive penetration into materials etc.) that can be widely employed to study fundamental physics and develop cutting-edge technologies [12].

However, the THz range (loosely defined as 0.5 THz – 10 THz) is the least developed electromagnetic range owing to the lack of promising sources and detectors. As presented in Fig 1.1, for frequencies below the THz range, electronic devices [30] are commonly utilized as sources and for those above the THz range, lasers or photonics devices are widely used. However, THz frequencies are too high for electronic devices to reach and, for photonic devices, there is currently no practical material whose band gap is as low as a few meV for THz transitions.

In 1994, the first quantum cascade laser (QCL) [21], with emission in the mid-infrared (~4 μm, 2340 cm^{-1}), was realized at Bell Laboratory by *J. Faist* et al, over 20 years after the initial theoretical proposition. This unipolar semiconductor device was based on inter-subband transitions in quantum wells [31], instead of inter-band transitions between conduction and valence bands of standard laser diodes [32] [33]. Its emission frequencies and bandwidth could be therefore easily engineered by changing the width of the quantum wells, instead of changing the semiconductor materials. This breakthrough overcame the 'bandgap slavery' limitation of the wavelength (or frequency) emission of semiconductor lasers. Since 1994, there have been considerable achievements in the performance of QCLs as shown in Fig 1.2 below, including

significant increases in output power [34], max operating temperature [35] [36] and emission wavelength range [37].

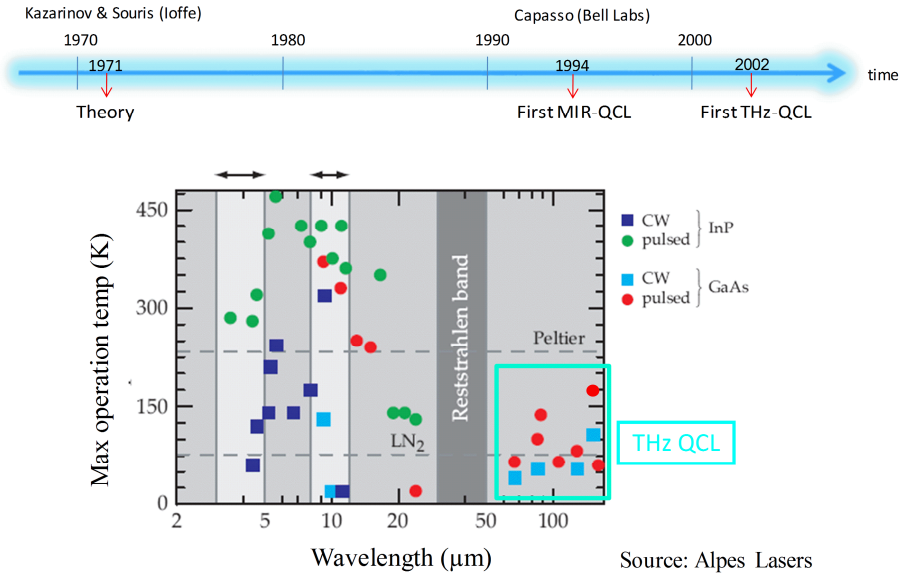

Fig 1.2 | Maximum working temperature of QCLs as a function of wavelength. The THz range corresponds to wavelengths longer that the Restrahlen band (~ > 50μm).

In 2002, the concept was extended to the THz range with the first compact THz semiconductor laser – the THz QCL [20]. This was experimentally demonstrated by *Köhler* et al at Scuola Normale Superiore of Pisa about 8 years after the first QCL. This promising THz source is compact, powerful and coherent, permitting a plethora of possible applications. In this chapter, I will focus on THz QCLs, introducing its working principle, the type of active region, different waveguides, geometric characteristics and presenting its fabrication technologies.

1.2 Inter-sub-band transitions

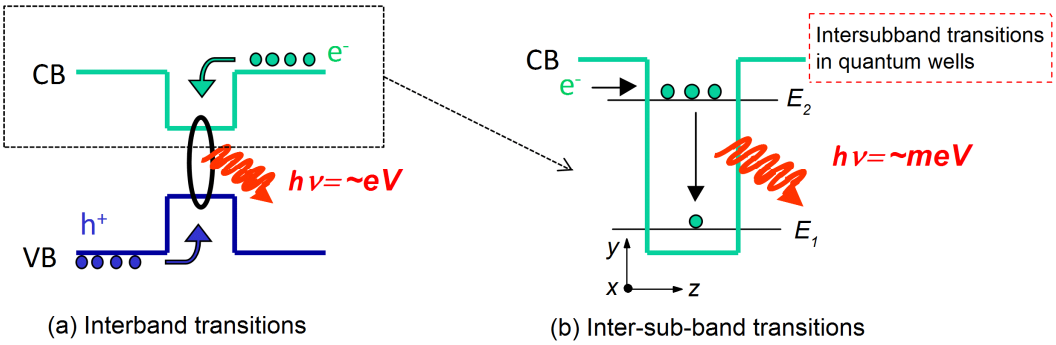

Fig 1.3 | Schematic of laser transitions in semiconductor materials. (a) Inter-band transitions between the valence band (VB) and conduction band (CB). (b) Inter-subband transitions between 2 artificial energy levels in a set of quantum wells.

Classical semiconductor lasers ('laser diodes') are based on inter-band transitions [32]. The recombination of an electron in the conduction band (CB) and a hole in the valence band (VB) will result in the emission of a photon whose frequency (or energy) is completely determined by the band gap of the semiconductor materials as schematically demonstrated in Fig 1.3 (a). If we wish to change the emitted frequency of a semiconductor laser, materials with different band gap are required ("bandgap slavery"). Generally, the band gap of semiconductor materials ranges from ~0.3 eV to a few eV in nature. By employing different semiconductor materials such as GaN/AlInGaN, InP/GaInAsP, laser emission can be varied in a broad frequency range from the ultraviolet to the mid-infrared [33]. However, the far-infrared/THz frequency range cannot currently be reached with such a concept owing to no practical material that possesses a band gap as small as ~ meV for THz emission.

Although it is difficult for semiconductor lasers based on inter-band transitions to emit THz waves, inter-sub-band transitions in quantum wells (made of semiconductor materials GaAs/AlGaAs or InGaAs/InAlAs) are a promising solution, as illustrated in Fig 1.3 (b). In a quantum well, the electronic energy levels are discrete owing to quantum confinement at the nanoscale, which can be described by the wave functions in Schrödinger equation:

$$H_0\psi(\mathbf{r}) = \left(\frac{p^2}{2m_0} + V(\mathbf{r})\right)\psi(\mathbf{r}) = E\psi(\mathbf{r}) \tag{1.1}$$

where p is the momentum, m_0 is its mass, $V(\mathbf{r})$is the potential, E is the energy of electron and $\psi(\mathbf{r})$ is its wave function. By applying Eq. (1.1) only to the confinement direction z as shown in Fig 1.3, the vector equation can be further modified to a scalar equation for simplicity:

$$\left(\frac{-\hbar^2}{2\mathrm{m}^*}\frac{\partial^2}{\partial z^2}+V(z)\right)\psi_n(z)=E_{z,n}\psi_n(z) \tag{1.2}$$

where $\hbar$ is the reduced Planck constant, m^* (m^*=0.067m for GaAs material) is the effective electron mass in the quantum well, $E_{z,n}$ is the eigen-energy of the n^{th} order sub-band level and n is the quantum number. For a given quantum well with a width of L (z=L) and an infinite potential, the eigen-energy of electrons in the quantum well can be expressed as:

$$E_n=\frac{\hbar^2\pi^2n^2}{2m^*L_z^{\,2}} \tag{1.3}$$

From Eq. (1.3), we can see that by choosing an appropriate width of the quantum well (generally a few *nm* for the GaAs/AlGaAs material system), we can engineer the inter-subband gap between E_1 and E_2 ($\Delta E= E_2 - E_1$) to be a few meV as shown in Fig 1.3 (b). Therefore, the electronic transition between these 2 energy levels will result in a THz photon. This process is called ***''intra-band transitions'' or*** ***''inter-subband transitions''***.

This is the largest advantage of using inter-subband semiconductor lasers where by varying the width of quantum wells, the photon energy of laser emission can be easily varied in a wide frequency range without changing the constituting semiconductor materials. Using this principle, the first THz semiconductor laser was successfully demonstrated in 2002 and we will discuss how it works in detail in the next section of this chapter.

1.3 Quantum cascade lasers

1.3.1 Cascade schema

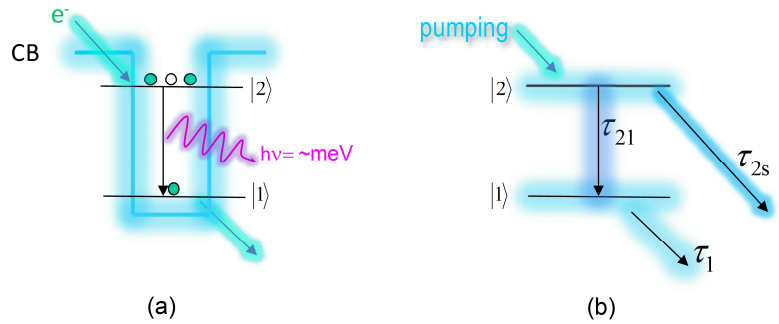

Fig 1.4 | Population inversion in a quantum well. (a) Inter-subband transitions in a single quantum well for THz emission. (b) Schematic diagram of electron lifetimes for subbands levels.

Inter-subband transition can be easily engineered to correspond to THz frequency emission by choosing a suitable quantum well width (~nm) as presented in section 1.2. However, to observe laser action in such a structure, two conditions should be satisfied:

1. The population inversion between these 2 artificial inter-sub-levels has to be realized.

2. The gain g_{total} of the material needs to compensate the total losses α_{total}.

The above need special consideration as, for inter-subband transitions, there are considerable and efficient scattering non-radiative processes, such as optical phonon emission, electron-electron scattering, ionized-impurity scattering and acoustic-phonon emission [38] [39]. All these scattering processes result in extremely short lifetimes (~1 - 10 ps) [22] [23] of the excited state $|2\rangle$, τ_2, and very low electron-photon quantum efficiency that is directly related to the gain of laser. These very short subband lifetimes are in contrast to those of interband transitions (~nanoseconds to ~microseconds).

In order to achieve population inversion, the excited level $|2\rangle$ lifetime τ_2 ($1/\tau_2=1/\tau_{21}+1/\tau_{2s}$ where τ_{2s} is corresponds to other electron escape routes other than through level $|1\rangle$) should be longer than the fundamental level lifetime τ_1 i.e. $\tau_2>\tau_1$ as schematically illustrated in Fig 1.4. This can be realized by making τ_1 shorter by using the non-radiative mechanisms, such as mini-band scattering [40] and longitudinal optical (LO) phonon depopulation [41], which can pump away immediately these electrons away from the fundamental level on the sub-picosecond scale. This is detailed below in the active region description.

On the second condition, to achieve a higher gain, multi-periods (generally $\boldsymbol{N}$=100-200 periods for THz QCLs) of each quantum well system are used. This is able to directly multiply by $\boldsymbol{N}$ times the gain. This is the 'cascade' concept within QCLs. Below, I describe how electrons are injected into through a quantum well system and the cascade structure.

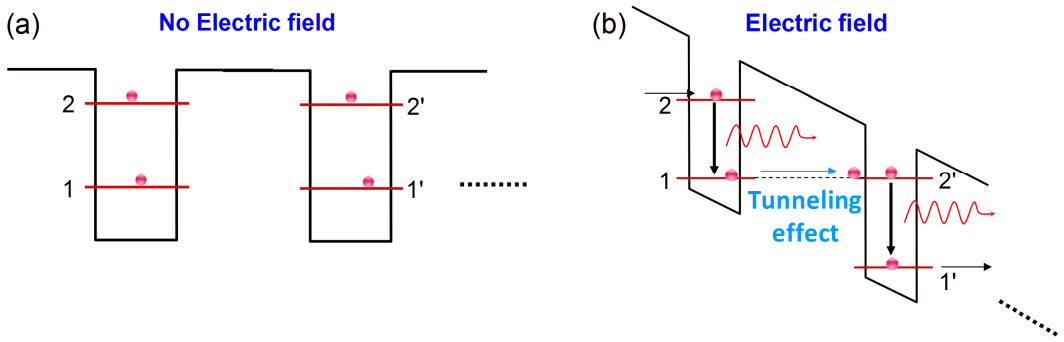

Fig 1.5 | Cascade schema of two periods of a QCL without (a) and with (b) an electric field applied across the coupled quantum wells.

In reality, a QCL is constructed with thousands of quantum wells (e.g. GaAs) that are separated by barriers (e.g. AlGaAs), which are split into periods, as illustrated in Fig 1.5 (two periods for simplicity). When the QCL is not biased as shown in Fig 1.5 (a), electrons cannot be injected into the excited states and population inversion cannot be achieved. However, when a bias is applied, the potential of quantum wells will be linearly tilted. By appropriate design of the structure, an appropriate external static electric field can align the fundamental level $|1\rangle$ of the one period with the excited level $|2'\rangle$ of the following period as presented in Fig 1.5 (b). After an electronic transition ($|2\rangle \rightarrow |1\rangle$) in the first period of the quantum well system, electrons will be transported ($|1\rangle \rightarrow |2'\rangle$) to the excited level $|2'\rangle$ of the following period via resonat tunneling. This process is repeated over many periods, permitting one electron to emit ***N*** photons when passing through ***N*** periods, which can greatly increase the gain of the material and result in laser action. This is the reason for name "***quantum cascade laser***". The emission is transverse magnetic (TM) polarized due to the inter-subband selection rules [42] [43]. Therefore, only photons with the electric field component parallel to the growth direction are emitted. This is important for the type of plasmon-based waveguides [44] that are employed for photon confinement.

1.3.2 Active region design of quantum cascade lasers

Fig 1.5 is a schematic diagram of cascade structures showing the principle of cascade amplification of QCLs. However, in the actual case, the band structure of a THz QCL is considerably more complicated [45]. Here we will discuss the three main families of THz QCLs that will be involved in this thesis with their band structures calculated using Schrödinger equations: 1. ''bound-to-continuum'' QCLs; 2. ''LO phonon depopulation'' QCLs; 3. ''hybrid phonon and bound-to-continuum'' QCLs. All the THz QCLs in this thesis are based on GaAs/AlGaAs system (GaAs quantum wells and AlGaAs barriers).

Bound-to-continuum design

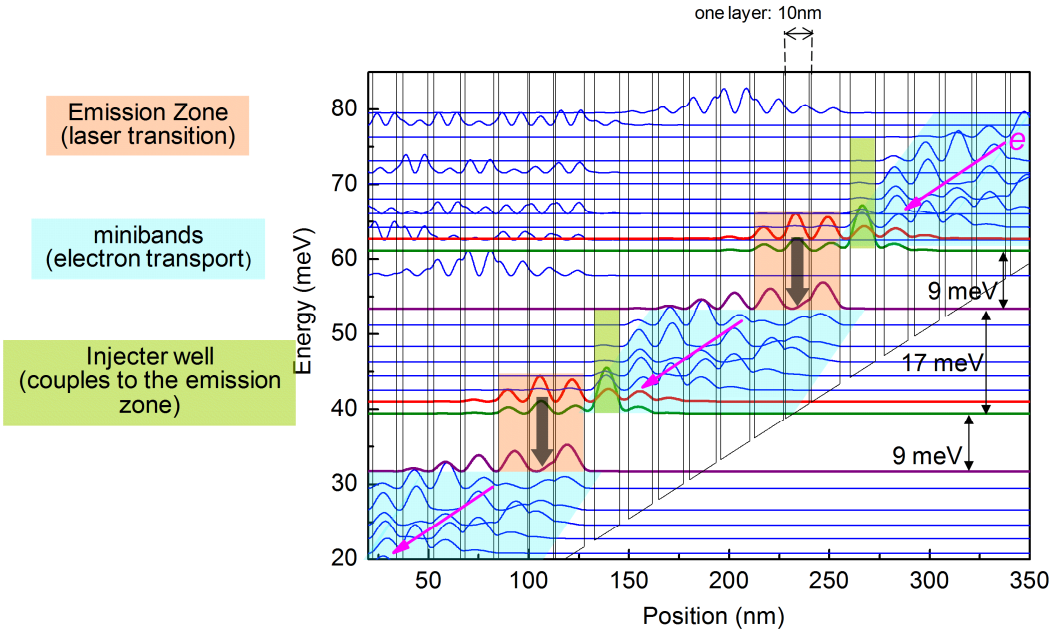

Fig 1.6 | Band structure of a bound-to-continuum THz QCL. Emission zone (orange zone): where laser transitions take place; mini-bands (blue zone): where electrons are transported from the previous period to the following one; Injector well (green zone): a quantum well that collects electrons from the mini-band and injects them onto excited level.

Fig 1.6 shows the band structure of a bound-to-continuum THz QCL centered at 2 THz under a bias of 1.5 KV/cm [46]. In this figure, 2 periods of band structure are illustrated and each period consists of typically 8 quantum wells (GaAs) and barriers ($Al_{0.1}GaAs_{0.9}$). The horizontal axis presents the growth direction (position) of the quantum wells and barriers and the vertical one presents the energy potential of the subbands. The curves with different colors (blue, red and green) are the squared electronic wave-functions of the quantum wells calculated using the Schrödinger equation, showing the probability of the electron distributions in the quantum wells.

In Fig 1.6, the light blue zones are called mini-bands, which serve as an electronic transport link between any 2 neighboring periods. After the laser transition in one period (orange zone), the electrons will be transported from the fundamental level to the mini-band, though electron-electron scattering and resonant tunneling, where they will be transported from the end of one period to the beginning of the following one. The light green zones are called injector wells. They collect electrons from the bottom of the mini-bands and resonantly inject them onto the excited levels of the electronic transitions. The injector well is next to the quantum well where the excited level is localized. The two wave functions overlap strongly to guarantee efficient resonant tunneling. The orange zones are the emission area where the laser transition take place. The inter-subband energy gap here is around ~9 meV corresponding to a frequency ~ 2.1 THz. The THz QCLs based on bound-to-continuum design permits low operating voltages owing to

the small applied fields. However, the design typically results in relatively low temperature operation and narrow gain bandwidth owing to the miniband depopulation of the lower state that results in a relatively long lifetime [47]. The narrow bandwidth of these structures limits their use for short pulse generation.

LO phonon depopulation design

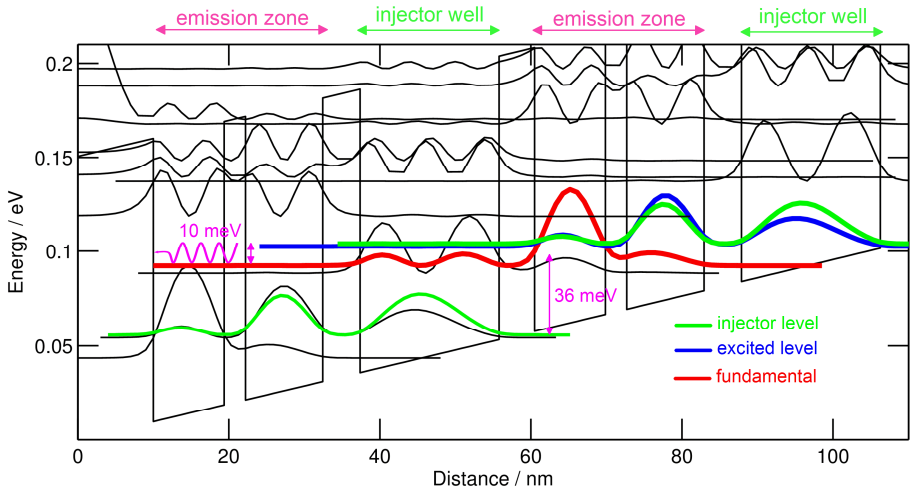

Fig 1.7 | Band structure of THz QCLs based on LO phonon depopulation scheme. Emission zone: where laser transition take place; Injector well: a quantum well that collects electrons from fundamental levels of the previous period and injects them into excited level of the following period.

In contrast to bound-to-continuum designs, which has a large mini-band, LO phonon depopulation schemes have a reduced number of wells and typically consist of an injector well and a transition zone [41]. In this design, after a laser transition in one period, electrons will be directly transported from the fundamental level to the injector level of the following period via a “LO depopulation” (36meV transition) as shown in Fig 1.7. The structure here is for an emission frequency centered at 2.4 THz under a bias of 8 KV/cm. In one period, there are just 3 quantum wells. The green wavefunction represents the injector level, the blue represents the excited level and the red represents the fundamental level of the laser transition. The energy difference between the fundamental level of one period and the injector level of the following period is roughly ~36 meV corresponding to the transition energy of a GaAs LO phonon as illustrated in Fig 1.7. This allows for resonant depopulation of the lower laser state, resulting in a very short lifetime (~0.2 ps) ensuring population inversion. In addition, this short lifetime results in a broad spectral gain bandwidth, making them ideal candidates for ultra-short THz pulse. This short lifetime also permits the highest temperature operation of a QCL (~200 K) [48]. However, the large applied field results in a large power dissipation, normally preventing high duty cycle and CW operation at high temperatures. We will further discuss and compare these 2 types of QCLs in the following chapters.

Hybrid LO phonon- bound to continuum design

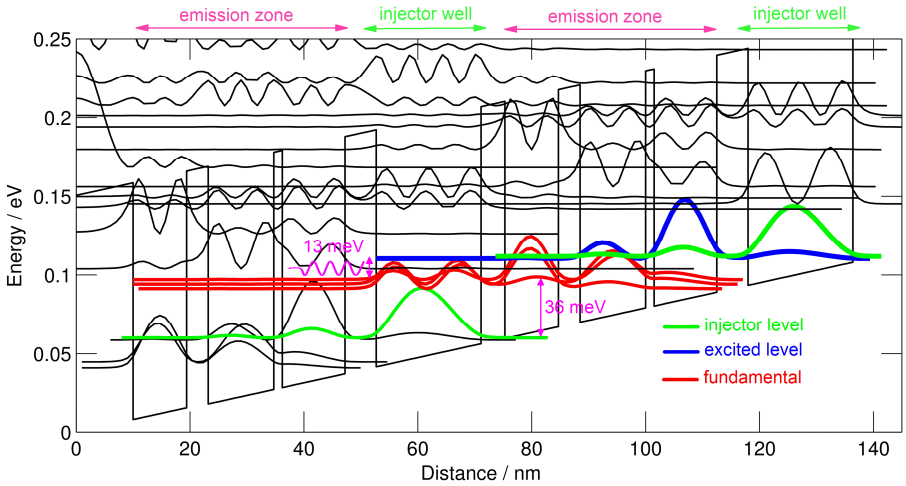

Fig 1.8 | Band structure of a THz QCLs based on hybrid depopulation that combines LO phonon and bound-to-continuum schemes. Emission zone: where laser transitions take place; Injector well: a quantum well that collects electrons from fundamental levels of the previous period and injects them into excited level of the following period.

The band structure of this hybrid design is presented in Fig 1.8, emission frequency centered at ~3.2 THz under a bias of 9 KV/cm and can be considered a combination of a bound-to-continuum and a LO phonon structure [49]. As with the LO phonon design discussed above, the injector level (green) collects electrons from the previous fundamental level by resonant tunneling and injects them into the excited level (blue). The laser transition takes place between the single excited band level (blue) and the fundamental continuum levels (red). After the transition, the electrons will be transported through this small miniband (red states) and then be depopulated to the injector level (green state) of the next period by LO phonon interaction. This hybrid depopulation scheme results in an electron lifetime of the fundamental level being slightly longer than that of pure LO phonon design. This directly results in a gain bandwidth that lies between pure LO phonon QCLs and bound-to-continuum active region designs. However, it has an advantage in requiring a smaller applied field than LO phonon based devices.

1.3.3 Waveguide of THz quantum cascade lasers

For THz QCLs, a ‘special’ waveguide is required to confine the THz waves within a cavity. Dielectric confinement used for conventional semiconductor lasers are technically difficult owing to large wavelengths involved that would require very thick dielectric claddings. Instead using the TM polarized photons generated by inter-subband transitions, surface plasmon based waveguides can be used that have distinctive properties for the THz photon confinement [20].

In this section, I will introduce the single-plasmon and metal-metal waveguides that are used in QCLs for THz modal confinement [44].

Single-plasmon waveguide

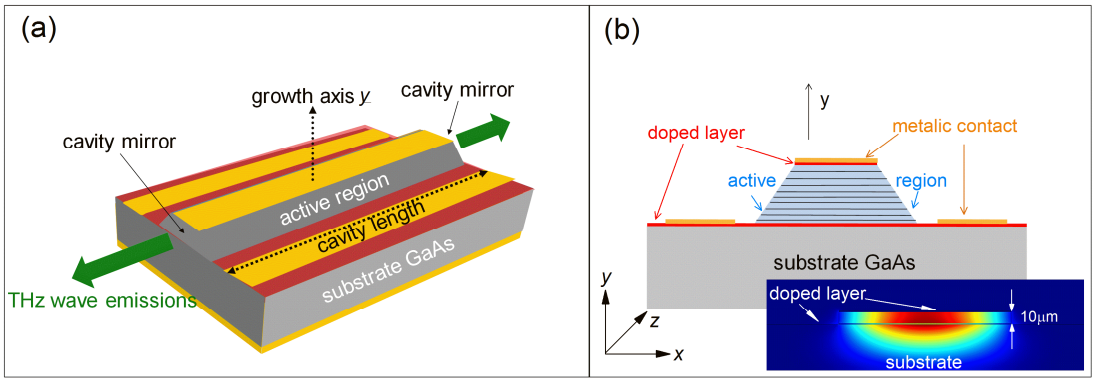

Fig 1.9 | (a) Schematic diagram of a typical single-plasmon THz QCL (b) Cross section of the single-plasmon QCL. Inset: THz wave intensity distribution in a typical single-plasmon waveguide.

Single-plasmon waveguide THz QCLs are currently the most used THz QCLs in scientific applications due to their directional far-field patterns [50] and strong out coupling powers [51]. The quantum well active medium is sandwiched between a metal and a lower doped layer as illustrated in Fig 1.9 which shows (a) a 45°-view and (b) a cross-section-view. The metal layer (typically Ti/Au (10nm/200nm)) and the bottom doped layer (~700nm thick) results in a TM mode – a surface plasmon mode – that can confine the TM polarized THz emission in the laser cavity. The active region, GaAs/AlGaAs quantum wells, is ~10μm thick (the dark grey zone in Fig 1.9 (a) and trapezoidal zone in Fig 1.9 (b)), which is the gain medium for the THz emission. The generated single-plasmon mode is illustrated the inset in Fig 1.9 (b) calculated by COMSOL Multiphysics. It loosely restricts the THz mode to the laser cavity, with the majority of the optical mode penetrating into the substrate (GaAs substrate, bottom thick light grey layer).

We can define a confinement factor Γ [39] to describe the modal overlap of the mode within the active region as:

$$\Gamma = \frac{\int_{active} dxdyE^2(x,y)}{\int_{x,z=\infty} dxdyE^2(x,y)} \tag{1.4}$$

where x, y are respectively the horizontal and vertical direction of QCL's cross-section as shown in Fig 1.9. For a single-plasmon QCLs, the confinement factor Γ typically lies between 0.1 – 0.5 [44].

If we suppose the mirror and waveguide losses are α_m and α_w, respectively, the gain required for lasing action in a QCL can be defined as [52] [44]:

$$g_{th} = \frac{\alpha_m + \alpha_w}{\Gamma} \tag{1.5}$$

From Eq. (1.5), this weak confinement of the THz mode in single-plasmon QCLs will leads to a requirement of higher gain to reach threshold, high lasing current threshold, and consequently results in low operating temperatures, compared to metal-metal QCLs (see below). It needs to be mentioned that the ridge width of a single-plasmon QCLs is generally larger than ~150 µm. If it is too narrow, for example less than ~100 µm, the THz waves will be pushed further into the substrate and be less confined to the active regime, increasing further the threshold current.

Nonetheless the low THz mode confinement of single-plasmon waveguides allows strong out coupling powers which allows the QCL to be easily applied to applications such as spectroscopy or imaging [53]. Further the low confinement permits high coupling efficiencies of external radiation. This allows to easily inject THz waves into QCLs that will be important for time resolved coherent detection (see chapters 4 to 6).

Metal-metal waveguide

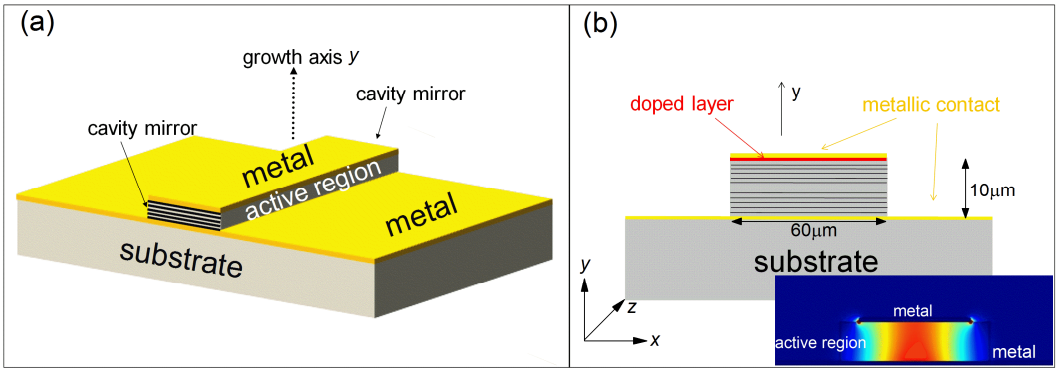

Fig 1.10 | (a) Schematic diagram of a typical metal-metal waveguide THz QCL (b) cross section of the metal-metal waveguide QCL (inset: THz wave intensity distribution in a typical metal-metal waveguide).

Rather than having a lower doped layer, metal-metal (MM) THz QCLs are structured from top to bottom as *metal layer - active region - metal layer* [44]. This is illustrated in Fig 1.10 for (a) a 45°-view and (b) a cross-section-view. The top metal layer is typically ~300 nm thick. Below active region, the metal layer is ~ 600 nm. As the active region is sandwiched between two metal layers, the THz mode is confined in the active region and the confinement factor can be as high as ~1, as illustrated in the inset of Fig 1.10 (b) that presents the intensity distribution

of THz wave in metal-metal waveguide cavity. As the confinement is large, the threshold is typically less than that of single-plasmon layers and permits the highest temperature operation up to 200 K [48]. The ridge width of THz QCLs based on MM waveguide can be much narrower (< 40 μm) than that of single-plasmon QCLs owing to the strong confinement. However, a consequence of the strongly confined modes results in a huge impedance mismatching with free space radiated modes. This leads to highly diffracted far-field patterns, poorly out-coupled powers and low injection coupling efficiencies, which will be discussed in detail in chapter 7.

As will be discussed in chapter 5 and 6, we will use these MM QCLs to carry out active mode-locking experiments at nitrogen cooling temperatures at 77 K, whereas previous experiments have all been performed on single-plasmon QCLs at low temperatures (10K). In addition, this type of waveguide also permits a confinement of the microwave modulation used in active mode-locking.

1.3.4 Geometry and dimension

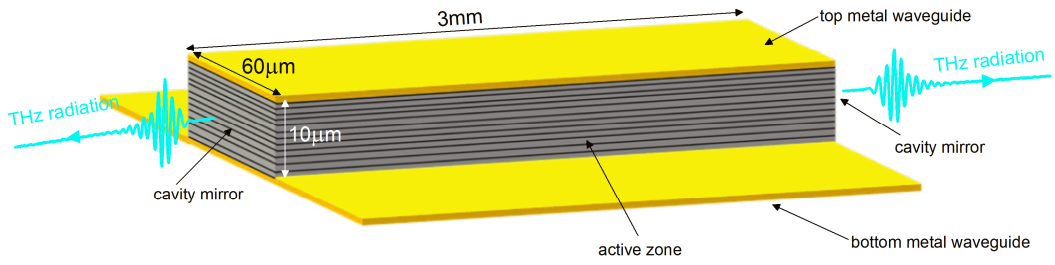

Fig 1.11 | Schematic diagram of the geometry and dimensions of a typical THz QCL

Fig 1.11 shows the schematic diagram of the geometry and dimensions of a typical metal-metal waveguide THz QCL ridge. The active region in ~10-μm high, the ridge width is ~ 10-250 μm wide and the length of the cavity is typically a few millimeters long. (In this thesis we use 3 mm lengths for active mode-locking around 13 GHz [54]). The 2 parallel facets act as end mirrors realizing a Fabry-Pérot cavity, which is one of the key elements (active medium, pumping, cavity, mirror) for laser action. Once the QCL is electrically pumped and laser action is realized, THz emission will be radiated from both facets.

Fig 1.12 illustrates several photos of THz QCLs with various resolutions from millimeters to nanometers: (a) is the optical photo, taken by a normal camera, of a QCL wafer placed on a coin of one eurocent, showing the compactness. (b) is a Scanning Electron Microscope (SEM) photo of a QCL wafer. In this picture, the laser ridges (the red rectangle, for example), GaAs substrate and bonded wires can be clearly observed. If we continue to zoom into active region of the QCL ridge in (b) using transmission electron microscope (TEM), many periodically

arranged layers corresponding to the multiple periods can be seen, corresponding to the QCL active region period. The blue arrows in Fig 1.12 (c) show the flow direction of electrons from top to bottom, traversing quantum wells and barriers while the yellow arrows illustrate the electronic laser transitions.

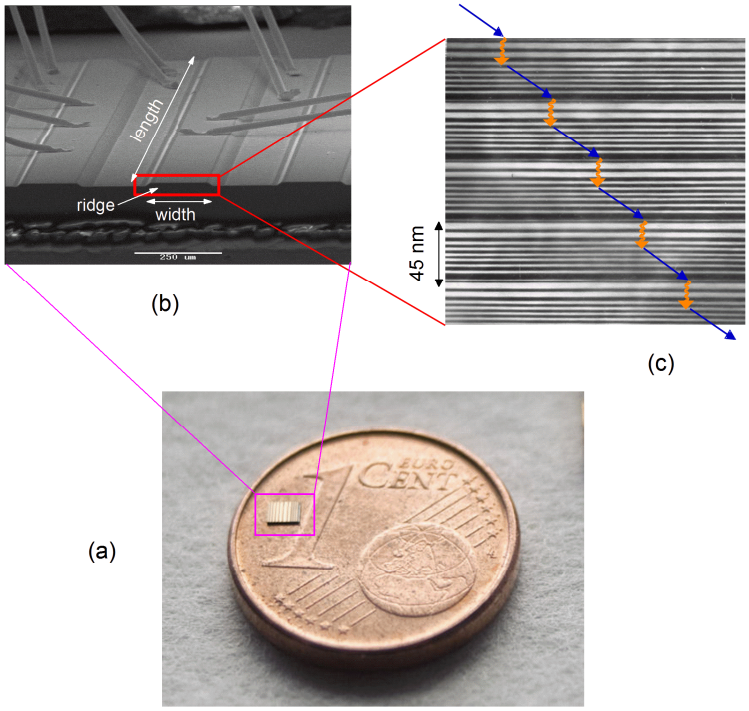

Fig 1.12 | The photo of THz QCLs. (a) Optical photo of a QCL wafer placed on a coin of one eurocent. (b) Scanning Electron Microscope (SEM) photo of a QCL wafer. (c) Transmission electron microscope (TEM) photo of the active region of a QCL.

1.3.5 The state-of-the-art

The material system mainly used for THz QCLs is based GaAs/AlGaAs [55]. However, the material system InGaAs/AlInAs/InP has also been used to successfully demonstrate THz QCLs [56]. The maximum temperature operation of THz QCLs is now ~200 K [48], using metal-metal waveguide and a LO phonon depopulation scheme. The max output power of THz QCLs can already reach ~1W [51] and its gain bandwidth can be over ~1 THz by stacking together three active layers with different central emission frequencies [29]. Besides, the waveguides of THz QCLs can be also engineered in a photonic crystal geometry for surface emitting and improvements of the far-field [57] [58]. Continuous-wave THz QCLs have also been employed to real-time imaging [59] [53], gas sensing [60] [61]and THz spectroscopy [62] [63], recently.

1.4 Technology

1.4.1 Molecular beam epitaxy

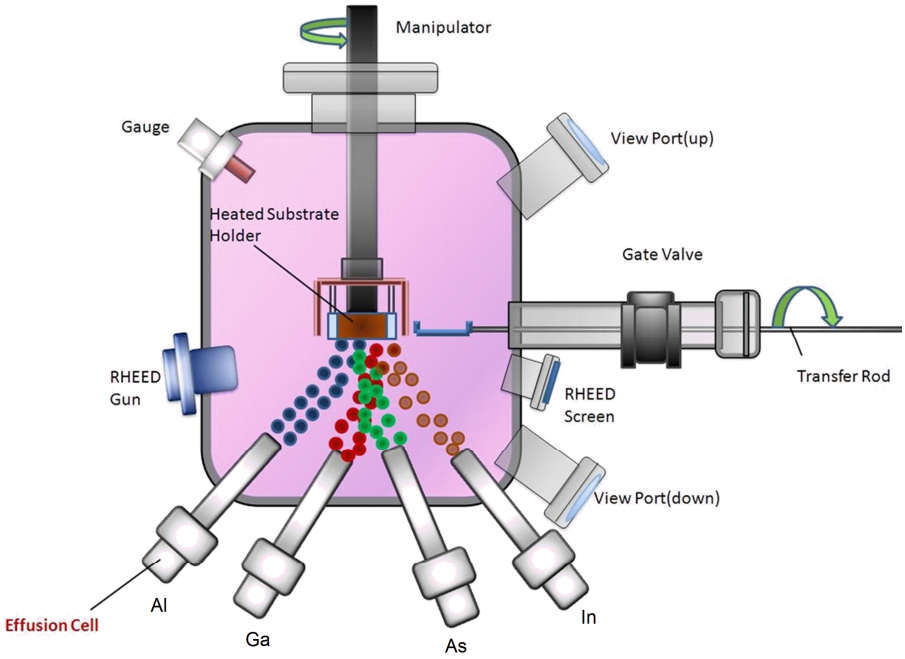

Fig 1.13 | Schematic diagram of the deposition chamber of a Molecular Beam Epitaxy (MBE) system. RHEED: Reflection High-Energy Electron Diffraction. [Picture source: http://www. dualsignal.com.tw/20998233762646330922262 30mbe.html].

Molecular beam epitaxy (MBE) is a thin-film deposition technique allowing fabrications of exceptional crystalline quality materials [64]. This technique is commonly used for the growth of high-quality QCLs. The schematic diagram of a MBE system is illustrated in Fig 1.13. In this figure, the large chamber is pumped to ultra-high vacuum (around 10^{-11} mbar), and is the main environment for sample growth. The quantum well growth is performed on a GaAs substrate which is fixed on the heated holder and can be manipulated by the external manipulator. To fabricate QCLs, we need to alternately and periodically grow thin films of GaAs (quantum wells) and AlGaAs (barriers) on the substrate with a layer accuracy of about 0.1 nm for individual quantum wells and barriers. The effusion cells, filled by Al, Ga, As, are heated to become a molecular gas and directed onto the substrate. For example, to grow a 5-nm thick GaAs quantum well, the effusion cells of Ga, As need to be opened and directed on the substrate. They will be bond together to become GaAs via a chemical reaction and be deposited on the GaAs substrate. (Similarly for AlGaAs barriers, where we require the Al, Ga, As cells). The thickness of quantum wells and barriers are precisely determined by switching off-on the mechanical shutters of effusion cells with a transition time below 100 ms and also by controlling the flux of materials with an accuracy of 1% or better. In the figure the RHEED

gun and screen are the reflection high-energy electron diffraction system, which is employed for the surface sensitive characterization of the growth layers. In a MBE chamber, the epitaxial rate is generally about 0.5-1 μm per hour. To entirely complete the growth of a QCL wafer, it generally takes about 10-14 hours or longer.

1.4.2 Processing

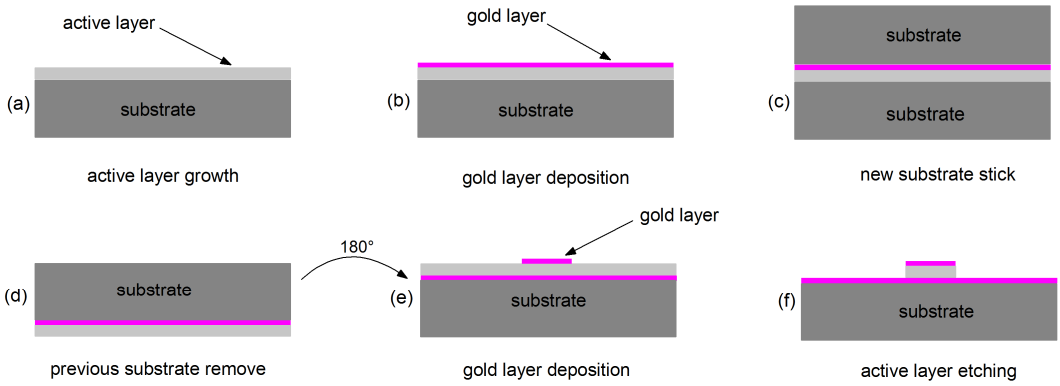

Fig 1.14 | Simplified processing steps for the fabrication of metal-metal waveguide quantum cascade lasers.

Although the work performed in this thesis is not directly implicated in growth and post-growth processing of THz QCLs, I will give a briefly introduction as it is important to understand the fabrication of QCLs. Fig 1.14 shows the simplified processing steps for THz QCLs based on MM waveguides. (a) is the 10-μm height active layer (thousands of quantum wells and barriers) growth on the GaAs substrate realized in a MBE chamber, which has been presented in section 1.4.1. Then it is followed by the deposition of a Ti/Au layer with a thickness of ~300 nm on the active layer as illustrated in (b). In (c) a host GaAs substrate (also with a deposited layer of Ti/Au) is wafer bonded to the Ti/Au layer on the QCL substrate. Then in (d) the original GaAs substrate is removed using physical thinning and selective etching. This is followed by a deposition a ~300-nm Ti/Au layer for the exposed active region as demonstrated in (e). In (f), the wafer is etched (chemical or dry etching) around the top metal to realise the QCL ridge.

1.4.3 Cleaving and device mounting

After the sophisticated active layer growth and metal-metal waveguide processing, the ends of the processed wafers are cleaved by a diamond point to realize the end cavity mirrors. This allows a high-quality Fabry-Pérot cavity before mounting the device on a Cu or Au mounting block. Figure 1.15(a) and (b) shows the end facets before and after cleaving. Fig 1.15 (c)

presents the bird eye view of the whole cleaved device, showing clearly a number of laser ridges with different ridge sizes.

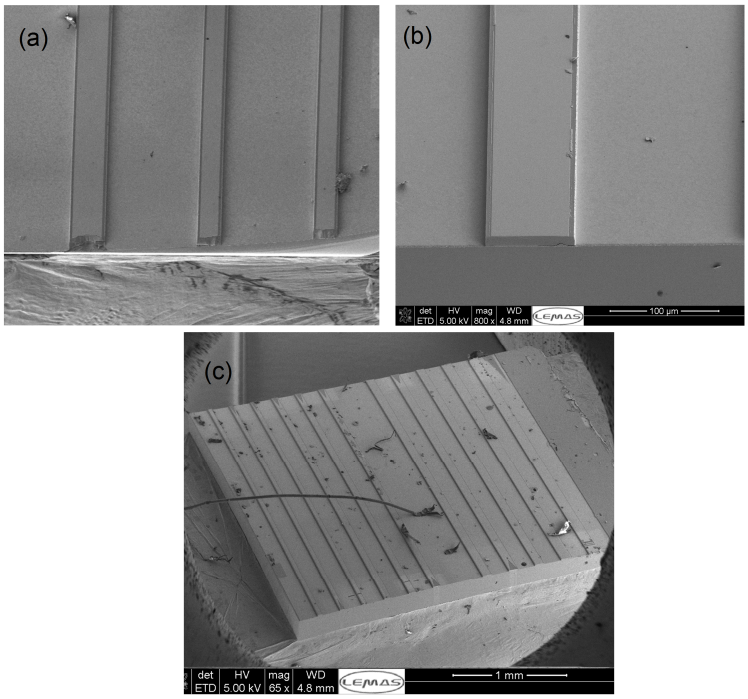

Fig 1.15 | Scanning electron microscope (SEM) photos of a THZ-QCL wafer (a) before cleaving (b) after cleaving and (c) bird view of the whole wafer after cleaving.

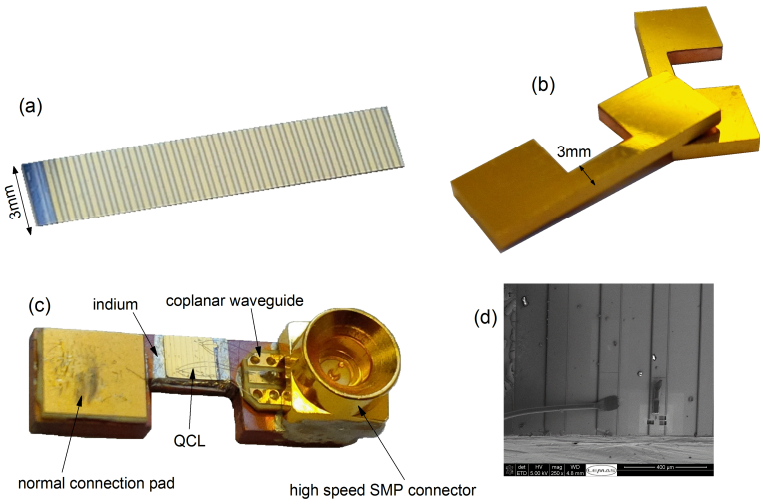

Fig 1.16 | (a) Photo of the wafer taken by normal optical camera after cleaving. (b) Gilded mounting block for THz QCLs. (c) THz QCLs mounted on a copper block with high-speed coplanar transmission line waveguide and integrated SMP connector. (d) SEM photo of the mounted QCLs with a micro-wire bonded on the ridge.

Fig 1.16 from (a) to (d) briefly shows the mounting process of QCLs. (a) is the photo of QCL wafer after cleaving. Fig 1.16 (b) is the gilded mounting block where we solder the QCL wafer onto using a layer of indium foil heated to 150 C° - 200 C°. Besides serving as an adhesive, the indium is also utilized to conduct heat from the wafer to the Au or Cu block. Fig 1.16 (c) is the photo of a completely mounted QCL, from which we can clearly observe the QCLs (gold color) and indium layer (silver color) below it. The left side connection pad, on which wires can be bonded, is generally employed to bias the QCL at low speed (less than 100 MHz). The right-angle connecter at the right side of mounting block is a high-speed SMP connecter with integrated coplanar transmission line waveguide. This allows fast electrical signals to pass through it for electrical modulation it up to ~ 26 GHz for mode-locking. The electrical connections between the QCLs and connector (or waveguide) are realized through micro wire bonding as shown in Fig 1.16 (d), where a micro wire is bonded on a QCL ridge and linked with the central line of the coplanar waveguide. The QCL is completely prepared and can be directly mounted on a continuous flow He cryostat for characterization.

1.5 Conclusion

In this chapter, I have given a brief introduction to THz QCLs, the active regions, the waveguides and the fabrication technologies. At the beginning in section 1.1, the THz frequency was introduced and it position in the entire electromagnetic spectrum was also briefly discussed. As there is no promising semiconductor material whose band gap is as small as a few meV, artificially engineered energy levels in quantum wells were presented in section 1.2 for THz emission through inter-subband transitions. In section 1.3, the working principle and geometrical shape as well as dimensions of THz QCLs were discussed in detail. At the end in section 1.4, the active layer growth technologies and the ridge processing steps were schematically demonstrated.

2

Ultrafast Detection of Terahertz Quantum Cascade Laser emission

To demonstrate mode-locking of THz QCLs and investigate their ultrafast properties on the femtosecond scale, high-speed THz detectors or detection systems are needed to characterize their THz emission in the time domain. However, there is currently a lack of such THz detectors. In order to solve this problem, a few years ago, we developed a time-resolved injection seeding system that allows us to coherently detect the QCL's electric field in the time domain with a *femtosecond (fs)* resolution, based around THz time domain spectroscopy (TDS). The main principle of this system is to inject a phase-resolved THz pulse, generated from a *fs* optical pulse excitation of a photoconductive antenna, into the cavity of a QCL to initiate laser action before it is initiated by its inherent spontaneous emission, where the phase of the latter is random. In this way, the phase of the QCL can be completely seeded and synchronized to the THz emitter as thus to the *fs* optical excitation pulse. The electric field of the phase-controlled QCL radiation can be then coherently detected and precisely measured in time domain with standard sampling techniques.

In this chapter, we will first introduce the working principle of THz-TDS, where *fs* optical pulses are simultaneously used to generate and detect phase resolved THz pulses through photoconductive switches and electro-optic sampling, respectively. Then, we will present the injection seeding technique and show how it is used to detect the electric field of the THz QCL emission in the time domain. And finally, the results of THz QCL emission measured from 0 ps to 2000 ps, from amplification to the steady state, will be experimentally demonstrated and analyzed.

Chapter 2

2.1. Ultrafast terahertz detection

The THz range covering the frequencies from 0.5 THz to 10 THz is the least developed in the electromagnetic spectrum as there is a lack of promising THz sources and detectors. The demonstration of the first coherent compact and powerful THz source – the THz QCL in 2002 is a milestone in the THz source development history. Since then, there have been considerable achievements in the performance of this source, including significant increases in output powers up to 1 W and operating temperatures up to 200 K. However, the commonly used THz detectors [65] [13]such as pyroelectric detectors and Golay cells can only respond to a very slow modulation frequency of less than 50 Hz that is extremely far-away from our requirements (~12 GHz). Other THz detectors, for example hot electron bolometers, are able to work at response frequencies from a few KHz to a few GHz, but do not normally attain frequencies above 10 GHz [66].

To further investigate the ultrafast properties of THz QCLs, such as their dynamics and short pulse generation, high-speed detectors or detection systems of a response frequency at > 10 GHz are required. In order to solve this problem, we have developed a coherent detection technique called ‘‘***injection seeding***’’ [67], based on THz-TDS [68] [69], allowing us to detect the time-resolved emission of THz QCLs with a high resolution of less than 20 *fs*. The aim of this chapter is to introduce this phase-resolved injection seeding system, which will be widely utilized in the following chapters for mode-locking investigations.

As is in all laser systems, laser action in QCLs is initiated by its inherent spontaneous emission, where the phase is completely random. In other words, every time a laser is switched on, its phase will be totally different. This uncontrolled lasing action will prohibit the coherent detection of the electric field of the QCL using sampling techniques (see section 2.2.3). The main idea of our technique is to inject a broadband (~4 THz bandwidth) THz pulse generated by a photoconductive antenna [70], excited by a Ti: Sapphire *fs*-laser pulse, into the cavity of QCLs to start the laser action and replace the QCL’s spontaneous emission. In this way, the phase can be fixed by the injected THz pulse. Once the emission phase is controlled, we can coherently detect the electric field of the QCL emission, using standard electro-optic sampling [71] described later in this chapter.

In this chapter, GaAs photoconductive antenna for THz generation will be introduced at the beginning. Then electro-optic sampling system will be presented and be employed to measure the electric field of THz pulses radiated by a photoconductive antenna. And finally, the time-resolved injection seeding system will be discussed and be applied to detect the electric field of a metal-metal waveguide THz QCL.

2.2 Terahertz Time domain spectroscopy

2.2.1 Introduction

THz-TDS is a technique that allows us to coherently detect the time-resolved electric field of THz pulses emitted by synchronized THz sources with a *fs* resolution [72]. It typically includes 3 parts: 1). A femtosecond optical/near-infrared laser 2). THz generation system and 3). THz detection system. A commonly used generation system in THz-TDS is based on photoconductive antennas and the detection system is typically based on electro-optic sampling [71].

Using this technique, we can directly measure the THz absorption and THz transitions of specific materials and nanostructures in the time domain to further study their electrical and optical properties. Using THz TDS, the THz QCLs emission can be synchronized to the femtosecond laser permitting the QCLs' time resolved electric field to be directly measured [67]. Therefore, prior to introducing injection seeding system, it is necessary to present the THz-TDS system.

2.2.2 THz generation - photoconductive antenna

There is a wide range of techniques to generate THz pulses with femtosecond lasers, such as frequency mixing in nonlinear crystals, plasma generation in air, and photoconductive antennas [11] [73] [74]. Here, we use the photoconductive antenna as THz generator as it easy to implement realized and can be modulated at high frequencies to reduce noise. A photoconductive antenna is a device that is able to generate broadband THz pulses covering the frequency range from 0.1 – 4 THz [70]. It consists of 2 metal electrodes deposited on a GaAs semi-insulating substrate as illustrated in Fig 2.1 in its simplest form. When a femtosecond infrared laser pulse, typically from a Ti:sapphire laser ($\lambda \sim 800$nm), with a photon energy is larger than the band-gap of the material, excites the GaAs substrate between the positive and negative contacts, electrons in valance band will be excited to the conduction band and become free carriers. With the antenna biased, a transient photocurrent I_{PC} will be generated between the electrodes. The time-dependent photocurrent, which is proportional to the applied static electric field and the temporary optical pulse profile can be expressed as the convolution of the optical pulse envelope and the impulse response of the photocurrents [11]:

$$I_{PC}(t) = \int I_{opt}(t-t')\left[e \cdot n(t') \cdot \upsilon(t')\right]dt' \propto E_{DC} \cdot I_{opt} \cdot f(\mathrm{t}) \qquad (2.1)$$

where I_{PC} is the intensity profile of the optical pulses, e is the electron charge, $n(t)$ is the carrier density, $\upsilon(t)$ is the average electron velocity, E_{DC} is the static electric field applied between the two metal electrodes and f(t) is a time-dependent function to describe the generated photocurrent response I_{PC}.

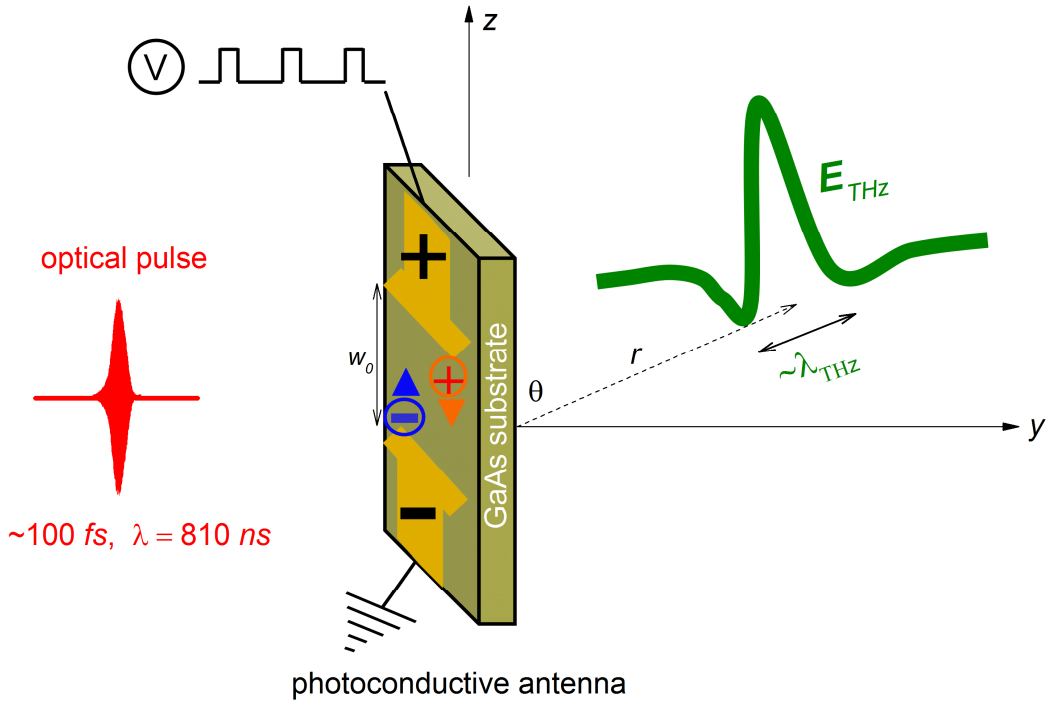

Fig 2.1 | Schematic diagram of a photoconductive antenna for THz pulse generation under femto-second optical pulse excitation.

Appling Hertzian dipole antenna model to the radiation of a photoconductive antenna, we can get its time-dependent emission expression in free space [11]:

$$\mathrm{E}_{THz}(t) = \frac{\mu_0 w_0}{4\pi}\frac{\sin\theta}{r}\frac{d}{dt_r}\left[I_{PC}(t_r)\right]\hat{\theta} \propto \frac{dI_{PC}(t)}{dt} \tag{2.2}$$

where μ_0 is vacuum permeability, w_0 is the gap distance between the negative and positive electrodes, r and θ are, respectively, the distance and angle of photoconductive antenna radiation, $t_r = t - r/c$.

We can see from the Eq. (2.2) that the temporal characteristics of the radiated electric fields strongly depend on the time differential of the photocurrent. If an ultrafast, for example ~100 *fs*, laser pulse is employed to create the transient photocurrent, the generated electric fields will also last a few hundred femtoseconds (the exact value is dependent on the dynamics of substrate materials), which corresponds exactly to the THz frequency range. Generally, the produced THz pulses are centered at ~1-1.5 THz with a broad bandwidth of ~3-4 THz and a maximum radiation power of ~10-200μW. For different applications, different electrode geometries and different fabrication processes can be utilized to engineer the central radiation frequency, emission bandwidth, maximum emission power and maximum excitation power as shown in Fig 2.2 from (a) parallel line photoconductive antenna to (f) large area interdigitated photoconductive antenna (iPA). Each antenna is described in the figure caption. In this thesis,

I used the large area interdigital photoconductive antenna owning to its high average radiative power of tens of μW under an infrared excitation power of ~500mW and a modulation frequency of a few tens of kilohertz, for example ~20 KHz. For a given photoconductive antenna, its output electric field is proportional to the bias voltage and the optical excitation power (unless the response saturates at high values).

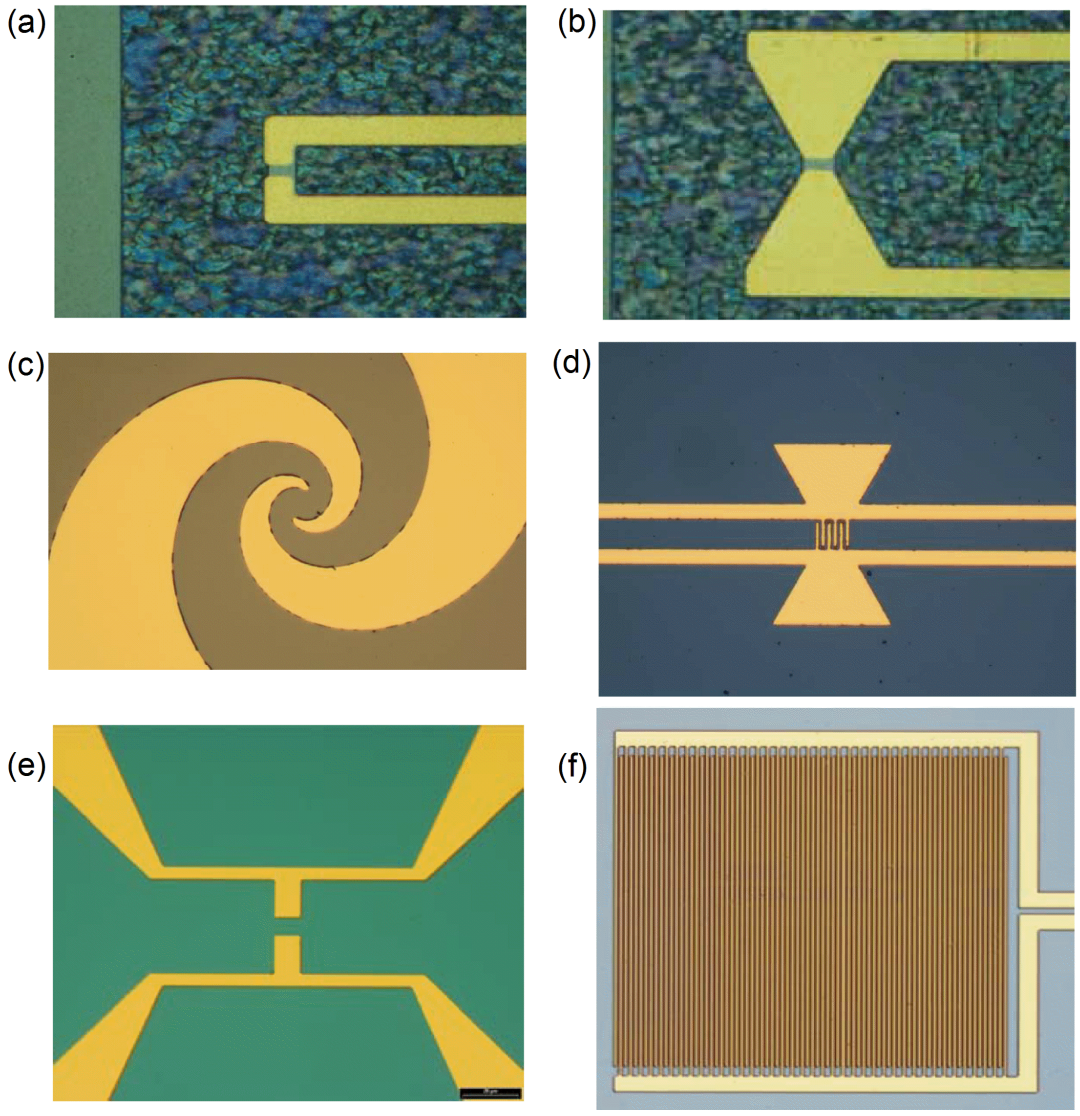

Fig 2.2 | Photoconductive antenna with different geometries. (a) Parallel line antenna - broadband emitter antenna. (b) Bow-tie emitter antenna. (c) Logarithmic spiral antenna - broadband emitter. (d) Finger gap antenna - emitter at low optical excitation power. (e) Butterfly antenna - highly sensitive low frequency antenna. (f) large area interdigital photoconductive antenna - high power THz transmitter. Most of the above designs can also be used a detector with the appropriate material (i.e. LT-GaAs). [From http://www.batop.de/products/terahertz/photoconductive-antenna/photoconductive-antenna-1060nm.html].

2.2.3 THz detection - electro-optic sampling

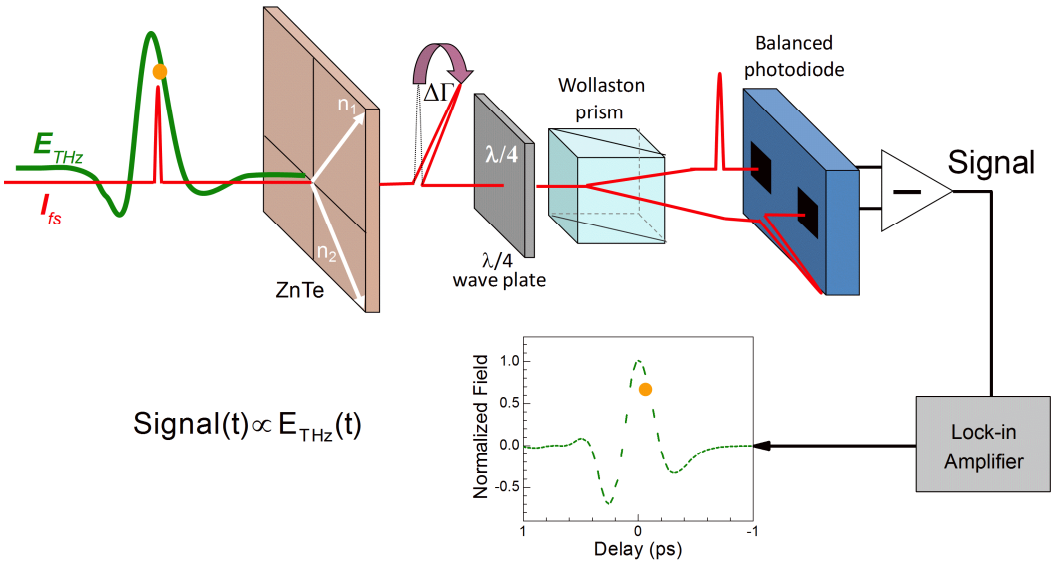

Fig 2.3 | Schematic diagram of electro-optic sampling system for THz electric field detection. ZnTe: nonlinear crystal for Pockels effect. λ/4 wave plate: change polarization of *fs* optical pulses. Wollaston prism: separate horizontally and vertically polarized components of *fs* optical pulses after quarter-wave-plate. Balance photodiode: detect respectively the horizontal and vertical components of *fs* optical pulses and their difference is determined and sent to a Lock-in amplifier for coherent detection.

There is also a range of techniques to detect THz waves using ultrafast lasers (photoconductive switches [75], plasma based air photonics [76], nonlinear crystals [77]). Here were employ electro-optic crystals as it permits a relatively high spectral bandwidth when compared to photoconductive devices. Electro-optic (EO) sampling permits to measure the actual electric field of THz waves using a second order nonlinear effect - ***Pockels effect*** in nonlinear EO crystals. It is used in a variety of scientific and technical applications, for example, switching between no optical rotation of the polarization and 90° rotation of the polarization creates a fast shutter with a response time in nanoseconds. The same technique can be also used to carry information by modulating the rotation between 0° and 90°. The second-order nonlinear polarization for Pockels effect is given by [11]:

$$P_i^{(2)} = 2\sum_{i,k} \varepsilon_0 \chi_{ijk}^{(2)}(\omega;\omega,0) \cdot E_j(\omega) \cdot E_k(0) = \sum_j \varepsilon_0 \chi_{ij}^{(2)}(\omega) \cdot E_j(\omega) \qquad (2.3)$$

where $\chi_{ij}^{(2)}(\omega)=2\sum_k \varepsilon_0 \chi_{ijk}^{(2)}(\omega;\omega,0) \cdot E_k(0)$ is the static electric field induced susceptibility tensor. From Eq. (2.3), we can see that the susceptibility tensor is proportional to the static electric field amplitude $E_k(0)$, which will induce birefringence in a nonlinear EO crystal. By

measuring the birefringence of the nonlinear EO crystal, the static electric field applied on it can be quantitatively determined.

EO sampling to measure the electric field of THz pulses works exactly in this way. The schematic diagram of electro-optic sampling system for THz electric field detection is illustrated in Fig 2.3. Firstly, let's suppose that the infrared *fs* pulse (red) (the same as the used for THz generation defined above) is linearly polarized in the vertical direction. If no THz wave (green) passes through the EO crystal ZnTe with the *fs* optical pulse, there will be no induced birefringence and the polarization of *fs* pulse will remain vertically polarized. When this *fs* pulse passes through the quarter-wave plate after the ZnTe crystal, it will become circularly polarized. Using a balance photodiode to detect the power difference between the vertical and horizontal components of the optical pulse, which are separated by a Wollaston prism, the result will be zero. On the contrary, if a THz wave travels through the EO crystal together with the *fs* optical pulse, the refractive index in n_1 and n_2 directions, as is shown in Fig 2.3, will be different owning to Pockels effect (i.e. induced birefringence). Passing through the nonlinear EO crystal of a thickness of L, a phase retardation will be introduced between the linearly polarized components of n_1 and n_2 axis, which is given by [11]:

$$\Delta\phi = (n_1 - n_2)\frac{\omega L}{c} = \frac{\omega L}{c} n_o^3 r_{eo} E_{THz} \tag{2.4}$$

where n_o is the refractive index at the optical frequency and r_{eo} is the EO coefficient. Therefore, the *fs* optical pulse will become elliptically polarized after the quarter-wave plate. The horizontal x and vertical y components can be then written as:

$$I_x = \frac{I_0}{2}(1 - \sin\Delta\phi) \approx \frac{I_0}{2}(1 - \Delta\phi) \tag{2.5}$$

$$I_y = \frac{I_0}{2}(1 + \sin\Delta\phi) \approx \frac{I_0}{2}(1 + \Delta\phi) \tag{2.6}$$

where I_0 is the incident *fs* pulse intensity. Separating the horizontal and vertical components by the Wollaston prism and injecting them into the balance photodiode, the final detected signal on the balance photodiode is given by:

$$I_s = I_y - I_x = I_0\Delta\phi = \frac{I_0\omega L}{c} n_o^3 r_{eo} E_{THz} \propto E_{THz} \tag{2.7}$$

Eq. (2.7) indicates that the output signals of the balance photodiode is proportional to the THz electric field corresponding to the point that is in phase with the *fs* optical pulse (the yellow point in Fig 2.3 for example and assuming a delta-function for the optical pulse). Therefore, we can obtain the exact value of THz electric field at this point by reading the photodiode output signals. If the arrival time between optical pulse and THz wave is continuously changed by a mechanical delay-line, we can totally reconstruct the electric field (both amplitude and

phase) of the THz pulse as we shall see in detail in section 2.2.4. A lock-in amplifier is used to detect the signal from the balance photodiodes with the modulation frequency of the antenna as a reference.

Generally, the ZnTe [77] and GaP [78] are the mostly commonly used EO crystals for EO sampling as the group velocity of the near-infrared optical pulse is roughly equal to the phase velocity of the THz pulse. This phase-matching condition permits to maximize the nonlinear Pockels effect and allows us to treat the varying THz waves as static electric field. However, for different THz frequencies, their phase velocities are slightly different, resulting in an optimal thickness of the crystal (~ nonlinear coherence length) to detect a broad range of THz frequencies. For example, a 200 µm thick ZnTe crystal is used to detect THz frequencies from a few 100 GHz to greater than 3 THz. Thicker crystals will give a larger signal but at the expense of a smaller detection bandwidth.

2.2.4 Time domain spectroscopy setup

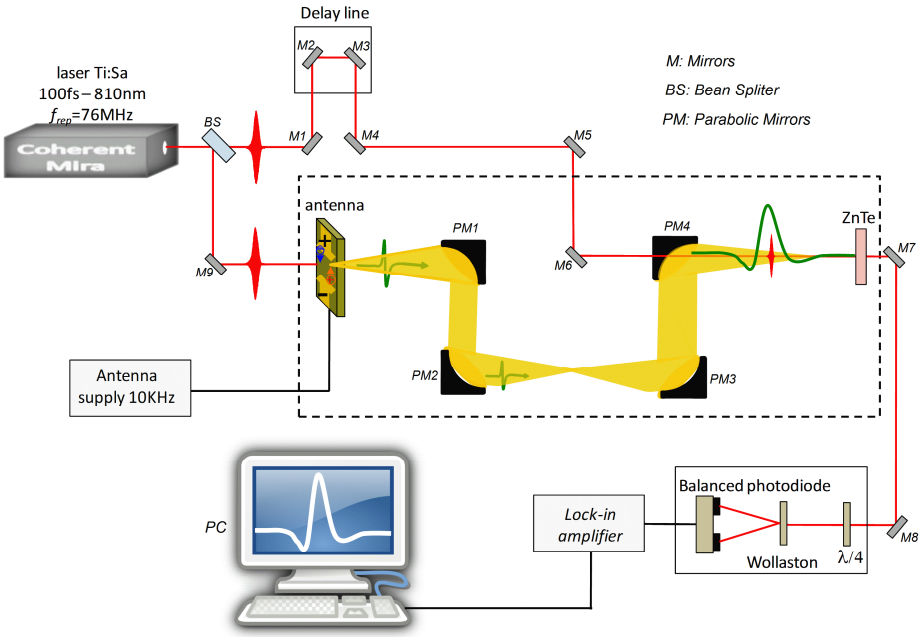

Fig 2.4 | Time domain spectroscopy setup for THz electric field generation and detection. Coherent Mira: *fs* laser generating ~100 *fs* optical pulse at ~810 nm with a repetition frequency of ~76 MHz and average output power of ~1.25 W. Delay line: 2 mirrors installed on a motorized movable stage to change the optical path (delay) of *fs* pulses. Loçk-in detector: to coherently detect and amplify the ~10 KHz signals (the modulation frequency of the photoconductive antenna) after the balance photodiode. PC: computer to record time-resolved data from lock-in amplifier. Red pulse (line): *fs* optical pulse (path). Green pulses: THz waves. Yellow zones: THz wave path. Black line: electrical connections. The photoconductive antenna, 4 parabolic mirrors and nonlinear crystal ZnTe are placed in a closed glass box and purged by compressed dry air.

Fig 2.4 shows the complete setup of the THz time domain spectroscopy system, bringing together the generation and detection schemes detailed separately above. A Ti:sapphire laser whose wavelength is centered at ~810 nm is employed to generated optical pulses of ~100 *fs* with a repetition rate of ~76 MHz. The *fs* optical pulses are divided into 2 parts by a 50/50 beam splitter as is illustrated in Fig 2.4 (*BS)*. One part passes through a delay line that consists of a motorized movable plate and 4 dielectric mirrors *M1 – M4* and then to the EO crystal (using mirrors *M5* and *M6* and a small hole on the last parabolic mirror *PM4*). The second part of the fs laser is focused onto the THz emitter (PC antenna) by the mirror *M9*. A THz pulse will be generated once an optical pulse is incident as introduced in section 2.2. Therefore, the THz pulse trains are always in phase with the *fs* optical pulse trains. (Typically, a 10 KHz square signal with ~2 V voltages and 50% duty cycle is applied on the electrodes of antenna). Then 4 parabolic mirrors (*PM1 – PM4*) are used to focus the THz waves onto a nonlinear EO crystal ZnTe with a thickness of 200μm or 500μm. When the THz and the first optical pulse

overlap and travel through the ZnTe crystal, the electric field of THz waves can be measured by the EO sampling system (section 2.2.3). If we continuously move the mirrors on the delay line to change the optical paths length (delay) of *fs* pulse, we can, as a consequence, continuously change the relative positions and phase relations between the THz and optical pulses. Therefore, the actual THz electric field can be reconstructed in time domain step by step as presented in Fig 2.5 (a) and (b) that show two time positions of the delay line of the optical pulse to sample different time positions of the THz spectrum. Here, it is important to mention that, as THz pulse is locked in phase to the *fs* pulse, the final result at a given phase delay is the average of thousands of measurements (repetitions) at exactly the same conditions, which will greatly reduce noise and improve signal-noise ratio as is shown in Fig 2.5 for five pulses separated by ~13 ns.

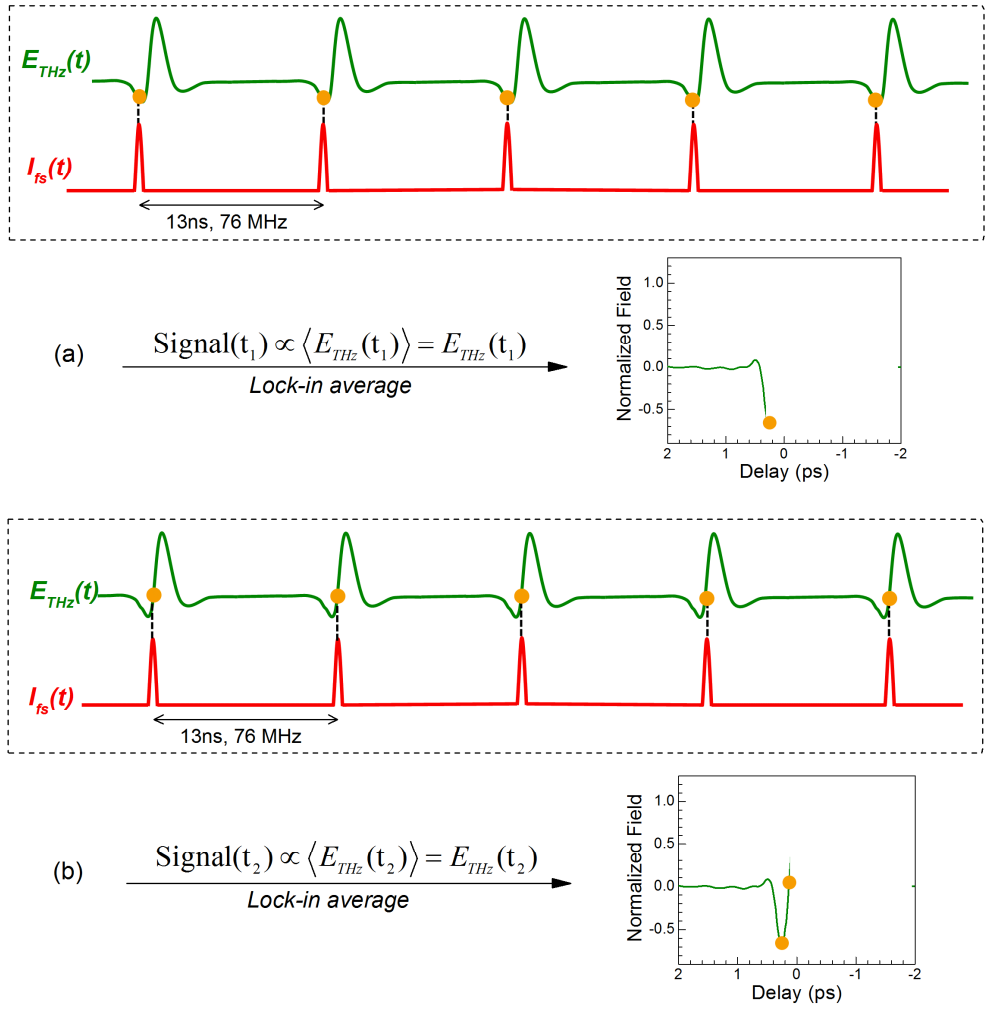

Fig 2.5 | Processes of electric field tracing by THz time domain spectroscopy and electro-optic sampling. The THz pulses are trig by *fs* optical pulses with a repetition rate of 76 MHz. Moving the delay line from (a) to (b), the electric field at different times can be measured and finally to reconstruct the full time profile of the THz pulse.

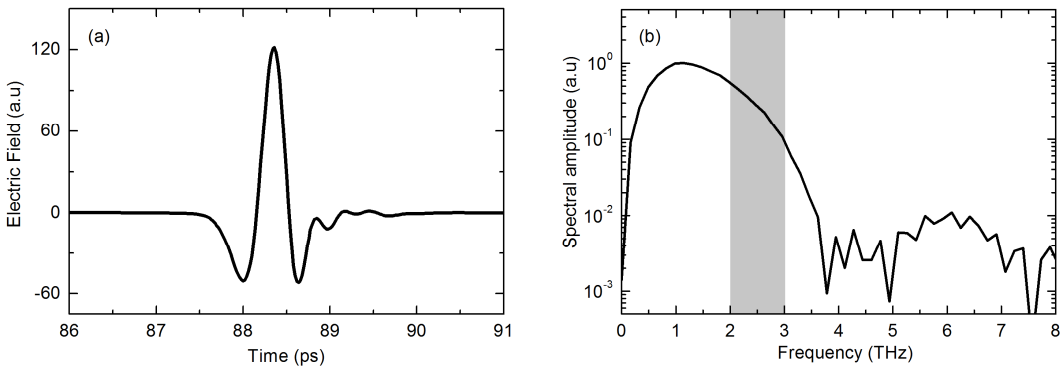

Fig 2.6 | THz generation from a GaAs photoconductive antenna in the (a) time domain (b) frequency domain.

Fig 2.6 (a) shows a typical time domain scan of the THz pulse from a GaAs photoconductive antenna under a ~100 *fs* optical pulse excitation with an average power of ~400mW and a central wavelength at ~810 nm. A ZnTe crystal was used for electro-optic sampling. Fig 2.6 (b) is the spectrum of the photoconductive antenna emission obtained by fast Fourier transform (FFT) of the temporal signals in (a). For this photoconductive antenna, the duration of the THz pulse is about ~1 ps and frequency response is centered at ~1.2 THz, covering the range from 0.1 THz to 3.8 THz. The grey zone in Fig 2.6 (b) is the spectral components between 2 to 3 THz, corresponding to the QCL frequencies that will be investigated in the latter chapters. This photoconductive antenna is the external THz source that will be employed to inject THz pulse into QCLs. This will control the emission phase of THz QCLs for detection of the ultrashort THz pulse generated by mode-locking in this thesis.

2.3 Injection phase seeding of THz QCLs

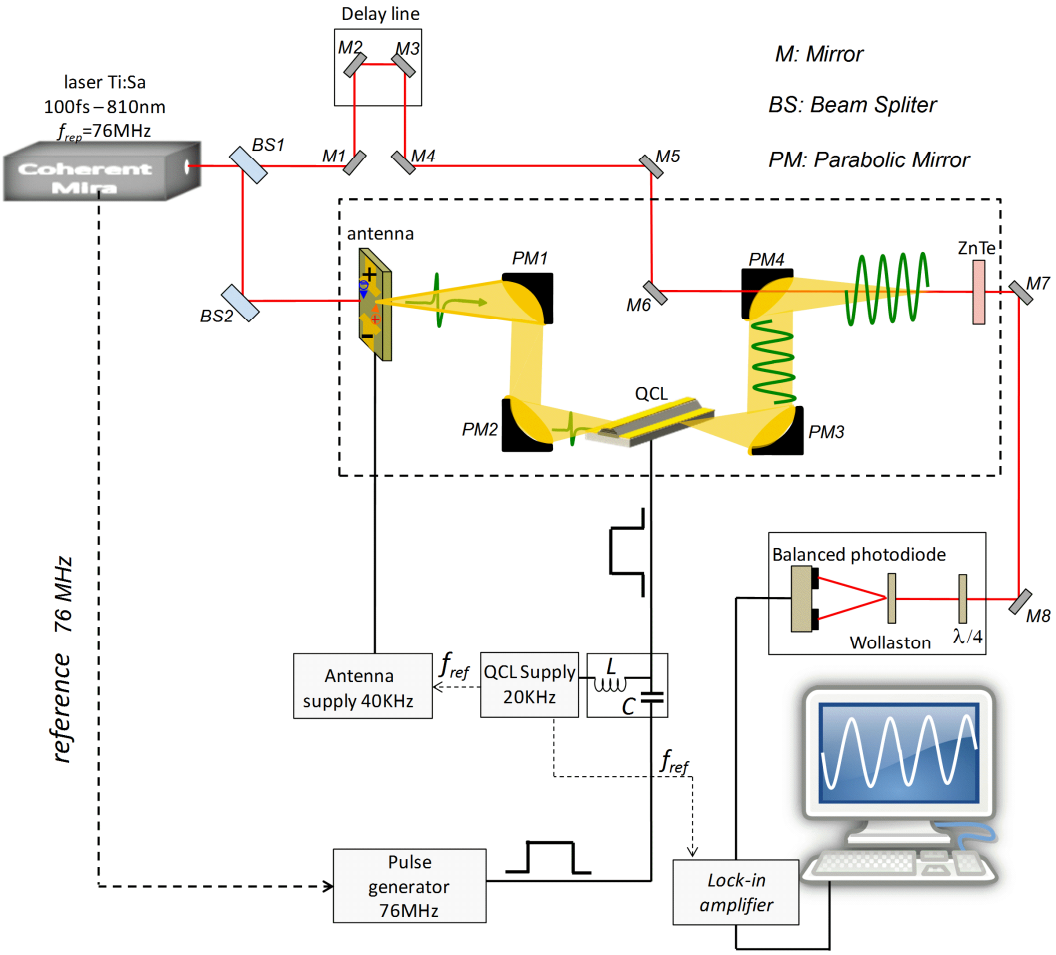

Fig 2.7 | Injection seeding setup for time-resolved detection of THz QCL emissions. QCL supply 20 KHz: a quasi-DC supply of 20-KHz frequency and 5-µs width to hold a QCL slightly below its lasing threshold. Pulse generator 76 MHz: electrical pulses trigged by *fs* optical pulse to bring a QCL above its threshold at a repetition frequency of 76 MHz (13 ns). Antenna supply 40 KHz: supply to switch on a photoconductive antenna with a width of 5 µs and a frequency of 40 KHz. Red pulse (line): *fs* optical pulse (paths). Green pulses: THz waves emitted by photoconductive antenna and QCLs. Yellow zones: THz pulse path. Black line: electrical connections.

Using THz time domain spectroscopy, we have shown the ability to coherently detect the actual electric field emitted by photoconductive antennas in the time domain as introduced above. We will now show how such a system can be used to detect the time-resolved emission of a THz QCLs, with an aim of to understand its ultrafast properties and short pulse generation that will be demonstrated in the following chapters.

A natural proposal for this is to simply replace the PC antenna in Fig 2.4 by a THz QCL. The QCL is then electrically synchronized to the *fs* laser by using a fast photodiode to trig its electrical supply. However, although the QCL can be electrically synchronized to the *fs* laser, the QCLs phase is random as the laser action is initiated by its spontaneous emission. If there is no fixed phase relation between the emission of THz QCL and *fs* optical pulses, thousands of times averages of the measurements will result in zero. Therefore, the electric cannot be resolved using this method and we therefore require a method to fix the phase of the QCL.

Fig 2.7 shows the injection seeding setup for the time-resolved detection of THz QCL. Based on THz-TDS, a QCL is placed at the focus point of the parabolic mirrors *PM2* and *PM3*. The principle is to inject a phase-resolved ‘‘seed’’ THz pulse emitted by photoconductive antenna into the QCL cavity to initiate its laser action through the phase-resolved external THz source, instead of QCL’s random spontaneous emission [79] [67]. In this way, the phase of the QCL emission can be fixed and synchronized to the THz pulses from the photoconductive antenna, and therefore also the *fs* optical pulses. Once its emission phase is controlled, its electric field of QCL emission in time domain can then be detected using EO sampling.

As is illustrated in Fig 2.7, the system is similar to that described in Fig 2.4. Here the antenna is biased by square signals with an amplitude of 3 V, a frequency of 40 KHz and a duty cycle of 20%. The THz pulses generated by the photoconductive antenna are collected by the *f#1* gold parabolic mirror *PM1* and then injected into the THz QCL by the *f#2* parabolic mirror *PM2* as is shown in Fig 2.7. The QCL is held below its threshold by a square electrical signal with a frequency of 20 KHz and a duty cycle of 10%. Simultaneously, when the THz pulse (seed pulse) is coupled into the QCL, the QCL is brought above laser threshold by a radio-frequency (RF) electrical pulse, trigged by the *fs* laser pulses via a high-speed photodiode within the Ti:Sapphire laser as shown in Fig 2.8. The RF pulses are short electric pulses with a width of 6 ns at the same repetition rate (~76 MHz) as the *fs* laser. They are employed to switch the QCL off and on alternately for coherent sampling between each fs pulse. In this case, the injected THz pulse will be amplified until the laser action of QCL will be initiated by the injected THz pulses, and therefore its phase can be completely controlled. In other words, every time the QCL is switched on, its emission has always a fixed phase determined by the *fs* optical pulses. This is shown in Fig 2.8 where the $\boldsymbol{E}_{THz}$ in green is the emission of the QCL - as the phase is the same between each THz pulse (13ns), the electric field of the THz is sampled at the same time. Averaging at a fixed position will therefore permit the electric field to be obtained with a high-signal-noise-ratio as presented by the yellow point in Fig 2.8. Continuously varying the delay between the QCL emission and the *fs* optical pulses, permits its time-resolved electric field be determined with a high time resolution (typically ~20 *fs*) as described above for the THz antenna. Further the entire dynamic of the QCL can be determined from the amplification range (generally for QCL from 0ps to ~600 ps) to the saturated range (stable emission range, after ~600 ps). This ultrafast technique with a bandwidth of up to ~100 THz (corresponding to ~10 *fs* resolution) not only permits us to demonstrate mode-locking of THz QCLs but also allows us to access to the ultrafast dynamics of QCLs.

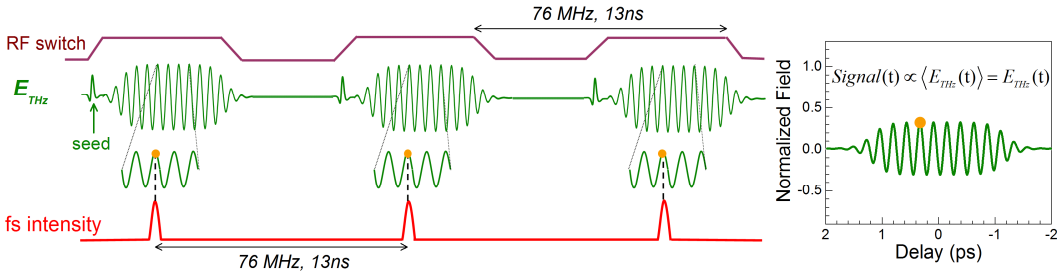

Fig 2.8 | Schematic diagram for electro-optic sampling of QCLs waves synchronized to *fs* optical pulses. RF switch: Electrical pulses to switch QCLs on and off alternately with a repetition frequency of 76 MHz trigged by the *fs* optical pulses. $\boldsymbol{E}_{\mathrm{THz}}$: Electric field of QCL emission in the time domain. Seed pulse: the THz radiation emitted by photoconductive antenna to be coupled into QCL cavity for phase control. *fs* intensity: 100 *fs* optical pulses generated by the Ti: Sapphire laser. Right: measured electric field by varying the delay between *fs* optical pulses and THz QCL emission.

Fig 2.9 shows the typical time-resolved emissions of a single-plasmon bound-to-continuum THz QCL with emission frequency centered at ~2.15 THz, which is measured by this injection phase seeding technique. (a) is the electric field of the QCL recorded from 0 ps to 1500 ps. The THz seed pulse radiated by antenna is injected into the QCL at around -30 ps from one of its facet mirrors. Propagating along the laser cavity, it will be amplified. When it arrives at the opposite facet, part of the THz pulse is coupled out and detected by our system as shown in Fig 2.9 (a) at around 0 ps (propagation time of ~25 ps corresponding to a single pass through a 2-mm long QCL). The remaining part is reflected back into the cavity and continues to be amplified. After one round-trip, after reflection at the opposite facet, it will again be partly coupled out and this becomes the second pass in the figure at ~50 ps and so on. This results in a quasi-pulsed type behavior with each pulse being amplified and separated by the round-trip time.

After each round-trip inside the Fabry-Pérot cavity, the pulse is broadened in time (and therefore sharpened in frequency), owing to the limited gain spectral bandwidth, until the THz wave completely fills the laser cavity. We can see in (a) that the dynamic range of the QCL starts from 0 ps until to ~600 ps, where the electric field is broadened and amplified. After ~600 ps, the QCL emission becomes stable where the gain of QCL is saturated (clamped to losses) and there is no further amplification. (b) is the amplification efficiency of the QCL as a function of time, which is calculated by comparing the pulse with its previous one. Before ~600 ps, the amplification is not clamped to the total losses and thus is above 1. After ~600 ps, the gain is clamped to the losses and therefore it is equal to 1. (c) is a zoom of the measured electric field in (a) from 1164 ps to 1172 ps. Oscillations of electric field with a time period of ~500 ps corresponding to a frequency of ~2 THz can be clearly witnessed. (d) shows the spectrum of QCL emissions centered at 2.14 THz, which is obtained by fast Fourier transform of (a). Importantly, to verify that the QCL is seeded by the input pulse, (e) is the amplitude of electric field of QCL radiation at about 1000 ps as a function of the photoconductive antenna voltages

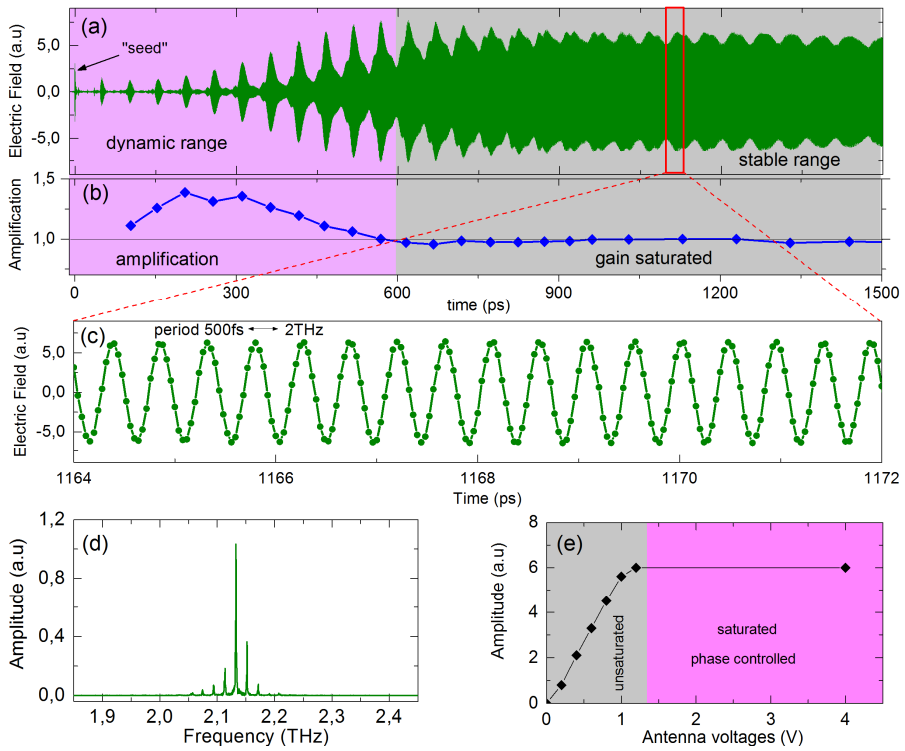

Fig 2.9 | Time-resolved emission of a THz QCL measured by injection phase seeding technique. (a) Electric field of QCL emissions from 0 ps to 1500 ps. (b) The amplification efficiency of the QCL as a function of time (c) Zooming of the electric field of QCL emission from 1164 ps to 1172 ps. (c) Spectrum of QCL emissions obtained by fast Fourier transform of its measured electric field. (d) Amplitude of electric field of the QCL emission as a function of the THz seed power (antenna voltage) injected into the QCL. [From: *Oustinov et al. "Phase seeding of a terahertz quantum cascade laser". Nat. Commun.1:69(2010).*]

(which is proportional to the electric field amplitude of the THz pulse sent into cavity). If injected power is too weak (from 0 V to 1.0 V), laser action of QCL will be partly launched by the injected THz waves and partly started by the spontaneous emission. In this detection scheme, only the phase controlled emission can be detected, while the emission initiated by spontaneous emissions cannot be detected (see previous section). If the injected THz power is strong enough (> 1.5V), laser action will be dominated by the seed pulse and laser action from the spontaneous emission will be inhibited. In this condition, the injected pulse initiates laser action and, as the gain is clamped, increasing the injected THz power will not lead to an increase of the electric field. Therefore, in order to characterize the QCL emission properties, we need to inject enough THz power into the laser cavity to totally seed its emission phase and carry out measurements in the saturated region shown in the purple zone of Fig 2.9 (e). This technique is now well established. It is able to entirely characterize the THz emission of QCLs in the time domain from dynamic amplification until gain clamping in the stable range. Therefore, this time-resolved technique is our main tool to study free-running emission and mode-locking of THz QCL on the femtosecond time scales as will be presented in the following chapters.

2.4 Conclusions

In conclusion, injection seeding technique based on THz time domain spectroscopy was introduced in this chapter. This technique allows us to coherently detect the time-resolved electric field of THz QCLs emission and to further study its dynamic and radiation properties. In this thesis, the phase seeding technique is the main experimental set-up employed to study QCLs. The technique will be utilized in all the experimental chapters for mode-locking and to investigate ultrafast THz pulse generation from THz QCLs.

3

Principle of mode-locking

Mode-locking [80] [81] is a widely used technique to generate ultra-short and intense pulses from lasers. The development of mode-locked lasers has permitted many interesting applications, such as exotic nonlinear effects [82], high precision metrology and investigations into fundamental physics.

Passive mode-locking [83] is extensively used and widespread in the visible and near-infrared for short pulse generation, and is typically based on a saturable absorber element within the laser cavity. However, passive mode-locking is extremely difficult for THz QCLs owing to its ultrashort gain recovery time (~5 - 20 ps) [22] [47] when compared to the cavity round-trip time (~100 ps for a few mm cavity) of the laser. Conversely, the gain recovery time can be used as an advantage for *active mode-locking*, where the laser is electrically modulated at the cavity round-trip at microwave frequencies. This is the technique that has been used to show that THz QCL can generate THz pulses, albeit that the pulses are relatively long (~10 to 20 ps) [24] [25] [27] [26].

This chapter will be used to discuss the principle of mode-locking in time and in frequency domains. At the beginning in section 3.1, mode-locking will be briefly presented and then in section 3.2, its principle will be discussed in-depth by introducing the susceptibility of active medium and dispersion in Fabry-Pérot cavity. Finally, in section 3.3, I will introduce the passive mode-locking principle used to generate ultrafast laser pulses from violet to near-infrared ranges.

Chapter 3

3.1. Introduction of mode-locking

Mode-locking is a widely used technique to generate ultra-short and intense pulses from lasers [1]. Generally, when a laser is in operation, there is more than one resonant frequency that can be amplified and propagate in its cavity as schematically illustrated in Fig 3.1 (green waves). These frequencies are called *longitudinal modes* of a laser, which are determined by the cavity length and the active medium of the laser. If all the modes are in phase and the mode spacing between these modes is identical, the electric field of all these modes will interfere constructively in a small region in time. This will result in an ultra-short and intense pulse (red in Fig 3.1 below) in the laser cavity. It will propagate back and forth within the cavity and then be partially coupled out from the out-couplers (cavity mirrors) at every round-trip time. Temporally, a train of pluses separated by the laser cavity round-trip time will be obtained. This is the so called *mode-locking*. To put all the longitudinal modes in phase (i.e. equal mode spacing $\Delta\omega$ and time-independent phase φ,) is the key factor for mode-locking.

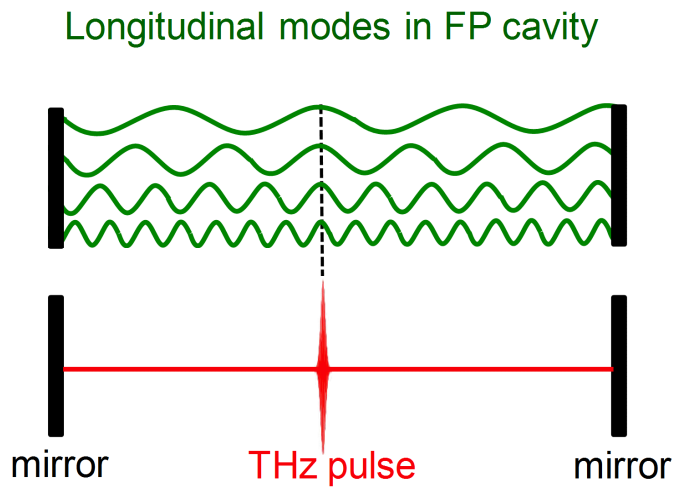

Fig 3.1 | Schematic diagram of mode-locking in time or space domain in a Fabry-Pérot cavity

The development of mode-locked lasers has permitted considerable scientific and industrial applications since its first demonstration in 1970s, from fundamental physics to high precision metrology. Generation of short pulses, through mode-locking of THz QCLs, is especially attractive owing to the unique properties of the THz range such as strong gas absorptions and small photon energy, which respectively allows high-sensitive gas sensing and non-destructive detecting in different fields such as biology, chemistry, security and military [11] [44]. In fact, using optical excited photoconductive antennas, THz pulse can be generated and satisfy many applications. However, the THz power is relatively limited, the spectrum is difficult to control and femtosecond Ti:Sapphire lasers are required. This prohibits the wide use of THz pulses in the domains mentioned above, especially in industries where compact devices and cost effective are required. Since the first THz QCL was experimentally demonstrated in 2002,

many leading research groups have been pursuing the generation of ultra-short pulses from these devices. Recently, this has been first realized by S. Barbieri et al [24] [84] at University of Paris-7 (2011) followed by our group [25] [27] [26] at École Normale Supérieure (2013), about 10 years after the realization of the first THz QCL and 40 years after the first mode-locked laser [81]. S. Barbieri et al demonstrated the active mode-locking of a 2.7-THz QCL, referenced to a mode-locked erbium-doped fiber laser, by sampling the electric field amplitude of the QCL and analyzing mode-locking in the frequency domain. Our work demonstrated mode-locking by directly measuring the THz pulses in the time domain using the injection seeding technique (Chapter 2). However, in both demonstrations, the generated THz pulses are large (greater or equal to 10 ps) resulting in a narrow spectrum and undermining their use for applications.

This thesis will address this problem directly and shorten the THz pulses and realize broadband frequency combs [28] [29] [85]. Before presenting the experiments and showing the results, we will provide an introduction to the principle of mode-locking. In this chapter, we will discuss, respectively in the time domain and frequency domain, what mode-locking is and methods to realize mode-locking.

3.2. Active mode-locking principle

3.2.1. Susceptibility of active medium in a 2-level atom system [86]

When mode-locking is presented, dispersion compensation [87] [88] and phase locking have to be unavoidably mentioned. Both of these elements are key factors for mode-locking and directly linked with the refractive index of the active medium. Furthermore, the refractive index of a medium is connected to the susceptibility by the relation: $n = (1+\chi)^{1/2}$. Therefore, to reveal how mode-locking operates, the susceptibility χ and its related parameters need to be understood. Therefore, before presenting mode-locking, the susceptibility of an active medium will be introduced and discussed.

The interaction between an atomic system and incident light will be used to describe the susceptibility. Here a 2-level system is considered for simplicity, interacting with an incident light beam as shown in Fig 3.2. The levels, level $|1\rangle$ and level $|2\rangle$, possess respectively energies E_1, E_2. The resonant frequency between them is given by: $\omega_0=(E_2-E_1)/\hbar$. The incident electric field with an angular frequency of ω is characterized by the equation: $\boldsymbol{E}=Ae^{-i\omega t}+c.c.$ Where A is the amplitude and $c.c$ represents the conjugate part of the electric field.

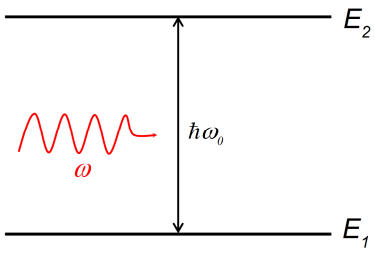

Fig 3.2 | Schematic diagram for light-matter interaction within a 2-level atom system

Light-matter interaction in this system can be described by the Von Neumann's equation:

$$i\hbar\frac{\partial\hat{\rho}}{\partial t}=\left[\hat{H},\hat{\rho}\right] \tag{3.1}$$

Applying the 2×2 density matrix $\rho=\begin{pmatrix}\rho_{11} & \rho_{12}\\ \rho_{21} & \rho_{22}\end{pmatrix}$ on Eq. (3.1), the differential equations for ρ_{11}, ρ_{22} and ρ_{12} can be obtained:

$$\dot{\rho}_{11}=-\dot{\rho}_{22}=\frac{i}{2}(\omega_1 e^{-i\omega t}+\omega_1^{*}e^{i\omega t})(\rho_{21}-\rho_{12}) \tag{3.2}$$

$$\dot{\rho}_{12} = i\omega_0\rho_{12} + \frac{i}{2}(\omega_1 e^{-i\omega t} + \omega_1^* e^{i\omega t})(\rho_{22} - \rho_{11}) \tag{3.3}$$

where ρ_{11} and ρ_{22} are respectively the population of quantum state $|1\rangle$ and state $|2\rangle$. ρ_{12} and ρ_{21}, conjugated to each other, represent the coherence of these 2 levels. $\omega_1 = 2dA/\hbar$ is the Rabi angular frequency [89] and $d \equiv d_{21} \equiv d_{12} = \langle 1|\hat{d}|2\rangle$ is the electric dipole of this interacting system. Removing the high oscillation parts by the quasi-resonant approximation, this set of equations can be further simplified to:

$$\dot{\rho}_{11} = -\dot{\rho}_{22} = \frac{i}{2}(\omega_1^* \rho_{21} e^{i\omega t} - \omega_1 \rho_{12} e^{-i\omega t}) \tag{3.4}$$

$$\dot{\rho}_{12} = i\omega_0\rho_{12} + \frac{i\omega_1^*}{2}(\rho_{22} - \rho_{11})e^{i\omega t} \tag{3.5}$$

If σ_{12} and σ_{21} are introduced to replace ρ_{12} and ρ_{21}:

$$\sigma_{21}(t) = \rho_{21}(t)e^{i\omega t} \tag{3.6}$$

$$\sigma_{12}(t) = \rho_{12}(t)e^{-i\omega t} \tag{3.7}$$

Then the Bloch equations for 2-level system can be naturally obtained:

$$\frac{\partial}{\partial t}(\rho_{22} - \rho_{11}) = -i(\omega_1^* \sigma_{21} - \omega_1 \sigma_{21}^*) \tag{3.8}$$

$$\frac{\partial}{\partial t}\sigma_{21} = i\delta\sigma_{21} - i\frac{\omega_1}{2}(\rho_{22} - \rho_{11}) \tag{3.9}$$

If relaxation and pumping processes are take into account in the Bloch equations above, Eq (3.8) and Eq (3.9) can be modified as:

$$\frac{\partial}{\partial t}\rho_{22} = \Lambda_2 - \gamma_2\rho_{22} - \frac{i}{2}(\omega_1^* \sigma_{21} - \omega_1 \sigma_{21}^*) \tag{3.10}$$

$$\frac{\partial}{\partial t}\rho_{11} = \Lambda_1 - \gamma_1\rho_{11} + \mathrm{A}\rho_{22} + \frac{i}{2}(\omega_1^* \sigma_{21} - \omega_1 \sigma_{21}^*) \tag{3.11}$$

$$\frac{\partial}{\partial t}\sigma_{21} = -(\Gamma - i\delta)\sigma_{21} - i\frac{\omega_1}{2}(\rho_{22} - \rho_{11}) \tag{3.12}$$

Where Λ_1, Λ_2 are the pumping rates for level $|1\rangle$ and level $|2\rangle$; γ_1 and γ_2 are relaxation rates for level $|1\rangle$ and level $|2\rangle$; A and Γ are respectively the associated decay rate induced by spontaneous emission and decay rate of coherences ρ_{12}.

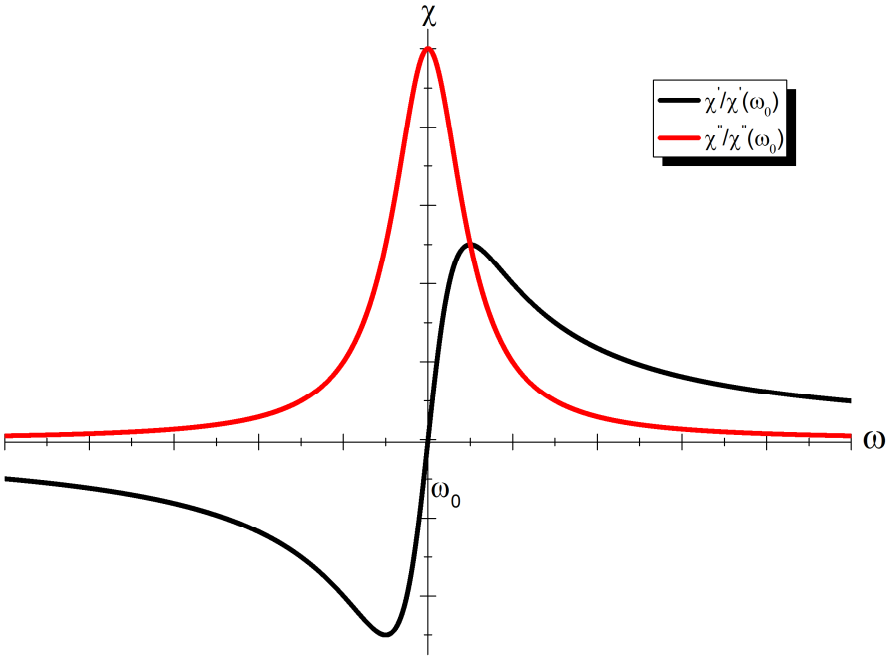

Fig 3.3 | Real and imaginary part of susceptibility as a function of frequency centered at transition frequency ω_0 for a 2-level atom system. $\chi'(\omega_0)$ and $\chi''(\omega_0)$ represent respectively the real and imaginary part of the susceptibility at $\omega=\omega_0$.

The steady state solutions of Eq. (3.10), Eq. (3.11) and Eq. (3.12) can be easily obtained by setting them to $\frac{\partial}{\partial t}\rho_{11}=\frac{\partial}{\partial t}\rho_{22}=\frac{\partial}{\partial t}\sigma_{21}=0$. Together with the steady state solutions, by comparing macroscopic polarization, $P=N\langle p\rangle=NTr\{\rho\hat{d}\}=2Nd\,Re\,\rho_{21}$, and the matrix polarization, $P=\varepsilon_0\chi E+c.c$, the real and imaginary part of susceptibility are given by:

$$\chi'=\frac{Nd^2}{\varepsilon_0\hbar}(\rho_{22}^0-\rho_{11}^0)\frac{1}{1+\frac{I}{I_{sat}(\delta)}}\frac{\delta}{\Gamma^2+\delta^2} \tag{3.13}$$

$$\chi''=-\frac{Nd^2}{\varepsilon_0\hbar}(\rho_{22}^0-\rho_{11}^0)\frac{1}{1+\frac{I}{I_{sat}(\delta)}}\frac{\Gamma}{\Gamma^2+\delta^2} \tag{3.14}$$

Where N is the atomic density, ε_0 is vacuum dielectric constant, $\hbar$ is the reduced Planck constant, $\delta=\omega-\omega_0$ is the detuning from resonant frequency, I is light intensity, I_{sat} is saturated light intensity and ρ_{22}^0, ρ_{11}^0 are respectively the initial population of level $|1\rangle$ and level $|2\rangle$. Therefore, $\chi^{'}/\chi^{'}(\omega_0)$ and $\chi^{''}/\chi^{''}(\omega_0)$ can be plotted as shown in Fig 3.3. The black curve, representing the real part of susceptibility $\chi^{'}/\chi^{'}(\omega_0)$, is a central-symmetric odd function at (ω_0, 0), while the red curve, representing the imaginary part $\chi^{''}/\chi^{''}(\omega_0)$, is an even function at $\omega=\omega_0$.

The refractive index of medium can therefore be described by the following equation:

$$n=\sqrt{1+\chi^{'}+i\chi^{''}}\approx n_0(1+\frac{\chi^{'}}{2n_0^2}+i\frac{\chi^{''}}{2n_0^2}) \tag{3.15}$$

Where n_0 is the refractive index at $\omega=\omega_0$. Therefore, we can see that the refractive index of active medium is not a constant as a function of frequency. Its real and imaginary parts have a similar shape as the real and imaginary part of susceptibility, respectively, as presented in Fig 3.3. It means that under free running conditions, the free spectral range of a laser (i.e. the separation between Fabry-Perot modes) $\delta f=c_0/2nL$ is not identical over the whole spectral range. This is one of the reasons why the free running emission of lasers is continuous instead of being pulsed. (The role of the phase of each mode is discussed in section 3.2.3). If we wish to generate shorter pulses from a laser with broad spectral bandwidth, it will be difficult due to the greater differences in the mode spacing.

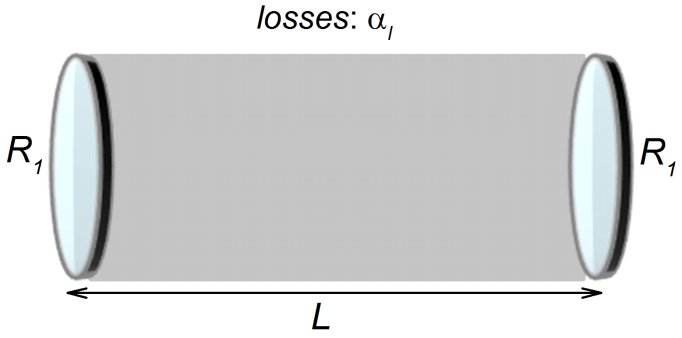

Fig 3.4 | Schematic diagram of a laser cavity

To obtain the exact expression of mode spacing, let us consider a laser cavity as shown in Fig 3.4, of length L, reflectivity R_1 and R_2, and total loss α_l. In the steady state, a wave travelling

through the cavity should give us the same wave both in phase and amplitude after a round-trip, which can be expressed as:

$$\sqrt{R_1 R_2 (1-\alpha_l)} e^{i2kL} = 1 \tag{3.16}$$

Using Eq. (3.15) to replace the refractive index, the wave vector *k* can be written as:

$$k = \frac{n_0 \omega}{c_0}(1 + \frac{\chi'}{2n_0^2}) + i\frac{\omega}{c_0}\frac{\chi''}{n_0} \tag{3.17}$$

Injecting Eq. (3.17) into Eq. (3.16):

$$\sqrt{R_1 R_2 (1-\alpha_l)} e^{i\frac{2n_0\omega}{c_0}(1+\frac{\chi'}{2n_0^2})L} \cdot e^{-\frac{2\omega\chi''}{c_0 n_0}L} = 1 \tag{3.18}$$

The real (amplitude) part $\sqrt{R_1 R_2 (1-\alpha_l)} e^{-\frac{2\omega\chi''}{c_0 n_0}L}$, which is responsible for laser gain, should be unitary while the phase part has to satisfy the integer 2π condition:

$$\frac{2n_0\omega}{c_0}(1+\frac{\chi'}{2n_0^2})L = 2\pi m \tag{3.19}$$

From Eq. (3.19), we can then get the expressions of resonant modes f_m' and their mode spacing $\delta f'$:

$$f_m' = \frac{c_0}{2n_0 L(1+\frac{\chi'}{2n_0^2})} m \tag{3.20}$$

$$\delta f' = f_{m+1}' - f_m' = \frac{c_0}{2n_0 L(1+\frac{\chi'}{2n_0^2})} \tag{3.21}$$

From these equations, how the mode spacing varies on frequency can be clearly witnessed and discussed below.

3.2.2. Free running emissions of lasers

A laser consists of an active medium, a pumping mechanism and a Fabry-Pérot cavity. The active medium is employed to amplify a wave travailing through it and pumping is used to realize a population inversion in the active medium. The Fabry-Pérot cavity serves as a resonant filter as well as an energy container to choose particular resonant frequencies (longitudinal modes) that are brought to threshold as illustrated in Fig 3.5 below.

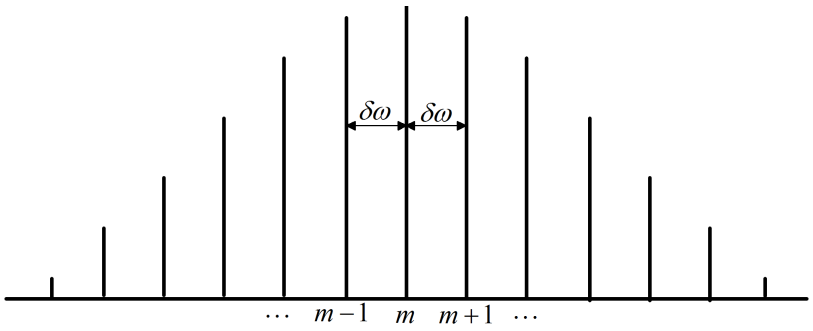

Fig 3.5 | Longitudinal modes of a laser in cold cavity

At first, let us consider a cold cavity, meaning that the refractive index n_0 does not depend on frequency. The resonant frequencies that can continuously exist in the cavity are given by:

$$f_m = \frac{\omega_m}{2\pi} = \frac{c_0}{2n_0 L} m \tag{3.22}$$

where m is an integer, c_0 is the light velocity in vacuum, n_0 is refractive index of medium in the cold cavity, L is cavity length. Therefore, the free spectral range (FSR) can be written as:

$$\delta f = f_{m+1} - f_m = \frac{\delta\omega}{2\pi} = \frac{c_0}{2n_0 L} \tag{3.23}$$

In a cold cavity, n_0 is a constant, so δf is fixed for a given laser. However, in the real case, as described previously, under free running condition, both resonant modes and their mode spacing are variables of frequency as presented in Eq. (3.20), Eq. (3.21) and illustrated in Fig 3.3. Compare Eq. (3.20) with Eq. (3.22), the resonant mode shifting between cold cavity and ‘‘hot’’ cavity can be calculated as:

$$f_m' - f_m = \frac{c_0}{2n_0 L(1+\frac{\chi'}{2n_0^2})} m - \frac{c_0}{2n_0 L} m = f_m(\frac{1}{1+\frac{\chi'}{2n_0^2}} \text{-1}) \approx -\frac{\chi'}{2n_0^2} f_m \tag{3.24}$$

As shown in Eq. (3.24), the m^{th} resonant mode f_m' in a hot cavity is slightly shifted from cold cavity mode f_m by an amount of $-\chi' f_m / 2n_0^2$. If $\delta = \omega - \omega_0 > 0$, Eq (3.13) will give us $\chi' > 0$. Consequently, the shift will be negative. In other word, for any frequency ω higher than central frequency ω_0, the resonant modes will be slightly pulled towards the central mode ω_0. On the other hand, if $\delta = \omega - \omega_0 < 0$, then $\chi' < 0$ and the shift will be positive. This means that for frequency ω lower than the central frequency ω_0, the modes will also be slightly pulled towards the central mode ω_0. Therefore, all the free running modes f_m' in hot cavity will be shifted towards the central frequency ω_0 compared with equal-spaced cold cavity modes f_m as illustrated in Fig 3.6. This is the ***pulling effect*** of free running lasers.

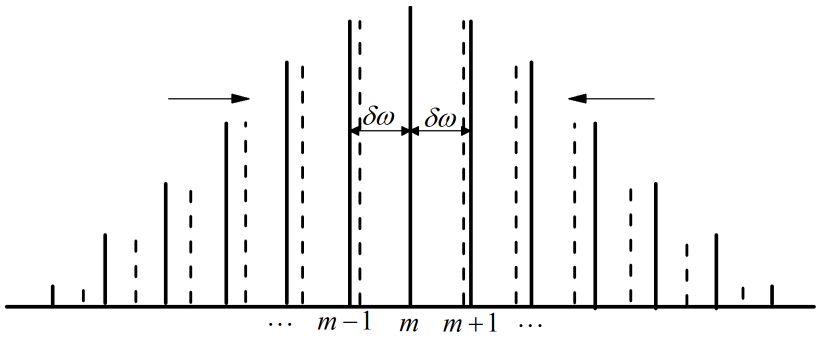

Fig 3.6 | Pulling effect of free running lasers. The solid lines represent equal-spaced cold cavity modes and the dashed lines represent non-identical modes in hot cavity.

Comparing with the cold cavity mode spacing in Eq. (3.23), the hot cavity mode spacing in Eq. (3.21) can be re-written as the sum of the identical cold cavity mode spacing and a hot cavity induced frequency-dependent term:

$$\delta f' = \frac{c_0}{2n_0 L(1+\frac{\chi'}{2n_0^2})} = \frac{\delta f}{1+\frac{\chi'}{2n_0^2}} = \delta f + \Delta f(\omega) \tag{3.25}$$

Where the cold cavity mode spacing δf is a constant, but the frequency-dependent term $\Delta f(\omega)$ will result in non-identical mode spacing, which prevents the formation of ultra-short pulses as discussed below.

The electric field of one mode, for example the m^{th} one, is $E_m(t) = A_m e^{2\pi i(f_m' t + \phi_m)} + c.c$. Adding electric fields of all these resonant modes together will give us the laser emission in the time domain:

$$
\begin{aligned}
E(t) &= \sum_{1}^{m} E_m(t) = \sum_{1}^{m} A_m e^{2\pi i(f_m' t + \phi_m)} + c.c \\
&= \sum_{1}^{m} A_m e^{i[2\pi(f_0 + m\cdot\delta f + \Delta f_m)t + \phi_m]} + c.c \\
&= \sum_{1}^{m} A_m e^{i[2\pi(f_0 + m\cdot\delta f)t + \phi_m + 2\pi\cdot\Delta f_m\cdot t]} + c.c \\
&= \sum_{1}^{m} A_m e^{i[2\pi(f_0 + m\cdot\delta f)t + \Phi_m(t)]} + c.c
\end{aligned}
\tag{3.26}
$$

Where A_m, f_m and ϕ_m are respectively the amplitude, frequency and time-independent phase of the m^{th} mode. $\delta\omega$ and $\Delta\omega_m$ are respectively the cold cavity mode spacing and the frequency-dependant mode shifting induced by hot cavity. $\Phi_m = 2\pi\Delta f_m t + \phi_m$ is the time-dependent phase of the m^{th} mode and ϕ_m is the time-independent phase of the m^{th} mode.

We will now consider how these parameters effect the temporal behavior of the electric field in Fig 3.7 and Fig 3.8. The time-dependent phase varies between modes and is always changing with time. This will bring a '*random (unfixed) phase-relation*' between the modes at any time and will result in continuous (non-periodic) wave emission in time. This is shown in the time resolved electric field and intensity (figure 3.7(a) and (b)) for a 3mm-long (δf=13 GHz) broadband (bandwidth ~ 500GHz) laser with emission frequency centered at 3 THz, if $\Delta\omega$ is randomly varied and assuming that ϕ_m = 0 (see next section). Fig 3.7 shows a time window from 200ps to 1000ps with the electric filed calculated from equation 3.26. We can see that the emission is not periodic, owing to non-equal mode spacing bringing a time-dependent floating phase. This is why even a broadband laser does not give us stable pulse emission under free running condition. Now if $\Delta f_m = 0$ (the spacing between these modes is constant), but ϕ_m varies for all modes (Fig 3.8), laser emission will become periodic with pulses being oberseved, but the pulse shape will be heavily deformed.

The key mission of mode-locking is to remove or fix the time dependent phase term and make mode spacing and mode phase identical via active/passive/hybrid techniques Generally, when a laser is mode-locked and periodic pulses are generated, δf and ϕ_m will be automatically fixed owning to the ''phase-matched'' modulation imposed on these modes, as described in the next section.

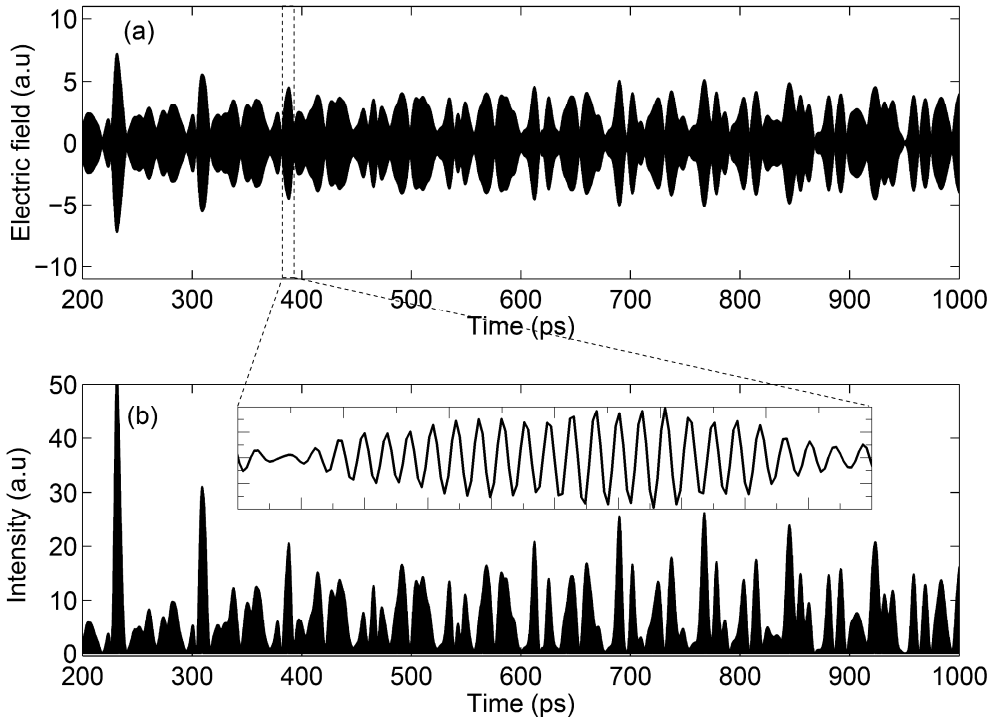

Fig. 3.7 | (a) Calculated electric field of laser emission from 200ps to 1000ps with a femtosecond time resolution with a time dependent phase and φ_m=0. (b) Intensity of laser emission corresponding to (a).

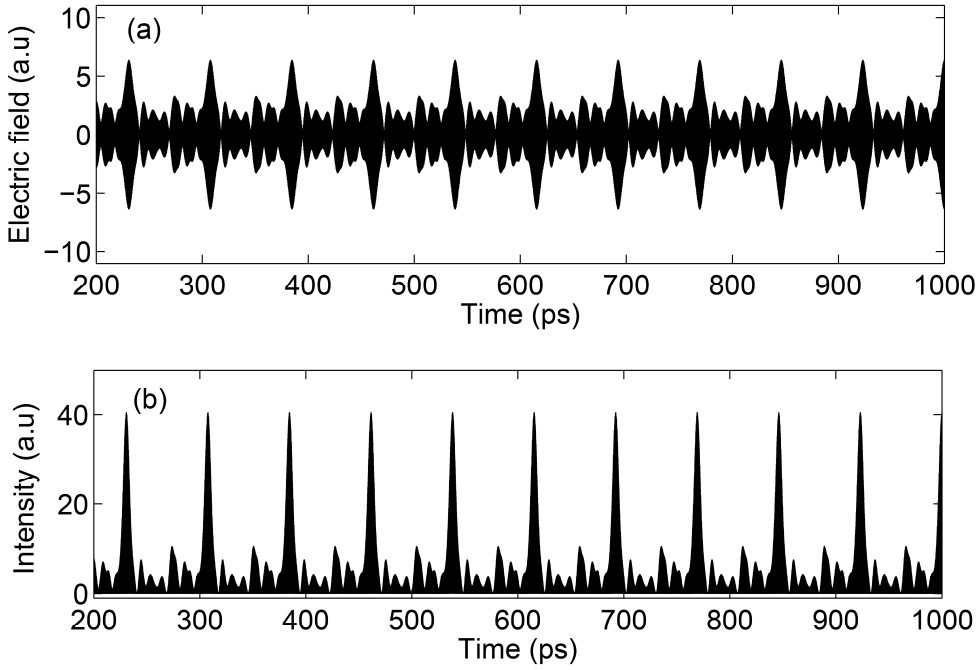

Fig. 3.8 | Calculated lasers emission with Δf_m=0 but phase ϕ_m of each modes is different. (a) Electric field from 200 ps to 1000 ps and (b) Intensity corresponding to (a).

3.2.3. Active mode-locking

If n is independent of frequency, the mode spacing $\delta f = c_0/2nL$ will be identical over the whole spectral range. Therefore, we can simplify Eq. (3.26), the electric field of the m^{th} mode in time domain, to $E_m(t) = A_m e^{i(\omega + m\delta\omega)t} + c.c$ by assuming ϕ_m=0. Adding all these modes together, the emissions of laser in time domain can be given by:

$$E(t) = \sum_{1}^{m} E_m(t) = \sum_{1}^{m} A_m e^{i(\omega + m\delta\omega)t} + c.c \tag{3.27}$$

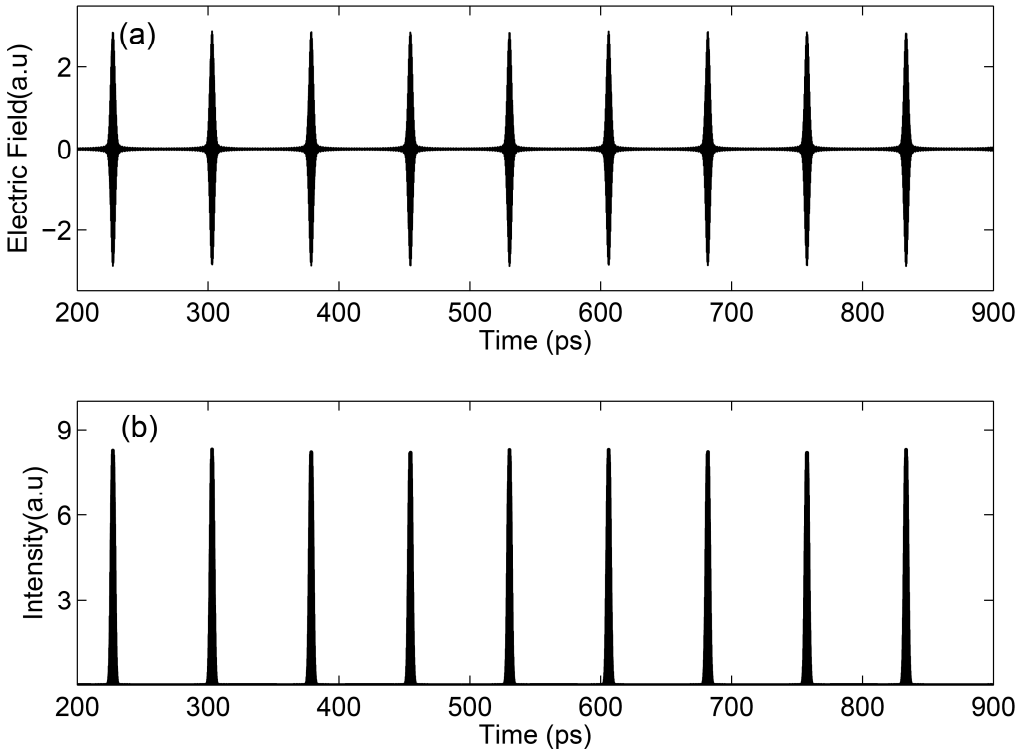

Fig 3.9 | (a) Electric field of a mode-locked laser emission as a function of time. (b) Intensity corresponds to the electric field above.

Here we will take the same example as previously, with a 3mm-long QCL (δf =$\delta\omega$/2π=13GHz) with 500GHz bandwidth centered at 3THz but now considered $\Delta\omega_m$ and ϕ_m are zero. Its temporal emission (electric field and intensity) are plotted as Fig 3.9 using Eq. (3.27). Ultra-short stable pulses, as short as 1ps, are produced. This is called mode-locking. However, in reality, as discussed in section 3.1.2, neither the free spectral range of laser δf is constant nor are their phases ϕ_m identical, leading to continuous waves or heavily deformed pulses being generated. Therefore, mode-locking is to use active or passive techniques to force the mode spacing δf and their phases ϕ_m to be constant over the entire emission spectrum.

How can we fix the spectral range δf of a laser and keeping the modes in phase? There are many ways that can be used to achieve this, including active mode-locking, passive mode-locking and hybrid mode-locking. Each type of mode-locking can be also realized by many different detailed techniques, such as direct current modulation [90], acoustic-optic modulation [91] [92], saturable absorption [93], nonlinear Kerr effect [94] etc. In this chapter, all these three types of mode-locking will be briefly described as this is the main subject of the thesis.

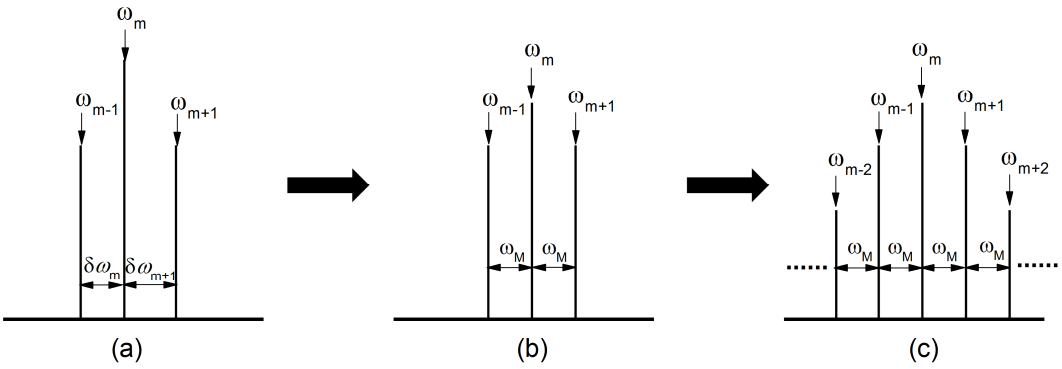

Fig 3.10 | Schematic diagram of active mode-locking in frequency domain (a) Spectrum of free running emission. (b) Modulation is applied on a laser. (c) laser is mode-locked.

How is active mode-locking realized ? Generally, we employ an electrical modulation ω_M, which is monochromatic and very close to the mode spacing $\delta\omega$, to directly modulate a laser (i.e. modulation at the round trip of the cavity). Firstly, let's consider the modulation effect on the frequency ω_m as is illustrated in Fig 3.10 (a). Before modulation is applied, the free running emission mode spacings are not identical $\delta\omega_m \neq \delta\omega_{m+1}$. When modulation is applied, the central frequency ω_m will transfer a part of its energies to its modulated sidebands ($\omega_m + \omega_M$, $\omega_m - \omega_M$) and are close in frequency to the 2 free running modes (ω_{m-1}, ω_{m+1}) of the cavity. If modulation power is strong enough, it will force the free running frequencies (ω_{m-1}, ω_{m+1}) to move towards the sidebands frequencies positions at ($\omega_m + \omega_M$, $\omega_m - \omega_M$) until they totally overlapped $\omega_{m-1}=\omega_m-\omega_M$, $\omega_{m+1}=\omega_m+\omega_M$. Finally, the mode spacing will be locked to the modulation frequency $\delta\omega_m=\delta\omega_{m+1}=\omega_M$ as presented in Fig 3.10 (b).

Above we have analyzed the modulation effect only on the central frequency ω_m. We can also use the same way to analyze the other frequencies: ω_{m-1} to get $\delta\omega_{m-1}=\delta\omega_m=\omega_M$, ω_{m-2} to get $\delta\omega_{m-2}=\delta\omega_{m-1}=\omega_M$, ω_{m-3} to get $\delta\omega_{m-3}=\delta\omega_{m-2}=\omega_M$.... At the end, we have $\delta\omega_{m-2}=\delta\omega_{m-1}=\delta\omega_m=\delta\omega_{m+1}=\delta\omega_{m+2}=\cdots=\omega_M$, i.e. the mode spacing over the whole spectrum of a laser emission will be fixed to the modulation frequency as shown in Fig 3.10 (c). Simultaneously, the time-independent phase ϕ_m will also be identical among all the modes, owing to the synchronization of the modes through the active modulation. As mentioned above in Fig 3.9, once the mode spacing is locked and their phases are identical, the laser emission in the time domain will be pulsed and active mode-locking will be realized.

3.2.4. Beatnote

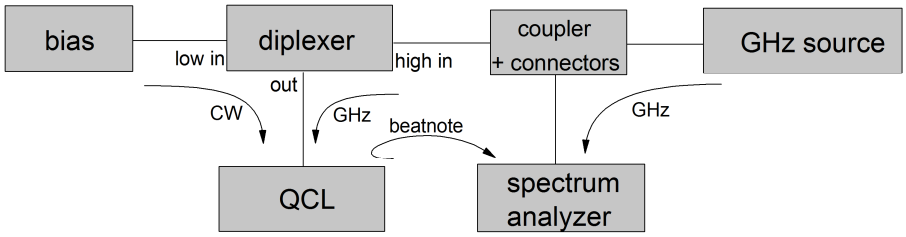

Fig 3.11 | Experimental setup for beatnote frequecy measurement in a THz QCL

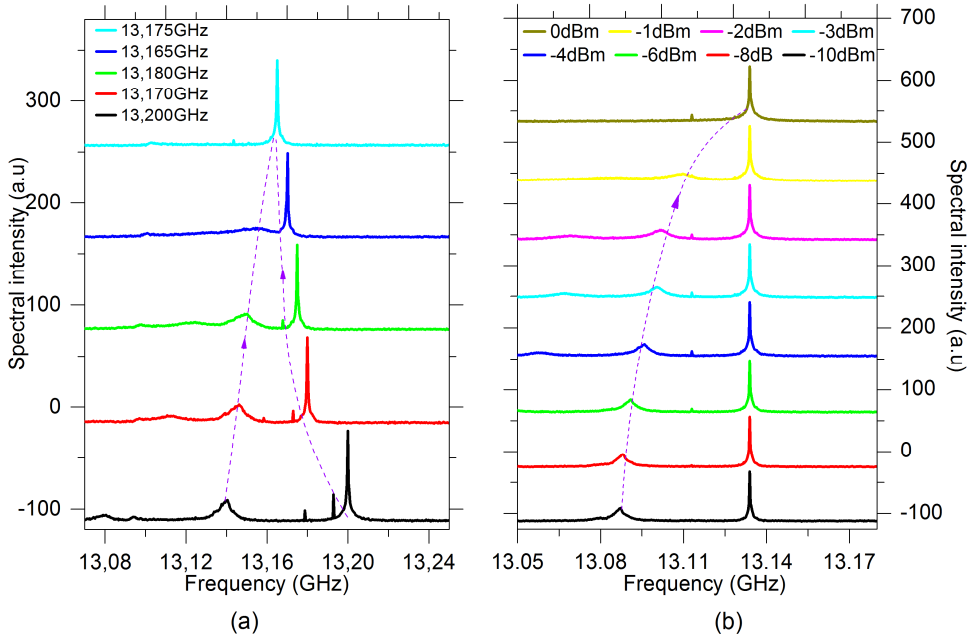

Fig 3.12 | Pulling effect of modulation in active mode-locking. (a) Moving modulation frequency towards beatnote with a fixed microwave power. (b) Increasing modulation power to extend locking range by increasing microwave power.

The electrical beatnote is a technique that can be used to illustrate how the modes behave when the laser is active mode-locked. It corresponds to the beating of the multiple fabry-perot modes of a laser cavity and is therefore is an indication of the mode spacing/round-trip frequency. For example, a 3mm long cavity will have fabry perot modes separated by ~13 GHz and therefore give a beatnote at this frequency. If the mode spacing is not identical across the whole spectrum, the beatnote frequency will be wide. On the contrast, if the mode spacing is identical, the beatnote will be narrow. (This technique has been used extensively to study frequency combs in QCLs). Now let us directly look at the beatnote and active mode-locking processes from the external induced “pulling” experiment in a THz QCL (the “pulling effect”

presented in section 3.2.2 is the intrinsic pulling effect owing to the dispersion of active medium and here the pulling of fabry-perot modes is induced by external modulation frequency and power). The device, wafer number V453 grown at the University of Cambridge, was a 3-mm long with an 80-µm wide ridge in a MM geometry, with an emission frequency centered at 2.1 THz. As shown in Fig 3.11, in the beatnote experiment, the bias is employed to electrically supply the QCL and the diplexer (11 SZ 10 - 6000 /T 18000-O/O)) is used to combine the low frequency bias and the high frequency modulation produced by the GHz generator (KEYSIGHT PSG E8251A) to actively mode-lock the QCL. We used a broadband high-speed spectral analyzer (Agilent N9344C 20GHz Spectrum Analyzer) to directly display the beatnote of the QCL and GHz modulation frequencies applied on the QCL at the same time. As illustrated in Fig 3.12 (a), the broad peak at the left side is the beatnote frequency, representing the mode spacing of the laser and the extra-fine line at the right side is the GHz modulation frequency applied on the laser. Before demonstrating the pulling effect, we define the locking range [95] as Eq. (3.28) below:

$$\Delta f_{locking} = \frac{2f_0}{Q}\sqrt{\frac{P_{injection}}{P_0}} \tag{3.28}$$

Where the f_0 is the free-running oscillation frequency, $P_{injection}$ and P_0 are the injected power and the free-running oscillator power respectively, and Q is the oscillator Q-factor. The locking range indicates the frequency range in which the free running oscillator can be locked to the injected power. This is an indication of mode-locking in our experiment where the beatnote frequency is fixed to the microwave modulation. If the injection power is high, the locking range will be wide. This means we can vary the modulation frequency in a wide range to mode-locked a laser. It needs to be mentioned that the modulation power required for actively mode-locking a laser depends on the optical intensity inside its cavity and its Q-factor of cavity. If we wish to actively mode-locking a laser with different stored energy or different fabry-perot cavity, generally different modulation power is required.

The pulling effect can be described as follows. At first, as shown in Fig 3.12 (a), we fix the microwave power at 0 dBm and we tune the modulation frequency towards the QCL beatnote peak. This causes the beatnote to move moves towards the modulation frequency while its broad band nature does not change. Finally, if $f_{mod} \approx f_{beatnote}$ the beatnote and the modulation frequency become a single narrow peak when they fall into the locking range. This indicates that the free running mode spacing is locked to the modulation frequency. Even though pulses are not directly demonstrated, this is an indication that active mode-locking has been achieved. From Eq. (3.28), we know that active mode-locking can also be realized by increasing the power of modulation, keeping the modulation frequency constant. This is demonstrated in Fig 3.12 (b) at f_{mod} = 13.13 GHz. The modulation power is increased from -10 dBm to 0 dBm, forcing the broadband beatnote to move toward the modulation frequency. When the modulation power is strong enough, the locking range will also be extended such that beatnote locks to the modulation frequency.

3.3. Passive mode-locking

Active mode-locking is relatively easy to achieve and has been shown to be stable. However, the sinusoidal electrical modulation limits the pulse width that can be reached by active mode-locking. In order to obtain ultrashort pulses, passive [83] [94] or hybrid techniques should be used. But for THz QCL, its gain recovery time is very short (~5 ps) owing to a plethora of ultrafast scattering processes in the inter-subbands structures. This makes passive mode-locking extremely difficult to be realized in THz QCLs. However, passive mode-locking is indispensable for generating ultrafast pulses of light in all kinds of and therefore I will briefly introduce the technique.

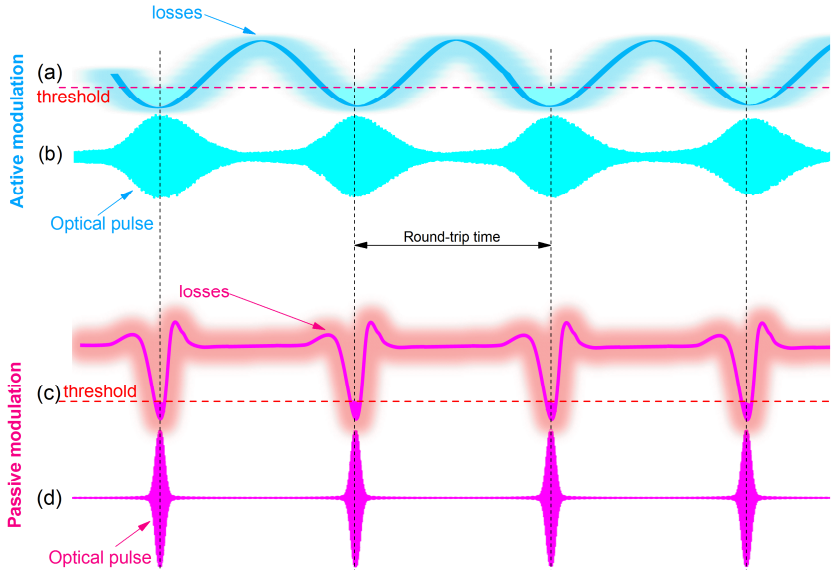

Fig 3.13 | Schematic diagram for active and passive modulation. (a) The losses of a laser as a function of time under the sinusoidal electrical modulation for active mode-locking. (b) The optical pulse train generated by active mode-locking. (c) The losses of a laser as a function of time under the sharp modulation of passive element for passive mode-locking. (d) The optical pulse train generated by passive mode-locking.

Fig 3.13 schematically shows the difference between active and passive mode-locking [96]. As discussed in section 3.2, for active mode-locking, an external electrical modulation at exactly the round-trip frequency is needed to be applied on the laser. The monochromatic frequency gives us a sinusoidal modulation in time domain as illustrate in Fig 3.13 (a). As a consequence, the generated optical pulses are relatively large. However, if we modulate the losses of a laser sharply using a passive element (i.e. saturable absorber, nonlinear effect etc.) as schemed in Fig 3.13 (c), the produced optical pulses will be much shorter as in Fig 3.13 (d). This sharp passive modulation can be achieved by inserting a saturable absorber inside the resonant cavity as shown in Fig 3.14. When optical waves with weak intensity pass through the saturable absorber, the optical power will be totally absorbed and strong losses will be

introduced. When an optical pulse with high enough intensity builds up in the cavity, its opens a small time window in the absorption and the saturable absorber will absorb the front and tail of the pulse as their intensities are relatively weak. The high intensity of the central part of the pulse will pass through the absorber without suffering any loss by saturating the absorber to make it transparent. In this way, the ultrashort optical pulse can be generated.

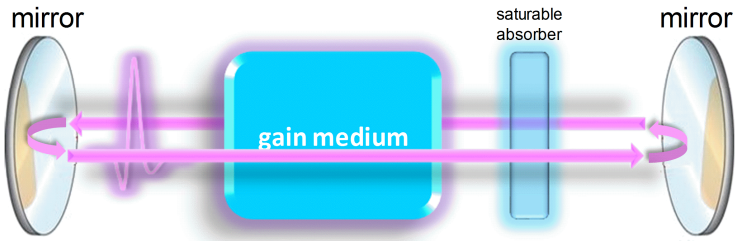

Fig 3.14 | Experimental setup for passive mode-locking by inserting a saturable absorber inside the laser cavity.

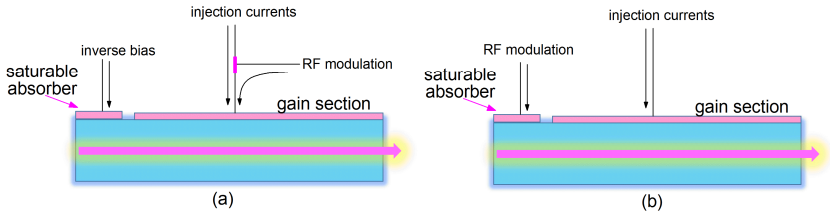

Fig 3.15 | Hybrid mode-locking configuration in conventional semiconductor lasers. (a) Inversely biased saturable absorber with RF modulated gain section. (a) RF modulated saturable absorber with DC gain section.

As discussed above, active mode-locking permits stable pulse generation using relatively simple modulation techniques, but it is not able to produce ultrafast pulses. On the other side, passive mode-locking allows ultrafast pulse generation, but it is difficult to be realized in a laser with ultrashort gain recovery time, for example THz QCL. Hybrid mode-locking is to combine the active and passive techniques in a single semiconductor laser to overcome the bottleneck of active and passive mode-locking, allowing to generate ultrafast stable optical pulse in a laser. Hybrid mode-locking can be found in conventional semiconductor lasers in visible/near infrared ranges using the same semiconductor materials as a saturable absorber for passive modulation and using microwave/RF for active modulation as shown in Fig 3.15 [97] [98] [99] [100]. Hybrid mode-locking is able to shorten the pulse of light from conventional semiconductor lasers down to a few picoseconds. However, for THz QCLs, as well the limitations of the fast gain recovery time mentioned above, inter-subband transitions are difficult to saturate prohibiting the use of its active medium as a THz saturable absorber. Therefore, conventional hybrid mode-locking cannot be used in THz QCLs unless novel schemes are implemented.

3.4. Conclusion

To conclude, in this chapter we have focused on the principle of mode-locking as a basis of pulse generation and pulse shortening of THz QCLs. At the beginning of this chapter, I presented the principles of mode-locking its importance for THz QCLs. As is known, the susceptibility of active medium is the fundamental reason for gain and its refractive index dispersion, which intrinsically prohibits the production of ultrafast pulses from lasers. The susceptibility of an active medium was then introduced for a 2-level system. By analyzing the expressions of susceptibility, we showed that the frequency-dependent refractive index between the longitudinal modes of lasers results in non-equal mode spacing for a free running device. Based on this, the unequal mode-spacing induces a frequency-dependent phase for each mode, which dephases the relations of modes and leads to continuous wave emissions. Mode-locking a laser permits to fix the spacing and phase between modes and permits short pulse generation and this was explained in the time and frequency domain. Finally, passive and hybrid mode-locking was also briefly introduced.

4

Active Mode-locking of Narrowband Single-plasmon THz Quantum Cascade Lasers

In previous chapters, I have introduced THz QCLs, the time-resolved detection technique for QCL emission and the principle of mode-locking. Starting from this chapter, I will concentrate on the experimental setups and results of THz QCL mode-locking.

This chapter will be based on the demonstration of active mode-locking a single-plasmon THz QCL at ~10 K by directly sampling its electric field via injection phase seeding. I will further show the possibility to continuously tuning the mode spacing (longitudinal modes) of QCL emission beyond a range of ~2 GHz by varying the active modulation frequency from 12 GHz to 14 GHz. This mode spacing tuning effect is then employed to characterize the absorptions in gas spectroscopy that will be introduced in *Appendix B*.

Chapter 4

4.1 Active mode-locking of a single-plasmon THz QCL

4.1.1 The state of the art

Active mode-locking of THz QCLs based on single-plasmon waveguide and a bound-to-continuum design have been demonstrated at 10 K in the time and frequency domains a few years ago [24] [25] [27] [54]. The generated THz pulses, however, are limited in the range of ~10 ps – 20 ps, owing to the bottleneck of the sinusoidal modulation, dispersion and the bandwidth of QCLs (see following chapters). In addition, the pulses from these actively mode-locked THz QCLs have not been manipulated for added functionalities. Here, I will demonstrate active mode-locking and the spectral tuning of THz QCLs by varying the modulation frequency. Then this spectral tuneabilty, which is generally extremely challenging for THz QCLs, will be employed in gas spectroscopy to identify the absorption lines of H_2O and CH_2OH.

4.1.2 Experimental setup

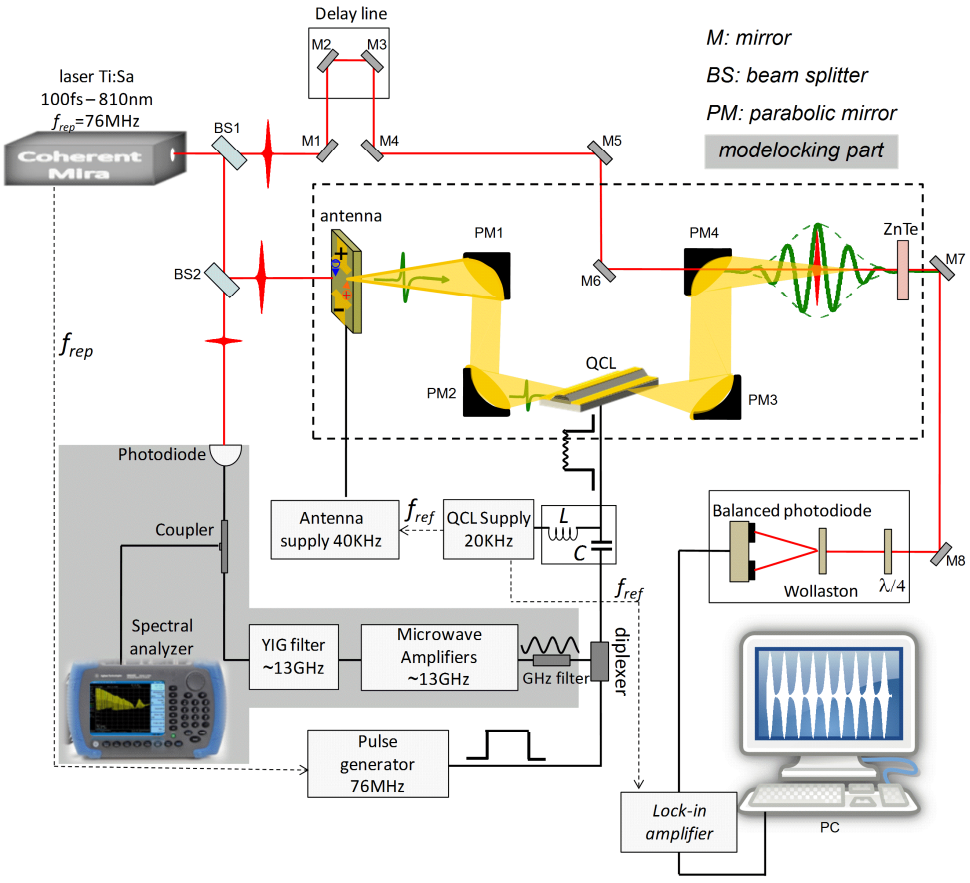

Fig.4.1 | Experimental setup for the demonstration of active mode-locking of THz QCLs using time-resolved coherent detection. (This is exactly the same as the injection seeding setup in chapter 2 except for the part highlighted in grey for the microwave modulation).

To demonstrate pulse generation via active mode-locking of THz QCLs, the injection seeding technique defined in chapter 2 or in ref [67] will be adapted here to show time-resolved electric field. Fig 4.1 shows the experimental setup for active mode-locking of the single-plasmon QCLs used in this chapter. The red lines and pulses represent the near-infrared femtosecond laser optical path and all the black lines stand for the electrical connections (dashed black line is the trig reference for the 76MHz pulse generator). The green pulses represent the THz pulses from the photoconductive antenna or the THz QCL and the yellow zones represent the THz waves path. The photoconductive antenna, parabolic mirrors, nonlinear crystal ZnTe and QCL are placed in a closed glass box (dashed rectangular region) and purged with a compressed dry air system. The experimental setup presented above is the same as injection seeding setup discussed in chapter 2 except for the high-speed electrical modulation system for active mode-locking at the QCL round-trip frequency. This includes a fast infrared photodiode, a coupler, a spectrum analyzer, a YIG filter and microwave amplifiers as highlighted by grey background in Fig 4.1.

To electrically modulate the QCL at the round trip, a pick off mirror (*BS2* in Fig 4.1) is utilized to separate the laser power into 2 parts, respectively 98% (~500mW) and 2% (~10mW) from femtosecond pulse trains as illustrated in figure above. The ~10mW infrared laser beam is focused into an ultra-fast photodiode (30ps response time for both rising and falling edges while keeping a low dark current less than 100pA (HAMAMATSU GaAs MSM Photodetector G4176-03)). The optical pulses will then be transferred into short electrical pulses. Using a high speed spectrum analyzer (Agilent N9344C 20GHz Handheld Spectrum Analyzer), we can observe a comb of electrical signals from around 76 MHz spreading to 20 GHz with a mode separation of 76.69MHz, exact the same as the femtosecond pulse repetition rate. A frequency-tunable Yttrium-iron-garnet filter (Micro lambda wireless MLFP-1593PD) is then used to pick out, for example, the 169th harmonic frequency (or some other integer harmonic frequency close to this one) from the electrical comb (76.69 MHz × 169=12.961 GHz) and to reject all the other frequency components. In this way, we can generate a GHz frequency at or close to the round-trip frequency of a 3mm-long QCL. As the power at 13 GHz directly after the YIG filter is low (-50dBm), microwave power amplifiers (Quinstar QPJ-06183846-B0) are employed to amplify the signals up to ~30dBm. This high power modulation is combined with the 20 KHz DC-bias and the 76 MHz RF pulses using a suspended substrate diplexer (11 SZ 10 - 6000 /T 18000-O/O) and injected into the QCL for mode-locking as shown in Fig 4.1.

Why do we use a YIG oscillation filter to choose the 169th harmonic frequency instead of using an external GHz wave generator (for example KEYSIGHT PSG E8251A), which is able to generate signals covering 250 KHz to 20 GHz with up to 20 dBm powers with sub-hertz resolutions? This is because our coherent detection system requires the GHz modulations to be synchronized with the 76 MHz RF pulses (or, equivalently, to the infrared femtosecond laser pulses). If an external unsynchronized generator is employed, the QCL emission will be sampled at different times for each round-trip period, as illustrated in Fig 4.2 (a). This will result in “zero” after thousands of averages by the lock-in amplifier. In contrary, when the 169th harmonic frequency of the RF pulses is used, the RF pulses and GHz modulations have a fixed phase relationship every time the QCL is switched on by the RF pulses as shown in Fig 4.2 (b).

This completely unchanged phase between RF pulses and GHz modulations allows to sample the time resolved emission of the mode-locked THz QCL.

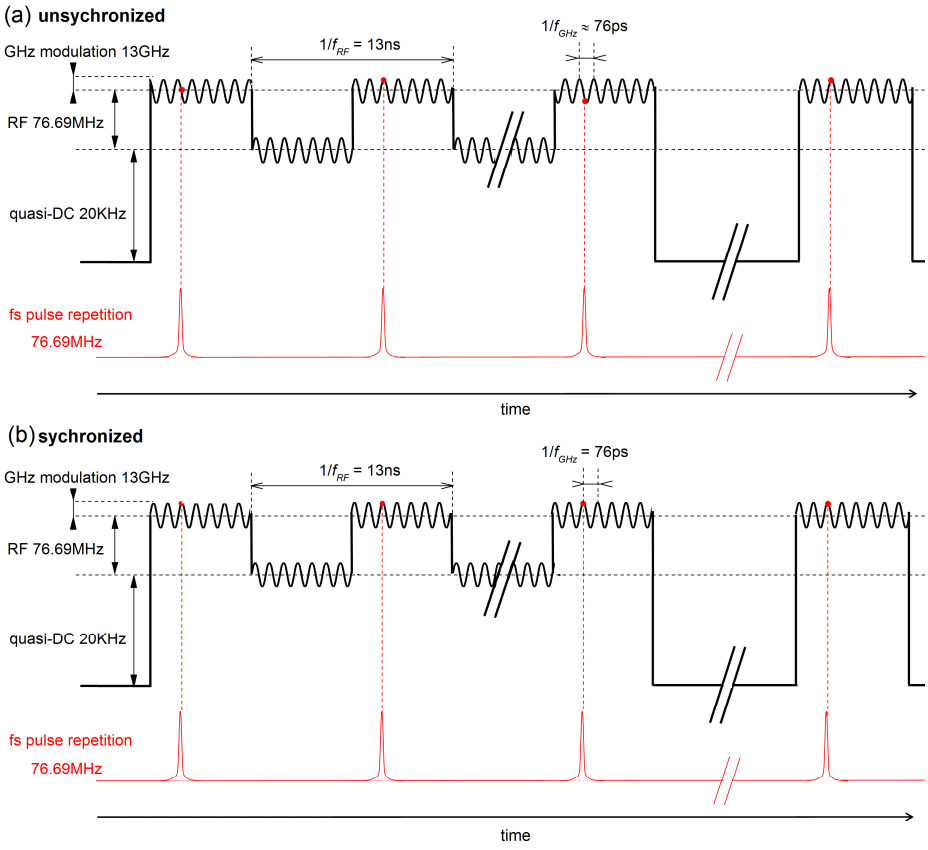

Fig 4.2 | Schematic diagram of electrical signals to switch on QCL (a) with an unsynchronized external microwave generator (b) with a synchronized Yttrium-iron-garnet oscillation filter.

The electrical signals guided onto the QCL include, as mentioned above, the 20 KHz quasi-DC supply to bias the QCL just below laser threshold, 76 MHz RF pulses to switch on and off the QCL periodically and the 13 GHz microwave modulation to initiate mode-locking as illustrated in Fig 4.1. These complicated signal components cover an extremely wide frequency range varying from kilohertz to gigahertz. Low speed cables cannot therefore be used, as the RF signals will be heavily deformed and high modulation frequency will not reach the QCL for mode-locking. Therefore, in our experimental setup, Mini-circuits high speed cables covering DC – 18GHz are utilized, limiting the loss and distortion. Just before the QCL chip, a customized high speed coplanar line microwave waveguide is employed, as drawn in Fig 4.3 (a), where wire bonding is used to connect to the QCL. Finally, right-angled SMP female & male connectors are used to connect the microwave waveguide and high speed cables as shown in Fig 4.3 (a). Fig 4.3 (b) show photos of the SMP female & male connectors and cables. Although this configuration cannot totally avoid losses and deformation at the wire bonding points, it can greatly minimize them and allow high-frequency signals to reach the QCL.

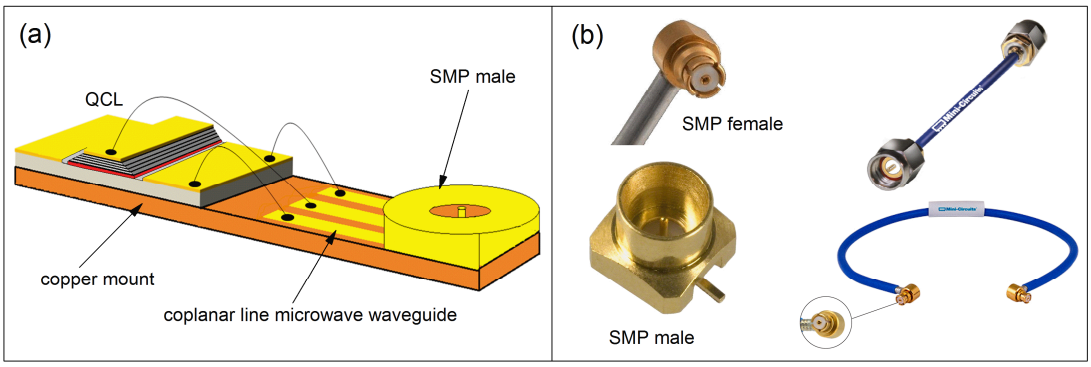

Fig 4.3 | (a) Diagram of a single Plasmon QCL mounted on a copper mount with a microwave waveguide and a SMP connector (b) Photos of right-angled SMP connectors and high speed mini-circuits cables.

Here we have presented only the high speed modulation part (light grey background part) of the experimental setup in Fig 4.1. The time-resolved coherent detection of the QCL emission has been discussed in detail in chapter 2.

4.1.3 Sample V455

The sample used in the chapter is from wafer ‘‘*V455*’’ and was fabricated (growth and processing) at the University of Cambridge, U.K by Dr. J. R. Freeman. It is a single-plasmon (see section 1.3.3 in the chapter 1) THz QCL based on the bound-to-continuum design (see section 1.3.2 for more details) with emission frequency centered at 1.95 THz [101]. In this design, GaAs/$Al_{0.1}Ga_{0.9}As$ quantum wells were employed. The thicknesses of quantum wells and barriers of the active region starting from injector are: **4.8**/*11.97*/**4.2**/*11.4*/**3**/*11.78*/**2.9**/*12.54*/**2.5**/*14.53*/**2.3**/*13.82*/ **0.99**/ *11.54*/**1**/*15.03nm*. Barriers are shown in bolds and quantum wells are shown in italics. Underlined quantum wells were doped at the level of 1.3×10^{16} cm^{-3}. The band structure of this design is presented in Fig 4.4, with the laser transition between the excited level (blue) and fundamental level (red). The energy gap between the blue line and red line in Fig 4.4 is ~ 8 meV, corresponding to an emission frequency centered at around 1.95 THz. The wafer was processed into a 3-mm-long cavity and 250-µm-wide ridge at the first step. Then it was cut into two sections by focused ion beam etching. The long section, roughly 3 mm, will be biased for lasing and the short section, ~150 µm, will be employed to investigate whether there are any influences or not on the time-resolved emission of this single-plasmon waveguide bound-to-continuum QCL under free-running and mode-locked conditions, respectively. Generally, the full bandwidth at half maximum (FWHM) of this kind of QCLs is expected to be very narrow (less than ~50 GHz) and their lasing threshold is relatively low, which permits low electrical power consumption.

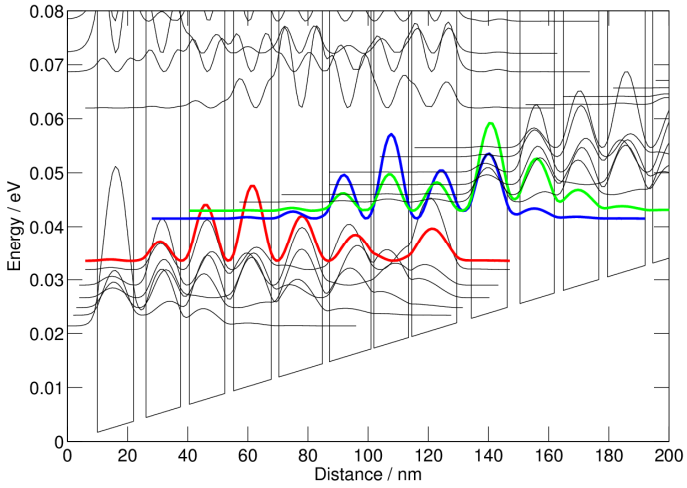

Fig 4.4 | Band structure of the 1.95 THz bound-to-continuum THz QCL. Green line: injector level, blue line: excited level of laser transitions, red line: fundamental level of laser transitions, black lines: mini-band for electron transports.

4.1.4 Coherent detection of QCL emission: seeding and mode-locking

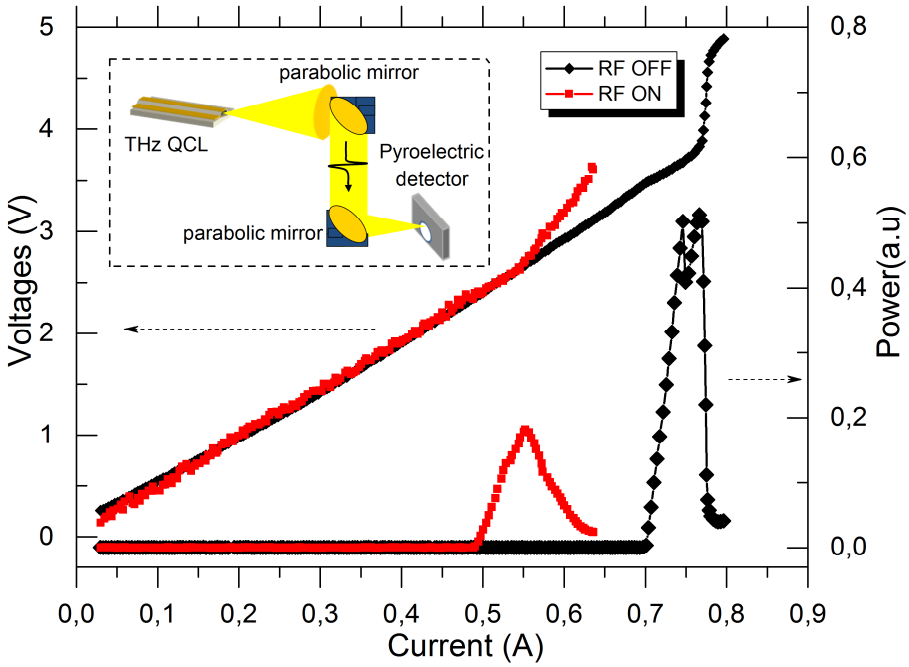

Fig | 4.5 Light-current-voltage (LIV) curves of the QCL with (red) and without (black) the 76.69 MHz RF pulses. Inset: experimental setup for LIV measurements.

Before investigating mode-locking, the time-resolved electric field of the free-running QCL emission will be shown using injection seeding. There are 2 reasons for this: 1. From the time-resolved profile of the QCL, the spectrum (mode spacing) of a QCL can be obtained, which allows us to roughly extract the modulation frequency for active mode-locking. 2. A comparison with the mode-locked emission of the QCL can be performed. Fig 4.5 shows the light-current-voltage (LIV) characteristics of the QCL at 10 K with (red) and without (black) MHz RF pulses. The QCL was operated in pulsed mode with 5-µs-long electrical pulses at a repetition frequency of 20 kHz. A 25 Hz electrical envelope modulation was used to enable lock-in detection of the output power using a pyroelectric detector. A #f/2 parabolic mirror was used to collect the output radiation from the QCL and a #f/1 parabolic mirror used to focus it into the pyroelectric detector as illustrated the inset in Fig 4.5. Without RF pulses, laser action starts at ~700 mA and ceases at ~770 mA with a narrow dynamic range of ~70 mA. The effect of applying the RF pulse for injection seeding can be seen in Fig. 4.5 where ~200-mW-power 6.2-ns-wide RF pulses trigged from the femtosecond laser (76 MHz) are applied to the QCL. It should be noted in the Fig 4.5, that the currents on the LIV curves are only the contributions of the 20 KHz quasi-DC bias and not the RF pulse. Comparing the 2 LIV curves, we can see that the RF drops the threshold of QCL from 700 mA down to 490 mA, implying that the RF pulse provides about 200 mA of current to push the QCL above its real threshold (~700 mA). We can also observe from that the peak emission power of the QCL with RF is only about half of that without RF. This is a result of the ~ 50 % duty cycle of the RF pulses – the RF pulse in on for 6.2-ns and off for 6.8ns (13ns - 6.2ns) the QCL.

In the injection seeding experiment, as previously, the QCL was operated in pulsed mode with 5-µs-long electrical pulses at a repetition frequency of 20 kHz. The electric currents injected in by this quasi-DC bias are 500 mA about 200 mA below the lasing threshold. The same RF conditions as detailed above were used. For electro-optic sampling, a 500-µm ZnTe nonlinear crystal is used to match the 1.9 THz frequency emission of the QCL.

Fig 4.6 shows the results of injection seeded emission of the QCL. (a) is the electric field of the QCL emission from 100 ps to 3000 ps with a 60 *fs* resolution. In this figure, the THz 'seed' pulse from photoconductive antenna is injected into QCL cavity at ~78 ps from one facet and after a single cavity trip, is partly coupled out from the other facet at the opposite side and becomes the first pass at 115 ps. The part that is not coupled out is reflected back in the cavity and amplified as it propagates in active medium. The pulse propagates back and forth, resulting in the second pass, third pass and so on, and the transmitted pulse recorded by the EO sampling system. From the recorded data in Fig 4.6 (a), we can see that the dynamic range starts from the beginning until 500 ps. After 500 ps, the QCL is saturated and falls into the steady state. (The amplitude of the QCL slightly decreases with time in the stable region owing to the imperfectly flat electrical RF pulse). Fig 4.6 (b) is the zoom of the electric field of QCL emission from 1094.5 ps to 1100.5 ps. We can clearly observe the oscillations of electric field with a period of ~0.5 ps, corresponding to an emission frequency of ~2 THz. (c) is the fast Fourier transform of the electric field in (a) representing emission spectrum of the QCL and showing Fabry Perot modes separated by ~13GHz. (d) is the amplitude of the QCL emission at 1538 ps as a function of THz power injected into the laser cavity (proportional the voltage

applied to the photoconductive antenna). When the injected THz pulse power is too weak (light grey region from 0 V to 1.5 V), the emission of QCL will be partly launched by the THz pulse and partly by the QCL's spontaneous emission. Only the phase-controlled emission can be coherently recorded by our system while the emission from the spontaneous emissions cannot be captured. Therefore, in this case, the detected electric field cannot totally characterize the emission properties of the QCL. However, after 1.5V in the purple region, the amplitude of QCL emission saturates, meaning that the QCL emission is entirely fixed by the injected THz pulse and the detected electric field is the total QCL emission. The measurements in figure 4.6 (a) are carried out with a voltage of 3 V on photoconductive antenna and therefore fully demonstrates the emission properties of this QCL under 'free-running' condition.

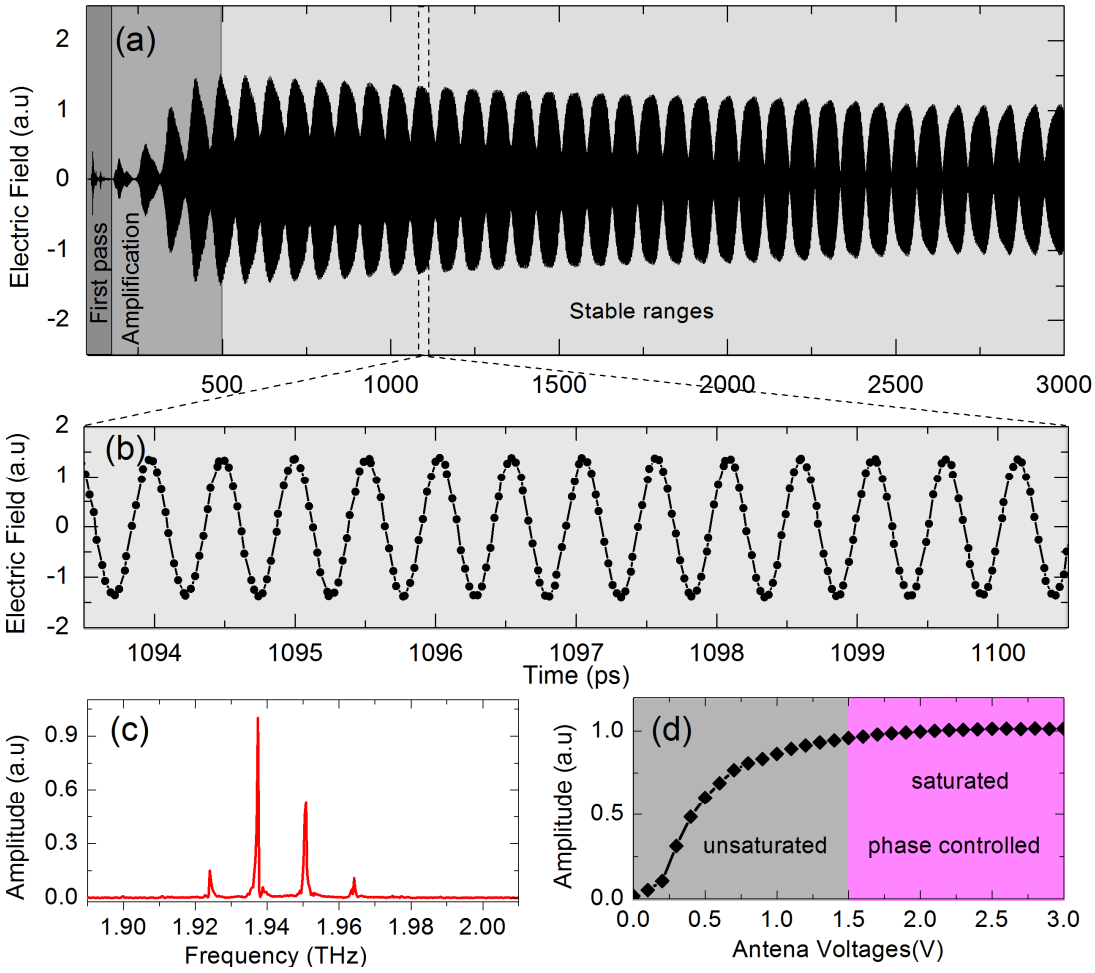

Fig 4.6 | (a) Phase-resolved electric field of the QCL emission from 100 ps to 3000 ps. (b) Zoom of the electric field of QCL emission from 1094.5 ps to 1100.5 ps. (c) Fast Fourier transform of electric field in (a). (d) Electric field of the QCL emission at 1538 ps as a function of injected THz power (voltages on photoconductive antenna) into laser cavity for emission phase control.

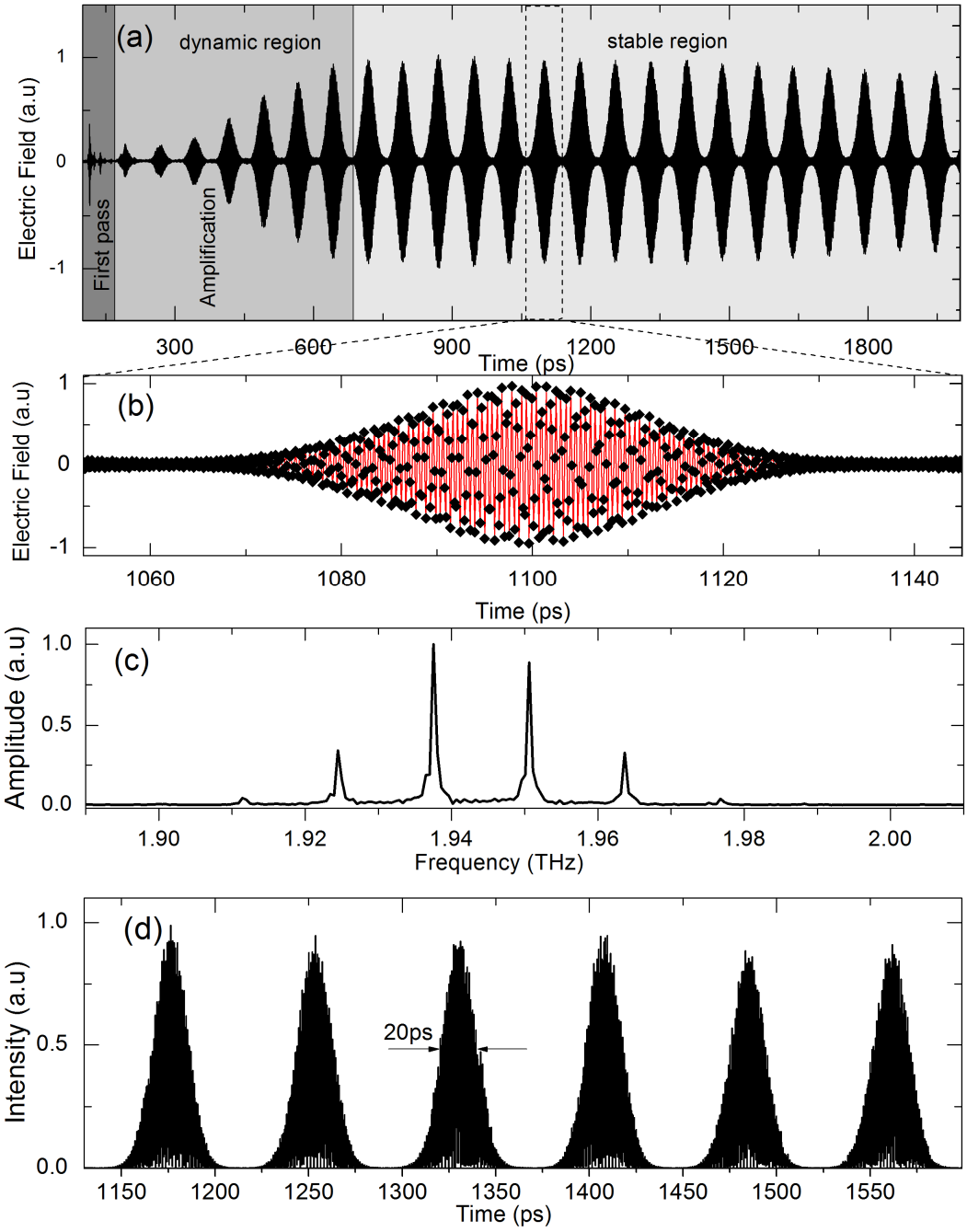

Fig 4.7 | (a) Phase-resolved electric field of the QCL emissions under mode-locking conditions (13 GHz microwave modulation) measured from 100 ps to 2000 ps. (b) Zoom of the 14th pulse in (a) from 1060 ps to 1140 ps. (c) Fast Fourier transform of the measured electric field in (a). (d) Intensity of the QCL emissions from 1130 ps to 1600 ps.

An interesting point of fig 4.6 (a) is that we can already clearly see a pulse behavior although they are very wide. This is contrast to the reference sample presented in chapter 2, Fig. 2.9. Why are pulses already generated without any active modulations? This is because the 150-

µm-long coupled cavity integrated into this sample automatically introduces a modulation at the round-trip frequency and forces the pulses to start being generated. The modulation is a result of the short 150 µm section is held at zero bias and where there is an inter-subband absorption of the QCL. If there is no coupled cavity, the emission of QCL will be quasi continuous mode as shown in Fig 2.9 in chapter 2 or in ref [67]. We will discuss this phenomenon in detail later in chapter 6 for ultrafast THz pulse generation.

For active mode-locking, a ~30 dBm electrical modulation at 13 GHz is applied on the QCL under the exact condition as for injection seeding presented above (see the highlighted by grey background in Fig 4.1). The results are presented in Fig 4.7. In this figure, (a) shows the phase-resolved electric field of QCL emission under GHz modulation measured from 100 ps to 2000 ps. We can see a very different behavior is observed compared to free-running case. Here very distinct pulses are produced with a round-trip separation of 76 ps. The dynamic region starts from the first pass pulse to 700 ps and shows how the pulses are established from the first pass to the steady state. (b) is the zoom of the 14^{th} pulse from 1060 ps to 1140 ps and the black diamonds shows the real sampling points of the measurements. (c) is the resulting spectrum obtained by fast Fourier transform of (a). Comparing with the spectrum of seeding in Fig 4.6 (c), we can observe that there are 2 more modes appearing in the mode-locked spectrum, although they are weak. The mode-locked spectrum also has a more Gaussian-distribution, meaning the QCL power is well balanced among its longitudinal modes by active modulation. From Fourier transform theory, we know that the Fourier transform of a Gaussian function in time domain gives us also a Gaussian function in frequency domain and vice versa. Therefore, the Gaussian-distributed spectrum gives us Gaussian-distributed temporal pulses as is observed in (a) and (b). Indeed, the Gaussian-distributed profile both in time and frequency domains is the unique stable state for mode-locking which balances both the spectrum and pulse profiles. (d) shows the intensity of the QCL emission from 1130 ps to 1600 ps and we can see the FWHM pulse width is relatively long ~20 ps, which is limited by the narrow gain bandwidth (less than intensity FWHM ~50 GHz) of this bound-to-continuum design.

4.1.5 Frequency comb tuning in mode-locked THz QCLs

There is always a locking range [95] [102], defined in Eq. (3.28), for a mode-locked laser. If a modulation frequency with enough power falls into the locking range of QCLs, lasers will be mode-locked and periodic pulse trains will be generated. Otherwise, lasers will operate on continuous mode or on shallowly (sinusoidal) modulated mode. In the section 4.1.3, mode-locking of the QCL at only one single modulation frequency at 13 GHz was presented. What could happen, if we vary the modulation frequencies step by step away from 13 GHz? There are 2 cases: 1. If the locking range is narrow in frequency, for example below 76.69 MHz (the step size of GHz modulation in our configuration), the QCL will be turned from mode-locking mode into a shallow modulation or a continuous mode. Distinct stable pulses cannot then be produced as in Fig 4.7. 2. However, if its locking range is wide enough, for example a few GHz, periodic stable pulses can still be obtained even though modulation frequency is shifted far-away from 13 GHz. In the second case, the uniform mode spacings of the QCL can be

continuously tuned within its locking range by simply continuously varying the modulation frequency. (On-chip frequency tuning is a major challenge for THz QCLs as the refractive index varies little at low temperatures [103] [104]) As is widely known, THz frequencies correspond to the vibration and rotation energy levels of many molecules. Therefore, we can apply the mode-locked THz pulses and its corresponding frequency combs to gas spectroscopy to temporally and spectrally investigate their absorption properties. When the emission frequencies of QCL are continuously tuned, the whole absorption spectrum of some special molecular can be potentially be traced by analyzing the precise absorption frequencies and absorption percentages.

Under the same operating conditions of mode-locking used in section 4.1.4 and also presented in table 1 below, we will mode-lock the QCL at different modulation frequencies by varying the modulation frequency from 12 GHz to 14 GHz (Lower than 12 GHz or higher than 14 GHz is not permitted in our system owing to the limitation of a 2 GHz band-pass electrical filter used to reduce the amplified noise as shown in Fig 4.1). The results are illustrated in Fig 4.8. (a) shows the time-resolved electric field of the QCL emission at different modulation frequencies from bottom 12 GHz (red) to top 14 GHz (dark blue). We can see that Gaussian-distributed THz pulses are produced within the whole 2 GHz modulation range, meaning the locking range of the QCL is broader than 2 GHz centered at around 13 GHz. The THz pulses have been artificially aligned with different modulation frequencies in time at ~1240 ps as shown the vertical cyan line in Fig 4.8 (a). As time goes on, these pulses are not in phase any more at around 1400ps, which means the continuously tuned microwave modulation frequency continuously changes the round-trip time of the THz pulses in the same Fabry-Pérot cavity by changing its refractive index. This multi-modes tuning effect (with a tunability extending to ~70 GHz on the whole spectrum) is achieved for the first time in THz QCLs, which allows us to sweep the emission frequency across a wide range to get the information of molecular in gas spectroscopy. Fig 4.8 (b) is the spectra corresponding to the electric field of the QCL emission in (a) obtained by fast Fourier transform. It is obvious that the mode spacing of the mode-locked QCL follows exactly the modulation frequencies applied on it, proving again that mode locking process is to lock the mode spacing (or longitudinal modes) to the modulation frequency (or sidebands of central frequency). In this way, we are able to continuously tune the emission frequency comb of actively mode-locked THz QCL by varying the modulation frequency beyond ~2 GHz. We have also employed this frequency comb tuning effect to gas (water and CH_2OH) spectroscopy experiments in collaboration with the G. Mouret et al from the University of Dunkerque, France. The results are detailed at the end of this thesis in *Appendix B.*

Table 1 – Operating parameters of the QCLs used in this chapter

Quasi-DC bias	RF	Nonlinear crystal	Modulation frequency
Currents: 500 mA Frequency: 20 KHz Width: 5 µs	Frequency: 76 MHz Power: 200 mW	ZnTe: 500 µm	Varying between: 12 GHz - 14GHz

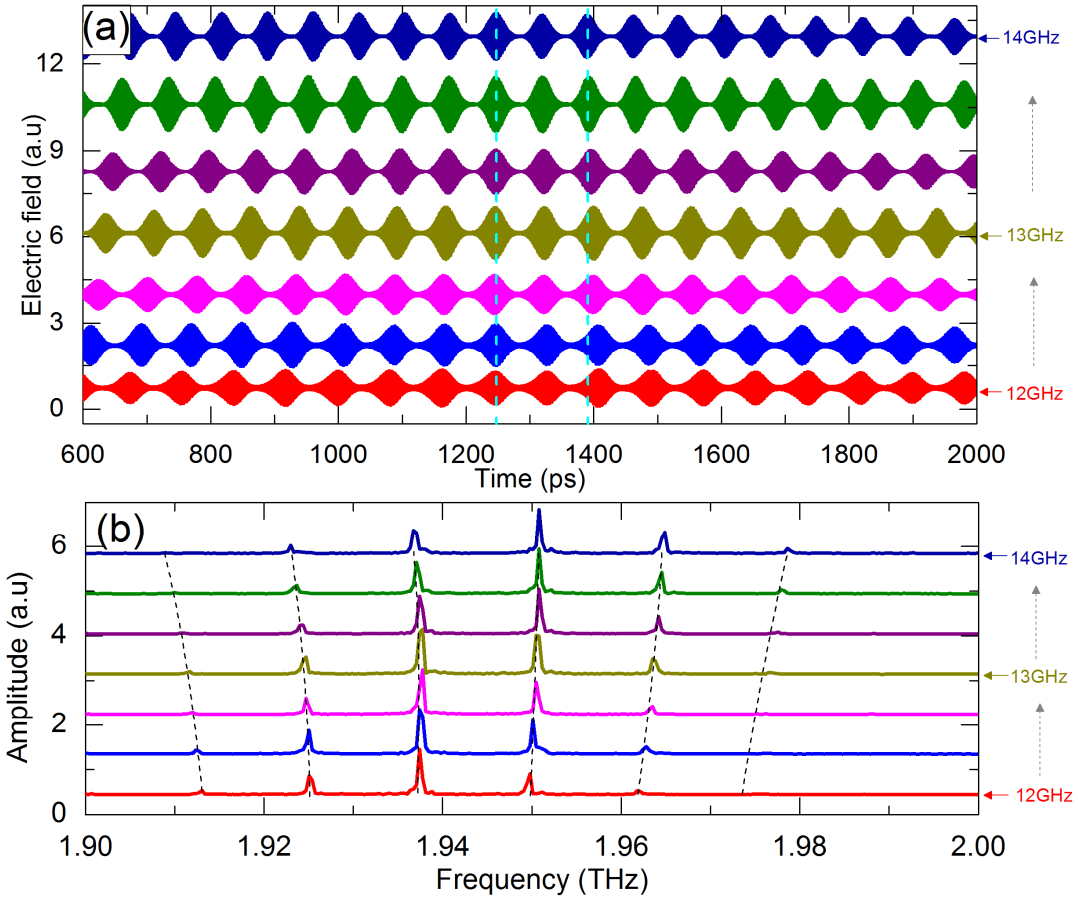

Fig 4.8 | (a) Time-resolved electric field of the QCL emissions from 600 ps to 2000 ps with different modulation frequencies varied from bottom 12 GHz (red) to 14 GHz top (dark blue). (b) Spectra corresponding to the electric field in (a) obtained by fast Fourier transform.

4.2 Conclusion

To summarize, in the chapter 4, I presented the experimental setup for active mode-locking as well as the bound-to-continuum QCLs designs utilized here. This QCL was active mode-locked and the time resolved electric field was detected using injection seeding. This permited 20 ps THz pulses with emission frequency centered at 1.94 THz to perfectly generated with the full electric field profile resolved. From the mode-locking and the large locking range, we showed that the mode-spacing and emission frequencies of QCL can be controlled by tuning the modulation frequency by 2 GHz from 12 GHz to 14 GHz. Based on this, the frequency-comb tunable mode-locked THz QCL has been employed for gas spectroscopy (detailed in *appendix B).* However, we observed very long pulses and narrow spectrum, and the following chapters will investigate methods to generate shorter pulses with a broader spectrum.

5

Active Mode-Locking of Broadband THz Quantum Cascade Lasers at 77 K

Mode-locking of a single-plasmon THz QCL based on bound-to-continuum design has been experimentally demonstrated at 10 K in chapter 4. However, the extremely narrow gain bandwidth (FWHM: ~50 GHz) of this bound-to-continuum QCL strongly limits the pulse width to ~20 ps. In order to generate shorter THz pulses, QCLs with large spectral bandwidths are needed. In addition, this design combined with the single-plasmon waveguide does not permit QCLs working at higher temperature, reducing their potential for scientific and industrial applications. This chapter investigates the effect of a large gain bandwidth on mode-locking. Further MM waveguides are used to reach higher temperatures as well permitting a waveguide for the microwave modulation.

In this chapter, I will to attempt to generate shorter pulses at a higher temperature of 77 K from two broadband (full bandwidth ~500GHz) THz QCLs with center frequencies of 2.7 THz and 2.45 THz, respectively. Both are in metal-metal waveguide geometry. The broadband nature of this QCL will be shown using injection seeding and to extract the mode spacing. I will show that these samples can be mode-locked with operation at liquid nitrogen temperatures. However, I will show that a broadband width does not translate into shorter pulses and that the modulation frequency required to generate pulses is radically different compared to the free running mode spacing of the QCL. I will discuss these results and the mode-locking mechanism in THz QCLs and the key limitation for generating ultrashort THz pulses from QCLs.

Chapter 5

5.1 Introduction

In chapter 4, active mode-locking of a single-plasmon THz QCL at 10 K was demonstrated. The generated THz pulses are ~20 ps, which is not short enough for broadband frequency comb metrology and other applications. The key limitation for generating shorter THz pulses from this QCL is its extremely narrow (FWMH: ~50 GHz) gain bandwidth due to the bound-to-continuum design of the active region. In addition, THz pulses have never been generated from QCLs above 10 K, limiting their wider use in applications.

In this chapter, with the purpose to greatly shorten the THz pulses down to below 5 ps and above liquid nitrogen cooling temperature, a metal-metal waveguide THz QCL with a longitudinal optical phonon (LO Phonon) depopulation active region will be utilized. This active region possesses an extremely broad bandwidth, larger than ~500 GHz (full), a center frequency of 2.7 THz and high operating temperature up to 150 K, in a metal-metal geometry. This QCL is able to potentially drop the THz pulse width down to ~ few picoseconds. However, the time-resolved emission of metal-metal QCL based LO phonon depopulation scheme has never been previously attempted owing to the large difficulty of coupling the external THz pulse into this high confinement subwavelength waveguide to seed the QCL emission. Here, for the first time, I will injection seed this QCL to detect the time resolved electric field and generate THz pulses at 77 K via active mode-locking.

I will further show that although a broadband LO phonon QCL is employed, the generated THz pulses are limited to ~11 ps, equivalent to the state-of-the-art from narrow bandwidth QCLs and considerably longer than expected. We will show that this limitation is a result of the sinusoidal modulation of the microwave applied on the QCL. This mechanism will be discussed in detail through this chapter. We will also show similar behavior from a second broadband sample, centered at 2.45 THz showing the effect is not limited to a single sample.

The chapter will be divided as follows. I will briefly introduce the 2.7 THz LO phonon depopulation active region of the QCL and the metal-metal waveguide used. Laser emission under injection seeding and mode-locking conditions will then be compared at 77 K and the active mode-locking mechanism will be discussed. Finally, I will present the active mode-locking of a second broadband sample operating around 2.45 THz at 20 K.

5.2 Active mode-locking of L1074

5.2.1 Sample L1074

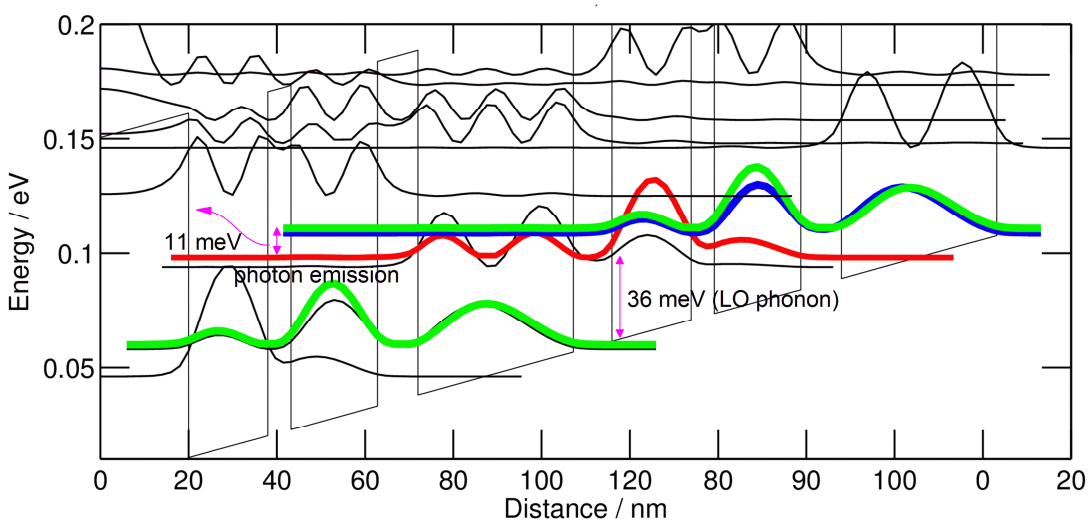

Fig 5.1 | Band structure of the THz QCL based on LO phonon depopulation scheme. Green line: injector level, blue line: excited level of laser transitions, red line: fundamental level of laser transitions, black lines: high order energy levels of quantum wells.

A QCL (wafer number ‘‘*L1074*’’) with a LO phonon depopulation scheme is used in this chapter, based on a 3.1 THz QCL, which has been shown to operate up to ~200 K [3] and presented in detail in chapter 1. The design was modified to operate at lower frequencies (~2.7 THz) by increasing the well and barrier widths, thereby improving the spectral overlap with the THz seed pulse [67] for injection seeding. Starting from the injection barrier, the well and barrier widths are **4.6**/*9.8*/**2.6**/*9.0*/**4.4**/*17.6* nm (barriers in bolds and quantum wells in italics). The 17.6-nm-wide underlined wells are *n*-doped at a level of 5×10^{16} cm^{-3} over a length of 5 nm. The detailed growth sheet is attached at the end of the thesis in *Appendix A*. Its band structure is schematically shown in Fig 5.1 and similar to that presented in chapter 1. The energy gap between the blue line and red line is roughly ~11 meV corresponding to an emission frequency centered at 2.7 THz, while the gap between the red line and the bottom green line is ~36 meV corresponding to the LO phonon energy in GaAs. 200 periods of the active region were grown. The very short lifetime of electrons (sub-picosecond) in the lower laser transition results in a broad emission band extending to ~500 GHz (full bandwidth), considerably wider than the gain bandwidth of bound-to-continuum scheme discussed in chapter 4.

The growth was performed by MBE in the group of Prof. Linfield and Prof. Davies at the University of Leeds, UK. The wafer was then processed into a metal-metal geometry using standard photolithography in the group of Dr. Colombelli at the University Paris-South, France. This type of waveguide, coupled with the LO phonon depopulation active region design, provides state-of-the-art THz QCL temperature performance. Ridge widths of 60 μm were

selected to suppress higher lateral modes such that the fundamental mode is able to dominate the laser action [105] [106], important for active mode-locking to avoid multiple pulses within the laser cavity. (A point to note is that MM waveguides, unlike single plasmon waveguides, permit considerably smaller ridge widths and therefore reduce the absolute current required for laser action). The processed wafer was cleaved in 3-mm-long laser ridges. The QCL was coupled with a high-speed mount for GHz frequency modulation and placed in a continuous-flow cryostat as presented in Fig 4.3 in chapter 4. At 77 K, the laser threshold is observed at around 722 A/cm^2 and lasing ceases at around 998 A/cm^2 with a duty cycle of 6%. Fig 5.2 shows the LIV characteristics of this QCL, using a pyroelectric detector. Laser action is observed up to ~130 K with a duty cycle of 6%. The electrical characteristics are typical for this type of active region. The inset of Fig 5.2 shows the calculated mode profiles, using the RF module of COMSOL Multiphysics in 3D, in facet and surface views confirming that only one lateral mode is present in the metal-metal cavity.

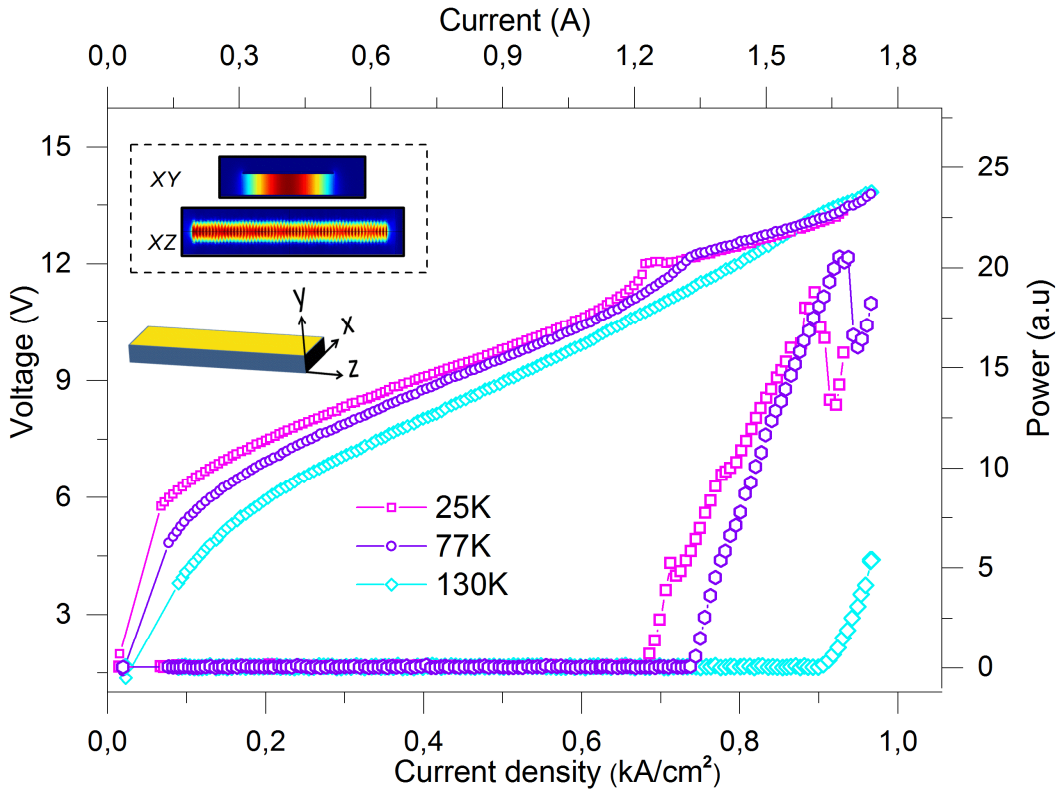

Fig 5.2 | Light–current–voltage characteristics of the 2.7 THz metal-metal waveguide QCL based on an LO phonon depopulation active region at 25 K (magenta), 77 K (violet), and 130 K (cyan). Top inset: transverse (*XY*) and longitudinal (*XZ*) mode simulations of the THz mode profile inside the metal-metal waveguide QCL. Bottom inset: schematic diagram showing the QCL coordinate system *XYZ*.

5.2.2 Injection seeding

Prior to carrying out the mode locking experiment, the technique based on ultrafast injection seeding was again employed to measure the time-resolved electric field emitted by the QCL (as described in chapter 2 and 4), which allows us to identify the bandwidth and the mode spacing for active modulation, and compare with the mode-locked emission. THz frequency pulses, of bandwidth ~3 THz centered at 1.2 THz, were generated using a photoconductive antenna (the emission properties detailed in chapter 2) excited by ~100 fs near-infrared pulses (centered at ~810 nm) from the Ti:sapphire laser. These free-space THz pulses were then injected into the metal-metal QCL cavities using 2 high-numerical-aperture parabolic mirrors (f/1, f/2), enabling injection seeding of the QCL and permitting the coherent detection of its emission. The THz pulse injection is synchronized with the electrical RF pulse that switches on the QCL, triggered by the same 100 fs near-infrared pulses. This allows the THz input pulses to be amplified and eventually seed the QCL emission, rather than the emission being initiated by the QCL's inherent spontaneous emission. Electro-optic sampling was then used to measure the amplitude and phase of the QCL emission. Further details of the technique can be found in Ref. [67] or in chapter 2. (The time-resolved output intensity of an unseeded QCL can be measured using a cross-polarizer technique [54], but is orders of magnitude less sensitive compared with that using the seeded technique. It is thus not suited to the low output power of metal-metal QCLs.)

Fig 5.3 (a) shows the measured electric field as a function of time for the QCL injected with an ultrafast THz seed pulse, at 77 K. Compared to the emission of the single-plasmon QCLs based on bound-to-continuum designs in chapter 2 and chapter 4, the time profile is very different as a result of the ultrashort gain recovery time of this LO phonon depopulation design, which will be discussed in detail later in this chapter (section 5.2.3). The QCL was held below the threshold with a quasi-DC current of 609 A/cm^2 with a 3.6 ns electrical switching pulse used to bring the QCL above the threshold, the latter synchronized with the THz seed pulse. The seeding THz pulse is injected into the QCL through one of its facets at t = 64 ps and is amplified as it propagates along the laser cavity. At the output facet, part of the pulse is transmitted and detected coherently, whereas the remainder is reflected back into the cavity and continues to be amplified. The pulse is again reflected at the input facet. This results in successive pulses exiting the QCL output facet, which increase in field amplitude, separated by the cavity round-trip time of 76 ps corresponding to a refractive index of 3.665. Subsequently (>300 ps), complex behavior emerges with weaker emission observed between the round-trip pulses, similar to bound-to-continuum devices [67] [107]. This is a result of a number of longitudinal modes present in a long cavity [23] and the ultrafast gain recovery time. Furthermore, owing to the finite gain bandwidth of the QCL, the input THz pulse is broadened in time with the number of round-trips, resulting in the output pulses becoming less distinguishable at later times (> 400 ps). A magnified view of the output emission around 430 ps is highlighted in Fig. 5.3 (b), which clearly shows the time-resolved form of the electric field with a resolution of 30 fs. (The inter-round-trip pulses can be inhibited when using active mode locking as detailed below.)

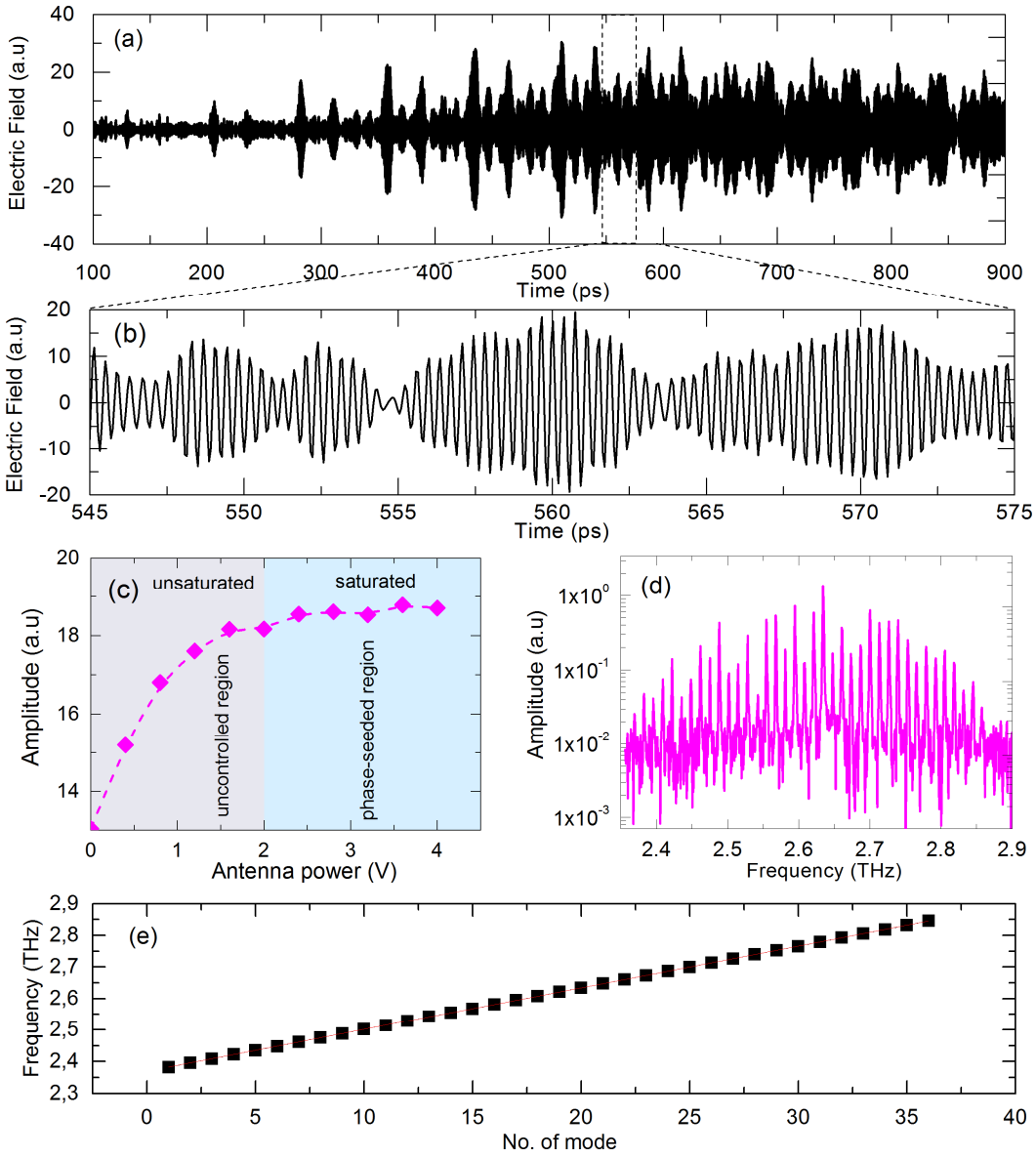

Fig 5.3 | Injection seeding of the MM waveguide QCL at 77 K. (a) Emitted electric field from the QCL as a function of time with a bias of 3 V on the seed antenna. (b) Expanded view of the emitted QCL electric field between 545 and 575 ps. (c) QCL output field amplitude at 431 ps as a function of the voltage applied on the THz photoconductive antenna. (d) FFT of the QCL output electric field. QCL output field amplitude at 431 ps as a function of the voltage applied on the THz photoconductive antenna. (e) The frequency of each mode as a function of the mode number from 2.3 THz to 2.9 THz.

After ~400 ps, corresponding to six round-trips, there is no further amplification of the output electric field. (The small reduction in amplitude after 700 ps is a result of the electrical switching pulse not being perfectly flat.) Although the stabilization of the field is an indication that the QCL is entirely synchronized with the input pulse, the variation of the output field was investigated as a function of the input THz field to confirm this. Fig 5.3 (c) shows the QCL

output field at a time of 431 ps as a function of voltage on the THz antenna, with similar behavior observed for later times. (The electric field emitted by the antenna is proportional to the applied voltage [67].) For applied fields greater than ~2 V, the QCL output field saturates, implying that the QCL gain is clamped by the THz input pulses, with the latter therefore initiating (i.e., seeding) the laser action, replacing entirely the inherently random spontaneous emission of the QCL. (A small unsynchronized part of the electric field may still be present, but this will be considerably smaller than the synchronized field [107] and, in the case of mode locking, will have a similar time profile [54].). For antenna voltages < 2 V, however, the measured QCL output field depends on the input THz pulse amplitude. This implies that only amplification of the input THz pulse is detected with contributions to the QCL output from the seed and spontaneous emission [107].

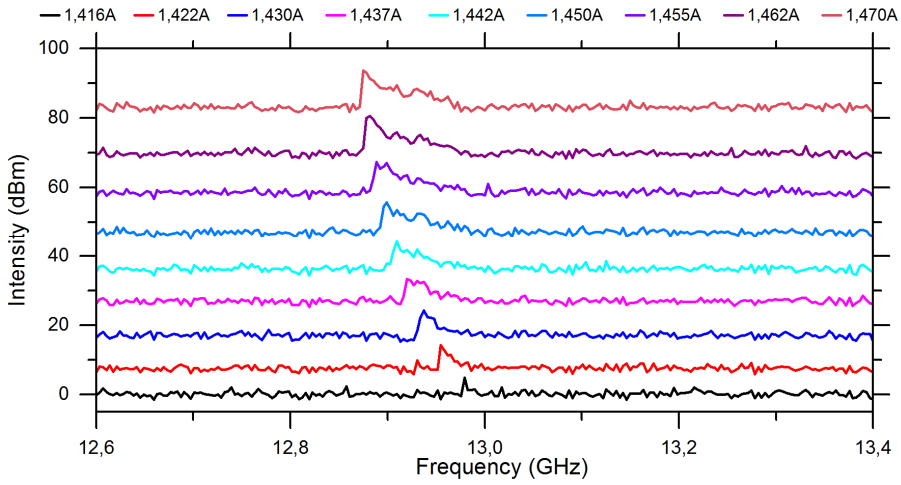

Fig 5.4 | Beatnote of the 3-mm-long 60-µm-wide QCL (L1074) as a function of the operating currents at 77 K.

Fig 5.3 (d) shows the FFT of the measured time-domain signal in Fig. 5.3 (a), permitting access to the QCL output spectrum. The spectrum is centered at ~2.6 THz with a full bandwidth greater than 500 GHz, considerably larger than that in previous demonstrations (full width: ~100 GHz, FWHM: ~50 GHz), owing to the large spectral gain of LO phonon depopulation active region designs. The mode spacing is 13.2 GHz as expected for a 3-mm long waveguide. Furthermore, the frequency of each Fabry–Perot mode is linear with mode number as shown in Fig 5.3 (e), demonstrating that the QCL is operating on only one lateral mode and there are no higher-order modes present. The microwave beat note was also measured at 77 K (Fig. 5.4), which showed a narrow linewidth at only one frequency at the round trip just above the laser threshold, which gradually became wider with increasing current as illustrated in Fig 5.4. Similar behavior of the beat note has been demonstrated previously in, for example, Ref. [29]. The beatnote in Fig 5.4 is around ~13 GHz, slightly different from the measured mode spacing from the FFT of the measured electric field, possibly owing to small floating of the sampling step in the measured electric field.

5.2.3 Gain recovery time

Before presenting mode-locking of this sample, I will present the effect of the band structure on the time profile and its relation to the gain recovery time. Comparing Fig 5.3 with Fig 2.9, we can observe that the time profile of the LO phonon depopulation based QCL is very different to that of bound-to-continuum QCL. This is a direct result of their different gain recovery times T_1 and dephasing times T_2 of the inter-subband transition. Conversely, if we know the time resolved electric field profile of a QCL, its gain recovery T_1 can in principle be determined using Maxwell-Bloch finite-difference time-domain (FDTD) simulations [108], [109]. The principle of the simulations is as follows: we assume the active medium of the QCL is an open 2-level system with an upper level $|2\rangle$ and a lower level $|1\rangle$ with the latter always empty. Its characteristics are mainly described by the gain recovery time T_1 and the dephasing time T_2 in Maxwell-Bloch equations. The gain medium is within a laser cavity of length L. The propagating broadband THz pulse in the cavity is simulated using the predictor-corrector method proposed by Ref. [108]. The simulation process is exactly the same as the injection seeding experiment and therefore the time-resolved emission profile of the QCL can be computed. By changing the gain recovering T_1 (critical to the emission profile) in the simulations to approximately match the measured emission profile, we can obtain an estimate of the gain recovery time T_1 of the QCL.

In our case, the Maxwell Bloch equations can be written as [23]:

$$\partial_t H_y = -\frac{1}{\mu_0}\frac{\partial E_x}{\partial z} \tag{5.1}$$

$$\partial_t E_x = -\frac{1}{\varepsilon}\frac{\partial H_y}{\partial z} - \frac{NM}{\varepsilon T_2}\rho_a + \frac{NM\omega_{21}}{\varepsilon}\rho_b - lE_x \tag{5.2}$$

$$\partial_t \rho_a = -\frac{1}{T_2}\rho_a + \omega_{12}\rho_b \tag{5.3}$$

$$\partial_t \rho_b = -\frac{1}{T_2}\rho_b - \omega_{12}\rho_a + \frac{2E_x M}{\hbar} w \tag{5.4}$$

$$\partial_t w = -\frac{w - w_0}{T_1} - \frac{2E_x M}{\hbar}\rho_b \tag{5.5}$$

Where z is the cavity length direction, N is the number of identical two-level systems. The polarization of the medium is $P_x = -2N\mathrm{M}\rho_a$, $M = e\langle 2|x|1\rangle$ is the dipole matrix element and E_x is the electric field. $2\rho_{12} = \rho_a - j\rho_b$, where ρ_{12} is the coherence between the level $|1\rangle$ and level $|2\rangle$. $w = \rho_2 - \rho_1$ represents the population inversion between the two states and w_0 is the initial population inversion. ρ_1 and ρ_2 are the populations of the state $|1\rangle$ and state $|2\rangle$, respectively. The energy of the laser transition is $\hbar\omega_{12}$. T_1 is the gain recovery time and T_2 is the dephasing time. The term lE_x is the loss introduced by the waveguide.

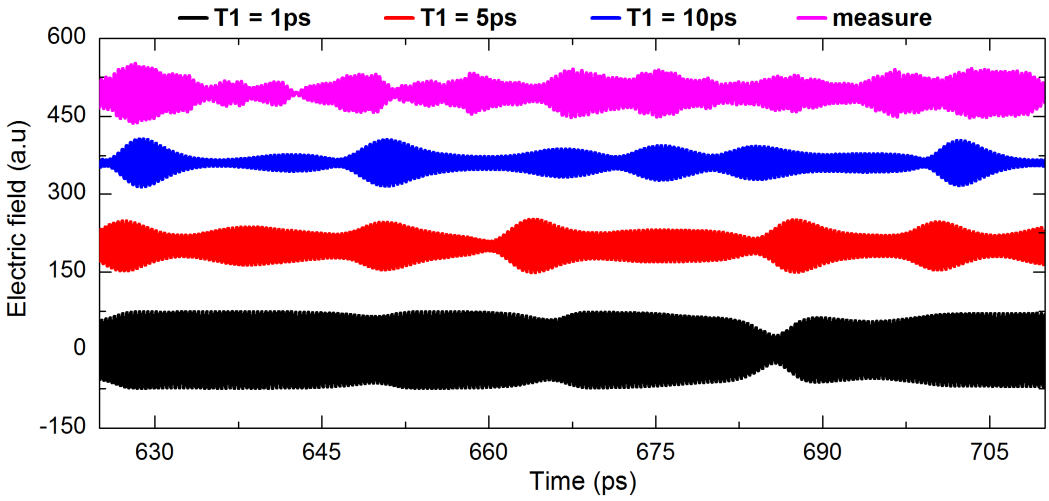

Fig. 5.5 | Calculated time domain profiles of QCL output emission over one round-trip period for gain recovery times of 1ps (black), 5ps (red) and 10ps (blue curve). The magenta curve corresponds to experimental data. [Calculated by Dr. Joshua R. Freeman].

Table 2. Parameters used in the Maxwell-Bloch FDTD simulations

Symbol	Name	Value
ε_r	Relative permittivity	12.9
T1	Gain recovery time	1-10 ps
T2	Dephasing time	0.6 ps
w_0	Equilibrium population inversion	1
N	Number of oscillators	3.7×10^{20} m^{-3}
M/e	Dipole matrix element	6 nm
ω_{12}	Transition frequency	2×2.7 THz
l	Waveguide loss	12 cm^{-1}
L	Cavity length	3 mm

The gain recovery time *T1* of the 2.7 THz LO phonon depopulation QCL "L1074" was calculated using Eq. (5.1) – Eq. (5.5) above by Dr. Freeman at the University of Leeds with the FDTD predictor-corrector method. The procedure is detailed in-depth in ref. [23], [108]. Here we have used a dephasing time of 0.6 ps from the full-width half-maximum of the gain and a total waveguide loss of 12 cm^{-1} from the first pass gain measurements [110] of the LO phonon depopulation based QCL. All the other parameters are shown in table 2 above. Fig 5.5 shows the calculated time response of the output electric field with different gain recovery times, compared to the experimental data over one round-trip period (magenta curve). The data shows multiple pulses between a round-trip period. For *T1* = 1 ps, the calculated time profile shows a quasi-CW behavior while for *T1* = 10 ps shows a more modulated behavior with the intra-round trip peaks having a much lower field when compared to the main peaks. A time data with a gain recovery time of ~ 5 ps shows the best 'fit' with the data. This is considerably faster than for bound-to-continuum devices, which have gain recovery times of ~15 ps, and is

considerably shorter than the round-trip time (76 ps). (Note that the gain recovery time for mid-infrared QCLs is of the order of ~1 ps [111], [112].). The shorter gain recovery time is also indicated in the time-resolved electric field [Fig 5.3 (b)], which shows multiple "pulses" between cavity round-trips separated between 5 and 7 ps. This is a result of the faster dynamics of the LO phonon depopulation designs and owing to the absence of a mini-band for inter-period transport.

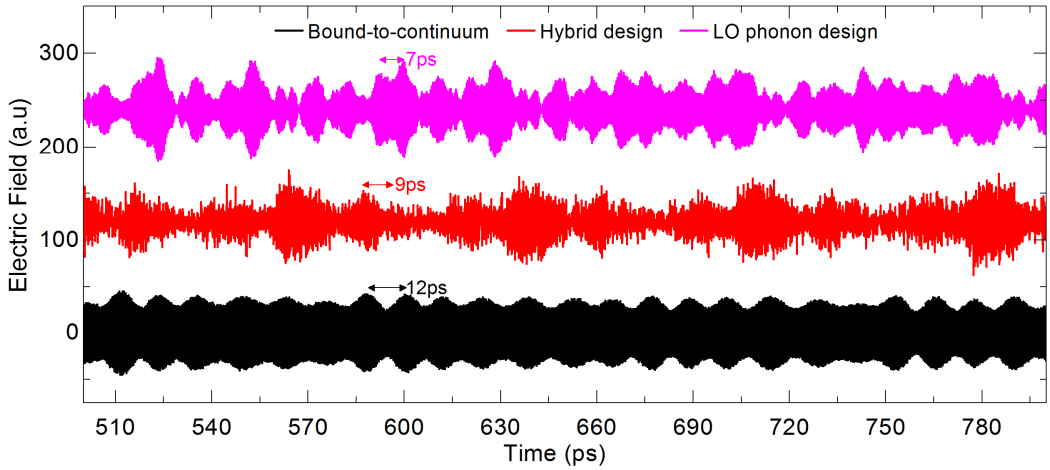

Fig 5.6 | Measured time domain profiles of QCL output emission over 300 ps respectively for bound-to-continuum (black), hybrid (red) and LO phonon (magenta) designs.

As shown the emission profile of a QCL strongly depends on its gain recovery time. To illustrate this, we measured the time resolved electric field (Fig 5.6) for three QCLs with different active region designs where the gain recovery time is expected to vary: bound-to-continuum design (long T_1, frequency 2.5 THz, black), LO phonon QCL (short T_1, 2.7 THz, magenta) and a hybrid QCL (intermediate T_1, 3.2 THz, red curve) that combines both a bound-to-continuum structure and LO phonon design. Fig 5.6 shows the measured time domain profiles from 500 ps to 800 ps corresponding a few round trips. It can be observed that their emission profiles are indeed quite different. We measured the temporal peak separations of these 3 cases, which are 7 ps, 9 ps and 12 ps for the LO phonon depopulation, hybrid and bound-to-continuum QCLs, respectively, as indicated by arrows in figure above. This increase in gain recovery time between the 3 structures behavior is as expected. Therefore, the injection seeding techniques permits an estimate of the gain recovery time, a parameter that has been difficult to determine previously. It also clearly shows that the gain recovery time is considerably shorter than the round trip time (~70 ps).

5.2.4 Active mode-locking

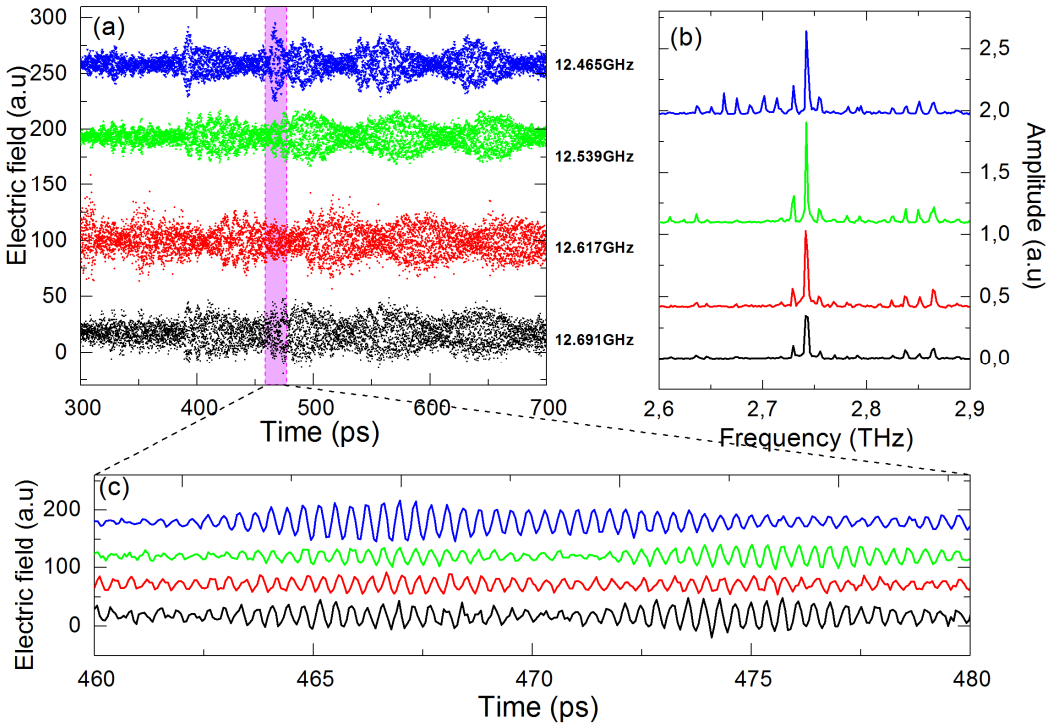

Fig 5.7 | QCL emission under the microwave modulation frequency of 12.465, 12.539, 12.617, and 12.691 GHz. (a) The sampling points of the electric field of QCL emission. (b) The corresponding spectra of the measured electric field. (c) The zoom of (a) from 478 ps to 498 ps.

Continuing from the injection seeding of L1074, the mode locking of these LO phonon QCLs was investigated with the expectation that the large bandwidth available in these devices should lead to shorter pulses in comparison with mode-locked bound-to-continuum active region designs [27]. Specifically, pulses as short as sub-5 ps would be expected from a seeding bandwidth of ~500 GHz (full), assuming transform-limited pulses. To actively mode-lock the QCL, a microwave modulation was applied corresponding to the round-trip time (i.e. ~13 GHz for a 3-mm-long cavity) to modulate the gain across the entire gain medium. (Note that it is also possible to modulate a short section of the cavity at the round-trip frequency to actively mode-lock a QCL to open a picosecond time window in the net gain, as in Ref. [113]. However, this requires a specially designed QCL with a long gain recovery time.) The bonding wire on top of the QCL is placed close to the facet onto which the external THz pulse is incident. In this case, the microwave modulation will propagate between the input and output facets together with the seed pulse, allowing the QCL to be seeded and mode-locked for pulse generation. No pulse generation is observed when the bonding wire is placed in the middle of the QCL cavity as this results in a counter-propagating modulation.

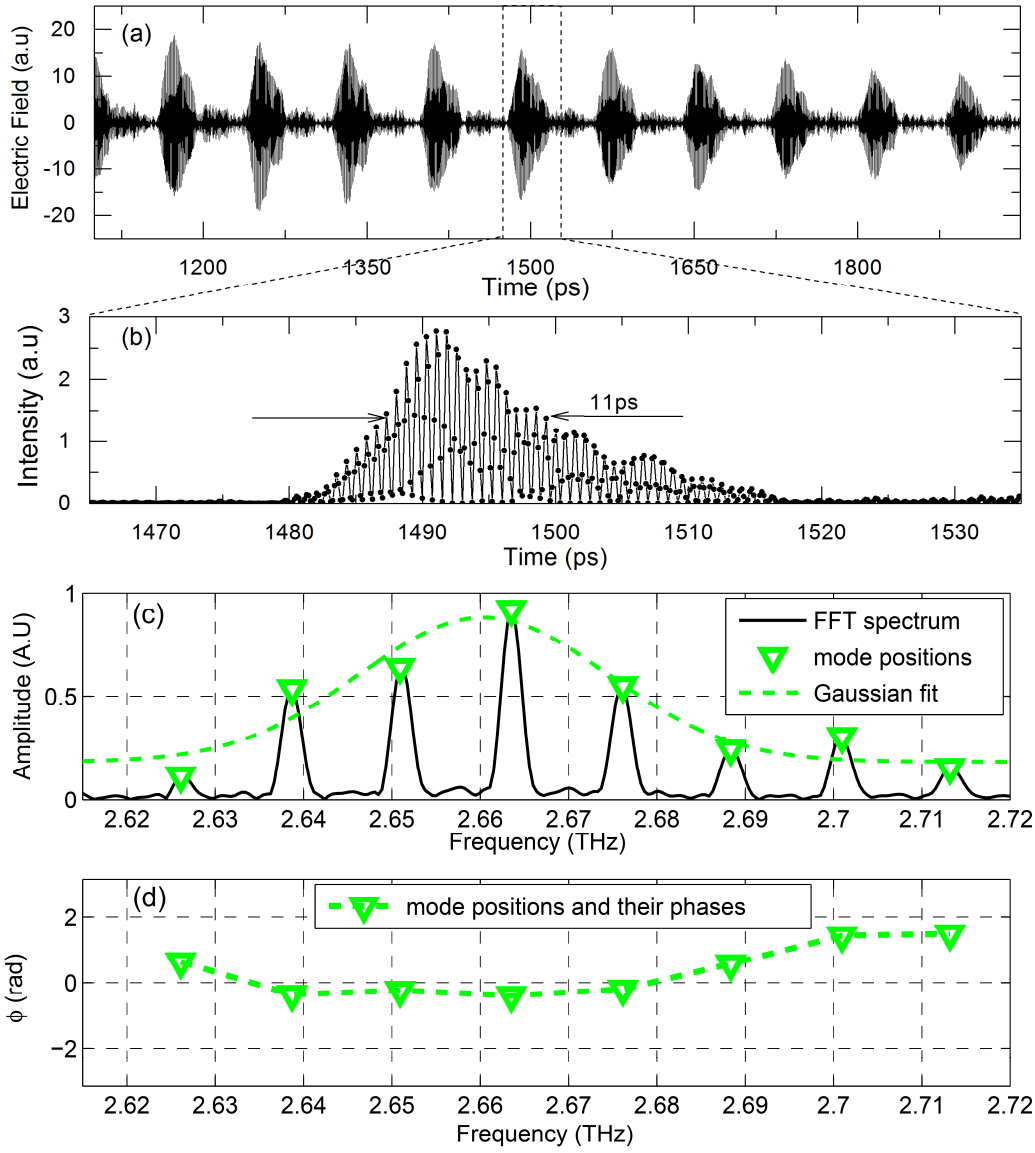

Fig 5.8 | Active mode locking and phase analysis of the metal-metal QCL (L1074) at 77 K. (a) Output electric field for mode-locked QCL with an applied microwave modulation of 12.46 GHz. (b) Expanded view of the THz pulse intensity between 1465 ps and 1535 ps. (c) FFT of panel (a) for mode-locked QCL. (d) Phases of the eight mode-locked longitudinal modes (green triangles).

The experimental arrangement for active mode locking is the same as that reported in Ref. [27], and in chapter 4, where an yttrium iron garnet band-pass filter is employed to choose a harmonic of the reference laser repetition rate (for example, the 163 harmonic × 76.47 MHz ≈12.46 GHz) to synchronize the round-trip microwave modulation of the QCL with the seeding pulses. A microwave power of 30 dBm was used. This is the maximum available in our current setup and showed the clearest pulse behavior. The modulation frequency was varied between 12.4 GHz and 14 GHz, with 12.465 GHz giving the best quality pulses. Fig 5.7 shows the

output electric fields and the corresponding spectra for various modulation frequencies (RF power of ~500 mW), which show that the pulse behavior becomes clearer and more Fabry–Perot modes appear as the microwave frequency is reduced. No clear pulse behavior was observed for frequencies greater than 12.7 GHz, even though the beatnote was measured at 13GHz.

Fig 5.8 (a) shows the electric field between 1100 ps and 1950 ps emitted by the seeded QCL with microwave modulation. The QCL was operated at 77 K and the electrical pulse power was chosen such that it brought the QCL above the laser threshold. The variation in intensity between the pulses in the time domain is a result of the non-flat RF electrical pulses and the low output fields of metal-metal QCLs resulting in a low signal, close to the noise level. The FFT in Fig 5.8 (c) shows the corresponding effect on the spectrum; eight uniformly spaced modes are observed between 2.61 and 2.72 THz. The average pulse width (in intensity) is found to be 11 ps as shown in the inset of Fig 5.8 (b). The number of modes and the pulse widths are larger and shorter, respectively, than those demonstrated from our previous investigations on bound-to-continuum active regions in chapter 4, showing the effect of the broader gain bandwidth of LO depopulation active region designs. However, the entire ~500 GHz bandwidth is not fully used. This is a result of dispersion and the microwave modulation, which limits the pulse width and the number of modes - pulse formation is only present close to the laser threshold owing to the direct sinusoidal modulation of the QCL gain above and below the laser threshold (i.e., turning the QCL on and off rapidly), which limits the number of modes that can be brought above the threshold. Applying this microwave modulation when the quasi-DC current or the RF power supplying the QCL is closer to or above the laser threshold results in a sinusoidal amplitude modulation of the detected field, owing to the finite microwave power, with the pulse behavior destroyed [54]. (The effect of dispersion is discussed in detail in chapter 6).

The application of a round-trip modulation of 12.47 GHz for the shortest pulse generation is different from the mode spacing found in the QCL seeding and the beat note frequency ($\Delta\nu$ ~ 13.2 GHz and 13 GHz). From the mode spacing, we find THz group refractive indices of 3.871 and 3.665 for the mode-locked and seeded regimes, respectively. It has been shown previously that the QCL round-trip can be locked to an RF synthesizer over a locking range of several hundred megahertz with moderate microwave powers ("injection pulling"), but it is a surprise that the 12.47 GHz modulation frequency generates the clearest pulses. In our previous work on single Plasmon waveguides, pulses were generated over a wide range of round-trip modulations (12 GHz–14 GHz). The difference here comes from the metal-metal waveguide, which confines the microwave modulation and brings an extra dispersion in the refractive index of the microwave modulation and permits a THz–GHz phase matching [114], where the effective microwave index is equal to the THz group refractive index, i.e., $n_{G(THz)} = n_{eff\ (GHz)}$. As shown in Fig 5.9, the group effective index of a THz wave at 2.3 THz (n_G^{THz} , blue line) and effective index of a microwave at 20 GHz (n_{eff}^{GHz} , red line) are highly dispersive, when the ridge width is below 80 μm. The cross point in this figure corresponds to a THz–GHz phase matching condition that permits mode-locking to function.

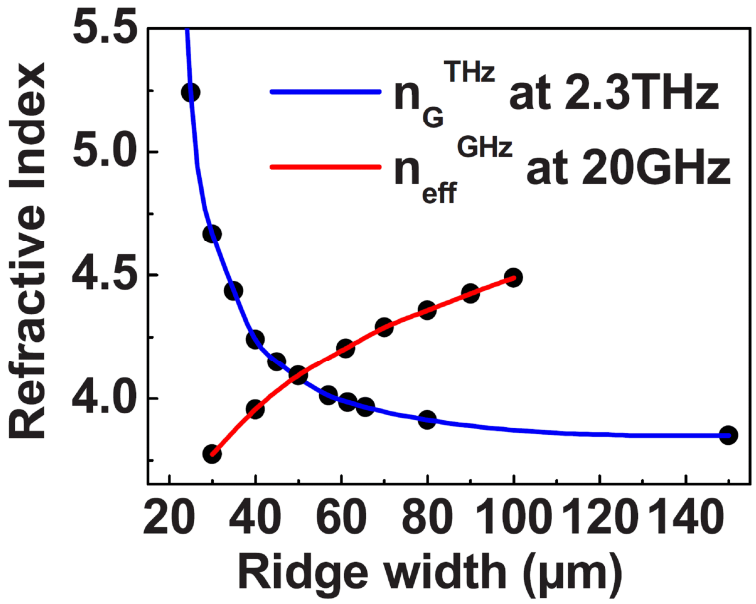

Fig 5.9 | The group effective index of a THz wave at 2.3 THz (n_G^{THz} , blue line) and effective index of a microwave at 20 GHz (n_{eff}^{GHz} , red line) as a function of the ridge width. [*This figure is from the published article: W. Maineult et al, Appl. Phys. Lett. 96, 021108 (2010)*]

Although this phase matching has been discussed in the context of modulation bandwidth, its demonstration and impact on short-pulse generation had not been envisaged. The microwave index depends strongly on the ridge width and microwave frequency [114] as demonstrated in Fig 5.9. In our work the effective microwave refractive index of the QCL waveguide was calculated from the 2D mode using COMSOL (the frequency domain analysis of RF module) and the procedure described in ref [26], where a permittivity of 25 was used for the active region. The modal profile is shown in Fig 5.10 for a ridge width of 60 μm and height of 10 μm for a frequency of 12.4 GHz. Owing to the large overlap of the mode with the surrounding air, a reduce effective index of 3.91 is determined. This indicates that the velocity of the THz pulse envelope is dictated by the microwave modulation wave as is shown in Fig 5.11 and it is this direct modulation close to the threshold that permits pulse generation. This phenomenon is also supported by the fact that pulse generation is only observed when the microwave modulation is applied from the cavity end of the QCL, suggesting that the microwave propagates in-phase with the THz pulse. This also explains why it is easier to mode-lock THz QCLs in comparison with mid-infrared QCLs as, for the latter, the group refractive index is smaller (~3.3) than that in the THz range and, thus, a microwave modulation has a different velocity than the mid-infrared group velocity.

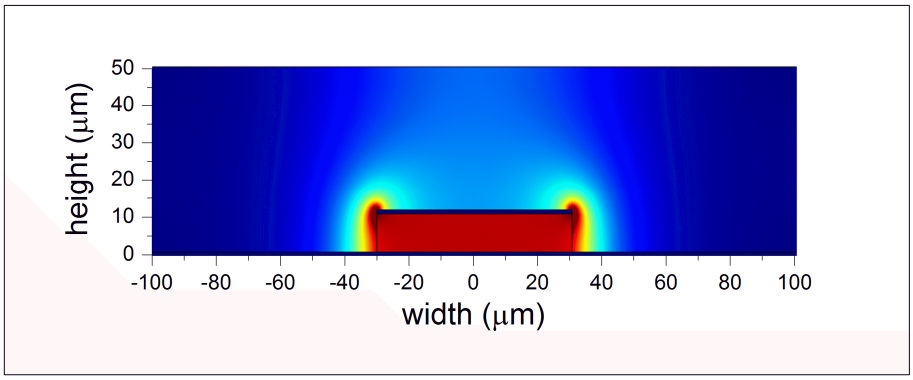

Fig 5.10 | Modal profile at 12 GHz of a 60 μm wide metal-metal QCL operating at a center frequency of 2.7 THz.

An advantage of injection seeding with phase-resolved pulses is that it permits access to the phase and amplitude of the emitted pulse train, allowing a complete analysis of the mode-locked pulse emission. As can be seen in Fig 5.8 (a), the mode-locked pulses are deformed from an ideal Gaussian profile. Taking the FFT of the pulse train permits the phase of each mode to be determined as shown in Fig 5.8 (d); the four central intense modes at 2.639, 2.651, 2.664, and 2.676 THz have the same phase, whereas the phase increases monotonically for the modes (2.626, 2.689, 2.701, and 2.714 THz) that are farther from the central frequency. This deforms the pulse from the transform-limited case. An improved pulse shape could be obtained by engineering the gain to have a flatter profile such that the group velocity dispersion is minimized [29] and to have improvements to the microwave modulation, which could be distorted by the inductance from the wire bonding. Further, dispersion compensation can be used to improve the pulse shape and this is discussed in chapter 6.

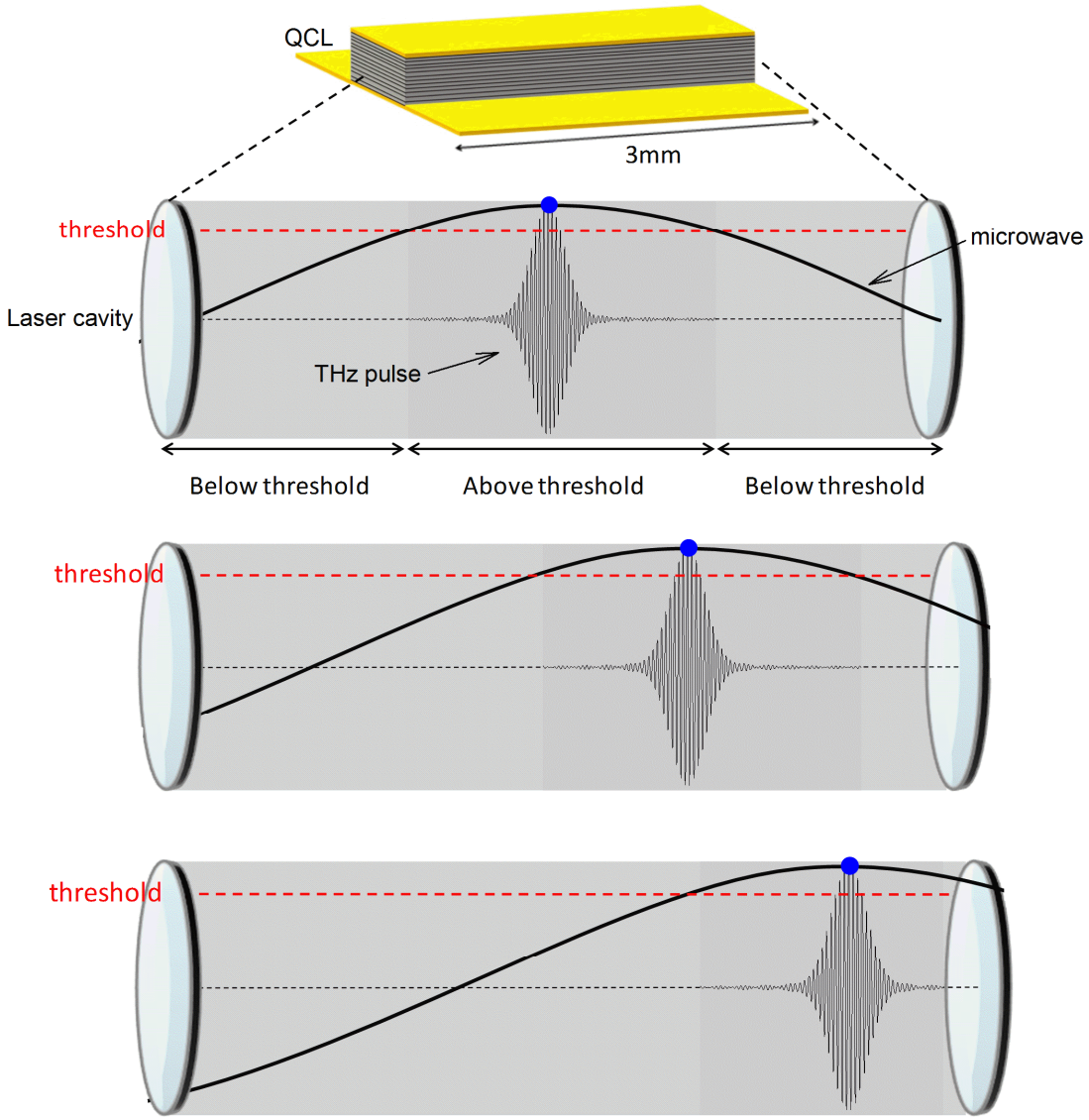

Fig 5.11 | Schematic diagram showing the phase velocity of microwave equals to the group velocity of THz pulse in a metal-metal waveguide QCL.

5.3 Active mode-locking of the 2.45 THz QCL (L1194)

5.3.1 Introduction

Active mode-locking of the metal-metal QCL "L1074" based on LO phonon depopulation has been demonstrated at 77 K in the previous section (5.2) of this chapter. To demonstrate that the observations are universal and not limited to one sample, similar experiments were performed on another family of metal-metal LO phonon depopulation QCLs with a central frequency of 2.45 THz (wafer code "L1194" (see growth sheet in *Appendix A*)). Further as the frequency is lower than the previous demonstration, a higher overlap in frequency with our seed pulse is obtained resulting in data with a higher signal-to-noise ration. Below I will introduce the basic information of this sample and its LIV curves, followed by injection seeding and active mode-locking of the 2.45 THz QCL. (The gain measurements of this sample are presented in appendix F).

5.3.2 LIV curves

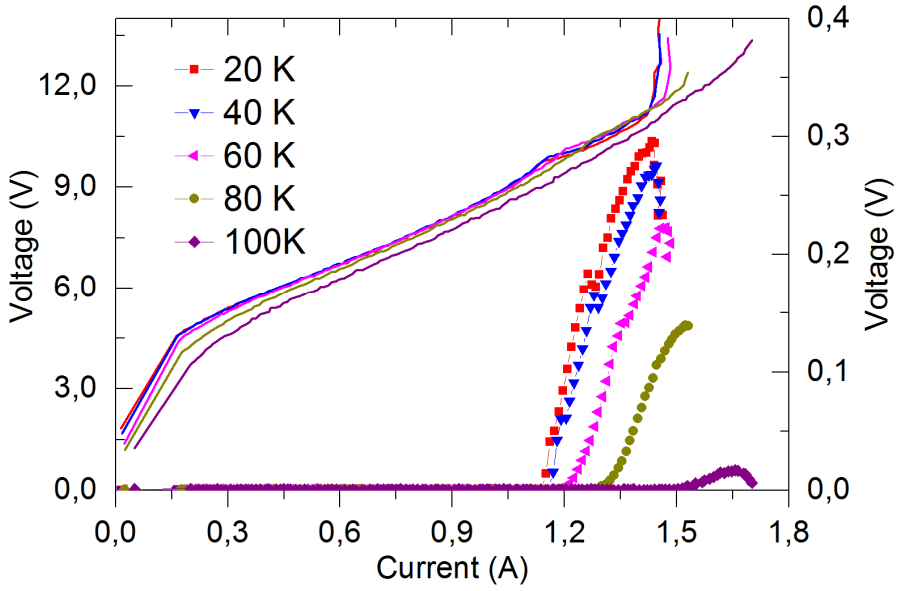

Fig 5.12 | The LIV curves of the 60-μm-wide 3-mm-long QCL "L1194" operating at 2.5 THz at different temperatures varied from 20 K to 100 K.

The band structure design of the the QCL "L1194" is a modified version of the sample "L1074" to operate at lower frequencies. It is obtained by increasing the width of all the quantum wells by 10% for emission centered at ~2.5 THz, whilst keeping a large bandwidth of ~500 GHz. The sample "L1194" was similarly processed into metal-metal waveguide with a

ridge width of 60 µm and cleaved into a 3 mm long cavity. Its LIV curves at different temperatures are illustrated in Fig 5.12 and are similar to L1074. At 20 K, laser threshold is at ~1100 mA and the out-coupled power increases quasi-linearly with operating currents until to ~1500 mA. The maximum operating current is approximately 100 K.

5.3.3 Injection seeding and active mode-locking

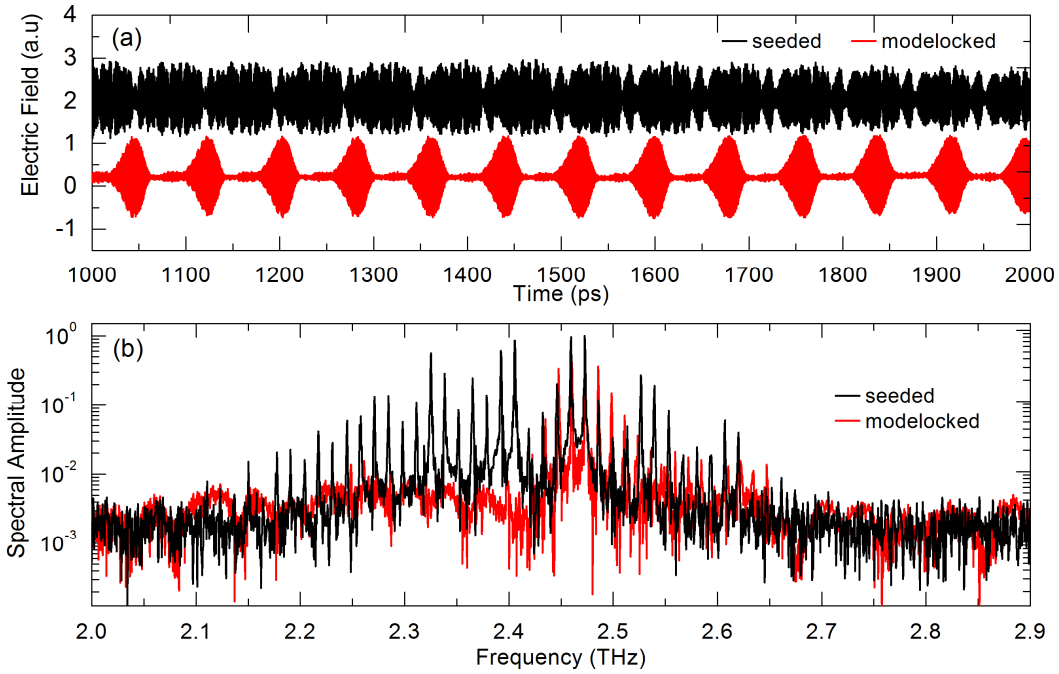

Fig 5.13 | Seeding and active mode-locking of the QCL "L1194". (a) The electric field of the QCL emission as a function of time from 1400 ps to 2000 ps under the injection seeding (black) and mode-locking (red) condition, respectively. (b) The corresponding spectra obtained by fast Fourier transform.

Now let's look at the injection seeded and mode-locked output of this 2.45 THz QCL "L1194". Fig 5.13 (a) shows the electric field time profiles of the QCL under injection seeded condition (black) and mode-locked (red curve) at 20 K. Fig 5.13 (b) is their corresponding spectra obtained by FFT. Again we observe similar behavior as previously with a complex time trace when seeded (i.e. free running) and a clear train of pulses when mode-locked. Further, the free running QCL has a mode spacing of ~ 13.4 GHz while for the clearest pulse behavior we need to apply a microwave frequency of 12.6 GHz. We also observe that the pulses remain limited to ~12 ps, a similar value as obtained on the QCL "L1074" in section 5.2 albeit with much better signal and less deformation. This is despite a broad bandwidth of ~500 GHz as shown in the seeded spectrum of Fig 5.13 (b). Indeed, when mode-locked, only a narrower bandwidth is observed in the spectrum. Therefore, we can conclude that the broad spectral

range of these QCLs (“L1074” and “L1194”) is not fully used for generating ultrashort THz pulses. It is the smooth electrical modulation of active mode-locking that appears to limit the pulses to ~11 ps. In order to get much shorter THz pulse, other mode-locking techniques should be introduced as discussed in chapter 6.

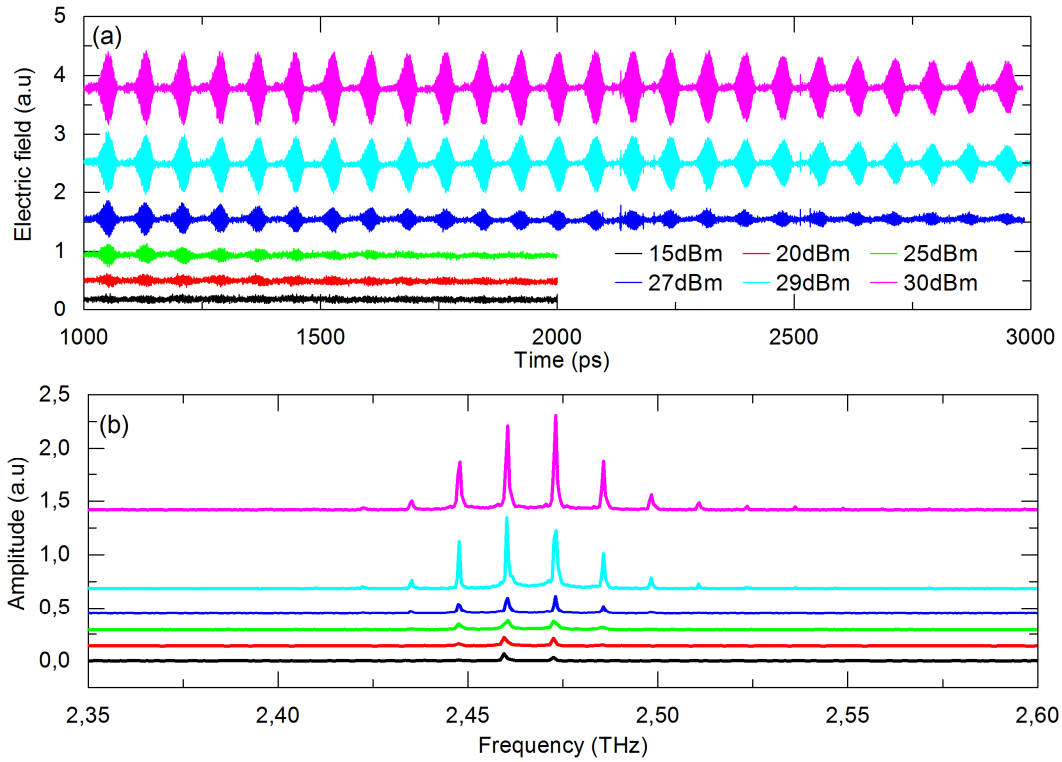

Fig 5.14 | Active mode-locking of the QCL “L1194” as function of the electric modulation power. (a) The electric field of the mode-locked QCL. (b) The corresponding spectrum of (a).

I also measured the emission of this QCL under different modulation power. The results are demonstrated in Fig 5.14. (a) is the time-resolved emission of the QCL from 1000 ps to 3000 ps with a modulation of 15 dBm, 20 dBm, 25dBm, 27 dBm, 29 dBm, 30 dBm, respectively. It can be observed that the signals increase, the pulses becomes more clear when increasing the electrical modulation power. (b) is the spectra corresponding to (a). We can see that the emission spectrum of the QCL broadens when increasing the modulation power. This is because the high modulation power has the capacity to lock more modes than weak modulation and therefore make the spectrum broader. However, the generated THz pulse width is always limited to ~11 ps. This shows us again the active modulation limits the mode-locked pulse width.

In next chapter, we will try to overcome this limitation of the sinusoidal electrical modulation and generate much shorter pulses from QCLs through dispersion compensation and a hybrid mode-locking scheme.

5.4 Discussion and conclusion

Our results on the mode locking of THz QCLs in metal-metal waveguides show that (i) clear pulse generation is only observed when the THz group index is equal to the effective modal index of the microwave modulation; (ii) pulse generation is only observed close to the threshold, resulting in low-output THz fields; and (iii) a considerable increase in the gain bandwidth does not translate into much shorter pulses. Taken together, these three points suggest that pulse generation from QCLs arises from a direct microwave modulation above and below the laser threshold, and that the pulse width is limited by the sinusoidal microwave modulation. However, the ultrafast gain recovery time measured here, which we show does not limit pulse generation, can be used as an advantage to generate more intense and shorter pulses if short intense electrical pulses can be used to switch on the QCL gain. For example, a Gaussian or Lorentzian profile could be used. Although difficult to generate electronically, optically generated electrical pulses using ultrafast lasers combined with ultrafast materials are feasible and these could then be used to switch the QCL on sub-pico-second time scales. Further techniques that could circumvent the current limitations would be the application of greater microwave power for higher pulse energies, the application of hybrid mode locking techniques and dispersion compensation to shorten the pulses that we shall present in detail in the next chapter.

To conclude, we have demonstrated injection seeding of THz QCLs with an LO phonon depopulation active region designs, fabricated in metal-metal waveguides. The ultrafast seeding permits access to the gain recovery time, which is shown to be faster than that in bound-to-continuum active region designs and approaches that of mid-infrared QCLs. Furthermore, we have shown that 11 ps mode-locked pulses can be generated from these metal-metal QCLs, with the pulse width determined by the microwave modulation and the phase matching between the microwave phase velocity and the envelope of the THz emission. The pulse generation is not limited by the inherent QCL bandwidth. This work implies that for QCL mode locking (THz and mid-infrared), the fast gain recovery time does not limit pulse formation, as postulated in the simulations in Refs. [115] [116], when a strong active modulation is applied at the correct frequency. Importantly, considerations need to be made to engineer the waveguide and refractive index dispersion to achieve phase matching. As well as pulse generation, this work could have an impact on stable comb generation [29] [117] when referenced to a microwave modulation. Owing to the metal-metal geometry, the output fields were low in amplitude, but this could be improved considerably by the integration of planar horn antennas, which will be discussed in detail in the last chapter, [118] designed for the active mode locking of such structures. Further, the QCL operating temperature and electrical power dissipation are compatible with liquid nitrogen or Stirling coolers.

6

Ultrafast Terahertz Pulse Generation from Quantum Cascade Lasers

In previous chapters, active mode-locking of single-plasmon bound-to-continuum QCLs and metal-metal QCLs based on LO phonon designs were demonstrated. Regarding the latter, I showed that, despite a large gain bandwidth, this did not automatically translate to much shorter pulses, suggesting that pulses were heavily limited by the sinusoidal-shaped electrical modulation. In this chapter, I will introduce a coupled QCL cavity consisting of a long (~3mm) and short (tens of μm) section separated by a small air-gap (~2μm). This scheme drastically shortens the pulses from mode-locked THz QCLs down to ~4 ps and dramatically expands their frequency comb bandwidth up to ~350 GHz. I will discuss the role of the coupled cavity as a method to introduce ***dispersion compensation*** through the small section (a Gires Tournois Interferometer [119]) and a fast passive modulation [1] introduced by the small air gap that combines with the active modulation i.e**.** ***hybrid mode-locking***.

At the beginning of this chapter, I will present the geometric structures of our samples, which is designed for dramatically shortening the THz pulses from QCLs. This concept will be applied to two different families of metal-metal waveguide THz QCLs based on 2.5 THz LO phonon depopulation (‘‘L1194’’) and 3.2 THz hybrid design (‘‘L857’’). This will be followed with experimental demonstrations of pulse generation and I will show that the THz pulses can be shortened down to ~5 ps, halving the previous record of ~10 ps that has been set for more than 5 years. The shortening effect introduced by these integrated passive structures are clearly observed on both of the QCL designs, showing this new scheme for ultrafast THz pulse generation is repeatable and can be widely applied. Finally, an in-depth analysis will be developed to explain this strong shortening effect of THz pulses through the role of dispersion compensation and hybrid mode-locking.

Chapter 6

6.1 Introduction and background

Although active mode-locking of THz QCLs of LO phonon based active region has been experimentally demonstrated in the previous chapter [26], the shortest pulse recorded was limited to ~11 ps, despite their large gain bandwidth. No demonstrations of stable pulse generation below ten picoseconds has been realized from THz QCLs.

The aim of this chapter, the core of this thesis, is to break this limitation of active mode-locking and to generate ultrashort THz pulses with therefore an extremely broadband frequency comb [28] [120]. Here, I will report the generation of sub 5 ps THz pulses, more than halve the previous record for THz QCLs [24] [25] [27], by engineering a small air gap and a coupled cavity that are monolithically integrated into the ridges of QCLs.

In this chapter, the geometric structures of this passive element scheme will be detailed at the beginning. Using the 2.45 THz QCL design detailed in *Appendix A* (‘L1194’), experimental pulse generation without and with the passive element will be shown and compared, with the pulse duration reduced from ~14 ps to ~4 ps, respectively. In order to further prove this scheme, the same concept was applied to a 3.2 THz QCL (wafer number ‘‘L857’’) based on a hybrid active region design. Similar results were obtained again. The pulse generation will be directly compared to the emission spectra of the mode-locked THz QCL ‘L857’, taken independently of the time resolved QCL emission, and compared to the measured time domain pulses. Finally, two coupled hypotheses will be proposed to explain how the THz pulses are dramatically shortened to ~5 ps through dispersion compensation and hybrid mode-locking.

6.2 The geometric structures of the samples

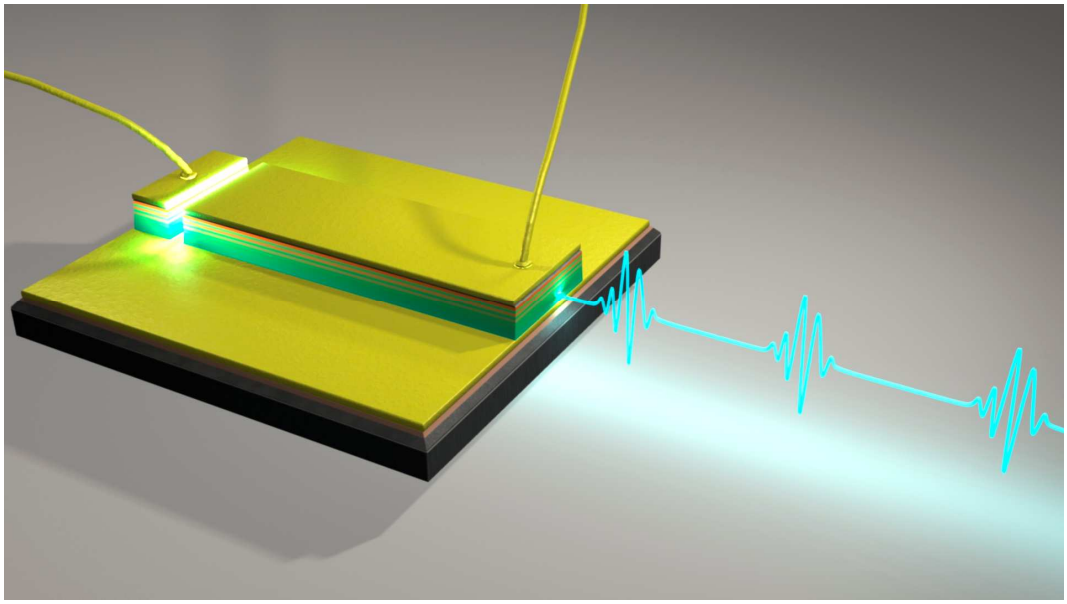

Fig 6.1 | Schematic diagram of a metal-metal waveguide THz QCL with an integrated small section varied from ~20 µm to ~60 µm and separated by a ~2-µm air gap for ultrafast THz pulse generation through hybrid mode-locking. (Figure credit: D. Darson).

Figure 6.1 shows the schematic of the QCL realized for the generation of ultrashort THz pulses from QCLs. It is based on a monolithic coupled cavity scheme with the MM QCL separated into a large active section and short passive section. The two sections are separated by a small gap. The following summarizes the final QCL schematic and with further details found below:

1. the 3-mm long section **2. the ~20µm-60µm small section** **3. the 2-µm air gap**

The entire QCL is in a MM geometry. The ~ 3-mm long section is active mode-locked around 12.5 GHz for THz pulse generation (as in previous chapters). The introduced small section (~20µm-60µm long coupled cavity) is directly etched into the laser ridge. The long and short section are separated by a small air gap, roughly 2 µm. It physically and electrically separates the two sections. The important roles that the air gap and the small coupled cavity play in the ultrafast THz pulse generation will be discussed in detail at the end of this chapter, based on the experimental results and simulations from the QCLs “L1074” and “L857”, respectively.

6.3 Experimental results on L1194

6.3.1 Samples L1194

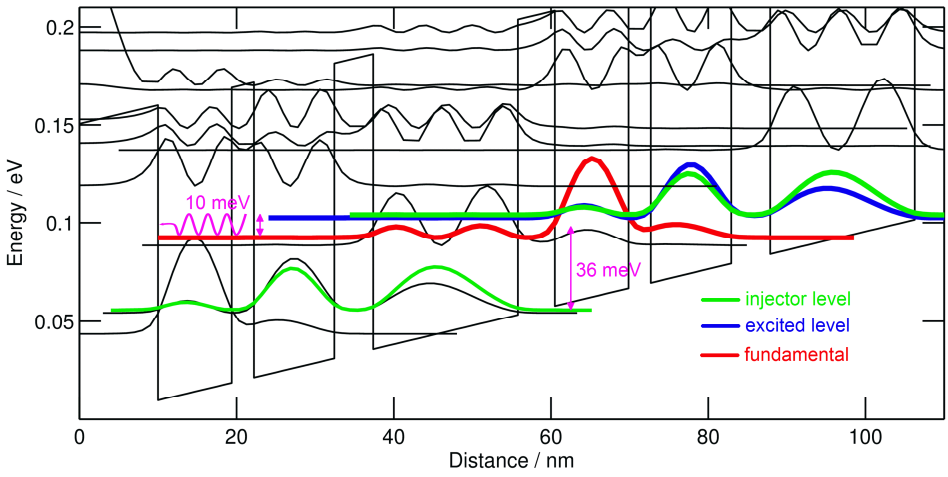

Fig 6.2 | Band structures of the QCLs "L1194" based on a LO phonon depopulation scheme with operation at ~ 2.5THz.

The first sample investigated with an integrated passive section is a 2.5 THz LO phonon depopulation QCL, wafer number 'L1194' grown at the University of Leeds. This structure has been previously employed for active mode-locking in chapter 5. As previously shown the QCL ''L1194'' possesses a broad spectral emission exceeding ~400 GHz in a MM geometry. Detailed growth sheet is attached in *Appendix A - L1194* at the end of the thesis. The band structure of this design is shown in Fig 6.2 showing a classic phonon depopulation scheme. The energy gap between the blue line and red line in Fig 6.2 is around 10.25 meV, corresponding to an emission frequency centered at ~2.5 THz.

The wafer was processed into MM waveguides using standard lithography with the ridge defined using ICP etching for a vertical ridge profile. (The processing was performed at the University of Paris-South). The air gap and coupled cavity were realized in the same processing step by etching through the active region at one end of the QCL ridge to realize short cavity lengths of ~38 or 58 µm, separated from the main QCL ridge by a small sub-wavelength (~1.5µm) air gap. The ridge width for the devices was 68µm and the total length of the cavity was ~ 3.2 mm. Figure 6.3 shows scanning electron microscope images of the final device (taken at University Paris South): (a) is the zoom of the 38-µm coupled cavity and (b) is the zoom of the ~1.5-µm air gap and (c) is the photo of the wafer with 2 ridges with 58µm and 38µm short sections in view. It can also be seen that on every short section there is a large pad. This allows to bias the section, positively or negatively to investigate the possibility of absorption (see *Appendix C*). In the work presented below, the short section was not biased. A 3-mm long standard QCL (i.e. without the small coupled cavity) was also realized with a ridge width of 60 µm for comparison.

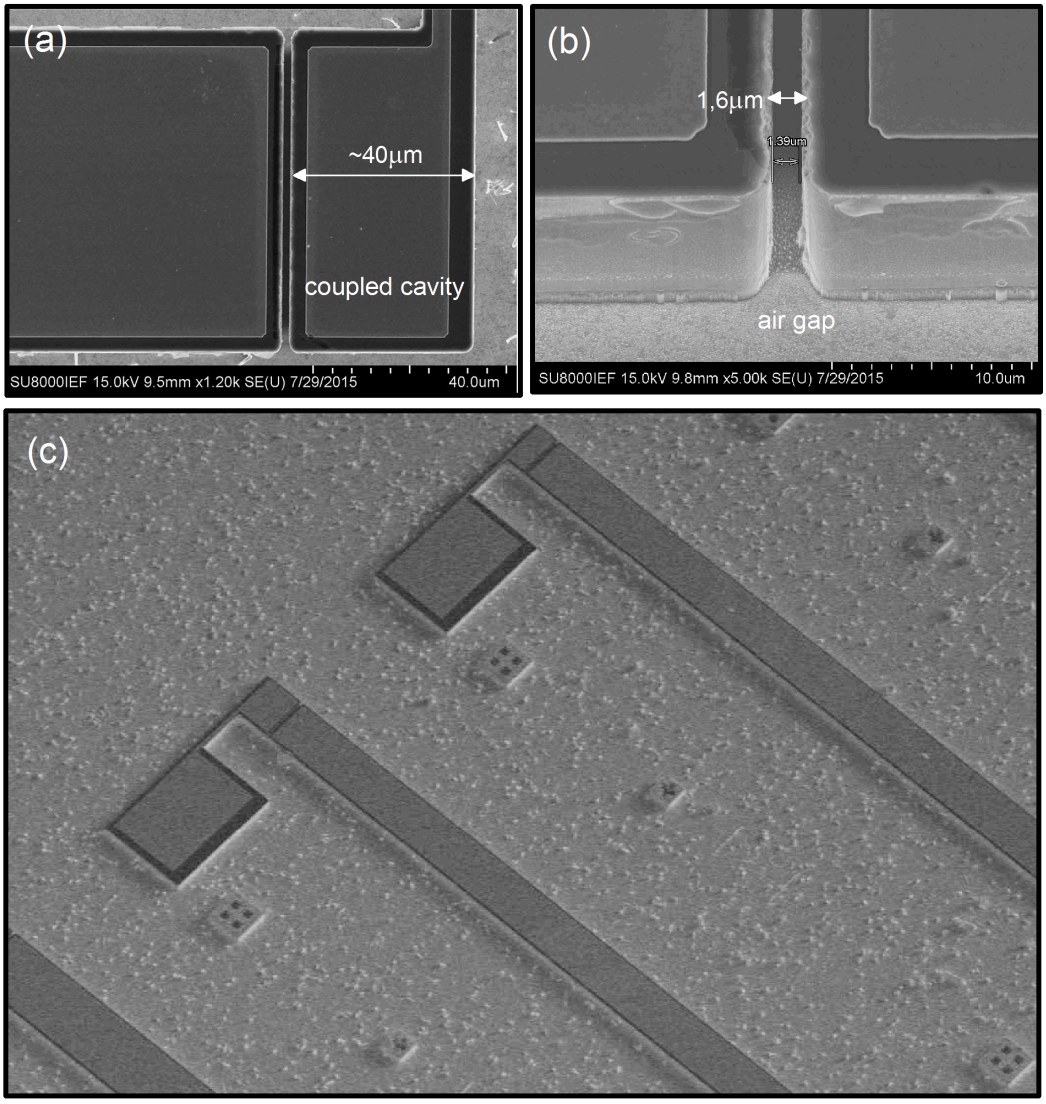

Fig 6.3 | SEM photos of QCL-L1194 with integrated air gap and coupled cavity. (a) Zoom on the coupled cavity (b) Zoom on the air gap (c) The QCL wafer with 2 ridges in view.

6.3.2 LIV characteristics

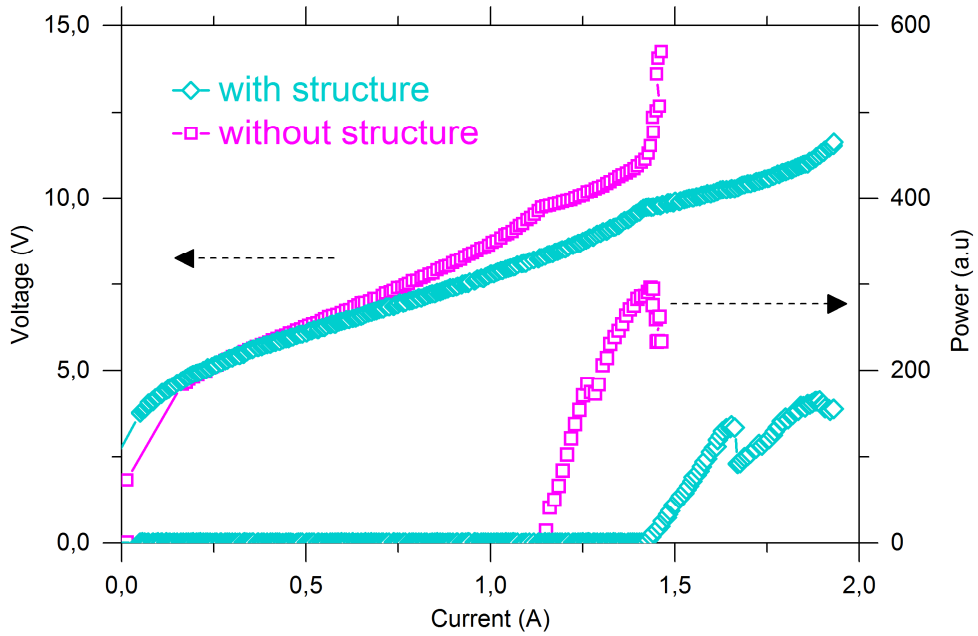

Fig 6.4 | Light-current-voltage characteristic of the samples L1194 respectively with and without coupled cavity integrated onto the monolithic chip.

Prior to investigating the ultrafast properties of QCL emission, I characterized the LIV curves of the samples "L1194" with and without coupled cavity using a pyroelectric detector as illustrated in Fig 6.4. The magenta and cyan curves shows the characteristics of the 3-mm-standard QCL and the 3.14-mm QCL with a ~58-µm coupled cavity, respectively. Both measurements were carried out in purged environment at 20 K with a modulation frequency of 20 KHz and a duty cycle of 10%. The standard QCL shows laser threshold at around 1.15 A with a linear increase in the out-coupled power with injected current until to ~1.42 A. The sample with passive elements shows a threshold of 1.44 A and lasing action slowly ceases at about 2.0 A with a smaller power slope efficiency. (The increase in threshold is related to the larger dimensions of the sample with passive elements). The out-coupling power presented by the right *y* axis is degraded by ~40% when compared to the standard QCL (the power density=power/volume degrades by ~60%). The lower slope efficiency of the coupled cavity is a result of the losses introduced by the ~1.5-µm air gap, which will be further discussed later in the chapter.

A point of note is that the collected output power for the QCL with passive elements was very different from the normal end mirror and the end mirror with the coupled cavity. It showed that the power coupled out from the coupled cavity facet was much weaker than that of the normal facet. This could further be a result of the THz waves that scatter out from the air gap and therefore introduce a loss mechanism.

6.3.3 Beat-note frequency

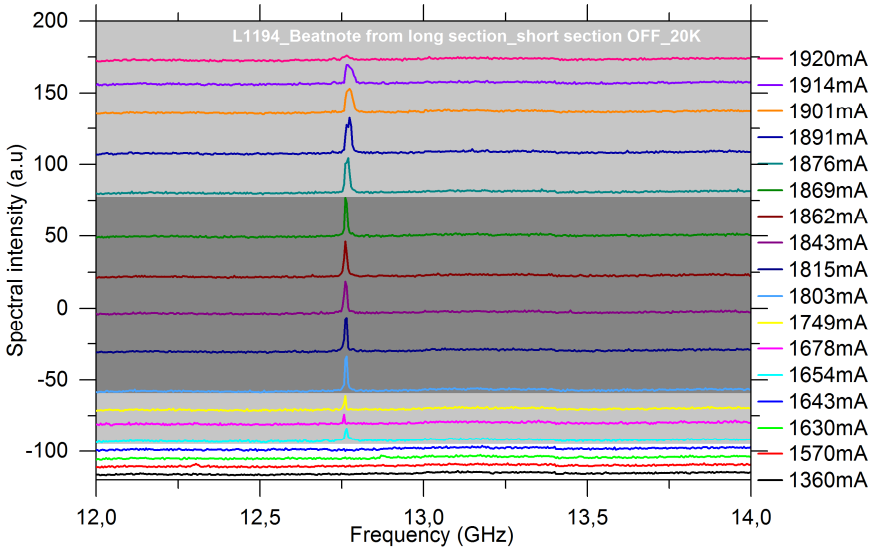

Fig 6.5 | Electrical beat-note frequencies of the QCL-L1194 with a ~58-µm coupled cavity separated by a ~1.5-µm air gap as a function of operating currents from 1360 mA to 1920 mA.

As presented in section 3.2.4, the electrical beat-note resulting from the beating of longitudinal modes represents the mode-spacing and indicates the dispersion level of medium [121]. A narrow beatnote indicates that the mode-spacing is almost identical and therefore the dispersion is low and will facilitate the mode-locking experiments. The beat-note of the samples “L1194” is measured to determine approximately the round-trip frequency that is needed to actively modulate the QCLs and to determine the best current operating range for mode-locking.

Employing the similar set-up used in Fig 3.11, the beat-note frequency of the 3.14-mm-long QCL with a ~58-µm small section was measured for currents from slightly below the threshold at 1360 mA (bottom) up to 1920 mA (top) as shown in Fig 6.5. Between 1360 mA and 1643 mA, no beat-note is observed owing to mono-mode operation or weak beating among a small number of modes that are above laser threshold. From 1654mA, the beat-note is observed at ~ 12.765 GHz and the width of the peak is of the order of ~1 MHz which slightly increases with currents. (Note that we are operating in pulsed mode so the beatnote is wider than reported values for QCLs operating in CW mode). From 1654 mA to 1749 mA, the beat-note is weak in intensity but with a very narrow peak width. This shows that the dispersion is low and the mode-spacing is roughly identical. Increasing the current from 1803 mA to 1869 mA, the beat note intensity increases and its width slightly broadens due to more longitudinal modes contributing to laser emission. This indicates the QCL is falling into the broader spectral range with a slightly larger dispersion. For current from 1876 mA to 1920 mA, the intensity of beat-note dramatically decreases and its width is strongly broadened to ~30 MHz, showing the QCL is working in the high-phase-noise region. Therefore, to mode-lock the QCL to generate THz

pulses, a modulation of ~12.8 GHz with a working currents range from above threshold to 1876 mA are required.

I have also attempted to characterize the beat-note of the standard L1194 (i.e. without integrated passive cavity). However, the sample broke at this time. Nonetheless we can compare with the beatnote of sample "L1074" discussed in chapter 5. This was a similar structure but with laser emission at 2.7 THz. Its beatnote was centered at ~13 GHz and was narrow close to threshold. However, unlike the QCL with passive structures, the beatnote became very broad quickly at higher currents indicating that the dispersion was large. Therefore, the beatnote of the sample with passive strucures indicates a lower dispersion when compared to a standard sample.

6.3.4 Mode-locking of samples L1194

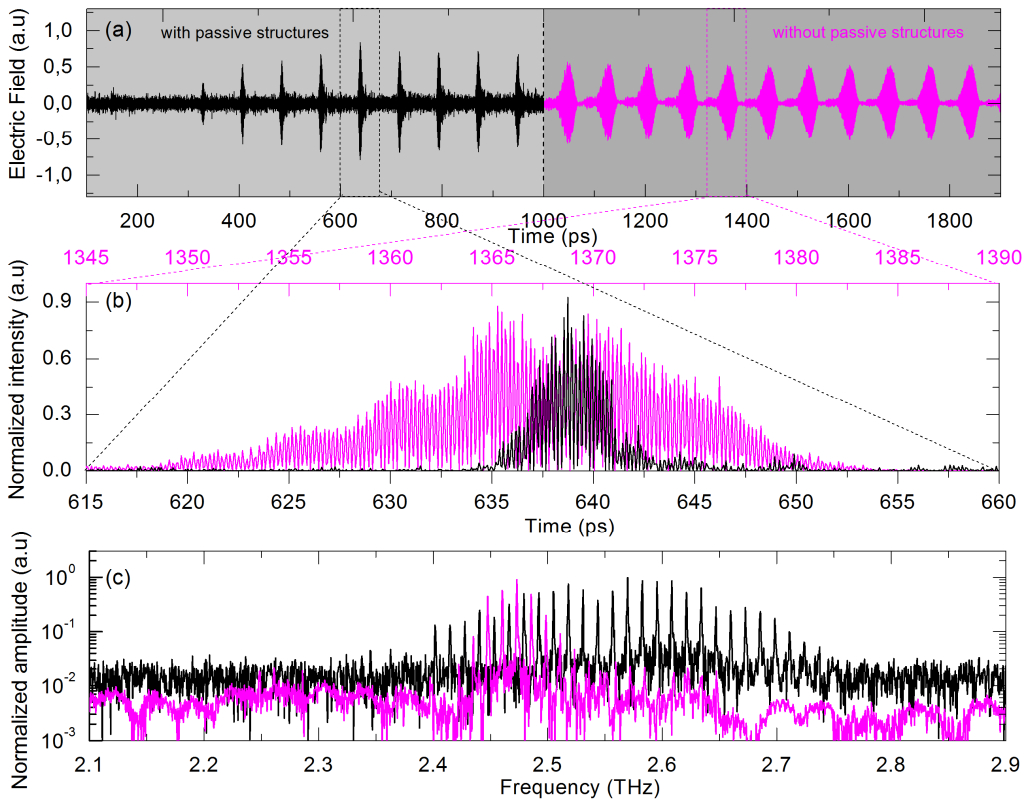

Fig 6.6 | Comparison of the standard (purple) and artificially engineered (58-µm small section and 1.5-µm air gap) (black) QCLs emission from "L1194" under a round-trip electrical modulation of ~30 dBm. (a) Time-resolved electric field of the QCL emission. (b) Normalized intensity of QCL emission, squaring of pulses in (a) at 1370 ps and 640 ps respectively. (c) Corresponding spectra of the QCLs (FFT of the measured electric field in (a)).

In this section, I will investigate mode-locking of "L1194" for THz QCLs with and without the passive elements (air gap and coupled cavity). Both of the two samples worked at the almost the same electrical parameters as shown in table 3, except for the DC current. For simple active mode-locking, a 12.617 GHz was applied on the standard QCL while for the QCL with integrated passive structures a 12.886 GHz was used. The time resolved electric fields were measured using the injection seeding technique described in previous chapters [67]. Here, the external THz pulses are injected into the QCL with passive structures via the small section (i.e. the coupled cavity side) and the emission detected from the opposite standard facet, owing to the much stronger power coupled out from the latter.

Table 3. Parameters used for active and hybrid mode-locking

Parameters	Active mode-locking	Hybrid mode-locking
DC bias	20 KHz, 5 µs	20 KHz, 5 µs
Currents	870 mA	1220 mA
RF for seeding	200 mW, 6.2 ns	200 mW, 6.2 ns
Temperature	20 K	20 K
GHz modulation	12.617 GHz, 30 dBm	12.886 GHz, 30 dBm

The measured electric fields of the two QCLs as a function of time are shown in Fig 6.6 and show the clear effect of the passive structures. The breakthrough shows that while the standard QCL produces pulses (purple) are ~14 ps, as previously presented in chapter 5, the coupled cavity QCL shows pulses (black) that are ~ 4 ps. This is more than half the previous record for THz QCLs pulses of ~10 ps, which has been set for more than 5 years. Therefore, it shows that the chip-integrated passive geometry structure completely breaks this previous bottleneck limitation. Fig 6.6 (b) shows a zoom of the intensity profile (square of the electric field in (a)) of the THz pulses for the standard QCL (purple curve from 1345 ps to 1390 ps) and the QCL with integrated passive structures (black curve from 615 ps to 660 ps) highlighting the strong contrast in pulse duration. The pulse widths mentioned above are taken as the FWHM of the intensity profiles. The Fig 6.6 (c) illustrates the spectra of these two lasers, obtained by the FFT of their electric field. Their differences are obvious. In the case of the standard QCL, there are only about 10 modes in the spectrum with a full bandwidth of ~150 GHz while in the case of the QCL with chip-integrated passive geometry, the spectrum is greatly expanded to more than ~380 GHz and more than 28 modes contribute to its emission and pulse formation. In order to verify whether absorption plays a role in the coupled cavity, the 58-µm small section was biased negatively and positively. No change in pulse form was found suggesting that absorption is not a predominant effect. Further details can be found in *Appendix C*. A point to note regarding the spectrum of the standard QCL is that, in the free running case, the free spectral range is 13.4GHz. However, as shown in chapter 5, a microwave modulation at a much lower frequency is required to generate the clearest pulses. As detailed in table 3, a modulation of 12.6 GHz is applied. Owing to this difference between the free spectral range and the applied

microwave modulation, this likely limits the number of modes that can be brought above threshold resulting in a narrow spectrum for the standard QCL. (For the coupled cavity the free spectral range was the same as the modulation frequency).

The above presented the results for a QCL with a 58µm short section. We have also preliminary characterised a QCL with 38µm short section. This showed a much wider electrical beatnote, indicating a higher dispersion. Its time resolved electric field emission is currently under investigation.

.

6.4 Experimental results on L857

This section will detail the second set of samples where a coupled cavity geometry was realized.

6.4.1 Samples L857

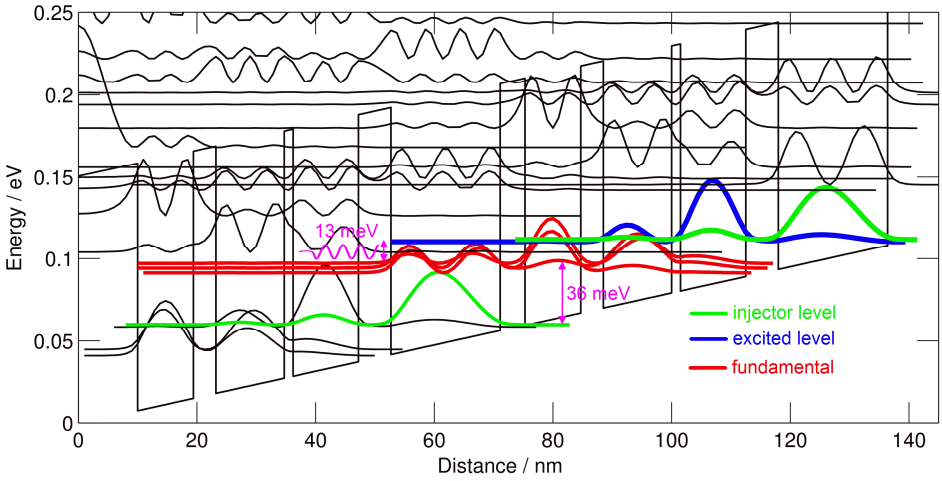

Fig 6.7 | Band structures of L857 based on a hybrid active region design combining bound-to-continuum and LO phonon depopulation schemes.

The sample ‘‘L857’’ is based on a hybrid active region design that combines the LO phonon depopulation and bound-to-continuum scheme (see chapter 1). Their full bandwidth is ~300 GHz with a frequency centered at ~ 3.25 THz. They were also grown by MBE at the University of Leeds, wafer bonded at the University of Paris-south and processed at the University of Paris-7 by M. Amanti (group of C. Sirtori) into metal-metal waveguides. In this design, GaAs/$Al_{0.15}Ga_{0.85}As$ material system was employed. The thicknesses of quantum wells and barriers of the active region are: *4.20*/**9.40**/*3.80*/**11.50**/*1.80*/**11.00**/*5.50* /**<u>18.40</u>** nm. Barriers are also shown in italics and quantum wells are shown in bolds. The underlined quantum wells were doped at the level of 2.0×10^{16} cm^{-3}. Detailed growth sheet is presented in *Appendix A – L857*. The band structure of this design are presented in Fig 6.7, with the injector level in green, excited level in blue and the fundamental continuum levels in red. The energy gap between the blue line and red line is ~13.3 meV corresponding to an emission frequency centered at ~3.2 THz. This hybrid depopulation scheme has an electronic life time for the fundamental levels that is slightly longer than that of pure LO phonon design and shorter than that of bound-to-continuum design. This results in a spectral bandwidth lying between those of LO phonon depopulation and bound-to-continuum designs.

The wafer was processed into a 3-mm-long 50/100/150 µm-wide ridges with an integrated ~20-µm-long coupled cavity separated by a ~2.5-µm air gap (40µm shorter and 1µm larger compared to “L1194”), as illustrated in Fig 6.8. These photos were measured at École Normale

Supérieure in Paris. In this figure, (a) shows the zoom of the ~20 µm coupled cavity observed by scanning electron microscopy, (b) is the zoom of the ~2.5 µm air gap with a much higher resolution and (c) shows a part of the completed device. As for L1194, a large pad is connected to the small section for biasing. The QCLs with 50-µm wide ridges were not used as they didn't lase owing to the larger loss from the waveguides. The 100-µm QCL is used in this section for ultrafast THz pulse generation and the 150-µm QCL is used in *Appendix D* for high order transverse modes investigation. To compare, a device without the coupled cavity was cleaved (length 2.7mm).

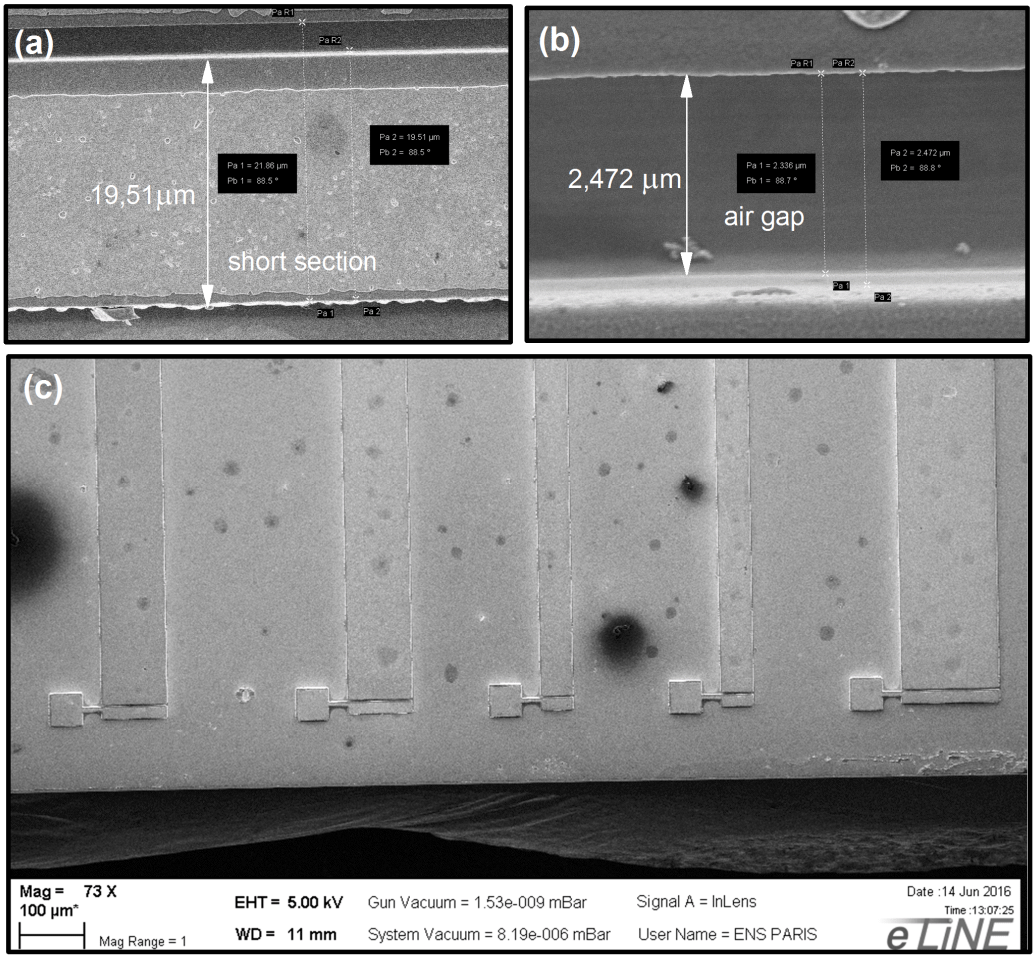

Fig 6.8 | SEM photos of QCL-L857 with integrated ~2.5 µm air gap and ~19.5 µm coupled cavity. (a) Zoom on the coupled cavity (b) Zoom on the air gap (c) The QCL wafer with 5 ridges of different widths (100µm/100µm/50µm/50µm/150µm from the left to the right) in view.

6.4.2 LIV characteristics and beatnote frequency

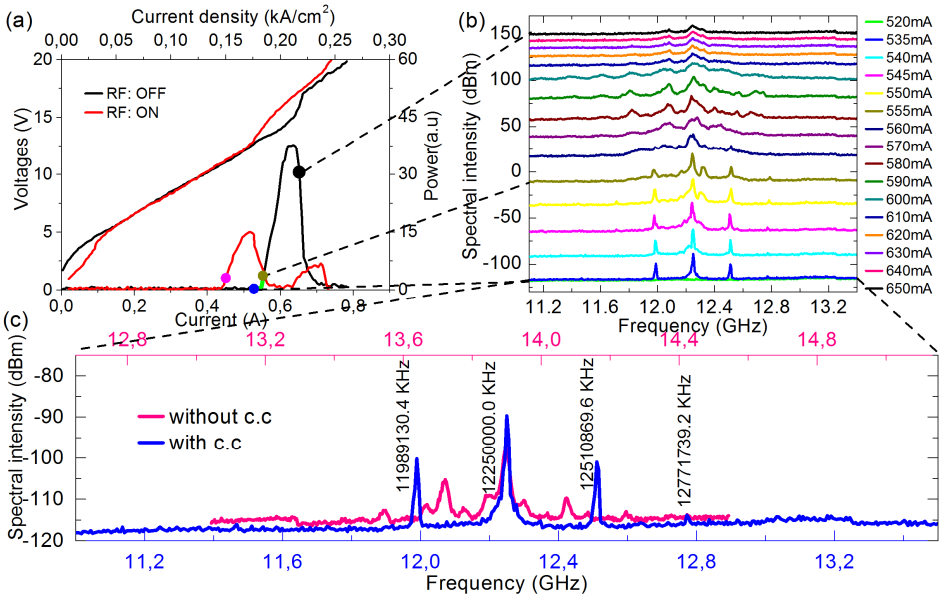

Fig 6.9 | Characteristics of the metal-metal THz QCL "L857" based on a hybrid design with emission frequency centered at 3.25 THz. (a) Light-current-voltage characteristics of a 3-mm-long 100-µm-wide passive-geometry-integrated THz QCL respectively with (red) and without (black) radio-frequency switching (used for injection seeding). (b) Beatnote frequency corresponding to the currents varied from 520 mA to 650 mA at right side showing from 11.1 GHz to 13.4 GHz. (c) Typical beatnotes of QCLs with (blue, bottom axis) and without (pink, top axis) integrated coupled cavity.

Fig 6.9 (a) shows the LIV characteristics of the QCL with integrated passive geometry with (red) and without (black) RF pulse (used for injection seeding - see section 4.1.3 in chapter 4). Without the RF pulse, the laser action starts at ~530 mA and ceases at ~720 mA. With RF switching, the threshold of QCL decreases down to ~420 mA, with the RF pulses providing ~110 mA. Fig 6.9 (b) is the electrical beat note without RF (chapter 3), representing the mode-spacing and dispersion of the laser, for a current range of 520 mA (bottom) to 650 mA (top). Between 535 mA and 550 mA, the beatnote is relatively narrow (~10 MHz) showing the QCL is operating in a quasi-comb regime where the mode-spacing is almost identical. Increasing the currents from 555 mA to 650 mA, the width of beatnote becomes much broader (~70 MHz) and the intensity becomes weaker indicating the QCL is falling into high-phase-noise region. Therefore, the QCL was kept below 555 mA, corresponding to the brown point and the purple point without and with the RF pulse, respectively in Fig 6.9 (a).

Fig 6.9 (c) shows a zoom of the beatnote at ~535 mA (blue curve). Four peaks are observed at 11.989 GHz, 12.250 GHz, 12.511 GHz and 12.772 GHz, with a spacing of exactly 260869.6 kHz (accuracy of 0.1 kHz, limited by the high-speed spectrum analyzer). These multiple peaks result from four-wave mixing between the high-order transverse mode TM_{01} and fundamental one TM_{00} inside the QC [117] [122], a result of the large ridge. This hypothesis is support by

(i) the 260 MHz peak spacing between beatnotes corresponds to a refractive index change of about ~0.08, which approximately agrees with the refractive index difference between fundamental TM_{00} and first high-order mode TM_{01}. (ii) Increasing the ridge width favors further high-order transverse modes [106], leading to further beatnote peaks as detailed in *Appendix D*; (iii) The multiple beatnotes were not observed in the case of QCL L1194 in the previous section as the ridge was narrow (~68 µm) that limits operation to the fundamental mode and (iv) nonlinear effect is the most probable process that leads to the high precision of the peak spacing. The peaks are not a result of the coupled cavity as multiple beatnotes are observed for a standard QCL of length 2.7mm of the same ridge width as illustrated in the pink curve of Fig 6.9 (c).

Importantly, comparing the beatnote of the QCLs with and without the coupled cavity in Fig 6.9 (c), we observe that the latter has a more uniform separation between the beatnotes and are considerably narrower. This again indicates that the dispersion is reduced with the coupled cavity.

6.4.3 Mode-locking of QCL L857

Fig 6.10 (a) shows the measured time resolved electric fields of the QCL, from 750 ps to 1850 ps, under free running ('seeded' black curve) and mode-locking (magenta curve) conditions by the detection technique detailed in chapter 2. The QCL was held below threshold at 20 K with a 20 KHz current of ~442 mA and an 8-ns RF pulse train of ~76 MHz was used to periodically bring the QCL above and below its threshold. In the free running case, although the pulses are neither perfectly Gaussian or ultra-short, a stable and periodic pulse train emission is observed, showing already the effect of the passive element integrated onto the QCL (see section on hybrid mode-locking). For active mode-locking, a ~30dBm active modulation at 12.310 GHz is added to this QCL, close to the central beanote of 12.250 GHz in figure 6.9. Ultrafast THz pulses as short as ~5 ps are generated as illustrated in Fig 6.10 (a). (The dynamic region before 750 ps where seeding pulse is amplified as shown in *Appendix E*). A zoom of the pulse from 1114.5 ps to 1135.5 ps is shown in Fig 6.10 (b), where the oscillation of electric field and the sampling points can be clearly observed. The spectrum of the seeded and mode-locked emission is shown in Fig 6.10 (c), obtained by the FFT of the electric fields in (a). The emission frequency is centered at 3.25 THz. Without microwave modulation, it can be seen that the coupled cavity QCL has already a uniform and relatively large spectrum width of up to ~250 GHz (black curve). With the electrical modulation, the longitudinal modes of QCL transfer their energy to the other Fabry-Perot modes, bringing more modes above laser threshold and further broadening the spectrum ~350 GHz (magenta curve). The phase of each mode was also analyzed and presented in Fig 6.10 (d). For the free-running case a random phase relation is observed. For mode-locking, all the modes are in phase and leads to the observed ~5 ps ultrafast THz pulses. These results shows that with the integrated passive elements, ultrashort THz pulse generation can be realized over a wide range of QCL frequencies.

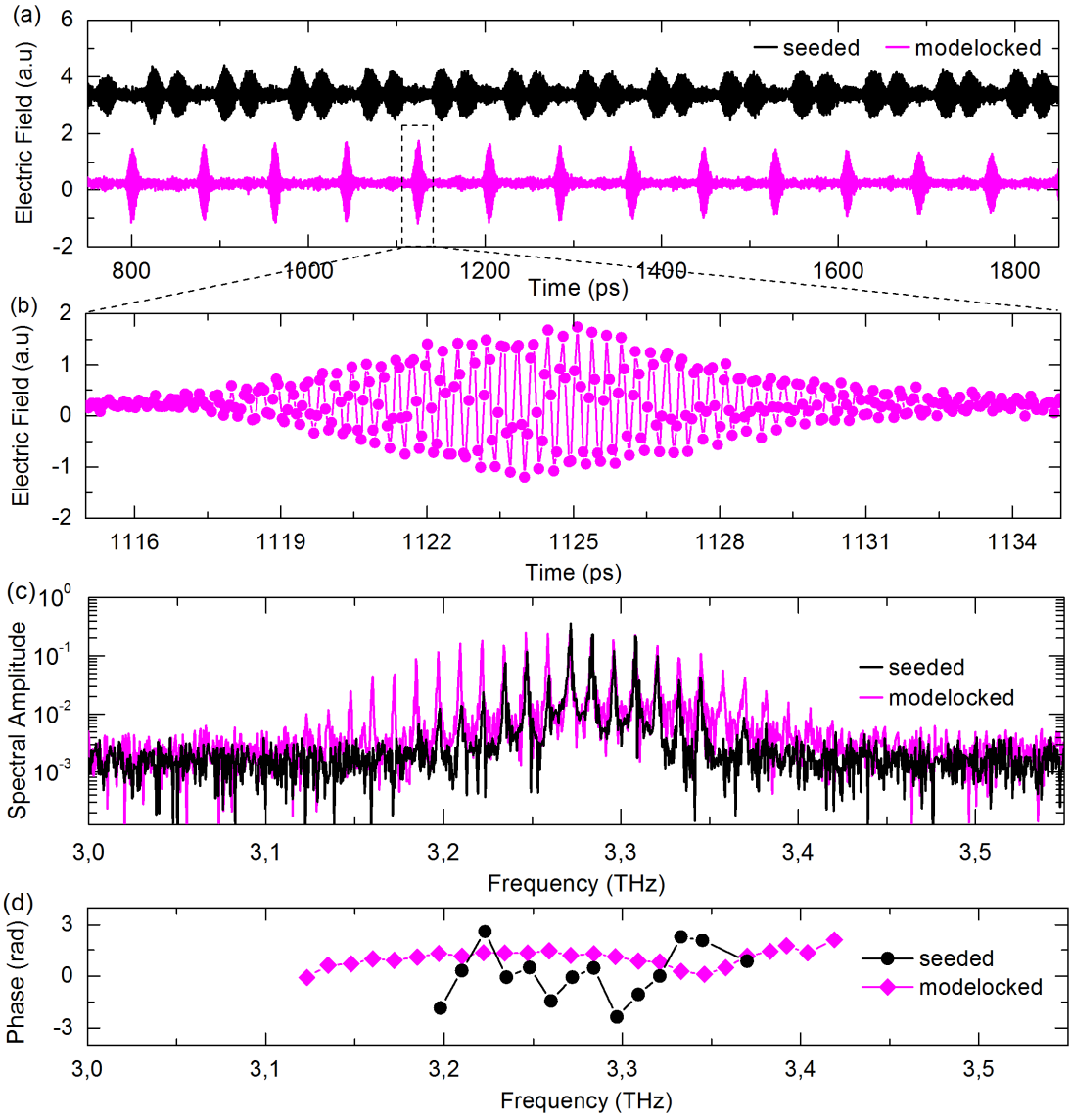

Fig 6.10 | Free running injection seeding (black) and mode-locking (magenta curves) of the THz QCL L857 centered at 3.25 THz. (a) Time resolved electric field of free-running and mode-locked emission shown from 750 ps to 1850 ps. (b) Zoom of the mode-locked pulse at 1125 ps in (a). (c) Spectra of the free-running and mode-locked emission of the QCL obtained by Fourier transform of the measured electric field. (d) Phase of each lasing mode under free-running and mode-locked conditions.

To conclude, in our experiments, the integrated passive structures play an important role in drastically shortening the active mode-locked THz pulses down to 5 ps. The exact shortening mechanism will be discussed at the end of this chapter in section 6.5.

6.4.4 Direct measurements of the emission spectra of THz QCLs L587

In the previous section I have demonstrated ~5 ps THz pulse generation from mode-locked THz QCLs "L857" in the time domain using an injection phase seeding technique. In this section, I will compare the results in the time domain with the spectra taken in the frequency domain (i.e. independently of the time data). No RF switching pulse is required and the QCL is therefore operated in a quasi-CW operation with the active modulation. The measurements were taken together with S. Houver at Ecole Normale Superieure.

The technique was based on the nonlinear up-conversion of the THz spectrum to the optical domain (~800nm, ~1.5eV) using a resonant nonlinearity of the QCL itself [123] [124] [125]. The spectrum can then be obtained using a standard near-infrared spectrometer coupled to a CCD camera. Further details of the technique can be found in ref [123] or *Appendix F* at the end of this thesis. When compared to Fourier transform infrared (FTIR) methods, the up-conversion technique permits the spectra to be taken very quickly (no moving parts) and with a high resolution depending on the dispersion properties of the grating spectrometer.

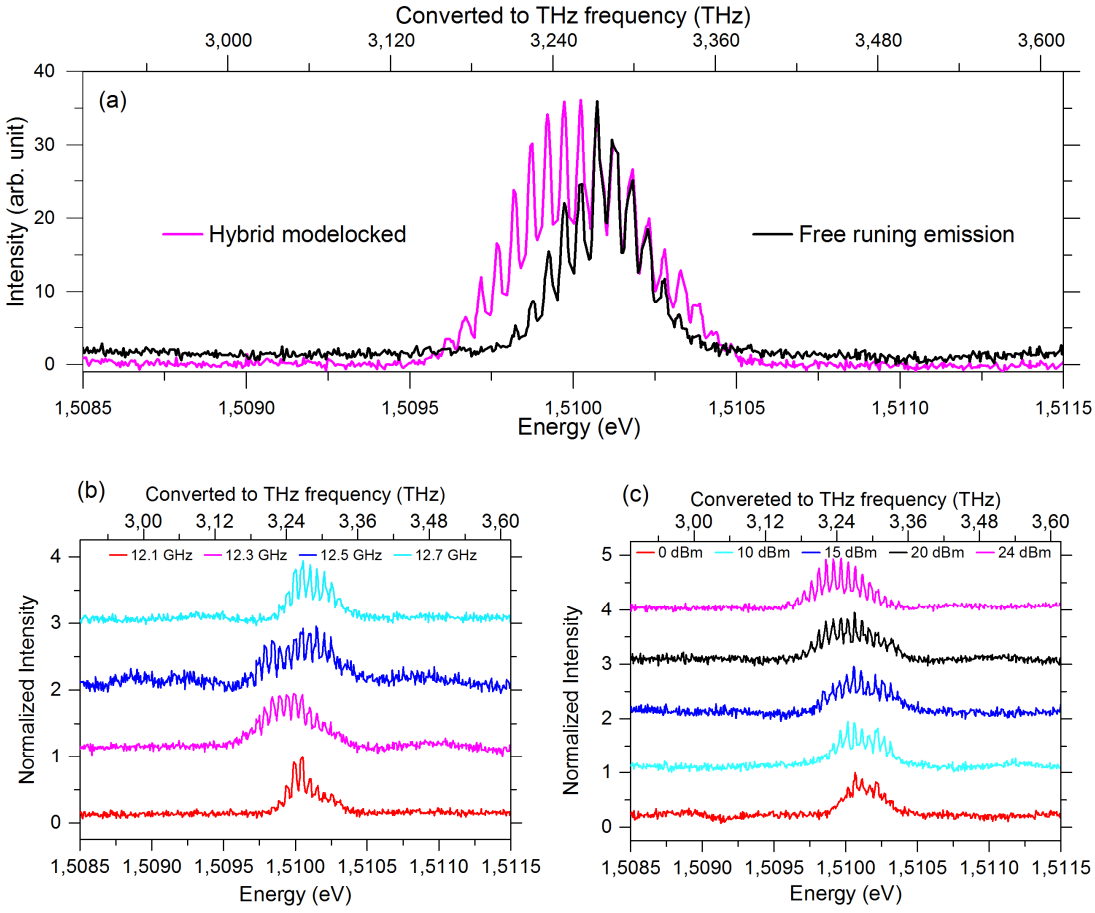

Fig 6.11 | Emission spectra of THz QCL L857 directly measured by up-converting the THz waves into the near-infrared range using difference frequency generation. (a) The emission spectrum of coupled cavity THz QCL L857 used in previous section in free running (black) and mode-locked (magenta)

modes. (b) The emission spectra of L857 as a function of active modulation frequency with a microwave power of 24dBm (c) The emission spectra of L857 as a function of active modulation power at a modulation frequency of 12.3GHz.

Fig 6.11 (a) shows the up-converted spectrum of the passive geometry integrated QCL "L857" with the lower *x*-axis showing the optical spectral range (in energy) and the top *x*-axis showing the converted THz range (in frequency). With a bias of 590 mA, a 24dBm modulation at 12.3 GHz was applied using a standard microwave generator (magenta) and compared to the emission without microwave modulation (black curve). From the free running spectrum, a few modes are brought about threshold with the mode spacing (~12.3 GHz) clearly distinguished. With the microwave modulation, we observe a strong enhancement of the number of modes brought above threshold as expected when the QCL is mode-locked. This spectrum is a typical mode-locked spectrum with an almost Gaussian distribution of the longitudinal modes. Comparing the above spectrum with the mode-locked spectrum measured by injection seeding technique in Fig 6.10 (c), a similar form is observed, although the up-converted spectrum shows less modes at the extremities of its spectrum. This is most likely a result of less microwave power used (24dBm limited by the generator) when compared to injection seeding experiment (~30 dBm). The black spectrum in Fig 6.11 (a) is the emission of the THz QCL "L857" without any electrical modulation.

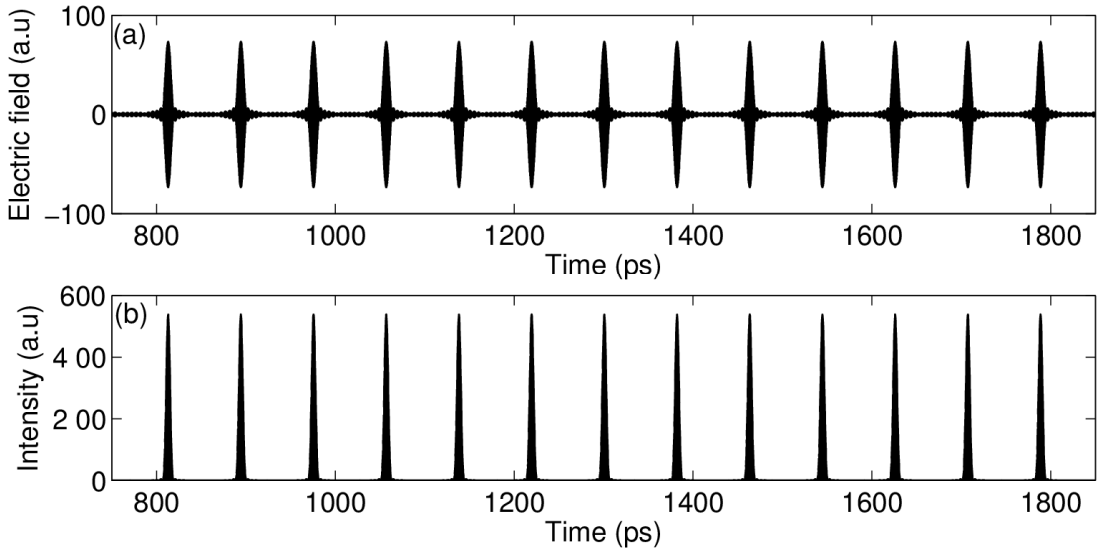

Fig 6.12 | Reconstructed electric field (a) and intensity (b) of the hybrid mode-locked QCL emission based on the measured spectrum in Fig 6.18 (a). magenta.

Figure 6.11 (b) shows the effect of the modulation frequency at a fixed microwave power (24dBm) where we observe the largest and most Gaussian spectrum at 12.3 GHz, close to the measured electrical beatnote. Finally, with the modulation frequency fixed, we varied the microwave power from 0 dBm to 24 dBm that showed more modes are brought above threshold

as the power is increased. This shows that the emission spectrum can be extended by locking more sideband modes through the modulation power.

As we expect the modes to have the same phase when mode-locked, the time resolved electric field can be reconstructed and compared to the measured time profiles (Fig. 6.10(a)). Fig 6.12 shows the reconstructed electric field (a) and intensity (b) of the QCL emission in time domain from 750 ps to 1850 ps from the mode-locked spectrum in Fig 6.11 (a), considering that all the modes are in phase. A stable pulse train is formed, very similar to the emission measured by injection seeding of Fig 6.10 (a). In addition, the reconstructed pulse width is ~5 ps, in agreement with the experimental time data, suggesting we are close to the Fourier limit. Although this method does not permit to access the time dynamics directly, it shows that equivalent reconstructed forms can be obtained with the QCL operating in a quasi CW mode. This method also permits to independently verify if we are at the Fourier bandwidth limit.

6.5 Analysis and discussion

6.5.1 Introduction

Comparing the mode-locking experiments on the samples “L1194” respectively with and without the passive structures in Fig 6.6, it can be concluded that it is the coupled cavity scheme (i.e. the air gap and the small coupled cavity) that results in considerably shorter THz pulses. (The only variable between them is the integrated passive structures). Here, we will discuss two coupled hypotheses to explain this effect. The first is dispersion compensation where the short cavity act as a Gires-Tournois interferometer (GTI) and compensates the gain and material dispersion of the QCLs [126] [127]. The flatter dispersion permits the fabry-perot modes to be separated more equidistantly. Therefore, more modes can be brought above threshold with the same microwave power resulting in shorter pulses. The second one is hybrid mode-locking. The air gap brings an ultrafast passive modulation that breaks the bottleneck of active mode-locking and therefore results in ultrafast THz pulses down to 5 ps by hybrid modulating the QCLs together with the electrical modulation. Although discussed separately, these two processes are most likely be linked.

6.5.2 Dispersion compensation introduced by the coupled cavity

The first hypothesis to explain the shortening effect is dispersion compensation (performed in collaboration with the group of N. Jukam et the University of Bochum). Here, I will present the small section in the coupled cavity configuration described in Fig 6.1, which can be engineered into a quasi Gires-Tournois interferometer (q-GTI), and provides dispersion compensation for stable short THz pulses. This is intrinsically linked to the refractive index dispersion that indicates how the refractive index depends on frequency and is often characterized by the group delay dispersion (GDD). This parameter is critical in ultrafast lasers and indicates how a pulse broadens as it propagates within a material with an uncompensated dispersion (a non-zero GDD). This becomes increasingly important for short pulses. In the case of the optical and NIR spectral regions, dispersion compensation in femtosecond lasers is readily accomplished with external elements such as prisms, grating or chirped mirrors that introduce a GDD that is opposite to that of the laser medium. This brings the overall GDD down to zero and avoids the broadening of short pulses.

When dealing with mode-locked broadband THz QCLs and ultrashort pulse generation, group delay dispersion (GDD) management is challenging due to several factors. First, the material GDD owing to bulk GaAs is an important factor as a result of the residual absorption from the Reststrahlen band [28]. Second, the gain GDD is even greater than material GDD owing to the dispersion added by the inter-subband transition and can significantly limit THz frequency comb operation [29]. Third, in contrast to optical and near infrared frequencies, there is a lack of dispersion compensation schemes for THz wavelengths. In fact, there are only a few concepts available to reduce the total GDD. Schemes that have been applied to THz QCL waveguides have used narrow corrugated waveguides to act as a chirped waveguide to show

frequency comb operation [28]. The integration of a dielectric-metal section into passive metal-metal waveguide has also been implemented.

Gires-Tournois interferometer

The GTI is a technique used in the optical and near-infrared domain to compensate the dispersion of ultrafast pulse [127]. It has also been applied to reduce the dispersion in mid-infrared QCLs for broadband frequency comb generation. A regular GTI generally consists of a small resonator (length l is of the same order as the wavelength of the laser in the material) operating in reflection where, in the ideal case, the front mirror is of low reflectivity ($(r_1)^2 \sim 0.1$) while the back mirror is perfect ($(r_2)^2 = 1$) as illustrated in Fig 6.13. (r_1 and r_2 are the reflectivity amplitudes). The reflectivity is unity over the entire frequency range, but the phase is strongly frequency-independent owing to the cavity effect of the resonator. The interference gives rise to both positive and negative group GDD given by:

$$GDD_{GTI}(\omega) = -\frac{2\tau^2(1-r_1^2)r_1\sin(\omega\tau)}{(1+r_1^2-2r_1\cos(\omega\tau))^2} \tag{6.1}$$

where $\tau = 2nl/c$ denotes the round trip time of the GTI where n is the refractive index, the speed of light in vacuum c and the length of the GTI l. By choosing the length of the resonator correctly, compensation of the material and gain dispersion can be achieved. (GTIs have been operated in the negative GVD regime in order to compensate for excess positive GDD in picosecond mode-locked Ti:Saphire lasers [128]). The GTI mirror is normally realised using dielectric coatings with thicknesses on the order of the wavelength. However, for the THz range where the wavelength is typically 100µm, thick dielectric coatings to realise the reflectivity conditions are difficult to fabricate. In this work, rather than depositing a dielectric, we use the QCL itself and the confinement of the electromagnetic mode to realise a q-GTI. Although the reflectivities are different from the ideal case significant dispersion compensation can be still achieved.

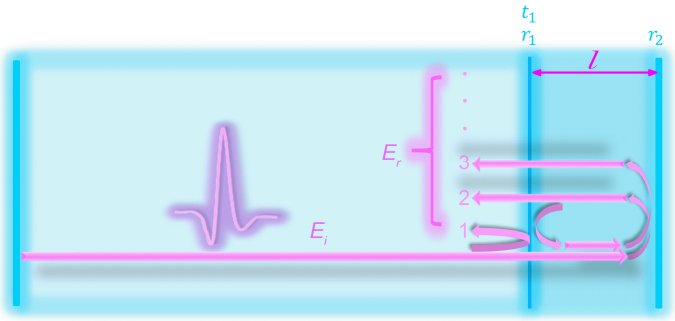

Fig 6.13 | Schematic diagram of Gires-Tournois interferometer

In particular, etching a small air gap (~2µm) into the metal-metal waveguide to realise a small cavity at the end of the QCL, results in a q-GTI with a contrast in the reflectivities of the

front (r_1) and back (r_2) mirror (see Fig 6.14). The reflectivities of the facet and the air gap were calculated from the finite-difference-time-domain method using the Meep software package by N. Jukam at the University of Bochum. From these simulations, the q-GTI realized in this work provides a front reflectivity of r_1=0.61 and a back mirror reflectivity of r_2= 0.83 and thus different from the ideal case of $(r_1)^2$=0.1 and $(r_2)^2$=1. (The high value of r_2 is a result of the strong confinement of the MM waveguide mode). Consequently, the well-established formula for the GDD introduced by a GTI needs to be generalized in order to take account of the non-unity reflection coefficient of the second mirror. This is discussed below.

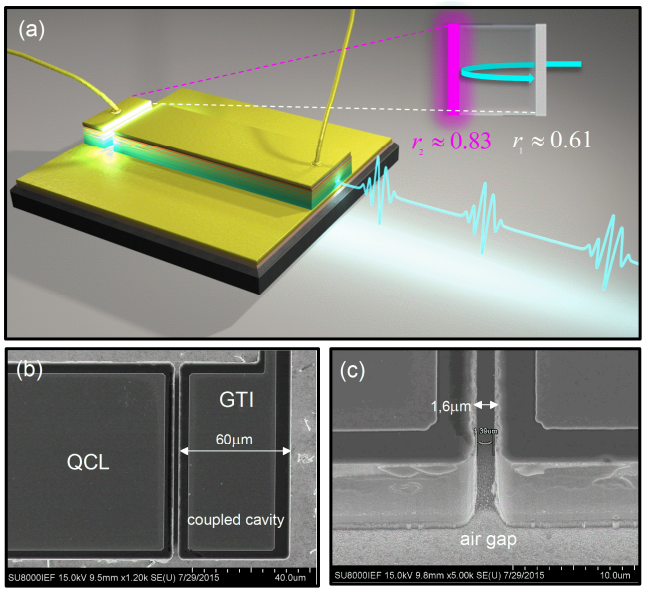

Fig 6.14 | (a) Schematic diagram of the coupled cavity acting as a Gires-Tournois interferometer. (b) SEM photon of the interface of the coupled cavity and the QCL. (c) The zooming of the interface (air gap) between the small section (GTI) and the long section (QCL).

In general case, determined by T. Fobbe (group of N. Jukam at the University of Bochum), if we suppose the electric field incident onto the GTI is E_i and the total reflected electric field is E_r, the total reflection coefficient can be then written as:

$$r_{tot}^{GTI} = E_r / E_i = -r_1 + r_2 t_1^2 e^{-2i\delta} + r_1 r_2^2 t_1^2 e^{-4i\delta} + r_1^2 r_2^3 t_1^2 e^{-6i\delta} + ... = \frac{r_2 e^{-2i\delta} - r_1}{1 - r_1 r_2 e^{-2i\delta}} \qquad (6.2)$$

For the speed of light in vacuum c_0, the refractive index n and the GTI length l, the phase $\delta=\omega nl/ c_0$ accounts for a single trip in the GTI resonator. In Eq. (6.2), the signs of the first term ($-r_1$) and the other terms are different, due to the half wave loss of the first reflection "1". As in the general case, the total reflection coefficient r_{tot}^{GTI} of the GTI is a frequency-dependent complex function. This will add a different phase term for different frequency and therefore provides a possibility to compensate the dispersion.

The GDD is the second derivative of the spectral phase with respect to the angular frequency and the general expression for the spectral phase of a q-GTI with a non-unity reflection coefficient. From Eq. (6.2), the spectral phase can be given by:

$$\Phi_{qGTI}(\omega) = \arctan\left(\frac{\mathrm{Im}\{r_{tot}^{qGTI}\}}{\mathrm{Re}\{r_{tot}^{qGTI}\}}\right) = \arctan\left(\frac{r_1^2\sin(\omega\tau)-\sin(\omega\tau)}{r_1/r_2 - r_1^2\cos(\omega\tau)+r_1 r_2-\cos(\omega\tau)}\right) \tag{6.3}$$

Here n is taken as the refractive index of GaAs. The effect of r_1 being considerably higher from the ideal case ($r_1 \approx 0.1$) results in more pronounced variations of the GDD near the resonant frequencies but with little effect off-resonance, where we will be using the q-GTI. Using Eq. (6.2), the dispersion compensation added to the THz pulse in QCLs by the coupled cavity can be then calculated as discussed below.

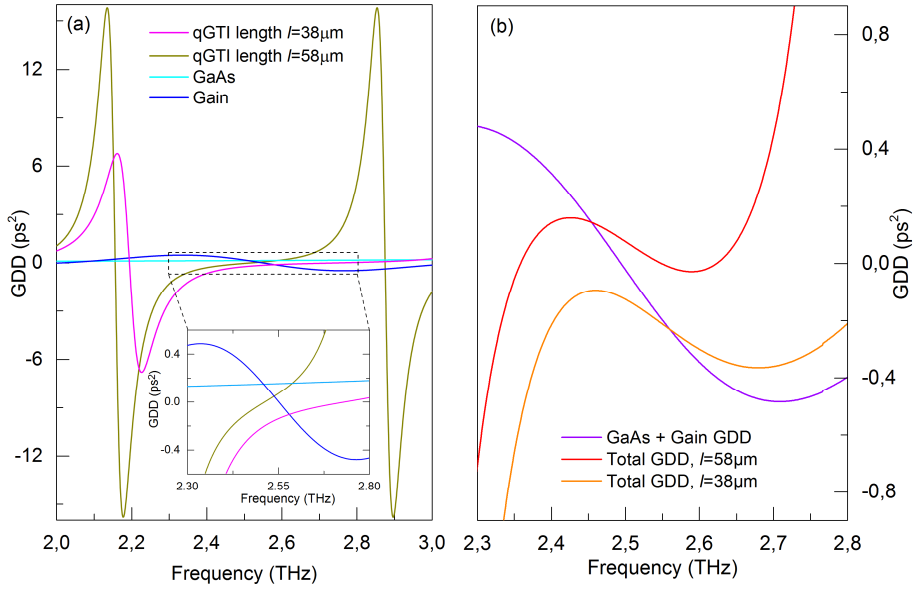

Fig 6.15 | Dispersion calculation for the QCL "L1194" with integrated coupled cavity. (a) The calculated GDD curves for gain dispersion (blue), material dispersion (cyan), q-GTI dispersion (dark yellow for the 58 µm q-GTI and magenta for the 38 µm q-GTI), respectively. (b) The total dispersion curves of this QCL for no q-GTI (purple), a q-GTI length of 38 µm (yellow) and 58 µm (red), respectively.

Fig. 6.15 (a) shows the individual GDD contributions from the q-GTI (with 58 µm and 38 µm lengths that are used in the experiments) from the above expression, the GaAs material, and the gain. The material GDD is obtained from the dispersion relation and the gain GDD is calculated from the Kramers-Kronig relation [129]. The latter is modelled with a gain of 15 cm^{-1} with a Gaussian-distributed bandwidth of 600 GHz at a centre-frequency of 2.5 THz. The gain GDD provides a zero-crossing at the centre-frequency and clearly dominates over the positive GaAs material GDD. As depicted in Fig. 6.15 (a), the GDD of the 58 µm q-GTI is negative below 2.55 THz, close to the centre-frequency of the gain (at 2.5 THz), and positive

above it. In contrast, a 38 µm q-GTI only provides negative GDD in the investigated region. Finally, Fig 6.15 (b) shows the sum of the gain and the material GDD compared to the total GDD with the q-GTIs. Remarkably, the total GDD is approximately flat and close to zero in the region from 2.4 to 2.7 THz for the 58 µm q-GTI, while it is entirely negative for the 38 µm GTI.

Therefore, a GTI with a non-ideal reflectivity can be realised using the QCL material itself. Furthermore, by designing the correct length of the GTI (58 µm for emission around 2.5 THz), the q-GTI can be used to compensate the dispersion induced by the gain profile and hence realise ultrashort stable THz pulses when mode-locked. Remarkably, a broad bandwidth of the GDD compensation is achieved by exploiting both the positive and the negative GDD regime of the q-GTI, thus compensating positive and negative gain GDD simultaneously. This dispersion compensation of the q-GTI will contribute to the generation of much shorter THz pulses. These simulations are in agreement with the observations in the previous section of L1194 with a 58µm short cavity that showed low dispersion in the beatnote and much shorter pulses when compared to a standard QCL. Furthermore, preliminary measurements were performed on a QCL with a 38µm cavity, where the beatnote showed a very wide peak indicating a large dispersion as in the simulations.

Regarding the results on 3.25 THz QCL L857, it possessed a short cavity length of ~20µm. This cavity length has a GDD profile similar to the 58 µm cavity for L1194 but with a GDD that crosses zero at 3.2THz i.e. close to the QCL emission. This cavity length therefore compensates for the dispersion at 3.25 THz. This is shown in Fig. 6.16 which illustrates the GDD of the q-GTI as a function of frequency with the crossing point between negative and positive GDD at 3.2THz. For comparison, the mode-locked spectrum (intensity) is shown. Furthermore, the beatnote of this sample was considerably narrower than a QCL without short section indicating that dispersion was reduced (see section 6.4).

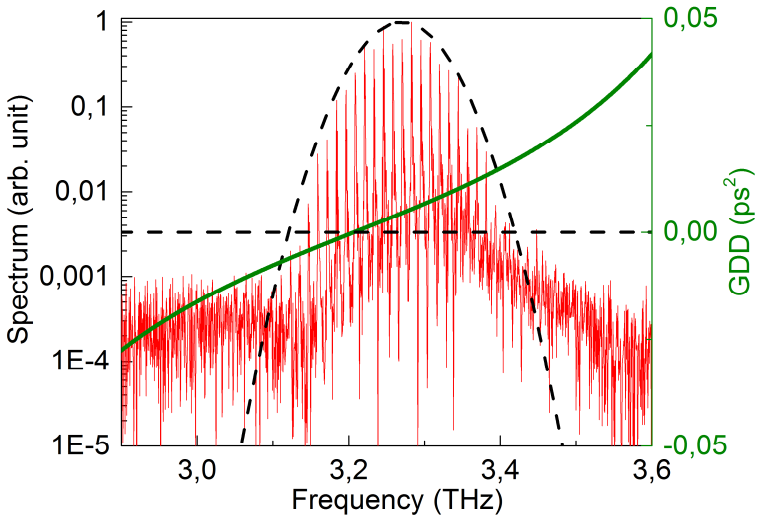

Fig 6.16 | GDD calculation for a 20µm long short GTI cavity (green curve). The intensity profile of the mode-locked pulses from a 3.25 THz QCL is shown for comparison.

6.5.3 Hybrid mode-locking introduced by air gap

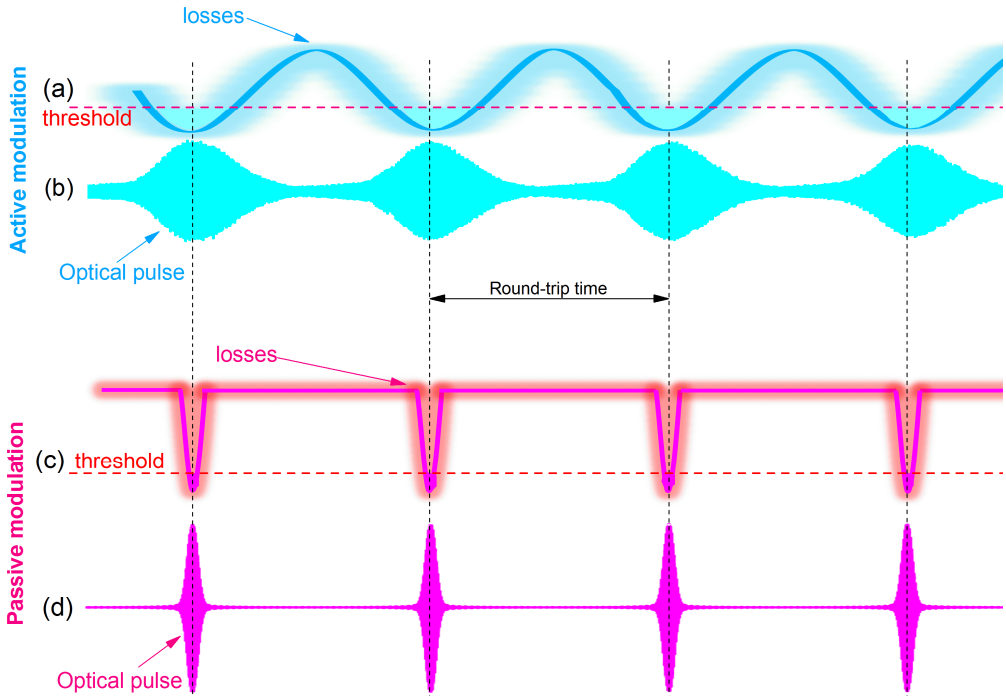

Fig 6.17 | Schematic diagram for active and passive modulation on the loss curves of lasers. (a) sinusoidal-shape active modulation on the loss of QCLs as a function of time. (b) THz pulses from sinusoidally modulated QCLs. (c) sharp passive modulation on the loss of QCLs as a function of time. (d) THz pulses from sharply modulated QCLs.

Dispersion compensation was mentioned above as a hypothesis to generate shorter pulses when the QCL is active mode-locked. However, as a sinusoidal active modulation is always applied, this will at some point limit the pulse width that can be attained [1] [96] [130]. Here the air-gap introduced by the coupled cavity could have a role as discussed below.

How can the air gap break the limitation of active mode-locking and dramatically shorten the THz pulses? Let's suppose that there is an actively mode-locked broad (~10 ps) THz pulse propagating back and forth in the laser cavity. After each round-trip, the THz pulse will pass through the small air gap where a part of the THz power will scatter out from the cavity owing to the reduced modal confinement between the long and short section as shown previously in Fig 6.4, a loss of 60% of the total power is observed from the LIV curves. This will also be shown by electromagnetic simulations of the coupled cavity (see below). The losses from the air gap will automatically introduce a passive modulation on the QCLs at exactly the round-trip frequency of THz pulse. If the passive modulation can be confirmed to be sharper and faster than the sinusoidal active modulation, it can result in much shorter/faster THz pulses. Below, I will show that the passive modulation introduced by this air gap is real much faster than active modulation.

For active mode-locking, the round trip of the sinusoidal gigahertz modulation is about 76 ps for a ~3-mm-long cavity as schematically shown in Fig 6.17 (a). This smooth modulation on the loss (or gain) of the QCLs will consequently lead to quite wide (~10 ps observed in our experiments) pulses as demonstrated in Fig 6.17 (b). For a passive modulation introduced by the air gap, the modulation duration will be roughly proportional to the time the THz pulse needs to pass through the air gap. If we suppose the THz pulse is infinitely short and crosses the air gap at the speed of light in vacuum, it will take $t = l_{gap}/c_0 = 2\mu m/3\times10^8$ m/s ≈ 10 *fs* to completely traverse the gap. However, as the THz pulse propagating in the cavity is ~10 ps, orders of magnitude wider than ~10 *fs*, the traversal time becomes approximately equal to the THz pulse width of ~10 ps (traversing the air gap from the rising edge of the THz pulse to its falling edge). Therefore, the passive modulation at each round trip lasts only ~10 ps in our case, and much faster than the 76 ps sinusoidal electrical modulation for active mode-locking [27], as illustrated in Fig 6.17 (c). This sharper and faster modulation on the loss (or gain) of QCLs will dramatically result in much shorter THz pulse trains as shown in Fig 6.17 (d). In other words, as lasers will operate in the mode with the lowest losses, the air gap, together with the laser feedback, will force the THz pulse in the cavity to be shortened.

Passive mode-locking is the most promising technique to break the pulse limitations set by active mode-locking and to deeply modulate the gain loss (gain) of laser for ultrashort THz pulse generation [131] [132]. But passive mode-locking by itself does not permit pulse generation from THz QCLs owing to their ultrafast gain recovery time, as mentioned previously. However, if we combine active mode-locking (to generate the THz pulse) and the air-gap introduced passive modulation (to introduce a faster modulation), together as mentioned above, this can result in shorter pulses. In other words, the bottlenecks of active mode-locking (i.e. smooth electrical modulation) and passive mode-locking (i.e. ultrashort gain recovery time) can be broken simultaneously and this will consequently result in ultrafast THz pulses from QCLs as we have seen in the experiments on “L1194” and “L857”. Combining active mode-locking and passive modulation together to generate ultrafast THz pulses is here called ‘‘***hybrid mode-locking***’’.

One of the most important factor in this hybrid mode-locking hypothesis is to make sure there are losses scattering out from the air gap (1.5µm for “L1194” and 2.5µm for “L857”). This has been experimental demonstrated by the LIV curves for L1194 in Fig 6.4. In order to computationally verify this and further show how the losses scatter out, the intensity distribution of THz waves travelling in the Fabry-Pérot cavity was stimulated in frequency domain using COMSOL Multiphysics (RF module). These computations based on finite element analysis via physically meshing the active region and metal waveguide were carried out on 3D models for a 3-mm-long 10-µm-thick rectangle cavity at 2.5 THz respectively with a 1 µm and 10 µm wide air gap as illustrated in Fig6.18. The *x* axis represents the cavity length and the *y* axis represents the ridge width. With the large gap we observe that the two section are barely coupled while for the small gap the shows a good coupling between the sections but with less power in the short section. This shows that even with a small gap, some power is lost between the two sections. This simulation confirms that there is a strong scattering of THz

waves from the subwavelength Fabry-Pérot cavity into free-space at the air gap, as observed in the loss of power in the LIV characteristics.

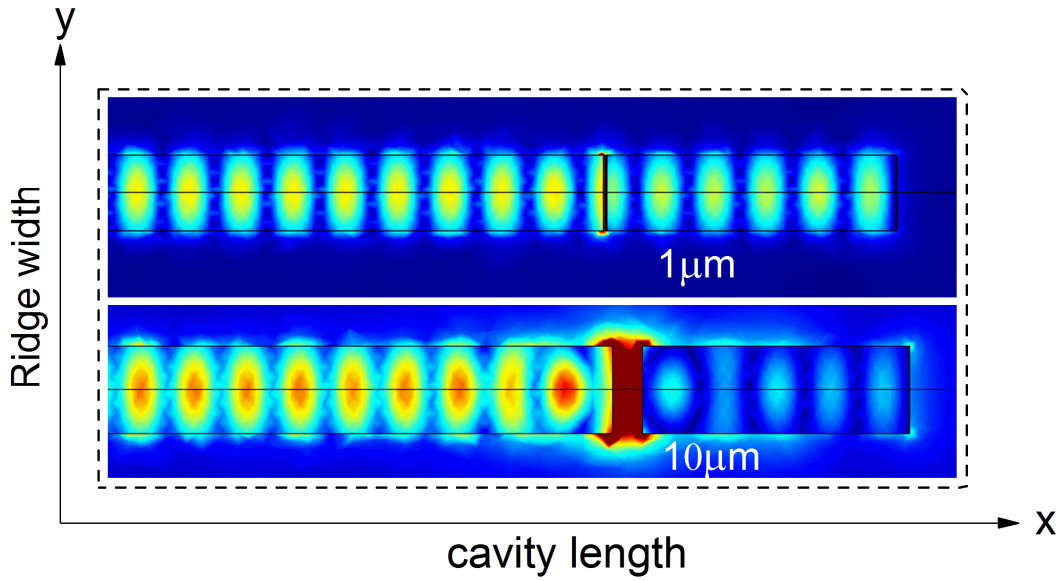

Fig 6.18 | Eigen-mode distributions of THz intensity in metal-metal waveguide QCLs around the passive structures designed for hybrid mode-locking. (Above: with an air gap of ~1 μm wide. Below: with an air gap of ~10 μm).

For the sample "L1194" used for hybrid mode-locking in section 6.3, its air gap is roughly 1.5 μm (small section ~ 58 μm) while for the hybrid mode-locking of the QCL "L857", the air gap is ~2.5 μm (small section ~20 μm), respectively. The role of the length of the small section was described in the dispersion compensation above. In both of the two cases presented above, similar results are obtained as demonstrated in section 6.3 & 6.4. This indicates that the shortening mechanism does not depend on the size of air gap (at least in the range of a few microns). This is because the size of the ~10-ps THz pulse translated in space is l=10 ps × 3×10^8m/s÷3.6≈1 mm, which is much larger than the size of the air-gap. So the time for the THz pulse passing through the passive structure doesn't depend on its size when it is much shorter than 1mm. This makes the passive modulation always at the scale of the active mode-locked THz pulse duration (~10 ps) within a round-trip time of ~76 ps. Therefore, the pulse width from hybrid mode-locking doesn't depend on the size of the air-gap as observed in the experiments on "L1194" and "L857".

In addition, this hypothesis can also explain why THz pulses are already formed on "L857" even without active modulation, shown in Fig 6.10, while this cannot be observed on "L1194". This is because the air gap of the "L857" is wider than that of the "L1194", which makes the loss of the "L857" much stronger and therefore the passive modulation of "L857" will be stronger (but importantly not faster). This strong passive modulation will start to generate THz pulses. However, the gain recovery time of THz QCLs is very short, leading to double pulses

within a round-trip. However, combining active modulation with the passive modulation allows a single pulse behavior.

To conclude, the hybrid mode-locking hypothesis can explain the phenomena observed in the experiments and is possibly combined with the dispersion compensation hypothesis of the short section that dramatically shorten the THz pulses down to sub-5 ps. Further experiments will be performed to conclusively prove this, for example, using "***second order hybrid mode-locking***". This can be realized by engineering a second air gap on the monolithic QCL chip to further shorten this ~5 ps down to sub-picosecond level.

6.6 Conclusion and perspective

The THz pulse width generated by active mode-locking of THz QCLs has been strictly limited by long pulse widths despite large gain bandwidths, as demonstrated and discussed in previous chapters. In order to break this limitation of active mode-locking, we integrated a coupled cavity onto two sets of QCL with a ~2-µm air gap and a ~20-60µm short cavity, permitting to overcome this bottleneck and generate ultrafast THz pulses. The structures were integrated monolithically with the QCL laser cavity, resulting in compact system. Two hypotheses based around dispersion compensation and hybrid modelocking have been discussed to explain the shortening mechanism. A combination of both effects cannot be ruled out with and will be the subject of further investigations.

This new technique has dramatically more than halved the previous pulse record of ~10 ps to sub ~5 ps and drastically broadens the frequency comb to ~350 GHz. This experiment is the first demonstration that THz pulses can be greatly shortened by mode-locking THz QCLs and dispersion compensation. From this point, it should be possible to further shorten these THz pulses from mode-locked QCLs down to sub-picosecond. This could open important applications in both scientific and industrial domains with new passive structures based on the same principle. This will be especially important for dual-comb spectroscopy [133] where the lack of tunability of the QCL emission can be avoided.

This works opens up exciting research directions where we can further shorten the THz pulses potentially down to the sub-picosecond and even the single cycle pulse level. THz QCLs have been shown to have bandwidths exceeding 1 THz using heterogeneous designs, and the q-GIT concept can be modified to compensate for slightly larger bandwidths. If the compensation is not sufficient, other concepts (e.g. chirped mirrors or reflectors) that have been employed in the optical domain and for THz QCL frequency combs can be adapted for short pulse generation. Regarding the proposal of passive modulation introduced by the air gap between the coupled cavity system to realize a hybrid mode-locking scheme, this can be also used to further shorten the THz pulse using a second order hybrid mode-locking scheme. This would be realized through engineering a second air gap on the QCL ridge based on the same principle. This would add a further modulation to further shorten the 5-ps THz pulses.

There are also considerable other potential schemes that may allow to realize short THz pulses from QCLs. Among them, is the use of a THz saturable absorber with a nonlinearity, for example graphene, on one of its facets to shorten the THz pulses via hybrid mode-locking, avoiding the associative problems of the fast gain recovery time. This can be combined with on-chip dispersion compensation schemes to realise ultrafast THz pulses.

7

Far-field Engineering of Metal-metal Waveguide Terahertz Quantum Cascade Lasers

As discussed in previous chapters, THz QCLs have developed significantly since the first demonstration in 2002. Nowadays, the most performing THz QCLs in terms of temperature, are those based on metal-metal (MM) waveguides, and can already operate up to ~200K [48]. The sub-wavelength waveguides of these QCLs are structured with the thin active region sandwiched between two metal layers. This results in a high modal confinement of the THz waves compared to single plasmon QCLs, which operate at relative lower temperatures [44]. However, the far-field patterns of MM QCLs are highly diffracted and output powers are weakly coupled out, owing to large impedance mismatch between the strongly confined cavity mode and free-space radiative mode [118]. These shortcomings prevent many important applications of THz QCLs beyond liquid nitrogen cooling temperatures.

The aim of this chapter is to overcome these bottlenecks mentioned above. I will show that the far-field emission profile of THz QCLs in metal-metal waveguides is controlled in directionality and form through planar horn-type shape structures, whilst conserving a broad spectral response for applications in THz pulse and frequency comb generation (see chapters 5 and 6). These structures produce a gradual change in the high modal confinement of the waveguides and permit an improved far-field emission profile and resulting in a four-fold increase in the emitted output power. The two-dimensional far-field patterns are measured at 77 K and are in agreement with 3D modal simulations. The influence of parasitic high order transverse modes is shown to be controlled by engineering the horn structure (ridge and horn widths), allowing only the fundamental mode to be coupled out.

Chapter 7

7.1 Beam profiles of metal-metal THz QCLs

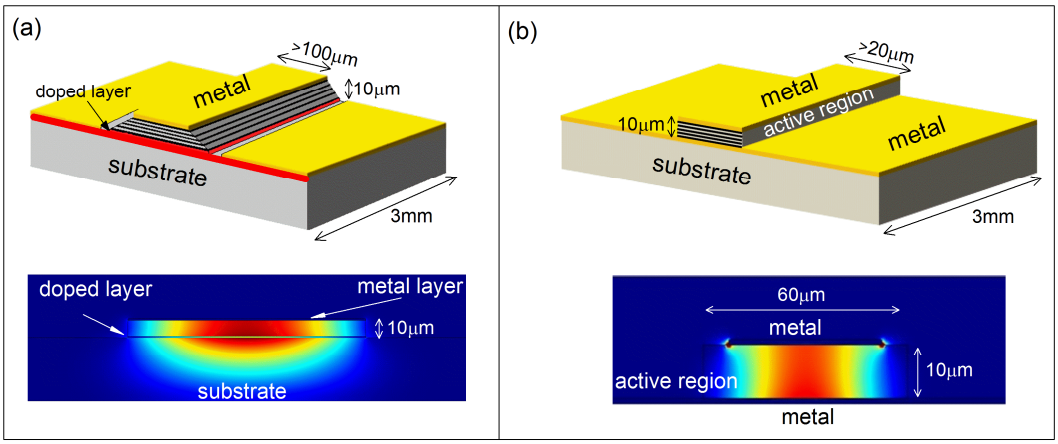

Fig 5.1 | Schematic diagrams of THz QCLs and their typical two-dimensional intensity distributions in a cross-section view for (a) Single-plasmon waveguide THz QCL and (b) Metal-metal waveguide THz QCL.

As presented in former chapters, THz QCLs have undergone considerable improvements in operation since their first demonstration [20], especially in terms of the achievable output power [51] and operating temperature [48]. However, typically these two parameters cannot be optimized simultaneously in a given QCL device. The highest temperature operation of ~200 K has been demonstrated through use of metal-metal (MM) waveguides, where a high modal gain is achieved through the high modal confinement. The detailed description of MM waveguides and single-plasmon (SP) waveguides have been presented in section 1.3.3 in the first chapter. Here, I will give a brief comparison again on these two types of waveguides as they have a dominating influence on the far-field patterns of THz QCLs. The schematic diagrams of THz QCLs based on SP and MM waveguides are shown in Fig 7.1, (a) & (b), respectively. In this figure, the waveguide structures of a typical SP QCL and MM QCL are shown in top part and the intensity distributions of the fundamental mode TM_{00} are shown in the bottom part. We can see that the THz mode of MM QCLs are strongly confined to the active region compared to SP ones (simulated by COMSOL Multiphysics at 3 THz). The confinement factor Γ, given by Eq. (1.4), of SP QCLs ranges from from Γ = 0.1 - 0.5 depending on doped layer while for MM QCLs, it is generally as high as $\Gamma \approx 1$ [44].

When the strongly confined THz mode ($\lambda \approx 100$ μm) within a MM cavity (40 μm ×10 μm) is coupled into a free-space propagating wave, the impedance mismatch between the cavity and air becomes of great importance. This results in a highly diffracted laser beam and a large facet reflectivity leading to weak directionality and low output powers, respectively, as measured by *W. Maineuit et al* [105] at University of Paris 7 and reproduced in Fig 7.2 (a) (Similar work has also been done at MIT). In this measurement, a MM QCL was placed in a cryostat and a Goley cell rotated around it on a spherical plane (coordinates $\theta, \phi, r \approx 10cm$). When θ was

varied from 0° to 110° and ϕ from -50° to 60°, the far-field pattern of this metal-metal QCL could be measured, characterized in 2D as shown in Fig 7.2 (a) right. We can see that the far-field pattern of MM waveguide QCL is highly divergent ($0° < \theta < 100°, -50° < \phi < 50°$) and the intensity fringes are widely distributed in the spherical plane due to interference between coherent THz waves radiated from the 2 out-coupling facets (each facet acting as a radiating dipole) while the far field pattern of SP waveguide QCL is considerably less diffracted ($20° < \theta < 20°, -20° < \phi < 20°$)) as illustrated in Fig 7.1 (b) [50]. Although SP waveguides have shown output powers of up to 1 W, such QCLs are typically limited to operate at temperatures below 77K. Therefore, in order to apply THz QCLs to applications, for example ultrafast pulse generation at high temperatures, the far-field patterns and radiated powers of metal-metal QCLs need to be improved.

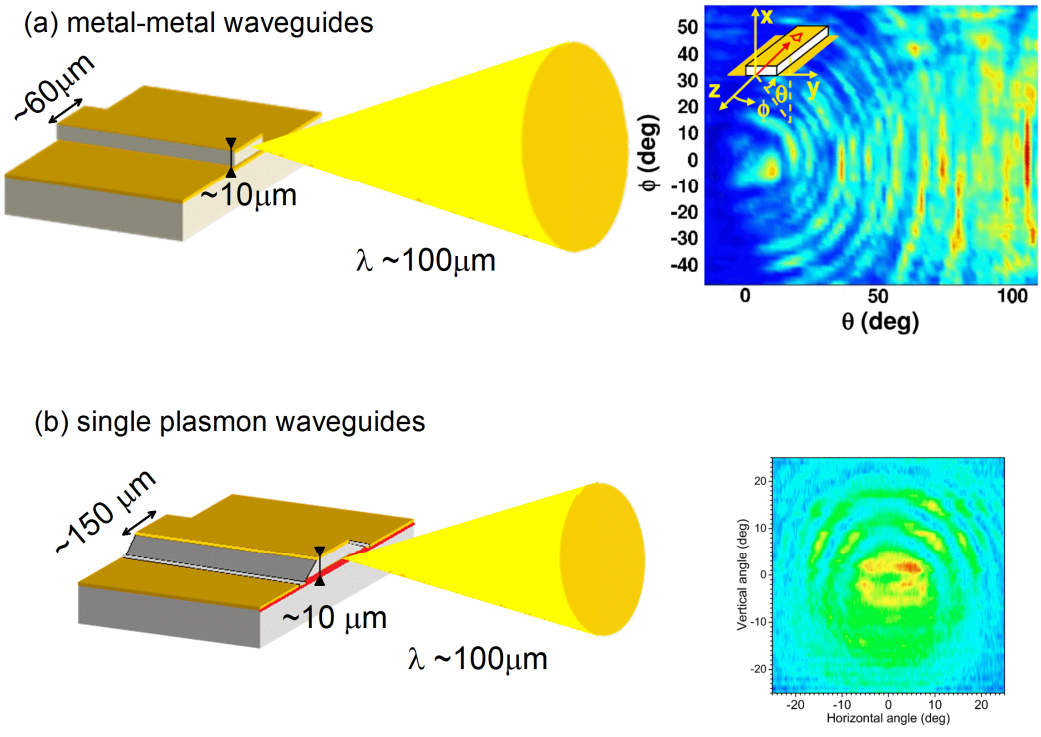

Fig 7.2 | (a) Highly diffracted far field of THz QCLs coupled out from sub-wavelength metal-metal cavity. [Measured far-field pattern at right side in (a) is from: *W. Maineuit et al, Appl. Phys. Lett. 93. 183508 (2008)*]. (b) Less diffracted far field pattern of THz QCLs coupled out from single plasmon cavity. [Measured far-field pattern at right side in (b) is from: *M. Hajenius et al, Opt. Lett. 33, 312 (2008)*].

7.2 State of the art for far-field pattern improvements

There has been a wide variety of techniques on extracting the power and low-divergence far-field patterns from MM QCLs. The following gives a few examples and is a non-exhaustive list.

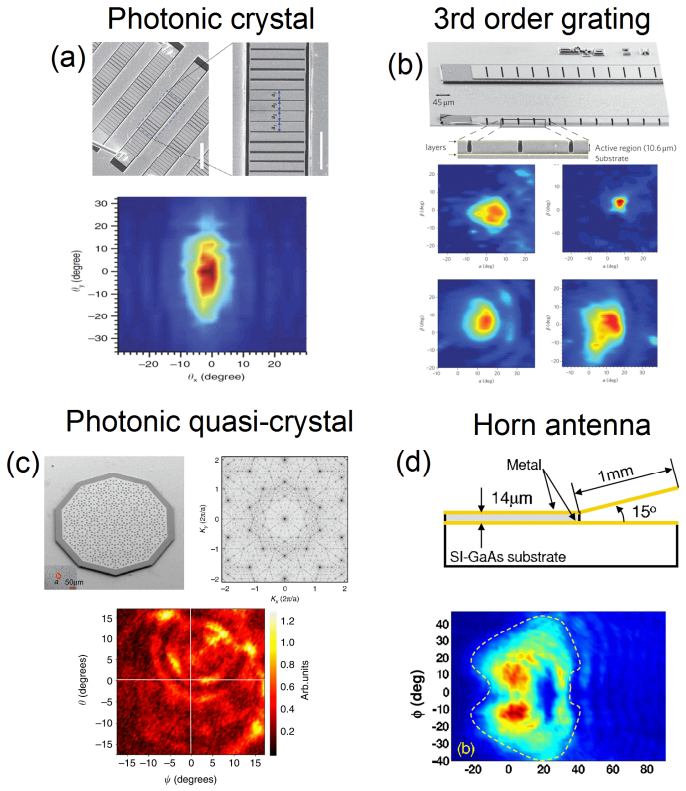

Fig 7.3 | Improved far-field of metal-metal QCLs by different methods (a) photonic crystal [From: *G. Xu et al, Nat. commun, 3, 952, (2012)*] (b) 3rd order grating [From: *M. I. Amanti et al, Nat. Photonics. 3, 586 (2009)*] (c) Photonic quasi-crystal [From: *M. S. Vitiello et al, Nat. commun, 5:5884 (2014)*] (d) Suspended horn antenna [From: *W. Maineult et al, Appl. Phys. Lett. 93, 183508 (2008)*]

In order to improve the highly diffracted patterns and poorly out-coupled powers of metal-metal THz QCLs, several monolithic methods based on photonic structures for surface emission have been proposed and realized. An example of this is illustrated in Fig 7.3 (a) [134] [135], which is based on graded photonic hetero-structures. Here the symmetric mode of a distributed feedback surface-emitting semiconductor laser could be localized in the device center while its anti-symmetric one would be confined close to laser facets. Application of this concept to MM THz QCLs led to high peak-power surface radiation and low-divergence, single-lobed far-field patterns.

Other powerful demonstrations have exploited 3rd order DFB gratings for emission along the ridge length as is demonstrated by *Amanti et al* at ETH Zurich in Fig 7.3 (b) [57] [136]. It

is based on end-fire antenna effect and permits controlled and narrow far field patterns. Although these techniques can extract the QCL power and engineer the far-field emission profile efficiently, they are inherently mono-frequency and not suitable for broadband emission that would be of interest to mode-locking [24] [25] [27] or frequency comb [28] generation applications.

In addition, 2D photonic quasi-crystal QCLs have been demonstrated by M. Vitiello *et al* [137]. This 2D scheme solved the problem of power cancellation and significantly improved the far field pattern of THz laser.

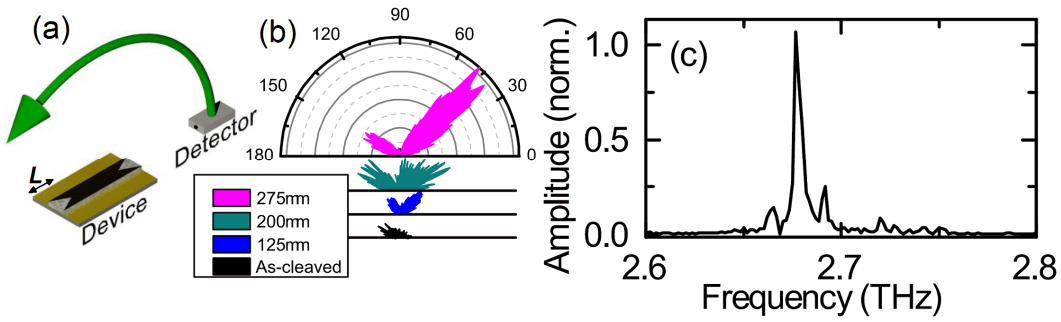

Fig 7.4 | (a) A schematic diagram showing the method of far-field measurements. (b) Far-field emission plots. (c) Emission spectrum of QCL measured by injection seeding. [From: *Brewer et al, Appl. Phys. Lett. 104, 081107 (2014)*]

There are also some methods to improve the far-field patterns of MM QCLs without disturbing their broadband properties. Most of them, however, have relied on manual positioning of external elements such as silicon lenses placed on the facet [138], suspended antenna structures [105] or rectangular waveguides [139]. For example, in Fig 7.3 (d), the horn antenna is attached to the end of a THz waveguide, and will guide out-coupled THz waves into free-space, gradually changing the confinement and wave impedance. In this way, the far-field can be improved as is presented in Fig 7.3. However, owing to the manual nature, the techniques have proved to be difficult or non-reproducible when thermally cycled.

A promising technique has been recently demonstrated in our group at École Normale Supérieure in collaboration with the University of Cambridge, in which planar horn-like structures (PHSs) are etched into the QCL surface metal layer, so that the confined mode is better matched to a radiative mode as shown in Fig 7.4 [118]. (a) illustrates the method to measure the far-field of this QCL device with PHSs using a Golay cell on a rotating arm. (b) shows the measured THz power as a function of the rotated angle of THz detector around the QCL for different PHSs length L as defined in Fig 7.4 (a) (varied from 0 µm to 275 µm) showing greater out coupled power with increased PHS length. (c) is the emission spectrum obtained by injection phase seeding. This simple approach has led to a considerable improvement in directionality and output power without significantly affecting the QCL

temperature performance, and has proven to be inherently stable. Indeed, injection seeding [67] of bound-to-continuum MM QCLs with PHS have been recently demonstrated [118]. However, no control of the far-field profile was demonstrated with only one-dimensional profiles of the far-field measured. Further the emitted spectrum from the PHS was not shown to be broadband owing to the use of low spectral bandwidth active regions. In this work, we demonstrate how the far field emission profile can be controlled by engineering the QCL's transverse modes and the geometry of the PHS, as well as showing the broadband nature of the emission. We further show two-dimensional far-field patterns that are in good agreement with electromagnetic simulations.

7.3 Far-field pattern and out-coupling power improvements of metal-metal THz QCLs

7.3.1 Sample designs and fabrications

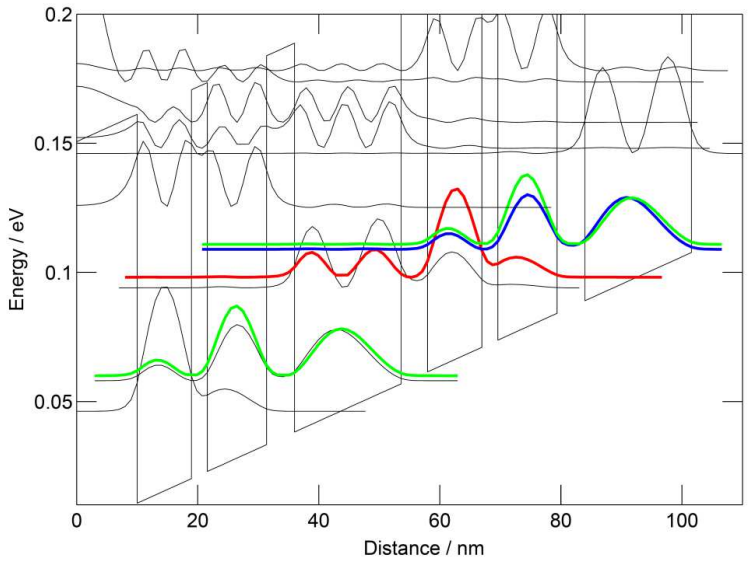

Fig 7.5 | Band structure of QCL based on longitudinal phonon depopulation with emission frequency centered at 3.1THz and full bandwidth around ~500 GHz.

In this chapter, QCLs with a central frequency at 3.1 THz and a full spectral bandwidth of ~500 GHz were used (wafer number ‘‘*L958*’’). This employed an active region design based on longitudinal optical phonon depopulation with the GaAs materials system and detailed previously in chapter 1. The thicknesses of quantum wells and barriers of the active region starting from injector are: **4.10**/*8.20*/**2.50**/*8.90*/**4.30**/*16* nm. Barriers are shown in bold and quantum wells are shown in italic. The quantum well with a thickness of 17.6 nm were divided into 3 parts (6.1/5.5/6.0 nm) with the 5.5-nm doped layer at the level of 5×10^{16} cm−3. These designs have the highest temperature operation (greater than 140 K) when placed in a MM waveguide, and allows the QCL to be operated at liquid nitrogen temperatures. The designs also possess an inherently large gain bandwidth, ideal in illustrating the broadband nature of the PHS. Fig 7.5 shows the wave-function distributions of electrons in one period of quantum wells and barriers in our design and is similar to sample “L1074” and “L1194” detailed in chapter 5 & 6. The growth was performed at the University of Leeds, UK by MBE followed by standard MM processing at University of Paris-South (France). The metal-metal wafers were processed with laser ridge widths of 40 μm, 60 μm and 80 μm, and cleaved into cavity lengths of 3 mm, 2 mm and 3 mm, respectively.

7.3.2 Planar horn-like structure design, processing and optimization.

The Planar horn-like structures (PHS) were realized by post processing through the use of focused ion beam (FIB) milling to remove the top metal layer (performed at the University of Leeds). A schematic is shown in Fig 5.6 (a) left. Fig 7.6 (a) right is the SEM images of post-processed QCLs. This gradual removal of metal allows the strongly confined mode to gradually adapt into a propagating beam, reducing the facet reflectivity, and therefore resulting in a higher output power and a directional far-field pattern. Fig 7.6 (b) is the THz intensity distributions, simulated by COMSOL Multi-Physics in 3D, of the QCLs with integrated PHSs. In this simulation, the THz wave is injected into the cavity from the left facet and coupled out from the right facet. The mode distribution is the convergent solution of this structure using finite element analysis. The simulation "P_1" is a top view of the ridge and the simulation "P_2" is viewed at the end of the PHS position ("P_2" in (a)). The latter shows that the THz waves are less confined around the PHS and some powers are coupled out into the radiative free space mode.

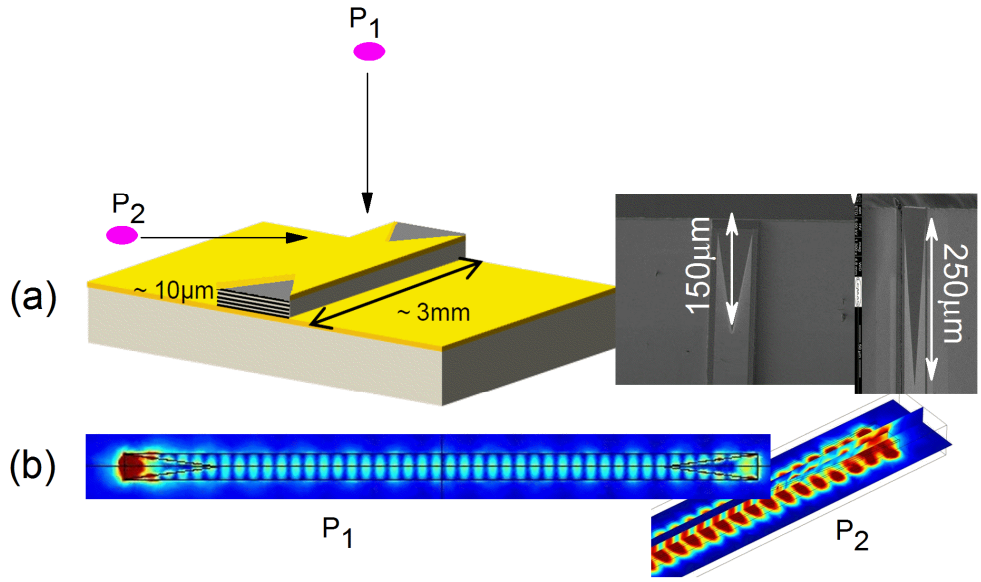

Fig 7.6 | (a) Schematic diagram of metal-metal QCLs with planar horn-like structures [left]. Scanning Electron Microscope photos of this kind of QCLs. (b) Intensity distributions and variations in QCLs with planar horn-like structures simulated by the RF module of COMSOL Multi-Physics.

Generally, the longer the horn structure length, the larger the output power and the more directional the beam, owning to the slower change and better impedance adaptation. However, a long PHS results in higher effective mirror losses and an increase in laser threshold, as detailed in ref [118] and could thus prevent laser action. Here a horn length of 150 μm was chosen as a compromise between high output power and high operating temperatures.

7.3.3 Light-Current-Voltage characteristics of QCL pre- and post- processes

The LIV curves allow us to investigate the key parameters of a laser such as threshold, output power, operation current as presented in former chapters. Here we used these curves to characterize our QCL pre- and post-FIB processes. The detailed experimental configure is presented in Fig 7.7: A Golay cell is employed as THz detector; A f/1.67 parabolic mirror was used to collect the output radiation from the QCL, and a f/2 parabolic mirror used to focus it onto the Golay cell.

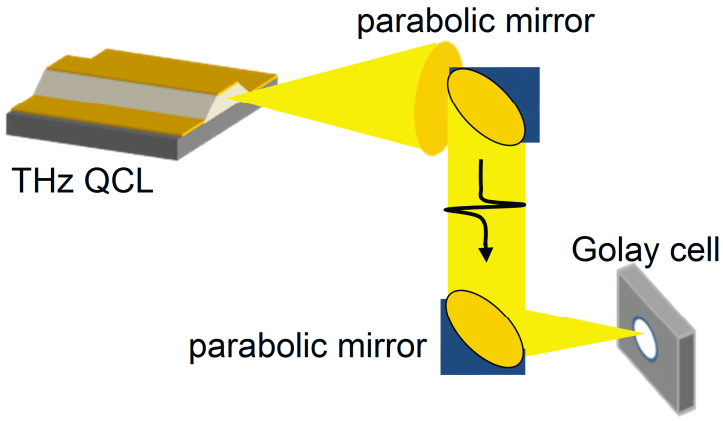

Fig 7.7 | Experimental set-up for light-current-voltage (LIV) cures measurement

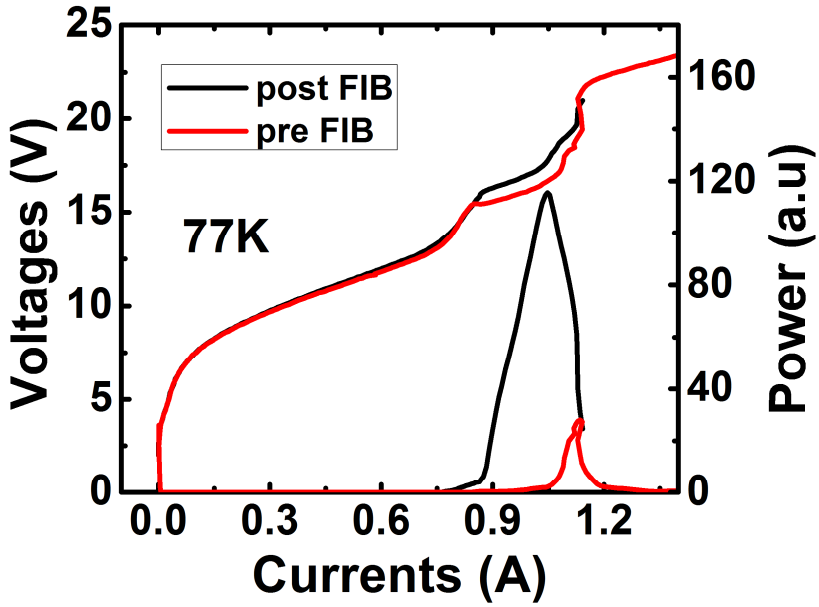

Fig 7.8 | Light-Current-Voltage curves (LIV) of QCL pre-FIB process (red) and post-FIB process (black) at 77K.

Fig 7.8 shows the output light-current-voltage characteristics of an 80-μm-wide ridge pre- and post-FIB milling, with the QCL at 77 K. The QCL was operated in pulsed mode with 500-ns-long electrical pulses at a repetition frequency of 50 kHz. A 20 Hz electrical envelope modulation was used to enable lock-in detection of the output power with the Golay cell detector. A factor of four-fold increase in measured output power was observed for the QCL incorporating the horn (post FIB). This increase is partly due to a reduced facet reflectivity. The threshold currents of the pre- and post-FIB sample (from the change in differential resistance in the V-I curve) are 0.849 A and 0.875 A, respectively, corresponding to a reduction in reflectivity from approximately 0.8 to 0.65, respectively, with a calculated waveguide loss of 22 cm^{-1} (see below). This reduction in reflectivity would only result in a two-fold increase in output power, and so does not account for the four-fold increase observed. (The L-I was not used to determine the threshold owing to a small overshoot in time of the electrical characteristics, resulting in the threshold in the light emission appearing smaller for the horn structure sample. The V-I is taken over a large time window that does not include the electrical overshoot and is therefore more robust to determine the laser threshold). The remaining 2-fold increase of output power comes from improved directionality of far-field of QCL with PHSs. With a far-field that is more directional, the first parabolic mirror can collect more power. Therefore, the LIV characteristics of pre- and post-FIB QCLs can show that the output power is improved and indicates a more directional far-field. However, direct demonstration of the latter will be discussed in detail from the measured and simulated far-field patterns in following sections.

7.3.4 Transverse mode control of metal-metal THz QCLs

The far-field pattern is the intensity distribution of the QCL's emission at long distances ($\gg \lambda$) from its output facet. It is determined by the output facet (shape and size), transverse mode (intensity distribution at output facet) and the medium in which it propagates. An example of a simulated far field pattern is indicated in Fig 7.9. In our case, the propagation medium (free-space: air) and the laser material) is fixed. The only 2 variables are the waveguide mode and the facet (or ridge) width, which are also coupled. Hence, we can engineer the far-field profile of QCLs by controlling the transverse mode that propagates in QCL waveguide through modifying the ridge width.

For the fundamental mode (TM_{00}), its intensity distribution in the laser cavity is more uniformly distributed to that of a higher order (TM_{mn}, m, $n>0$) mode. When it is coupled out, its far-field should be more directional than the far-field pattern of a higher order (TM_{mn}, m, $n>0$) mode, whose intensity distribution is more emanative in cavity. Indeed, by favoring the fundamental transverse mode (TM_{00}) through choosing a suitable ridge width, we show that the far-field profile can be changed from a double (TM_{01}) to a single (TM_{00}) lobed emission. The far-fields profile of three samples were measured and simulated; an 80-μm and a 40-μm-wide ridge each with a PHS, and a 60-μm-wide ridge as cleaved.

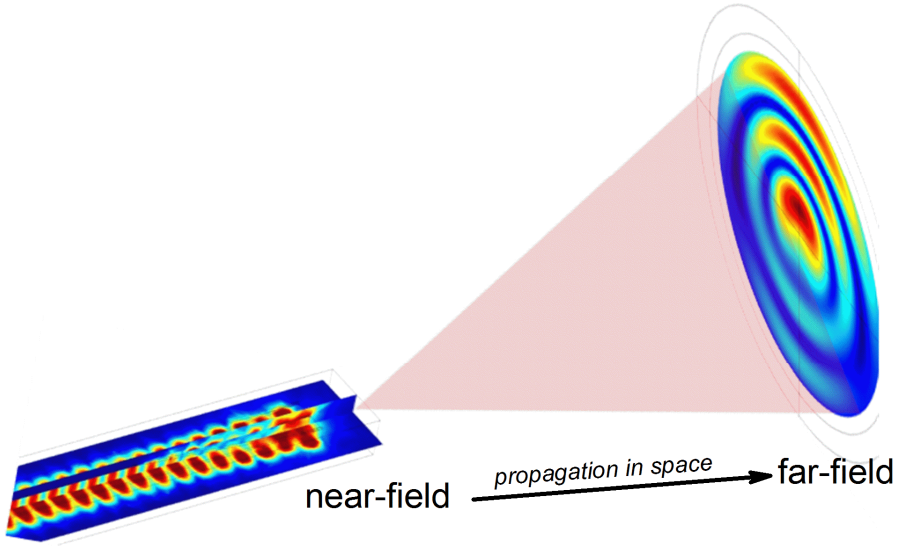

Fig 7.9 | Schematic diagram to show the relationships between far-field and transverse mode (near field) of THz QCLs.

The effect of the ridge width can be seen by a simple analysis of the modes that are permitted to propagate. For the general case of a rectangle waveguide of width a and height b with no loss, we calculate the transverse modes in the Cartesian coordinates (x, y, z) to determine which transverse modes can propagate. From Maxwell equations, the propagation constant, β, can be given by [140]:

$$\beta = \sqrt{k^2 - (k_x^2 + k_y^2)} = \sqrt{\omega^2 n^2 \mu\varepsilon - (k_x^2 + k_y^2)} \tag{7.1}$$

where n is the refractive index, ω is the angular frequency, and $k_x = m\pi / a$ and $k_y = l\pi / b$ are the wave vectors in x (horizontal) and y (vertical) directions with propagation in the z-direction. (m and l are the integer mode numbers). For a mode to propagate, $\beta^2 > 0$ and therefore:

$$(k_x^2 + k_y^2) < \omega^2 n^2 \mu\varepsilon \rightarrow (\frac{\pi m}{a})^2 + (\frac{\pi l}{b})^2 < \omega^2 n^2 \mu\varepsilon \tag{7.2}$$

For inter-sub-band transitions, the electric field polarization is perpendicular to the laser surface (transverse magnetic (TM)), and with $(l = 0)$:

$$m < \frac{\omega a n}{\pi} \sqrt{\mu\varepsilon} = 2anf \sqrt{\mu\varepsilon} = \frac{2an}{\lambda} \tag{7.3}$$

where λ is the wavelength. From Eq. (7.3), it can be seen that the number of transverse modes can be limited by reducing the ridge width a. For example, choosing a ridge less than 30 μm will result in only the fundamental transverse mode (TM_{00}) propagating.

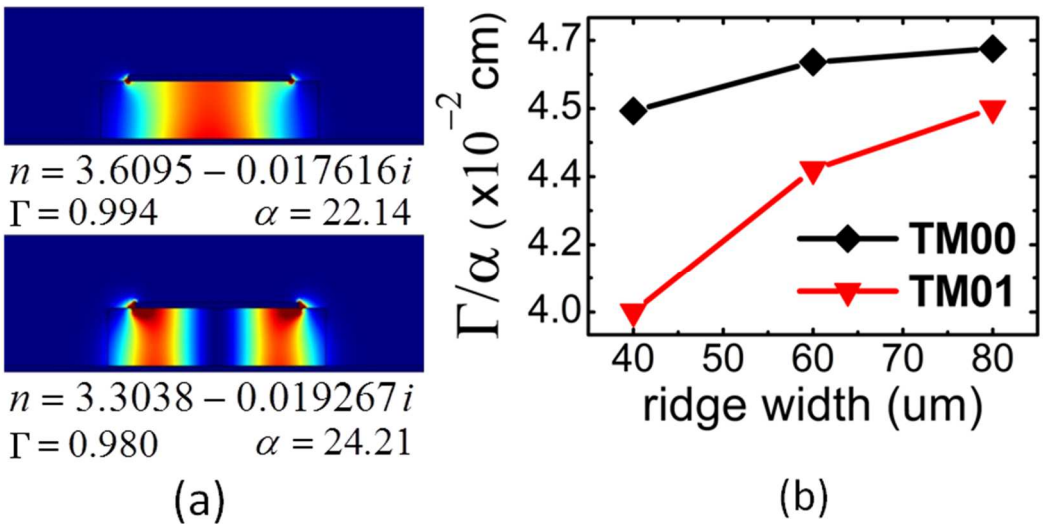

Fig. 7.10 | (a) Modal simulations of the fundamental TM_{00} (top) and second order mode TM_{01} (bottom) for a 40-μm-width metal-metal QCL. (b) The figure of merit, Γ/α, as a function of QCL ridge width for the fundamental TM_{00} (black) and second order mode TM_{01} (red).

To take into account the actual QCL structure with optical losses and the TM polarized light, simulations of the 2D waveguide modes were performed using COMSOL Multiphysics. Fig 7.10 (a) shows the mode profiles of the fundamental (TM_{00}) and second order mode (TM_{01}) at 3 THz for a 40-μm-wide ridge. The modal overlap with the active region, Γ, and the waveguide losses, α, are found to be 0.994 and 22 cm^{-1}, and 0.98 and 24 cm^{-1}, for the TM_{00} and TM_{01} modes, respectively. The modal overlap is smaller for higher order modes owing to a larger overlap with the surrounding air, and the losses increase owing to a larger overlap with the surrounding metal layers. This results in a reduction in the figure of merit, Γ/α, for higher order modes, which indicates that they are less likely to demonstrate laser action. This is summarized in Fig 7.10 (b) that shows the figure of merit as a function of ridge width, highlighting that the difference in the figure of merit between the fundamental and second order mode increases as the ridge width decreases. Therefore, we can choose a narrow ridge width to favor the fundamental mode (TM_{00}) propagating in QCL waveguides whilst removing or disfavoring others higher order modes (TM_{01}, TM_{02}…). (There are also other ways to suppress high order lateral mode by introducing ‘‘side absorbers’’ by Harvard University, which is detailed in *APL 92, 031106 (2008)*) [106].

7.3.5 Engineered far-field profiles of metal-metal THz QCLs

We show below that a more directional beam in the devices can be obtained using these horn-like structures. This can be further improved by choosing the fundamental mode through a small ridge width. These effects are directly demonstrated by the experiment and simulations of the far-field.

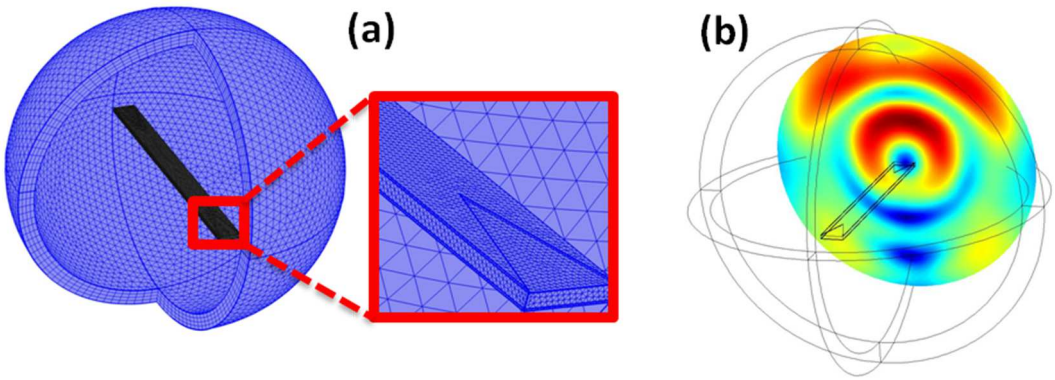

Fig. 7.11 | (a) Mesh used in air-field and QCL ridge to determine the far field emitted from the QCL. (b) Example of simulated far field projected on the air-sphere.

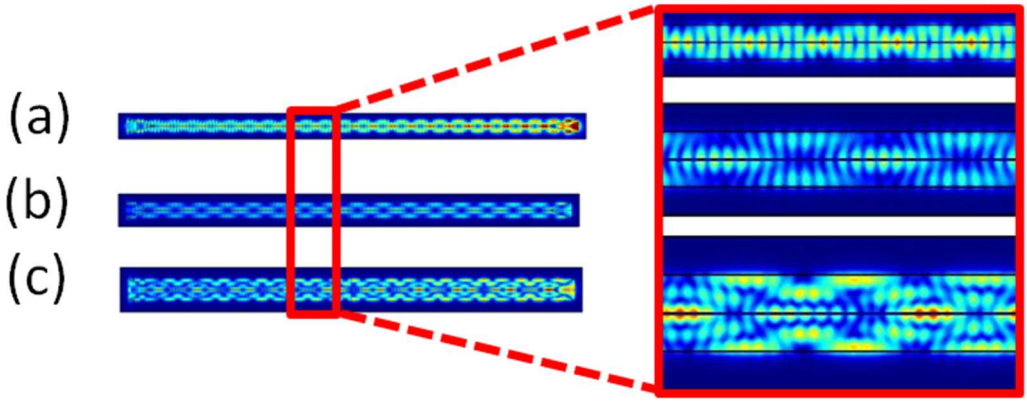

Fig. 7.12 | Top view of QCL showing transverse modes excited by a TM_{00} excitation on the right side of the ridge for 3-mm-long cavities with 150-μm-long planar triangle structures on the top metal layer on both facets. (a) Ridge width = 40 μm. (b) Ridge width = 60 μm. (c) Ridge width = 80 μm.

The far-field pattern was simulated using a finite element analysis tool (RF module of COMSOL Multiphysics). Here, the transverse modes were simulated in MM THz QCLs with a PHS on the top metal layer. The QCLs was modeled with a top metal gold waveguide layer (2 μm thick) with two 150-μm-long triangle horn shapes on each end of the laser, the active medium layer (10 μm thick GaAs) and the bottom gold metal layer (2 μm thick). The model was placed in an air sphere to determine the far-field profile with an appropriate mesh to get a good and fast convergence as shown in Fig 7.11. (As the model is described in 3D and the minimum meshing elements need to be small enough (0.5 μm) to cover all the geometry-structure detail of QCLs, the meshing element number is extremely large. For a computer with a memory of 20 GB, the computational time requires at least a few hours for only one simulation). As illustrated at the right side of the cavities in Fig. 7.12, a TM_{00} source is employed to excite the transverse modes within the cavities at right side of the ridge. Fig 7.12 (a) - 7.12 (c) shows the resulting simulations of the ridge width on the transverse modes for

ridge widths of 40 μm, 60 μm, and 80 μm. For the 40-μm-wide cavity, although the TM_{01} mode begins to appear, the fundamental TM_{00} mode still dominates. Further increases in the ridge width results in the stronger appearance of other high order transverse modes.

The measured and calculated far-field profiles corresponding to the transverse modes are shown in Fig. 7.13 (left and right side of figure, respectively). The measurements were performed at University of Paris-south with a Golay detector rotated around the QCL central axis in a spherical plane [141], the same method as utilized in section 7.1 for measuring the far-field pattern. In all cases, the QCLs were operated at a temperature of 77 K. Figures 7.13 (a) and 7.13 (b) show the far-field patterns of a 40-μm- and 80-μm-wide MM THz QCLs with PHSs, respectively. Fig 7.13 (c) shows the far-field profile from a QCL with an un-patterned ridge of width 60μm. The simulations and measurements are in good agreement, and demonstrate the effect of increasing the ridge width. As mentioned above, in the 40-μm-wide cavity with PHS, only the fundamental mode TM_{00} is present and results in a single lobed far-field profile. Compared to the 60-μm-wide un-patterned QCL (Fig. 7.13 (c)), the far-field profile is less diffracted with the power concentrated at $\theta = 10°$ and $\varphi = 15°$ (The slight difference in angle in the φ plane when compared to the simulations was a result of the QCL being mounted at a small angle on the cryostat cold finger). In the case of the 80 μm ridge with a horn structure, the QCL demonstrates laser action on a higher order mode (TM_{01}) that, as a consequence, results in a considerably different far-field profile. Indeed, the far-field shows a more diffracted double lobe pattern with $\theta = 43°$ and $\varphi = \pm 25°$ in agreement with the simulated profile.

Although the 60-μm-wide ridge can permit propagation of higher order modes, the QCL far field appears to be a result of just the TM_{00} mode, suggesting that the ridge is small enough to still favor the fundamental mode only. Although the ridge widths are different, the 2-mm-long 60-μm-wide QCL ridge has the same volume as the 3-mm-long 40-μm-wide ridge and so should have comparable output powers, which allows the effect of the horn to be determined. From the measured far-field profiles, the maximum power output of the horn coupled QCL is ~3 times greater than that of the QCL with no horn. The simulations, however, show a five-fold increase. The discrepancy could be a result of imperfections in the horn fabrication where the FIB milling can leave small metallic defects on the surface or on the quality of the cleaved facet.

From the far-fields profiles, the collection efficiency of the parabolic mirror used for the acquisition of the output power of Fig. 7.8 was determined. A horn coupled QCL would collect 28% of the total power emitted by the QCL while for the as-cleaved device, this falls to 16%. This adds to the reduction in reflectivity highlighted above for higher output power and explains the four-fold increase in power observed in Fig. 7.8.

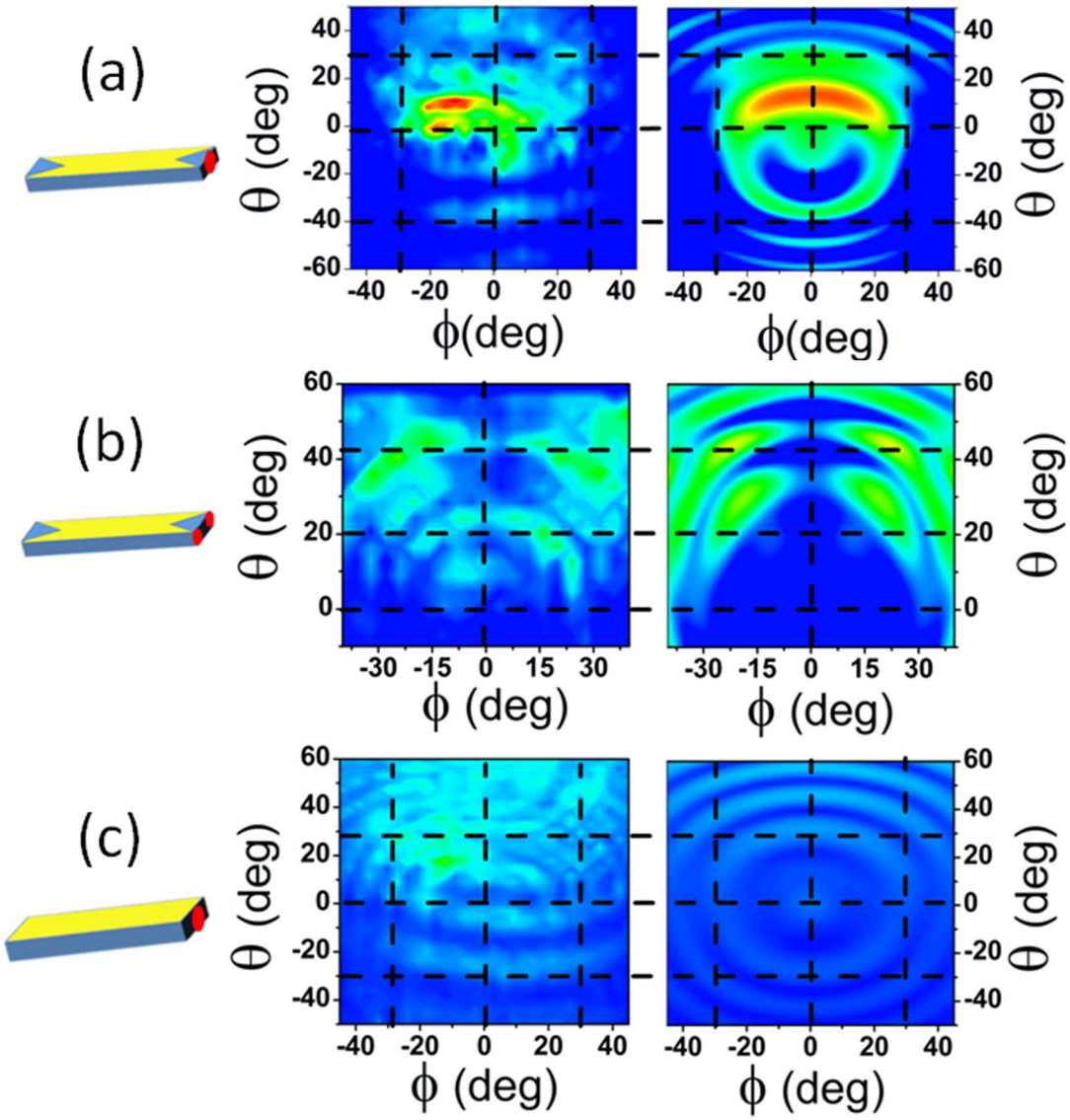

Fig. 7.13 | Simulated (right) and measured (left) far-field patterns of metal-metal THz QCLs with different waveguide structures. (a) 3-mm-long 40-μm-wide metal-metal THz QCL with 150-μm-long PHS. (b) 3-mm-long 80-μm-wide metal-metal THz QCL with 150-μm-long PHS. (c) 2-mm-long 60-μm-wide metal-metal THz QCL without any planar horn structure. The measurements were all taken at 77 K.

7.3.6 Broad band emission property of THz QCLs with PHS

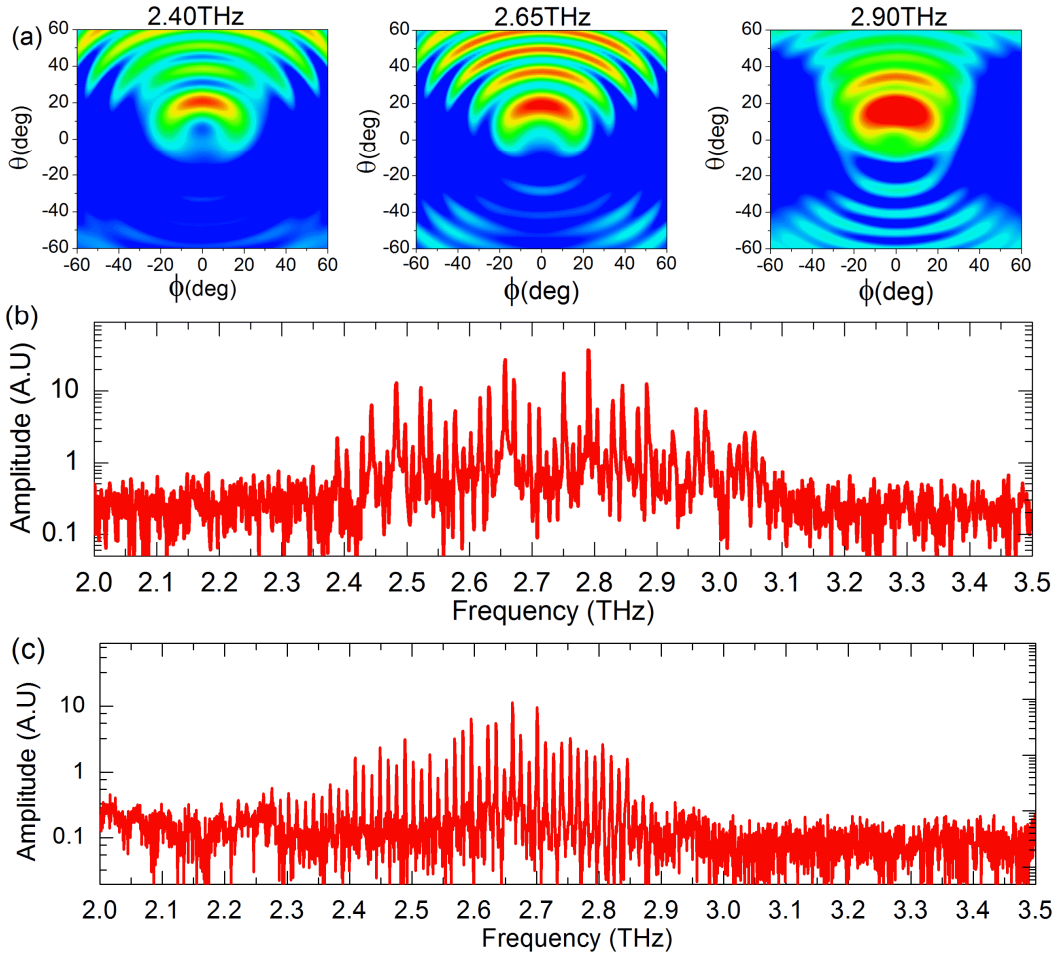

Fig. 7.14 | (a) Simulated far field profiles at 2.4 THz, 2.65 THz and 2.9 THz for QCL with central emission frequency of ~2.7 THz with a PHS of length 150 μm. (b) The measured spectrum taken at 10K showing a broadband response. (c) The spectrum of a QCL without PHS and with the same design of (b).

To illustrate the broadband spectral nature of the PHS, the spectrum of a QCL operating with a similar active region but operating around 2.7 THz with a bandwidth of ~600 GHz [20] was investigated. The sample ridge width here was 60 μm with a cavity length of 3mm and the PHS length was 150 μm. The calculated far-fields for 2.4 THz, 2.65 THz and 2.9 THz are shown in Fig. 7.14 (a). Although there is a slight dependence on the frequency with a larger divergence and more elliptical field for the lower frequencies, all the far-fields show a similar single lobed far field. Figure 7.14 (b) shows the resulting spectrum using an injection seeding technique [67] which shows that emission extends from 2.4 THz to 3 THz. Although there appears to be a stronger distribution in intensities of the Fabry-Perot modes when compared to

the as cleaved device [26], a similar bandwidth is obtained illustrating the broad spectral response of the PHS.

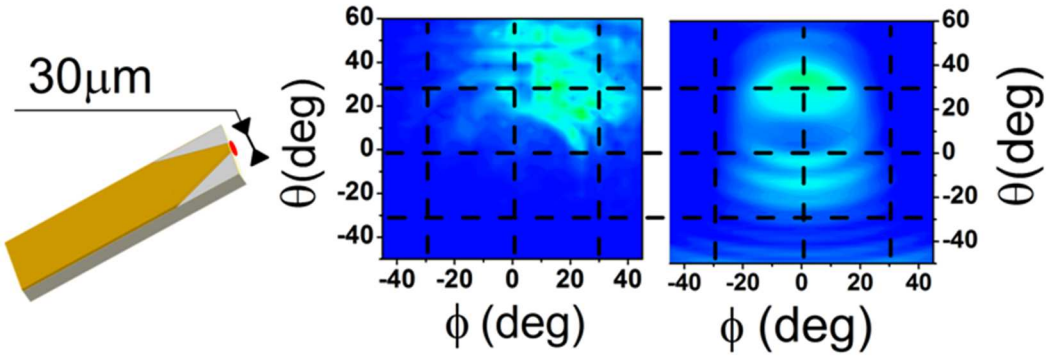

Fig. 7.15 | Simulated (right) and measured (left) far-field patterns of a 3-mm-long 80-μm-wide metal-metal THz QCLs with a 250-μm-long inverse planar horn structures. The measurements were all taken at 77 K.

As can be observed from Fig. 7.14, although larger output powers can be achieved, a large ridge with a PHS results in a double lobed far-field, which is not ideal for applications. To circumvent this, a tapered shape was realized on the end of the QCL. Here, rather than removing the metal layer from the center of the ridge, the metal layer was selectively removed from edges of an 80-μm-wide ridge to a 30 μm point at the QCL facet over a taper length of 250 μm (see Fig. 7.15). This scheme increases the losses of the higher order modes and therefore limits laser action only to the fundamental mode. Fig 7.15 shows the measured (left) and simulated (right) far-field profiles for an 80-μm-wide ridge. The far-field is improved considerably and, in contrast to Fig. 7.14 (b), is single lobed. (The slight angle in $\varphi = 18°$ in the measurement data is a result of a slight asymmetry in the realized PHS fabrication). This shows that the PHS shape can be adapted to the ridge width and is not limited to small ridge widths for lasing on the fundamental mode.

7.4 Conclusions

In conclusion, the application of a broadband PHS to MM THz QCLs has been demonstrated and the ridge width engineered to favor single lobed emission in the far field. All measurements were performed at temperatures and electrical power dissipation compatible with liquid nitrogen cooling or cryocooler temperatures. The 150-μm-long planar horn structures integrated onto the top metal surface of the QCL reduces the reflectivity and improves the quality of the far-field profiles. This permits a four-fold increase in the detected power whilst conserving a broad spectral response. Further, with longer PHS lengths, the output powers and directionality can be increased considerably further. This stability and the inherent broadband nature of these structures will allow these devices to be employed for applications such as injection seeding of QCLs for coherent detection, QCL mode-locking for high pulse powers and the generation of high power frequency combs.

Conclusion

In this thesis, I have successfully demonstrated that active mode-locked THz QCLs can be used to generate pulses as short as ~4 ps, considerably shorter than the previous state-of-the-art. This was achieved through a thorough step-by-step methodology, from the application of narrow spectral band width QCLs (20ps pulses) to QCLs with broad spectral emission (11ps pulse generated). The broad spectral emission was found to be not the limiting factor for short pulse generation but was rather limited by the sinusoidal modulation and the index dispersion. The major breakthrough was the application of a novel couple cavity system that overcome these bottlenecks through the introduction of dispersion compensation and hybrid mode-locking of QCLs. This was based on the realization of Gires-Tournois interferometer (GTI) and an air gap (passive modulator), respectively, monolithically integrated into the QCL waveguide. This flexible chip based solution, together with the high-speed active modulation, opens up a direct route to the generation of sub-picosecond pulses in the THz range from a semiconductor source, resulting in broadband semiconductor-based frequency combs, and could potentially enable a plethora of applications across the physical, chemical and biological sciences.

This thesis began with an introduction to THz QCLs in chapter 1. These semiconductor sources are based on inter-subband transitions, permitting laser action over the entire THz spectral range. A variety of properties were defined including the type of active regions and waveguides that were used extensively in the experimental chapters. As ultrafast THz detection is still in its infancy, in chapter 2 I presented the injection seeding technique used through this thesis. This technique permits to coherently detect the electric field of QCL emission in time domain with a *fs* resolution, and allows to directly demonstrate the THz pulse generation from QCLs and investigate their ultrafast dynamics. In chapter 3, I presented the mode-locking principle in both the time domain and frequency domains. The physical process of mode-locking was analyzed by consideration of resonant modes in the active medium filled Fabry-Pérot cavity and the role of dispersion. Further, the peculiarities of QCLs to mode-locking was discussed. Owing to their ultrafast gain recovery (~5 – 15 ps), which is up to an order of magnitude smaller than the photon round-trip time, passive mode-locking techniques are difficult to apply. However, the ultrafast dynamics of the QCL are ideally adapted for active mode-locking where the QCL cavity is modulated at the round trip frequency (13 GHz for a 3mm cavity).

Chapter 4 to 6 detailed the active mode-locking experiments and how THz pulses can be shortened, step-by-step, from ~20 ps to ~4 ps from active mode-locked QCLs. In chapter 4, a ~20 ps THz pulse train was generated from a single-plasmon bound-to-continuum QCL by active mode-locking at 10 K. The bandwidth of these QCLs is low (< 100 GHz) and expected to limit the pulse width that can be generated. We also showed that the spectrum of this QCL could by continuously tuned over a range greater than 2 GHz by changing the active modulation

frequency. This controlled emission spectrum was then employed for identifying the absorption lines of H_2O and CH_2OH via gas spectroscopy. Chapter 5 described mode-locking of THz QCLs with a large gain bandwidth (~500 GHz), based on LO phonon depopulation active region designs. The QCLs here were also imbedded in a sub-wavelength metal-metal waveguides and we were able, for the first time, to injection seed and mode-lock these devices at liquid nitrogen temperatures. Importantly the expectation of these broad bandwidth samples was for the generation of pulses less than 5ps. However, although shorter pulses were observed, they were limited to ~11 ps, owing to the effect of the sinusoidal microwave modulation and the index dispersion. In chapter 6, these limitations were overcome by a chip-based coupled cavity scheme that introduced controlled dispersion compensation and hybrid mode-locking through a small resonator (the GTI) and a passive air-gap modulation, respectively. This permitted a stable train of pulses as short as 4ps to be demonstrated.

In chapter 7, independent of the previous chapters, the far-field emission profile and out-coupling power of THz QCLs in metal-metal waveguides were significantly improved through planar horn-like structures integrated on the monolithic chip of QCLs at 77 K. The structures produced a gradual change in the high modal confinement of the waveguides and permitted an improved far-field emission profile and resulting in a four-fold increase in the emitted output power. This improved far-field and output power in MM THz QCLs is a promising candidate for generating ultrafast THz pulses and broadband frequency combs with higher out-coupling power when compared to the devices presented in chapters 5 and 6. Further the horn-line structures could be eventually used to compensate for the index dispersion instead of the application of a GTI. This would integrate dispersion compensation as well as high output coupling efficiencies.

The research in chapter 6 opens up considerable perspectives for the generation of much shorter pulses, down to the sub-picosecond or even the single cycle regime. The results shown in chapter 6 appear to be a result of dispersion compensation and an additional passive modulation. Each of these possibilities can be manipulated to generate considerable shorter pulses: i) Firstly, QCLs with greater bandwidth can be used – bandwidths greater than 1THz have been previously demonstrated. Although GTIs have a limited spectral range that can be used for dispersion compensation, other on-chip techniques based on structuring of the surface (see chapter 7) can be applied to realize broadband dispersion compensation. (ii) Regarding the passive modulation, this can be optimized through second order hybrid mode-locking. Here a second air-gap modulator added to the first will introduce more losses and further reduce the pulse width. (iii) Owing to its small gap, graphene could be used as a THz saturable absorber, deposited on one of the facets of the QCL. This would be combined with the active modulation to realise a graphene-based hybrid mode-locking scheme. This would relax the constraints of the ultrafast gain recovery on passive mode-locking. These range of opportunities open up the possibility of ultrashort THz pulse generation from a compact semiconductor source. Furthermore, the realization of ultrashort THz pulses from active mode-locked QCLs will be permit THz frequency comb spectroscopy that are engineered and accurately controlled by microwave signal generators.

A

Growth Sheets of Quantum Cascade Lasers

A.1 V455

Active region and injector:

Growth Step	Composition	Thickness (nm)	Doping (cm-3)
1	AlGaAs	4.80	
2	GaAs	11.79	1.3E16
3	AlGaAs	4.20	
4	GaAs	11.40	1.3E16
5	AlGaAs	3.00	
6	GaAs	11.78	
7	AlGaAs	2.90	
8	GaAs	12.54	
9	AlGaAs	2.50	
10	GaAs	14.53	
11	AlGaAs	2.30	
12	GaAs	13.82	
13	AlGaAs	0.99	
14	GaAs	11.54	
15	AlGaAs	1.00	
16	GaAs	15.03	

A.2 L182

Growth Step	Composition	Thickness (Angs)		Doping (cm-3)
	SI GaAs SUBSTRATE			
1	GaAs (BUFFER)	2500.0		
2	AlGaAs	3000.0	x = 50%	
3	GaAs	7000.0		2.0E18
4	As INTERRUPT	-		*(Si -> 1.6E16)*
	Injector Grading:			
5	AlGaAs	42.00	x = 15%	
6	GaAs	118.00		
7	AlGaAs	35.00	x = 15%	
8	GaAs	113.00		
9	AlGaAs	27.00	x = 15%	
10	GaAs	114.00		1.6E16
11	AlGaAs	20.00	x = 15%	
12	GaAs	120.00		1.6E16
13	AlGaAs	20.00	x = 15%	
14	GaAs	118.00		
	START SL1 STRUCTURE - REPEAT LOOP x90			
	Active Region:			
15*SL1*	AlGaAs	18.00	x = 15%	
16*SL1*	GaAs	124.00		
17*SL1*	AlGaAs	15.00	x = 15%	
18*SL1*	GaAs	153.00		
19*SL1*	AlGaAs	6.00	x = 15%	
20*SL1*	GaAs	100.00		
21*SL1*	AlGaAs	6.00	x = 15%	
22*SL1*	GaAs	135.00		
	Injector Grading:			
23*SL1*	AlGaAs	42.00	x = 15%	
24*SL1*	GaAs	118.00		
25*SL1*	AlGaAs	35.00	x = 15%	
26*SL1*	GaAs	113.00		
27*SL1*	AlGaAs	27.00	x = 15%	
28*SL1*	GaAs	114.00		1.6E16
29*SL1*	AlGaAs	20.00	x = 15%	
30*SL1*	GaAs	120.00		1.6E16
31*SL1*	AlGaAs	20.00	x = 15%	
32*SL1*	GaAs	118.00		
	END SL1 STRUCTURE			
33	GaAs	200.00		*(Si -> 1.6E16)*
34	GaAs	800.00		5.0E18

A.3 L1074

Sample ID **L1074** **Description +10% in GaAs layers**

Matrix Layers

Layer	Material	[nm]	[μm]	Ratio	Doping (cm-3)
1	GaAs	250	0,2500		
2	AlGaAs	300	0,3000	$Al_{50}Ga_{50}As$	
3	GaAs	700	0,7000		2,00E+18
4	AlGaAs	4,6	0,0046	$Al_{15}Ga_{85}As$	
5	GaAs	6,1	0,0061		
6	GaAs	5,5	0,0055		5,00E+16
7	GaAs	6,0	0,0060		
	Start of 228 repeat periods				
8S1	AlGaAs	4,39	0,0044	$Al_{15}Ga_{85}As$	
9S1	GaAs	8,97	0,0090		
10S1	AlGaAs	2,63	0,0026	$Al_{15}Ga_{85}As$	
11S1	GaAs	9,79	0,0098		
12S1	AlGaAs	4,60	0,0046	$Al_{15}Ga_{85}As$	
	Injector grading				
13S1	GaAs	6,10	0,0061		
14S1	GaAs	5,50	0,0055		5,00E+16
15S1	GaAs	6,00	0,0060		
	End of repeat periods				
16	AlGaAs	43,90	0,0439	$Al_{15}Ga_{85}As$	
17	GaAs	50,00	0,0500		5,00E+18

A.4 L1194

Sample ID **L1194** **Description** **Rescale of MIT 200K design** **Date**

Matrix Layers

Layer	Material	[nm]	[μm]	Ratio	Doping (cm-3)	
1	GaAs	250	0,2500			
2	AlGaAs	300	0,3000	$Al_{50}Ga_{50}As$		
3	GaAs	700	0,7000		2,00E+18	
4	AlGaAs	4,85	0,0049	$Al_{13.3}Ga_{86.7}As$		injector
5	GaAs	6,20	0,0062			
6	GaAs	6,00	0,0060		6,00E+16	
7	GaAs	6,20	0,0062			
	Start of 200 repeat periods					
8S1	AlGaAs	4,62	0,0046	$Al_{13.3}Ga_{86.7}As$		collector
9S1	GaAs	9,37	0,0094			
10S1	AlGaAs	2,77	0,0028	$Al_{13.3}Ga_{86.7}As$		
11S1	GaAs	10,24	0,0102			
12S1	AlGaAs	4,85	0,0049	$Al_{13.3}Ga_{86.7}As$		injector
13S1	GaAs	6,20	0,0062			
14S1	GaAs	6,00	0,0060		6,00E+16	
15S1	GaAs	6,20	0,0062			
	End of repeat periods					
16	AlGaAs	4,62	0,0046	$Al_{13.3}Ga_{86.7}As$		collector
17	GaAs	50	0,0500		5,00E+18	

A.5 L857

Sample ID **Thales - xxx** **Description** **Date**

Matrix Layers

Layer	Material	[nm]	Ratio	Doping (cm-3)
1	GaAs	250		
2	AlGaAs	300	$Al_{50}Ga_{50}As$	
3	GaAs	600		3,50E+18
4	AlGaAs	1,8	$Al_{15}Ga_{85}As$	
5	GaAs	11		
6	GaAs	5,5	$Al_{15}Ga_{85}As$	
7	GaAs	18,4		2,00E+16
	Start of 180 repeat periods			
8S1	AlGaAs	4,2	$Al_{15}Ga_{85}As$	
9S1	GaAs	9,4		
10S1	AlGaAs	3,8	$Al_{15}Ga_{85}As$	
11S1	GaAs	11,5		
12S1	AlGaAs	1,8	$Al_{15}Ga_{85}As$	
13S1	GaAs	11		
14S1	AlGaAs	5,5	$Al_{15}Ga_{85}As$	
15S1	GaAs	18,4		2,00E+16
	End of repeat periods			
16	AlGaAs	4,2	$Al_{15}Ga_{85}As$	
17	GaAs	50		5,00E+18

A.6 L985

Sample ID **L985** **Description** **Date**

Matrix Layers

Layer	Material	[nm]	[μm]	Ratio	Doping (cm^{-3})
1	GaAs	250	0,2500		
2	AlGaAs	300	0,3000	$Al_{50}Ga_{50}As$	
3	GaAs	700	0,7000		2E+18
4	AlGaAs	4,3	0,0043	$Al_{15}Ga_{85}As$	
5	GaAs	5,5	0,0055		
6	GaAs	5	0,0050		5,00E+16
7	GaAs	5,5	0,0055		
	Start of 228 repeat periods				
8S1	AlGaAs	4,1	0,0041	$Al_{15}Ga_{85}As$	
9S1	GaAs	8,15	0,0082		
10S1	AlGaAs	2,46	0,0025	$Al_{15}Ga_{85}As$	
11S1	GaAs	8,9	0,0089		
12S1	AlGaAs	4,3	0,0043	$Al_{15}Ga_{85}As$	
	Injector grading				
13S1	GaAs	5,5	0,0055		
14S1	GaAs	5	0,0050		5,00E+16
15S1	GaAs	5,5	0,0055		
	End of repeat periods				
16	AlGaAs	4,1	0,0041	$Al_{15}Ga_{85}As$	
17	GaAs	50	0,0500		5,00E+18

B

Gas Spectroscopy using Mode-Locked THz QCLs

B.1 Application of mode-locked THz QCL to H_2O vapor spectroscopy

I firstly investigate the THz wave absorptions of water vapor in atmosphere environment with a humidity of ~42% using mode-locked THz QCL "V455". Prior to measuring the absorption spectrum of water vapor from THz QCL, we need an absorption spectrum as reference which should be obtained under the same environments conditions as the case of THz QCL. With it we will be informed that whether there are absorptions or not within the emission frequency range of the QCL. If there is no absorption at all, it is useless to apply any measurements on the THz QCL. In contrary, if there are some strong absorption lines within the emission range, we can apply it to the QCL and compare the reference spectrum with the absorption spectrum from QCL to check the preciseness of the measurements.

How can we obtain the reference spectrum of absorptions? As discussed in chapter 2, the emission of GaAs semi-insulator photoconductive antenna gives us a single THz pulse in time domain and a broadband continuous spectrum beyond 3.5 THz centered at 1.2THz in frequency domain. In order to get a continuous absorption reference, we measured the temporal signals of the photoconductive antenna through THz-TDS together with electro-optics sampling respectively under natural atmosphere environments (humidity ~42%) and purged atmosphere (humidity ~0.7%) as is illustrated in Fig B.1. In the experiments, we carried out a long scan from 0 ps to 1250 ps for getting a good frequency resolution. However, in the figure signals only from 79 ps to 120 ps are displayed for better comparing the temporal change of pulses in

these 2 different conditions. In Fig B.1 (a), the black smooth pulse $S_{antN}(t)$ was measured under dry air and the back inset is its spectrum $S_{antN}(\omega)$, while the red pulse $S_{ant}(t)$ and spectrum $S_{ant}(\omega)$ were obtained under ~42% humidity environments. Dividing $S_{ant}(\omega)$ by $S_{antN}(\omega)$, we will get the reference spectrum of water vapor from 0.5 THz to 3 THz: $Sp_{ref}(\omega) = S_{ant}(\omega)/S_{antN}(\omega)$ as is shown in Fig B.1 (b). Around 1.9 THz, there is a ~20 GHz broad absorption line, into which the QCL emissions are falling. Therefore, it is possible to observe absorption phenomenon of water vapor from this tunable mode-locked THz QCL.

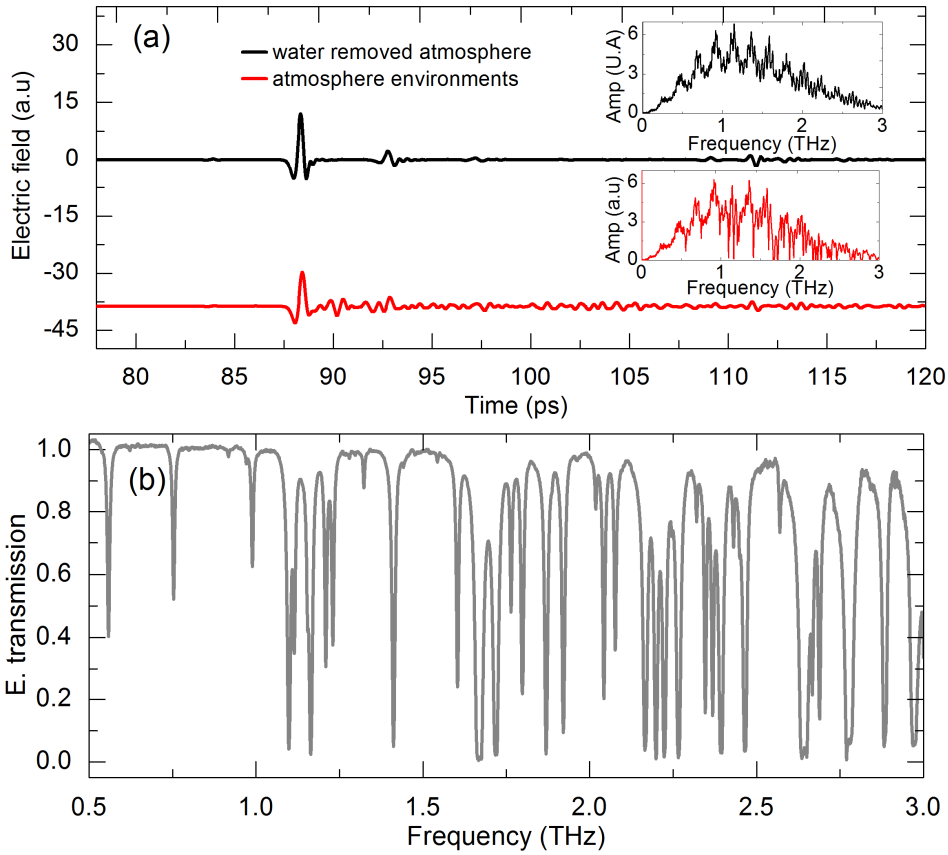

Fig B.1 | (a) THz pulses emitted by photoconductive antenna in natural atmosphere (red) and water-removed atmosphere environments (black) from 79 ps to 120 ps. Inset: spectra of signals at left sides from 0 THz to 3 THz. (b) The continuous absorption spectrum of water vapor in atmosphere obtained by comparing the 2 spectra in (a) inset.

Using again the operating parameters in table 1 in chapter 4 with a modulation frequency of 13 GHz, I measured the temporal emissions of the QCL respectively within ~42% and ~0.7% humidity environments by the time-resolved injection seeding detection system. The results are given in Fig B.2. The black pulses in (a) were detected in purged air while the red ones were in natural air. The most evident difference between the 2 scans lies in the valleys

between any 2 pulses peaks as zoomed in (c) for better observations. Within water vapor environments, THz waves were strongly absorbed, resulting in strong oscillations in temporal signals. The valleys between any 2 pulses were the weakest amplitude positions allowing us to clearly observe this phenomenon from absorptions. (b) is the spectra of (a) also allowing us to have an insight into the absorption phenomenon by comparing their absolute values of spectral intensities in these 2 cases. From Fig B.2 (b), we can see the strongest absorption line is located at around 1.923THz, the second longitudinal mode in the spectrum. For the others modes, the absorption is weak but it can still be witnessed. Using the same way as is used above for antenna absorption spectrum, we can get the absorption of each mode of the THz QCL via dividing the absorbed spectrum (red) by the non-absorbed spectrum (black) as is shown in Fig B.3 (b) the red line.

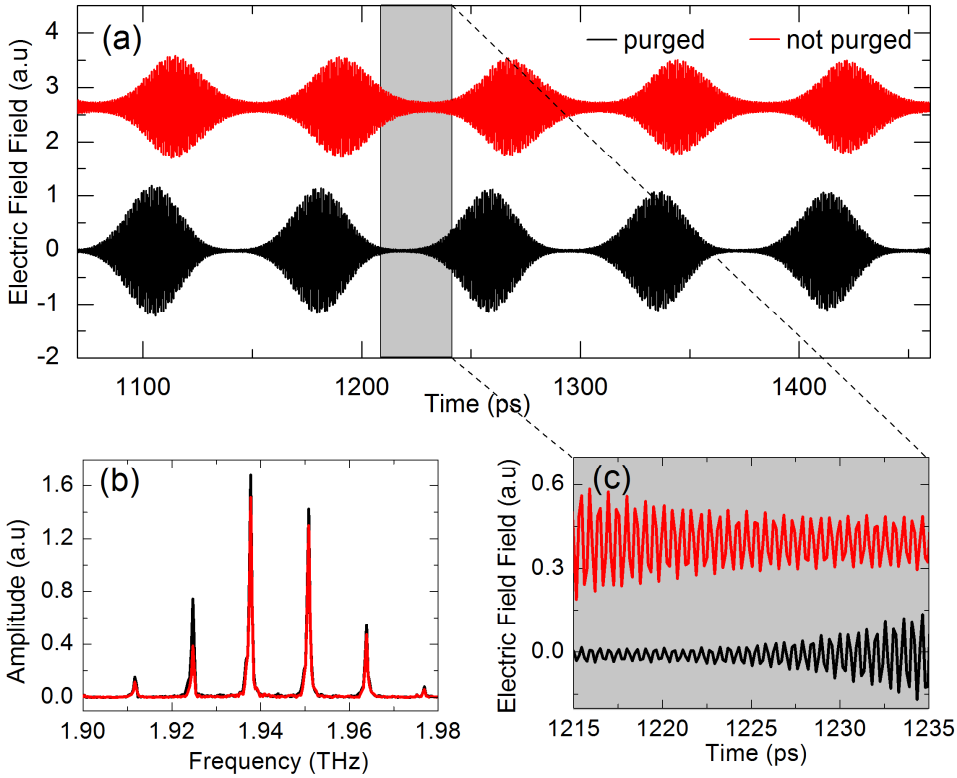

Fig B.2 | (a) Electric field of mode-locked THz QCL emissions at 13 GHz detected in atmosphere (red) and water-removed atmosphere (black). (b) Spectra correspond to (a) obtained by fast Fourier transform. (c) Zoom of (a) from 1215 ps to 1235 ps.

Varying the modulation frequency from 12 GHz to 14 GHz, we can quasi-continuously (step: 76.69MHz) tune the emission frequencies of QCL. Furthermore, their corresponding absorption spectra can be tuned with a tunable mode spacing range of over ~2 GHz. Here in Fig B.3, only the tuned absorption spectra with a mode spacing of 12.080 GHz (black), 13.000 GHz (red) and 13.919 GHz (purple) are shown. We can see that when the emission frequencies (or mode spacing) are slightly shifted by changing the modulation frequency, the absorptions

are also obviously varied at some strong absorption points for example the second mode at 1.923 THz. Comparing them with the reference from photoconductive antenna (the grey curves in Fig B.3 (a) and (b)), we can see they match quite well over the whole tunable emission spectra from 1.90 THz to 1.98 THz.

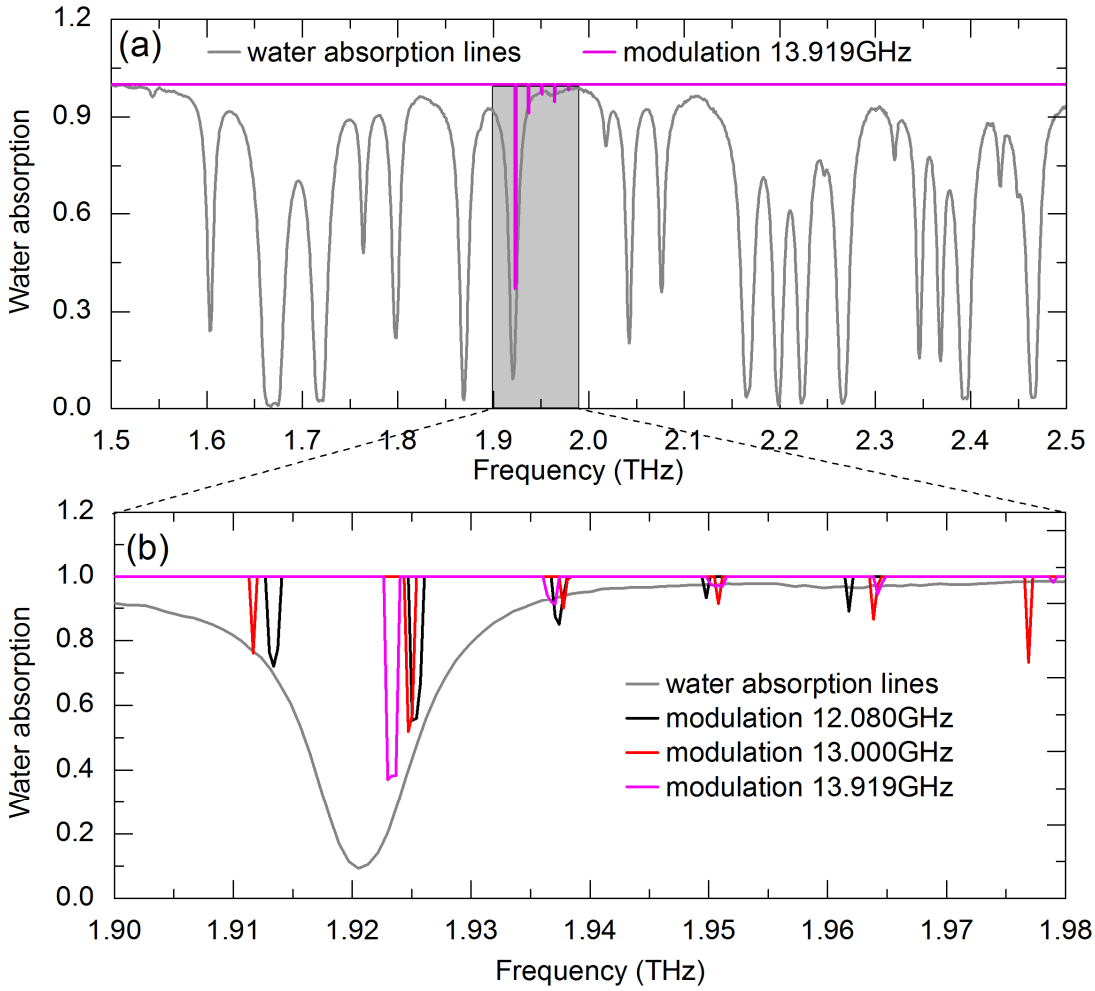

Fig B.3 | (a) THz absorption lines of water vapor respectively from photoconductive antenna (grey) and mode-locked QCL at 13.919THz (purple). (b) Absorption lines of mode-locked THz QCL with modulation frequencies tuned from 12.080 GHz (black) to 13.919 GHz (purple).

For some gases with narrow absorption lines within 2 GHz, we can use this way to completely trace their absorption spectra around 1.94 THz. If we want to characterize some extremely narrow absorption lines at the level of ~ 1 KHz, we can still use this THz QCL with a sub-hertz continuous tunable microwave modulator for example, KEYSIGH PSG E8251A generator, covering the frequency range from 250 KHz to 20 GHz with sub-hertz tuning steps. However, in this case, novel ultrafast and sensitive THz detection systems or detectors with extremely high resolutions need to be introduced.

B.2 Application of mode-locked THz QCL to CH_2OH gas spectroscopy

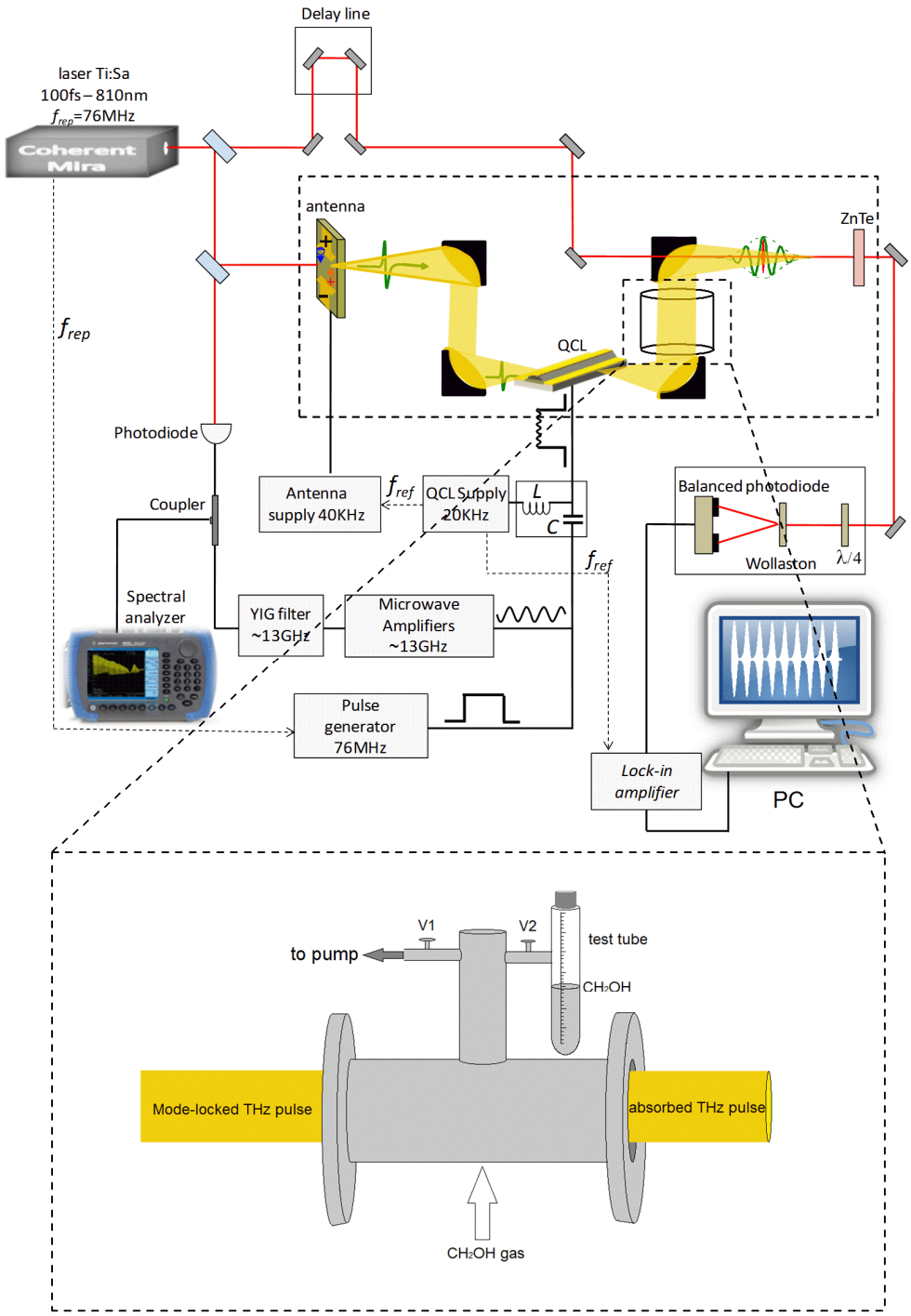

Fig B.4 | Experimental setup for CH_2OH gas spectroscopy. Above: complete experimental setup; below: detail of the gas container.

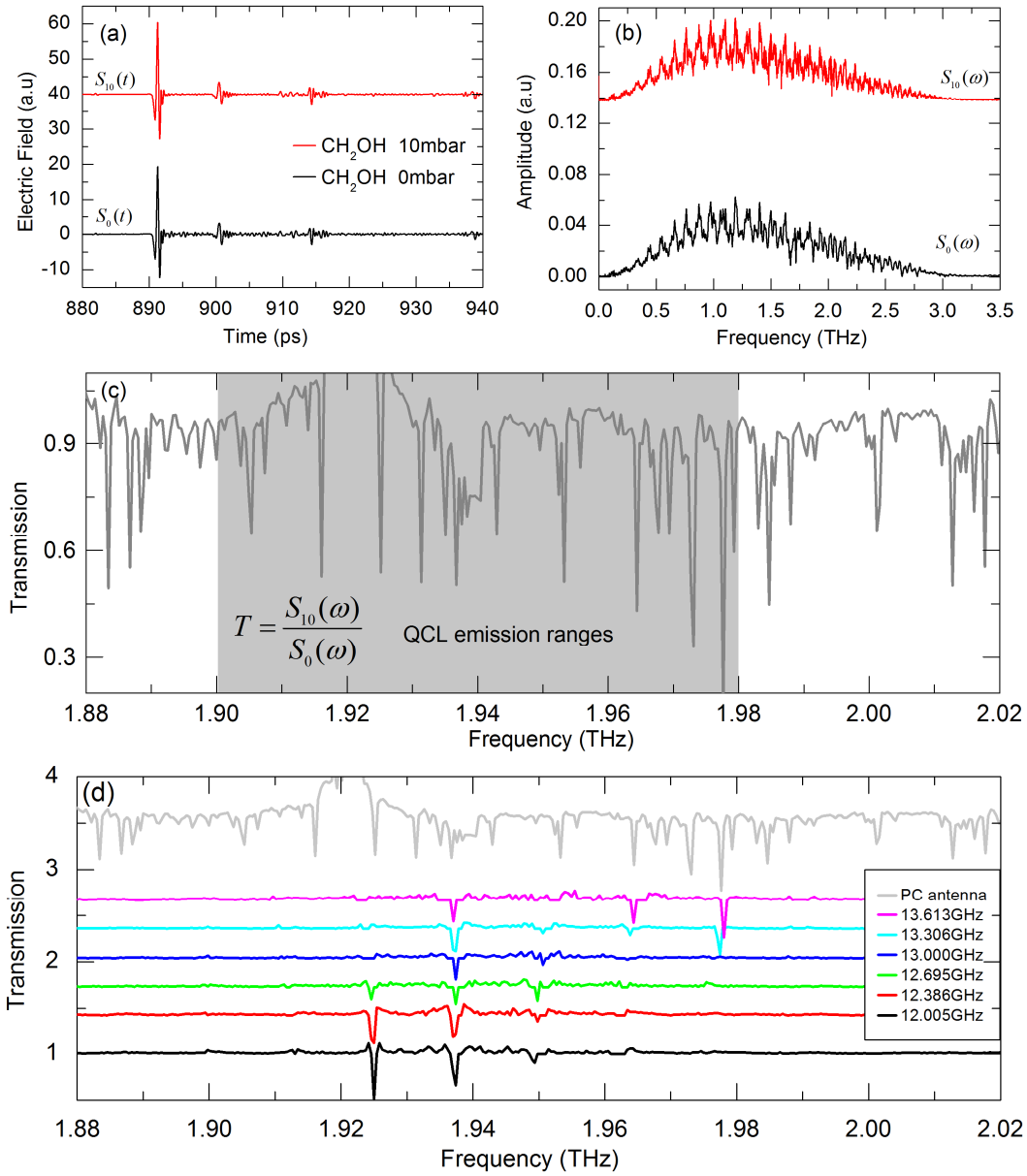

Fig B.5 | (a) Broadband THz pulses from photoconductive antenna respectively passing through vacuum and 10 mbar CH_2OH gas. (b) Spectra of the THz pulses in (a). (c) 10 mbar CH_2OH gas absorption spectrum from 1.88 THz to 2.02 THz. (d) Absorption lines of 10 mbar CH_2OH gas from mode-locked THz QCL with modulation frequency tuned from 12.005 GHz to 13.613 GHz.

After the tests in atmosphere water vapor whose absorption lines are super broad, we also tried on a kind of gas with narrow absorption lines: CH_2OH. The experimental setup is the same as we used for mode-locking except a THz-wave passable airtight gas container which is placed between the last 2 parabolic mirrors as illustrated in Fig B.4. In the test tube is the liquid CH_2OH. Prior to putting CH_2OH in the container, we totally close the valve switchV2 and let

the V1 open. Then we pump the gas container to vacuum and completely close V1. If we slightly open the valve V2 to connect the vacuum container with the test tube, under low pressure environments, the liquid CH_2OH will be transferred into gas to fill up the vacuum container. From a pressure gauge installed inside the container, we can control the density of gas. Once the pressure is increased to 10 mbar, we totally close the V2 to block the test tube and container. In this way, a fully filled container of CH_2OH gas can be prepared for absorption measurements using THz time domain spectroscopy.

Using the same ways used in water vapor spectroscopy, we get the reference absorption spectrum of CH_2OH gas from photoconductive antenna as presented in Fig B.5 (a), (b) and (c). Among them, (a) is the broadband THz pulses from photoconductive antenna respectively passing through vacuum and 10 mbar CH_2OH gas. (b) is the spectra of the THz pulses of (a) and (c) is the gas absorption spectrum in10 mbar CH_2OH environments from 1.88 THz to 2.02 THz. Then from the mode-locked QCL with mode-spacing tuned from 12.005 GHz to 13.613 GHz, we get the tunable absorption lines as illustrated in Fig B.5 (d). Taking the strong absorption point at around 1.98 THz for example, when the modulation frequency is 13.613 GHz and 13.306 GHz, emission frequencies of the QCL fall into the absorption valley of CH_2OH gas and we can clearly see the absorption effect. However, if we continue decreasing slightly the modulation frequencies, emission frequencies of the QCL are no longer located at the absorption point due to narrow absorption property of this gas. Therefore, no absorption can be observed any more. The same reason for the mode around 1.925 THz, 1.938 THz, 1.950 THz and 1.965 THz. In principle, we can trace the absorption lines of CH_2OH gas using the mode-locked THz QCL as a source, but here the low resolutions (a few hundred MHz) of our time domain spectroscopy system limited by delay line length don’t allow us to trace it accurately.

C

Absorption Investigation in the Coupled Cavity of Quantum Cascade Laser L1194

Absorption investigation in the coupled cavity of the QCL L1194

To investigate the absorption effect of the coupled cavity integrated onto the sample "L1194", I measured the emission of the mode-locked QCL with different biases applied on the small section (coupled cavity). The results are shown in Fig C. It can be obviously seen that there is no influence on the pulses (intensity and width) when changing the bias from 0 V to 9.6 V (corresponding to 180 mA), indicating that there is no absorption of THz waves in the coupled cavity. When the currents injected into the small section are above 190 mA, on pulse can be observed any more owing to the injection seeding technique. (When the small section starts lasing, the phase of QCL emission is not controlled anymore by the injected THz pulse and therefore, nothing can be detected). We also negatively biased the small section from 0V to -16 V. There is always no influence on the mode-locked THz pulses.

In this experiments, the THz QCL (long section) worked at the parameters below: QCL: 20kHz - 8% - 38.7V (1230mA) - T= 20K RF:300mV – 7.5ns pulse width – inverted GHz:12.886GHz/30dBm

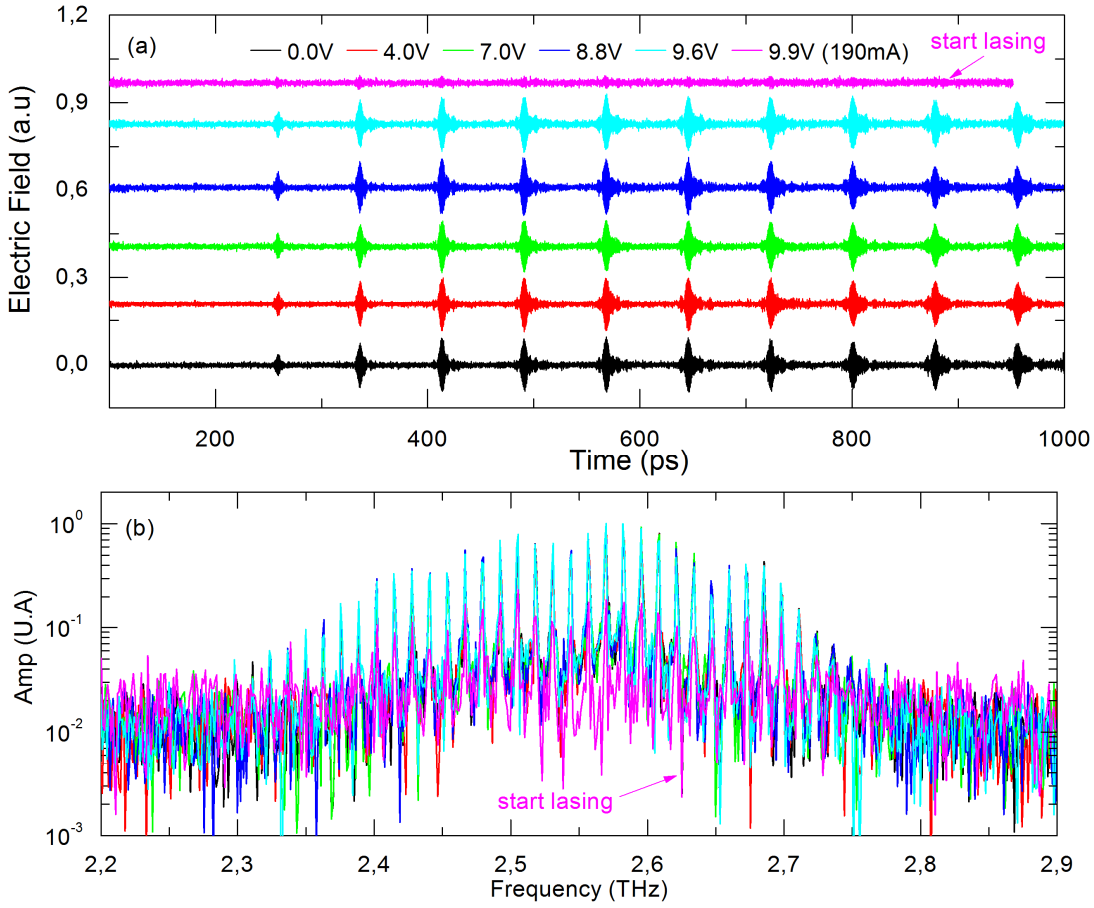

Fig C. | Absorption investigation in the coupled cavity integrated onto the sample “L1194” in chapter 6. (a) Time resolved-emission of the mode-locked QCL “L1194” as a function of the bias applied on the small section (coupled cavity). (b) The spectra corresponding to (a).

D

Beatnote of L857 with a ridge width of 150µm

Beatnote of QCL L857 with a ridge width of 150µm

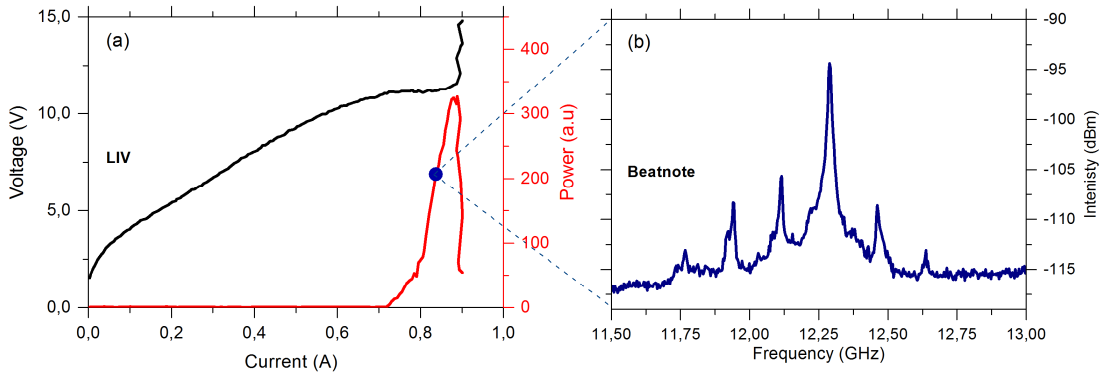

Fig D | (a) LIV of a 3-mm-long 150-µm-wide QCL L857 with integrated air gap and coupled cavity. (b) Beatnote of this sample with a working current at 835 mA.

E

Dynamics of mode-locking of THz QCL L857

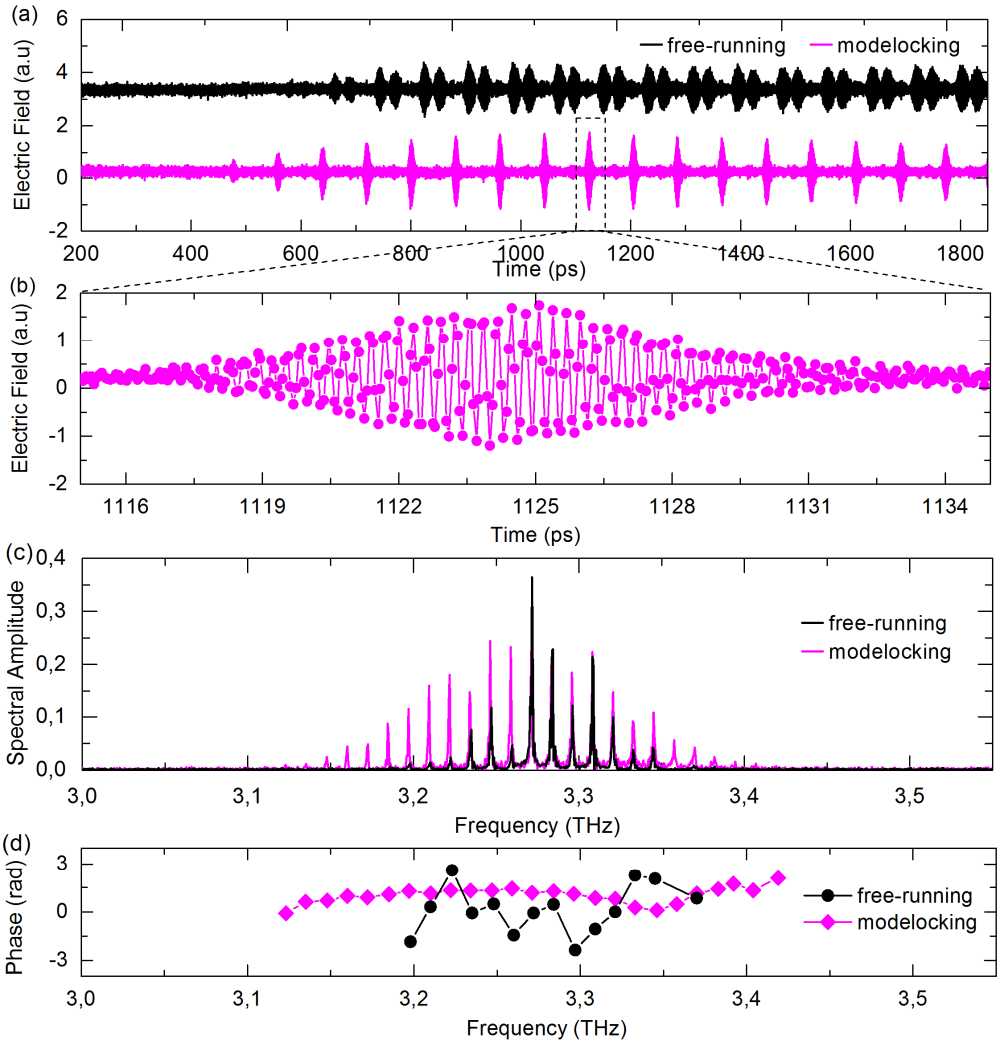

Fig. E | Dynamics of mode-locking of QCL L857. (a) Time resolved emission of QCL “L857” under free-running and mode-locking condition, respectively. (b) Zoom of the THz pulse between 1115 ps and 1135 ps. (c) The spectra of (a). (d) The phase of each mode for free-running (black) and mode-locking (magenta), respectively.

F

Gain Measurement of the Sample L1194

Gain measurement of the sample L1194

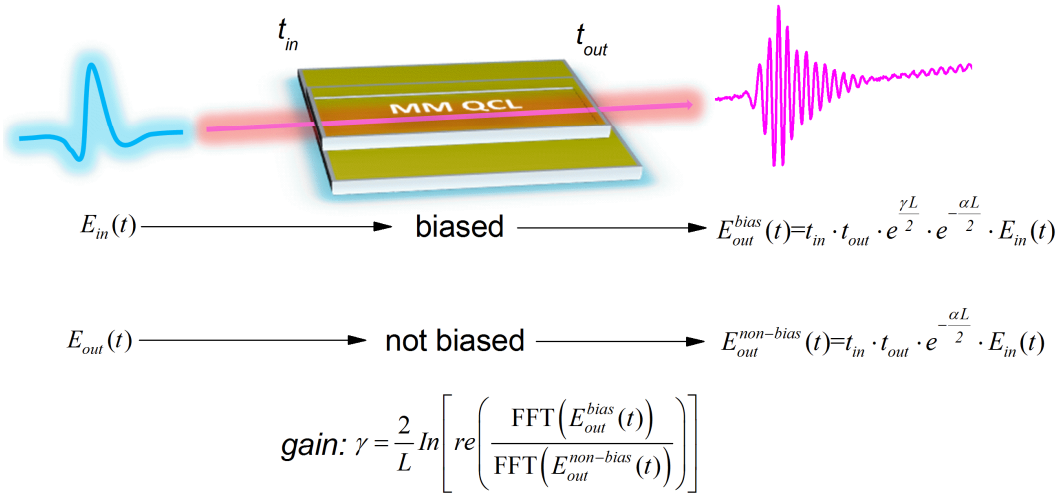

Fig F.1 | Schematic diagram for gain investigation of THz QCLs using time-domain spectroscopy.

It is challenging to investigate the gain of QCLs based on metal-metal waveguide using time-domain spectroscopy technique due to the difficulty of efficiently coupling a THz pulse of photoconductive antenna into the subwavelength and high confinement metal-metal waveguide. Here, this QCL “L1194” works at a relatively low frequency centered at ~2.5 THz, which has a better overlap with the spectrum of photoconductive antenna (see the spectrum of the photoconductive antenna in Fig 2.3) than L1074. These better overlapped spectra permit

more power to be coupled into/out the metal-metal cavity for gain investigation. Therefore, I will to characterize the gain profile of this QCL, here. The detail of this gain measurement technique is described in ref [110]. Here, I just briefly present its principle. As schematically illustrated in Fig F.1, we inject a broadband THz pulse (from a photoconductive antenna) into the cavity of the QCL and measure the electric field at the opposite side using the THz time domain spectroscopy. If we suppose the electric field of the THz pulse is $E_{in}(t)$, the transmission of electric field at the "in" and "out" facets are t_{in}, t_{out}, the gain and the loss are, respectively, γ and α, the output electric field travelling through the cavity can be then written as:

$$E_{out}^{bias}(t) = t_{in} \cdot t_{out} \cdot e^{\frac{\gamma L}{2}} \cdot e^{-\frac{\alpha L}{2}} \cdot E_{in}(t) \tag{F.1}$$

If the QCL is not biased, the amplification term in Eq. (E.1) should be taken away and the output electric field can be modified to:

$$E_{out}^{non-bias}(t) = t_{in} \cdot t_{out} \cdot e^{-\frac{\alpha L}{2}} \cdot E_{in}(t) \tag{F.2}$$

Dividing Eq. (F.1) by Eq. (F.2) in frequency domain, the factor t_{in}, t_{out} and $e^{-\alpha L/2}$ will be eliminated and the gain profile can be obtained:

$$\gamma(\omega) = \frac{2}{L} In\left[re\left(\frac{E_{out}^{bias}(\omega)}{E_{out}^{non-bias}(\omega)} \right) \right] \tag{F.3}$$

Fig F.2 (a) show the time-resolved electric field of the THz pulse after travelling through the laser cavity at different operating currents varied from 145 mA to 1350 mA. When the currents are below the threshold, the THz pulse will undergo all kind of losses while travelling through the cavity. So the measured electric field is very weak. When the working currents are above the lasing threshold, there is no loss any more for the THz pulse and therefore the measured electric field is much higher. Fig F.2 (b) shows the spectra of these THz pulses measured in (a). (c) is the gain profile of the QCL, which is calculated using Eq. (F.3). It can be observed that the central frequency is located at ~2.45 THz with a gain value of ~15 cm^{-1}. (d) presents the gain value of the sample as a function of injected currents from ~150 mA to ~1500 mA at the central frequency. It can be evidently observed that the lasing threshold is around ~1100 mA. Below the threshold, there is no gain, while above it, the gain is a constant of ~15 cm^{-1}.

Until now, we have roughly estimated that the gain of the metal-metal waveguide THz QCL is ~15 cm^{-1}, which is 2 times higher than the gain (~6.5 cm^{-1}) of the single plasmon bound-to-continuum QCL measured in ref [110]. This is in agreement with our expectation as the loss of metal-metal waveguide is much higher than single plasmon waveguide, allowing us to better understand the behaviors of metal-metal waveguide THz QCLs

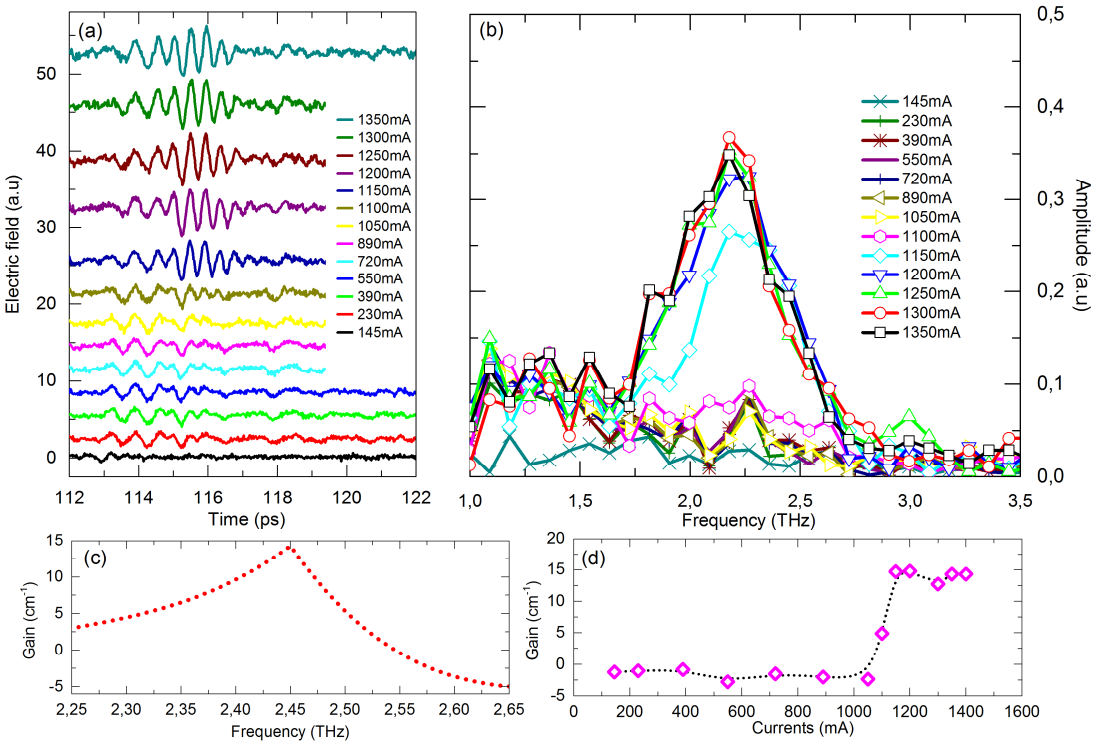

Fig F.2 | Gain measurement of the QCL "L1194". (a) The time-resolved electric field of the THz pulse after travelling through the laser cavity at different working currents. (b) The FFT of the THz pulses in (a). (c) The gain profile of the QCL "L1194". (d) The gain of the QCL as a function of injection currents.

.

G

THz Frequency Shifting Technique in Quantum Cascade Lasers

THz frequency shifting in quantum cascade laser using resonant nonlinearities.

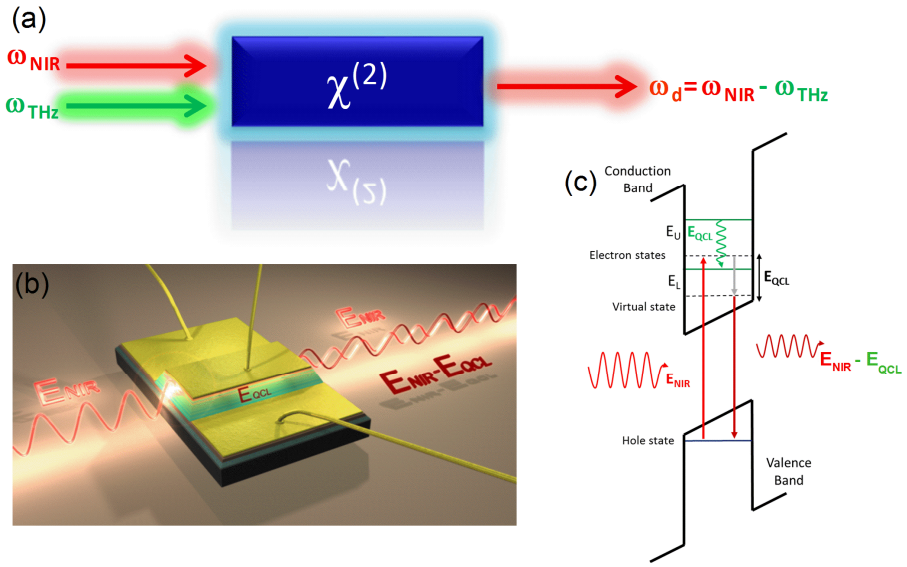

Fig G | Schematic diagram for directly measuring the emission spectra of THz QCL by transferring the THz waves onto near infrared frequency ranges through giant resonant nonlinearities in QCL L857. (a) The principle of difference frequency generation between THz waves and near-infrared frequencies by second order nonlinear effects. (b) Schematic diagram of frequency shifting in THz QCL by coupling near-infrared waves at 814.8 nm into a THz QCL with emission centered at 3.25 THz from one of its facets and frequency difference between these 2 frequencies can be directly captured from the other facet by infrared spectrometer with high sensibility and high resolution. (c) The nonlinear processes between THz waves and near-infrared frequencies in QCLs.

I have demonstrated ~5 ps THz pulse generation from mode-locked THz QCLs “L857” in time domain using time-domain spectroscopy together with injection phase seeding technique [67]. In this section, I, worked with S. Houver, will employ a new technique based on giant resonant nonlinearities in QCLs to transfer THz waves onto near-infrared ranges to directly measure the emission spectra of this QCL using a near-infrared spectrometer [123]. The principle of this technique is schematically presented in Fig G (a) where the frequency differing between THz waves and near-infrared waves is achieved in a THz QCL through second order resonant nonlinearity χ^2. Fig G (b) shows the schematic diagram of frequency shifting in THz QCL by coupling near-infrared waves ω_{NIR} at 814.8 nm into a THz QCL “L857” with emission centered at ω_{THz}=3.25 THz from one of its facets and frequency difference ω_D= ω_{NIR} - ω_{THz} between these 2 frequencies can be directly captured from the other facet by an infrared spectrometer with high sensibility and high resolution. The nonlinear processes in the GaAs-based THz QCL is detailed in Fig G (c). When the near-infrared lasers E_{NIR} are injected into the THz QCL, they will excite the electrons from valence band of semiconductor materials GaAs into the quantum wells in conduction band where THz laser transition take place. Then the excited electrons in conduction band will be released back to valence band by emitting photons with frequency shifted to $\omega_D = \omega_{NIR} - \omega_{THz}$ after second order nonlinear resonance with THz waves. Using a near-infrared spectrometer with high resolution that is smaller than the round-trip frequency ~12.3 GHz, the broadband THz frequency comb generated by hybrid mode-locking from THz QCL “L857” can be then copied and demonstrated in the well-developed near-infrared range. This method allows us to directly access to the emission spectrum of THz QCL to demonstrated mode-locking of THz QCLs in frequency domain.

H

Publications and Conferences

Publications:

[1] F. Wang, H. Nong, T. Fobbe, V. Pistore, S. Houver, S. Markmann, N. Jukam, M. Amanti, C. Sirtori, S. Moumdji, R. Colombelli, L. H. Li, E. H. Linfield, A. G. Davies, J. Mangeney, J. Tignon, and S. S. Dhillon, "Ultra-short terahertz pulse generation from modelocked semiconductor lasers," **submitted**.

[2] F. Wang, I. Kundu, L. Chen, L. Li, E. H. Linfield, A. G. Davies, S. Moumdji, R. Colombelli, J. Mangeney, J. Tignon, and S. S. Dhillon, "Engineered far-fields of metal-metal terahertz quantum cascade lasers with integrated planar horn structures," **Opt. Express** 24, 2174 (2016).

[3] F. Wang, K. Maussang, S. Moumdji, R. Colombelli, J. R. Freeman, I. Kundu, L. Li, E. H. Linfield, A. G. Davies, J. Mangeney, J. Tignon, and S. S. Dhillon, "Generating ultrafast pulses of light from quantum cascade lasers," **Optica** 2, 944 (2015).

[4] J. Maysonnave, S. Huppert, F. Wang, S. Maero, C. Berger, W. de Heer, T. B. Norris, L. A. De Vaulchier, S. Dhillon, J. Tignon, R. Ferreira, and J. Mangeney, "Terahertz generation by dynamical photon drag effect in graphene excited by femtosecond optical pulses" **Nano Lett.** 14, 5797 (2014).

Patent:

A patent on ultrashort terahertz pulse generation from quantum cascade lasers is in process.

Conference talks (*Invited keynote):

[1] F. Wang, K. Maussang, S. Moumdji, R. Colombelli, J. R. Freeman, I. Kundu, L. Li, E. H. Linfield, A. G. Davies, J. Mangeney, J. Tignon, S. S. Dhillon, ‘‘*Terahertz pulse generation from quantum cascade lasers*’’, **International Conference on Intersubband Transitions in Quantum Wells (ITQW)** (2015).

[2] I. Kundu, F. Wang, S. S. Dhillon, J. R. Freeman, A. Valavanis, L. Chen, L. Li, J. Tignon, P.Dean, E. H. Linfield, A. G. Davies, ‘‘*Laser dynamics of coupled cavity terahertz quantum cascade lasers – from multimode to single mode emission*’’, **International Conference on Intersubband Transitions in Quantum Wells (ITQW)** (2015).

[3]*****J. Mangeney, J. Maysonnave, S. Huppert, F. Wang, C. Berger, H. Walt, T. Norris, L. A. De Vaulchier, S. Dhillon, J. Tignon, R. Ferreira, ‘‘*THz emission from graphene induced by dynamical photon drag*’’, **International Conference on Infrared, Millimeter, and Terahertz Waves (IRMMW-THz)** (2015).

[4] F. Wang, I. Kundu, L. Li, E. H. Linfield, A. G. Davies, S. Moumdji, R. Colombelli, J. Mangeney, J. Tignon, S. S. Dhillon, ‘‘*Far-field engineering of metal-metal terahertz quantum cascade lasers with integrated horn antennas*’’, **International Conference on Infrared, Millimeter, and Terahertz Waves (IRMMW-THz)** (2015).

[5]*****F. Wang, K. Maussang, S. Moumdji, R. Colombelli, J. R. Freeman, I. Kundu, L. Li, E. H. Linfield, A. G. Davies, J. Mangeney, J. Tignon, S. S. Dhillon, ‘‘*Terahertz pulse generation from quantum cascade lasers*’’, **International Conference on Infrared, Millimeter, and Terahertz Waves (IRMMW-THz)** (2015).

[6] F. Wang, K. Maussang, S. S. Dhillon, J. Tignon, ‘‘*Functionalization of THz Quantum Cascade Lasers*’’, **IEEE International Symposium on Antennas and Propagation and North American Radio Science Meeting** (2015).

[7] F. Wang, A. Brewer, J. Freeman, J. Maysonnave, S. Moumdji, R. Colombelli, I. Kundu, L. Li, E. H. Linfield, A. G. Davies, H. E. Beere, D. A. Ritchie, S. S. Dhillon, J. Tignon, ‘‘*Injection seeding and modelocking of metal-metal terahertz quantum cascade lasers*’’, **CLEO: Science and Innovations, CLEO-SI 2015,** pp.2267. (2015).

[8] F. Wang, A. Brewer, J. R. Freeman, J. Maysonnave, S. Moumdji, R. Colombelli, I. Kundu, L. Li, E. H. Linfield, A. G. Davies, H. E. Beere, D. A. Ritchie, J. Tignon, S. S. Dhillon, ‘‘*Injection seeding of metal-metal Terahertz quantum cascade lasers*’’, **Optical Terahertz Science and Technology Conference (OTST)** (2015).

[9] F. Wang, A. Brewer, J. R. Freeman, J. Maysonnave, S. Moumdji, R. Colombelli, I. Kundu, L. Li, E. H. Linfield, A. G. Davies, H. E. Beere, D. A. Ritchie, J. Tignon, S. S. Dhillon, ‘‘*Injection seeding of metal-metal Terahertz quantum cascade lasers’’*, **International Quantum Cascade Lasers School & Workshop (IQCLSW)** (2014).

[10] F. Wang, A. Brewer, J. Freeman, J. Maysonnave, S. Moumdji, R. Colombelli, I. Kundu, L. Li, E. H. Linfield, A. G. Davies, H. E. Beere, D. A. Ritchie, J. Tignon, S. S. Dhillon, ‘‘*Injection seeding of metal-metal Terahertz quantum cascade lasers’’*, **Condensed Matter in Paris: CMD25-JMC14** (2014).

References

[1] A. E. Siegman, *Lasers* (University Science Books, 1986).

[2] W. T. H. III and C. H. Lee, *Light-Matter Interaction* (John Wiley & Sons, 2008).

[3] S. A. Diddams, L. Hollberg, and V. Mbele, Nature **445,** 627 (2007).

[4] M. Hohenleutner, F. Langer, O. Schubert, M. Knorr, U. Huttner, S. W. Koch, M. Kira, and R. Huber, Nature **523**, 572 (2015).

[5] R. F. Curl, F. Capasso, C. Gmachl, A. A. Kosterev, B. McManus, R. Lewicki, M. Pusharsky, G. Wysocki, and F. K. Tittel, Chem. Phys. Lett. **487**, 1 (2010).

[6] E. U. Rafailov, M. A. Cataluna, and W. Sibbett, Nat. Photonics **1**, 395 (2007).

[7] A. H. Quarterman, K. G. Wilcox, V. Apostolopoulos, Z. Mihoubi, S. P. Elsmere, I. Farrer, D. A. Ritchie, and A. Tropper, Nat. Photonics **3**, (2009).

[8] P. Klopp, U. Griebner, M. Zorn, and M. Weyers, Appl. Phys. Lett. **98**, 71103 (2011).

[9] G. Keiser, in *Wiley Encycl. Telecommun.* (John Wiley & Sons, Inc., 2003).

[10] D. E. Spence, P. N. Kean, and W. Sibbett, Opt. Lett. **16**, 42 (1991).

[11] Y.-S. Lee, *Principles of Terahertz Science and Technology* (Springer, New York, 2009).

[12] M. Tonouchi, Nat. Photonics **1**, 97 (2007).

[13] B. Ferguson and X.-C. Zhang, Nat. Mater. **1**, 26 (2002).

[14] M. Kuznetsov, F. Hakimi, R. Sprague, and A. Mooradian, IEEE Photonics Technol. Lett. **9**, 1063 (1997).

[15] E. Towe, R. F. Leheny, and A. Yang, IEEE J. Sel. Top. Quantum Electron. **6**, 1458 (2000).

[16] M. Kuznetsov, in *Semicond. Disk Lasers*, edited by O. G. Okhotnikov (Wiley-VCH Verlag GmbH & Co. KGaA, 2010), pp. 1–71.

[17] A. S. Weling, B. B. Hu, N. M. Froberg, and D. H. Auston, Appl. Phys. Lett. **64**, 137 (1994).

[18] Y.-S. Lee, T. Meade, V. Perlin, H. Winful, T. B. Norris, and A. Galvanauskas, Appl. Phys. Lett. **76**, 2505 (2000).

[19] D. A. Deacon, L. R. Elias, J. M. Madey, G. J. Ramian, H. A. Schwettman, and T. I. Smith, Phys. Rev. Lett. **38**, 892 (1977).

[20] R. Köhler, A. Tredicucci, F. Beltram, H. E. Beere, E. H. Linfield, A. G. Davies, D. A. Ritchie, R. C. Lotti, and F. Rossi, Nature **417**, 156 (2002).

[21] J. Faist, F. Capasso, D. L. Sivco, C. Sirtori, A. L. Hutchinson, and A. Y. Cho, Science **264**, 553 (1994).

[22] R. P. Green, A. Tredicucci, N. Q. Vinh, B. Murdin, C. Pidgeon, H. E. Beere, and D. A. Ritchie, Phys. Rev. B **80**, (2009).

[23] J. R. Freeman, J. Maysonnave, S. Khanna, E. H. Linfield, A. G. Davies, S. S. Dhillon, and J. Tignon, Phys. Rev. A **87**, (2013).

[24] S. Barbieri, M. Ravaro, P. Gellie, G. Santarelli, C. Manquest, C. Sirtori, S. P. Khanna, E. H. Linfield, and A. G. Davies, Nat. Photonics **5**, 306 (2011).

[25] J. Maysonnave, K. Maussang, J. R. Freeman, N. Jukam, J. Madéo, P. Cavalié, R. Rungsawang, S. P. Khanna, E. H. Linfield, A. G. Davies, and others, Opt. Express **20**, 20855 (2012).

[26] F. Wang, K. Maussang, S. Moumdji, R. Colombelli, J. R. Freeman, I. Kundu, L. Li, E. H. Linfield, A. G. Davies, J. Mangeney, J. Tignon, and S. S. Dhillon, Optica **2**, 944 (2015).

[27] J. R. Freeman, J. Maysonnave, H. E. Beere, D. A. Ritchie, J. Tignon, and S. S. Dhillon, Opt. Express **21**, 16162 (2013).

[28] D. Burghoff, T.-Y. Kao, N. Han, C. W. I. Chan, X. Cai, Y. Yang, D. J. Hayton, J.-R. Gao, J. L. Reno, and Q. Hu, Nat. Photonics **8**, 462 (2014).

[29] M. Rösch, G. Scalari, M. Beck, and J. Faist, Nat. Photonics (2014).

[30] R. K. Hoffmann, *Handbook of Microwave Integrated Circuits* (Artech House, 1987).

[31] P. von Allmen, M. Berz, G. Petrocelli, F.-K. Reinhart, and G. Harbeke, Semicond. Sci. Technol. **3**, 1211 (1988).

[32] W. W. Chow and S. W. Koch, *Semiconductor-Laser Fundamentals* (Springer, 1999).

[33] L. A. Coldren, S. W. Corzine, and M. Mashanovitch, *Diode Lasers and Photonic Integrated Circuits*, 2. ed (Wiley, Hoboken, N.J, 2012).

[34] J. Faist, A. Tredicucci, F. Capasso, C. Sirtori, D. L. Sivco, J. N. Baillargeon, A. L. Hutchinson, and A. Y. Cho, IEEE J. Quantum Electron. **34**, 336 (1998).

[35] J. S. Yu, S. Slivken, A. Evans, L. Doris, and M. Razeghi, Appl. Phys. Lett. **83**, 2503 (2003).

[36] Y. Bai, N. Bandyopadhyay, S. Tsao, S. Slivken, and M. Razeghi, Appl. Phys. Lett. **98**, 181102 (2011).

[37] A. Lyakh, R. Maulini, A. Tsekoun, R. Go, and C. K. N. Patel, Opt. Express **20**, 24272 (2012).

[38] M. S. Vitiello, L. Consolino, S. Bartalini, A. Taschin, A. Tredicucci, M. Inguscio, and P. De Natale, Nat. Photonics **6**, 525 (2012).

[39] J. Faist, *Quantum Cascade Lasers* (OUP Oxford, 2013).

[40] J. Faist, M. Beck, T. Aellen, and E. Gini, Appl. Phys. Lett. **78**, 147 (2001).

[41] B. S. Williams, H. Callebaut, S. Kumar, Q. Hu, and J. L. Reno, Appl. Phys. Lett. **82**, 1015 (2003).

[42] G. Bastard, *Wave Mechanics Applied to Semiconductor Heterostructures* (EDP Sciences, Les Ulis Cedex, France : New York, N.Y, 1992).

[43] V. Liverini, L. Nevou, F. Castellano, A. Bismuto, M. Beck, F. Gramm, and J. Faist, Appl. Phys. Lett. **101**, 261113 (2012).

[44] B. S. Williams, Nat. Photonics **1**, 517 (2007).

[45] C. Jirauschek and T. Kubis, Appl. Phys. Rev. **1**, 11307 (2014).

[46] C. Worrall, J. Alton, M. Houghton, S. Barbieri, H. E. Beere, D. Ritchie, and C. Sirtori, Opt. Express **14**, 171 (2006).

[47] D. R. Bacon, J. R. Freeman, R. A. Mohandas, L. Li, E. H. Linfield, A. G. Davies, and P. Dean, Appl. Phys. Lett. **108**, 81104 (2016).

[48] S. Fathololoumi, E. Dupont, C. W. I. Chan, Z. R. Wasilewski, S. R. Laframboise, D. Ban, A. Matyas, C. Jirauschek, Q. Hu, and H. C. Liu, Opt. Express **20**, 3866 (2012).

[49] M. I. Amanti, G. Scalari, R. Terazzi, M. Fischer, M. Beck, J. Faist, A. Rudra, P. Gallo, and E. Kapon, New J. Phys. **11**, 125022 (2009).

[50] M. Hajenius, P. Khosropanah, J. N. Hovenier, J. R. Gao, T. M. Klapwijk, S. Barbieri, S. Dhillon, P. Filloux, C. Sirtori, D. A. Ritchie, and others, Opt. Lett. **33**, 312 (2008).

[51] L. Li, L. Chen, J. Zhu, J. Freeman, P. Dean, A. Valavanis, A. G. Davies, and E. H. Linfield, Electron. Lett. **50**, 309 (2014).

[52] C. Sirtori, F. Capasso, J. Faist, A. L. Hutchinson, D. L. Sivco, and A. Y. Cho, IEEE J. Quantum Electron. **34**, 1722 (1998).

[53] A. W. M. Lee, B. S. Wil, S. Kumar, Qing Hu, and J. L. Reno, IEEE Photonics Technol. Lett. **18**, 1415 (2006).

[54] J. R. Freeman, J. Maysonnave, N. Jukam, P. Cavalié, K. Maussang, H. E. Beere, D. A. Ritchie, J. Mangeney, S. S. Dhillon, and J. Tignon, Appl. Phys. Lett. **101**, 181115 (2012).

[55] S. Barbieri, J. Alton, S. S. Dhillon, H. E. Beere, M. Evans, E. H. Linfield, A. G. Davies, D. A. Ritchie, R. Kohler, A. Tredicucci, and F. Beltram, IEEE J. Quantum Electron. **39**, 586 (2003).

[56] L. Ajili, G. Scalari, N. Hoyler, M. Giovannini, and J. Faist, Appl. Phys. Lett. **87**, 141107 (2005).

[57] M. I. Amanti, M. Fischer, G. Scalari, M. Beck, and J. Faist, Nat. Photonics **3**, 586 (2009).

[58] Y. Chassagneux, R. Colombelli, W. Maineult, S. Barbieri, H. E. Beere, D. A. Ritchie, S. P. Khanna, E. H. Linfield, and A. G. Davies, Nature **457**, 174 (2009).

[59] G. Karunasiri, B. N. Behnken, P. R. Robrish, D. R. Chamberlin, and J. Faist, (2008).

[60] P. Patimisco, S. Borri, A. Sampaolo, H. E. Beere, D. A. Ritchie, M. S. Vitiello, G. Scamarcio, and V. Spagnolo, The Analyst **139**, 2079 (2014).

[61] H.-W. Hübers, S. G. Pavlov, H. Richter, A. D. Semenov, L. Mahler, A. Tredicucci, H. E. Beere, and D. A. Ritchie, Appl. Phys. Lett. **89**, 61115 (2006).

[62] S. Bartalini, L. Consolino, P. Cancio, P. De Natale, P. Bartolini, A. Taschin, M. De Pas, H. Beere, D. Ritchie, M. S. Vitiello, and R. Torre, Phys. Rev. X **4**, (2014).

[63] B. Argence, B. Chanteau, O. Lopez, D. Nicolodi, M. Abgrall, C. Chardonnet, C. Daussy, B. Darquié, Y. Le Coq, and A. Amy-Klein, Nat. Photonics **9**, 456 (2015).

[64] M. A. Herman and H. Sitter, *Molecular Beam Epitaxy: Fundamentals and Current Status* (Springer Science & Business Media, 2012).

[65] A. Rogalski and F. Sizov, Opto-Electron. Rev. **19**, (2011).

[66] J. Yan, M.-H. Kim, J. A. Elle, A. B. Sushkov, G. S. Jenkins, H. M. Milchberg, M. S. Fuhrer, and H. D. Drew, Nat. Nanotechnol. **7**, 472 (2012).

[67] D. Oustinov, N. Jukam, R. Rungsawang, J. Madéo, S. Barbieri, P. Filloux, C. Sirtori, X. Marcadet, J. Tignon, and S. Dhillon, Nat. Commun. **1**, 1 (2010).

[68] M. Van Exter, C. Fattinger, and D. Grischkowsky, Opt. Lett. **14**, 1128 (1989).

[69] N. Jukam, S. S. Dhillon, D. Oustinov, J. Madéo, J. Tignon, R. Colombelli, P. Dean, M. Salih, S. P. Khanna, E. H. Linfield, and A. G. Davies, Appl. Phys. Lett. **94**, 251108 (2009).

[70] J. Madéo, N. Jukam, D. Oustinov, M. Rosticher, R. Rungsawang, J. Tignon, and S. S. Dhillon, Electron. Lett. **46**, 611 (2010).

[71] Q. Wu and X.-C. Zhang, Appl. Phys. Lett. **67**, 3523 (1995).

[72] M. C. Nuss and J. Orenstein, in *Millim. Submillimeter Wave Spectrosc. Solids*, edited by P. D. G. Grüner (Springer Berlin Heidelberg, 1998), pp. 7–50.

[73] H. Zhong, N. Karpowicz, and X.-C. Zhang, Appl. Phys. Lett. **88**, 261103 (2006).

[74] K. Maussang, A. Brewer, J. Palomo, J.-M. Manceau, R. Colombelli, I. Sagnes, J. Mangeney, J. Tignon, and S. S. Dhillon, IEEE Trans. Terahertz Sci. Technol. **6**, 20 (2016).

[75] P. U. Jepsen, R. H. Jacobsen, and S. R. Keiding, JOSA B **13**, 2424 (1996).

[76] J. Dai, J. Liu, and X.-C. Zhang, IEEE J. Sel. Top. Quantum Electron. **17**, 183 (2011).

[77] Q. Wu, M. Litz, and X.-C. Zhang, Appl. Phys. Lett. **68**, 2924 (1996).

[78] Q. Wu and X.-C. Zhang, Appl. Phys. Lett. **70**, 1784 (1997).

[79] J. Kröll, J. Darmo, S. S. Dhillon, X. Marcadet, M. Calligaro, C. Sirtori, and K. Unterrainer, Nature **449**, 698 (2007).

[80] E. Willis and J. Lamb, Phys. Rev. **134**, (1964).

[81] L. E. Hargrove, R. L. Fork, and M. A. Pollack, Appl. Phys. Lett. **5**, 4 (1964).

[82] R. W. Boyd, *Nonlinear Optics* (Academic Press, 2003).

[83] E. P. Ippen, Appl. Phys. Lett. **21**, 348 (1972).

[84] S. Barbieri, P. Gellie, G. Santarelli, L. Ding, W. Maineult, C. Sirtori, R. Colombelli, H. Beere, and D. Ritchie, Nat. Photonics **4**, 636 (2010).

[85] J. L. Hall, Nobel Lect. Defin. Meas. Opt. Freq. Opt. Clock Oppor. More (n.d.).

[86] F. Kärtner, Lect. Notes Fundam. Photonics Quantum Electron. Electr. Eng. Comput. Sci. MIT OpenCourseWare (2006).

[87] R. L. Fork, O. E. Martinez, and J. P. Gordon, Opt. Lett. **9**, 150 (1984).

[88] S. Kane and J. Squier, JOSA B **14**, 661 (1997).

[89] Y. Kaluzny, P. Goy, M. Gross, J. M. Raimond, and S. Haroche, Phys. Rev. Lett. **51**, 1175 (1983).

[90] T. L. Paoli and J. E. Ripper, Proc. IEEE **58**, 1457 (1970).

[91] P. A. Schulz, IEEE J. Quantum Electron. **24**, 1039 (1988).

[92] R. Roy, P. A. Schulz, and A. Walther, Opt. Lett. **12**, 672 (1987).

[93] B. K. Garside, J. Appl. Phys. **44**, 2335 (1973).

[94] T. Brabec, C. Spielmann, P. F. Curley, and F. Krausz, Opt. Lett. **17**, 1292 (1992).

[95] P. Gellie, S. Barbieri, J.-F. Lampin, P. Filloux, C. Manquest, C. Sirtori, I. Sagnes, S. P. Khanna, I. Sagnes, H. E. Linfield, A. G. Davies, H. Beere, and D. Ritchie, Opt. Express **18**, 20799 (2010).

[96] E. P. Ippen, Appl. Phys. B **58**, 159 (1994).

[97] A. G. Weber, M. Schell, G. Fischbeck, and D. Bimberg, Quantum Electron. IEEE J. Of **28**, 2220 (1992).

[98] V. F. Olle, A. Wonfor, L. A. M. Sulmoni, P. P. Vasilev, J.-M. Lamy, J.-F. Carlin, N. Grandjean, R. V. Penty, and I. H. White, IEEE Photonics Technol. Lett. **25**, 1514 (2013).

[99] G. Fiol, D. Arsenijević, D. Bimberg, A. G. Vladimirov, M. Wolfrum, E. A. Viktorov, and P. Mandel, Appl. Phys. Lett. **96**, 11104 (2010).

[100] R. Arkhipov, A. Pimenov, M. Radziunas, D. Rachinskii, A. G. Vladimirov, D. Arsenijevic, H. Schmeckebier, and D. Bimberg, IEEE J. Sel. Top. Quantum Electron. **19**, 1100208 (2013).

[101] J. R. Freeman, O. Marshall, H. E. Beere, and D. A. Ritchie, Appl. Phys. Lett. **93**, 191119 (2008).

[102] R. Lang, IEEE J. Quantum Electron. **18**, 976 (1982).

[103] D. Turčinková, M. I. Amanti, G. Scalari, M. Beck, and J. Faist, Appl. Phys. Lett. **106**, 131107 (2015).

[104] K. Gürel, S. Schilt, A. Bismuto, Y. Bidaux, C. Tardy, S. Blaser, T. Gresch, and T. Südmeyer, Photonics **3**, 47 (2016).

[105] W. Maineult, P. Gellie, A. Andronico, P. Filloux, G. Leo, C. Sirtori, S. Barbieri, E. Peytavit, T. Akalin, J.-F. Lampin, H. E. Beere, and D. A. Ritchie, Appl. Phys. Lett. **93**, 183508 (2008).

[106] J. A. Fan, M. A. Belkin, F. Capasso, S. P. Khanna, M. Lachab, A. G. Davies, and E. H. Linfield, Appl. Phys. Lett. **92**, 31106 (2008).

[107] J. Maysonnave, N. Jukam, M. S. M. Ibrahim, R. Rungsawang, K. Maussang, J. Madéo, P. Cavalié, P. Dean, S. P. Khanna, D. P. Steenson, and others, Opt. Express **20**, 16662 (2012).

[108] R. W. Ziolkowski, J. M. Arnold, and D. M. Gogny, Phys. Rev. A **52**, 3082 (1995).

[109] S.-H. Chang and A. Taflove, Opt. Express **12**, 3827 (2004).

[110] N. Jukam, S. Dhillon, Z.-Y. Zhao, G. Duerr, J. Armijo, N. Sirmons, S. Hameau, S. Barbieri, P. Filloux, C. Sirtori, and others, Sel. Top. Quantum Electron. IEEE J. Of **14**, 436 (2008).

[111] W. Kuehn, W. Parz, P. Gaal, K. Reimann, M. Woerner, T. Elsaesser, T. Müller, J. Darmo, K. Unterrainer, M. Austerer, G. Strasser, L. R. Wilson, J. W. Cockburn, A. B. Krysa, and J. S. Roberts, Appl. Phys. Lett. **93**, 151106 (2008).

[112] Y. Wang and A. Belyanin, Opt. Express **23**, 4173 (2015).

[113] C. Wang, L. Kuznetsova, V. M. Gkortsas, L. Diehl, F. X. Kärtner, A. Belkin, X. Li, D. Ham, H. Schneider, P. Grant, C. Y. Song, S. Haffouz, Z. R. Wasilewski, H. C. Liu, and F. Capasso, Opt. Express **17**, 12929 (2009).

[114] W. Maineult, L. Ding, P. Gellie, P. Filloux, C. Sirtori, S. Barbieri, T. Akalin, J.-F. Lampin, I. Sagnes, H. E. Beere, and others, Appl. Phys. Lett. **96**, 21108 (2010).

[115] Y. Wang and A. Belyanin, Opt. Express **23**, 4173 (2015).

[116] A. K. Wójcik, P. Malara, R. Blanchard, T. S. Mansuripur, F. Capasso, and A. Belyanin, Appl. Phys. Lett. **103**, 231102 (2013).

[117] A. Hugi, G. Villares, S. Blaser, H. C. Liu, and J. Faist, Nature **492**, 229 (2012).

[118] A. Brewer, J. R. Freeman, P. Cavalié, J. Maysonnave, J. Tignon, S. S. Dhillon, H. E. Beere, and D. A. Ritchie, Appl. Phys. Lett. **104**, 81107 (2014).

[119] B. Golubovic, R. R. Austin, M. K. Steiner-Shepard, M. K. Reed, S. A. Diddams, D. J. Jones, and A. G. Van Engen, Opt. Lett. **25**, 275 (2000).

[120] D. Burghoff, Y. Yang, D. J. Hayton, J.-R. Gao, J. L. Reno, and Q. Hu, Opt. Express **23**, 1190 (2015).

[121] G. Villares, S. Riedi, J. Wolf, D. Kazakov, M. J. Süess, P. Jouy, M. Beck, and J. Faist, Optica **3**, 252 (2016).

[122] P. Friedli, H. Sigg, B. Hinkov, A. Hugi, S. Riedi, M. Beck, and J. Faist, Appl. Phys. Lett. **102**, 222104 (2013).

[123] J. Madéo, P. Cavalié, J. R. Freeman, N. Jukam, J. Maysonnave, K. Maussang, H. E. Beere, D. A. Ritchie, C. Sirtori, J. Tignon, and S. S. Dhillon, Nat. Photonics **6**, 519 (2012).

[124] S. S. Dhillon, C. Sirtori, J. Alton, S. Barbieri, A. de Rossi, H. E. Beere, and D. A. Ritchie, Nat. Photonics **1**, 411 (2007).

[125] S. Houver, P. Cavalié, M. R. St-Jean, M. I. Amanti, C. Sirtori, L. H. Li, A. G. Davies, E. H. Linfield, T. A. S. Pereira, A. Lebreton, J. Tignon, and S. S. Dhillon, Opt. Express **23**, 4012 (2015).

[126] F. Gires and P. Tournois, C R Acad Sci Paris **258**, 6112 (1964).

[127] R. Szipöcs, A. Köházi-Kis, S. Lakó, P. Apai, A. P. Kovács, G. DeBell, L. Mott, A. W. Louderback, A. V. Tikhonravov, and M. K. Trubetskov, Appl. Phys. B **70**, S51 (2000).

[128] J. D. Kafka, M. L. Watts, and J.-W. Pieterse, IEEE J. Quantum Electron. **28**, 2151 (1992).

[129] V. Lucarini, J. J. Saarinen, K.-E. Peiponen, and E. M. Vartiainen, *Kramers-Kronig Relations in Optical Materials Research* (Springer Science & Business Media, 2005).

[130] F. Kärtner, Lect. Notes Ultrafast Opt. Electr. Eng. Comput. Sci. MIT OpenCourseWare (2005).

[131] H. W. Mocker and R. J. Collins, Appl. Phys. Lett. **7**, 270 (1965).

[132] E. P. Ippen, D. J. Eilenberger, and R. W. Dixon, Appl. Phys. Lett. **37**, 267 (1980).

[133] G. Villares, A. Hugi, S. Blaser, and J. Faist, Nat. Commun. **5**, 5192 (2014).

[134] G. Xu, R. Colombelli, S. P. Khanna, A. Belarouci, X. Letartre, L. Li, E. H. Linfield, A. G. Davies, H. E. Beere, and D. A. Ritchie, Nat. Commun. **3**, 952 (2012).

[135] J. A. Fan, M. A. Belkin, F. Capasso, S. Khanna, M. Lachab, A. G. Davies, and E. H. Linfield, Opt. Express **14**, 11672 (2006).

[136] M. Wienold, B. Röben, L. Schrottke, R. Sharma, A. Tahraoui, K. Biermann, and H. T. Grahn, Opt. Express **22**, 3334 (2014).

[137] M. S. Vitiello, M. Nobile, A. Ronzani, A. Tredicucci, F. Castellano, V. Talora, L. Li, E. H. Linfield, and A. G. Davies, Nat. Commun. **5**, 5884 (2014).

[138] D. Burghoff, T.-Y. Kao, D. Ban, A. W. M. Lee, Q. Hu, and J. Reno, Appl. Phys. Lett. **98**, 61112 (2011).

[139] M. C. Wanke, 33rd Int. Conf. Infrared Millim. Terahertz Waves (n.d.).

[140] H. Eom, *Electromagnetic Wave Theory for Boundary-Value Problems: An Advanced Course on Analytical Methods* (Springer Science & Business Media, 2013).

[141] P. Gellie, W. Maineult, A. Andronico, G. Leo, C. Sirtori, S. Barbieri, Y. Chassagneux, J. R. Coudevylle, R. Colombelli, S. P. Khanna, E. H. Linfield, and A. G. Davies, J. Appl. Phys. **104**, 124513 (2008).

Panthéon (200 meters away from my laboratory)

The garden of the École Normale Supérieure (I have lunch and dinner here in the canteen)

The Centre Culturel Irlandais (I have lunch here sometimes if the weather is good)

The Campus Cordeliers, the University of Paris VI (the activities organized by doctoral school often take place here)

The statues in the École Normale Supérieure– Paris

My work place: Department of Physics of the École Normale Supérieure – Paris

Abstract

In the THz frequency range, a semiconductor based technology platform for intense and ultrashort pulse generation has yet to be realised. THz quantum cascade lasers (QCLs) are foundational semiconductor devices for laser action in the THz range and are suitable medium for pulse generation. However, to date, the generation of THz pulses from QCLs has been limited to 10 - 20 ps despite several years of research effort. In this thesis, I will show how this bottleneck in QCL technology can be overcome and demonstrate a novel method to realize ultrashort pulses in the THz range from this compact semiconductor device. Towards this final objective and realization of my thesis, I will show several milestones that permitted our goal of short pulses from QCLs to be achieved. Starting off from the current state-of-the-art, using narrow spectral bandwidth QCLs in single-plasmon waveguides, I will demonstrate ~20 ps long THz pulses at low temperatures (10K). This is followed by, for the first time, mode-locking of broad spectral bandwidth QCLs in sub-wavelength metal-metal waveguides at 'high' temperatures (77K). As a result, I will show ~11 ps that are limited by the electrical modulation and the index dispersion and, importantly, not limited by the inherent spectral bandwidth. This will then bring us to resolve these limitations and generate ultrashort pulses (~5 ps) with the potential to go considerably further to the single-cycle regime.

Keywords: Terahertz, Ultrafast Pulse, Quantum Cascade Lasers, Mode-locking, Time-domain Spectroscopy, Far-field